Draft: February 16, 2026

Fragmented Aperture Antennas

Computational Design of Antenna Structure

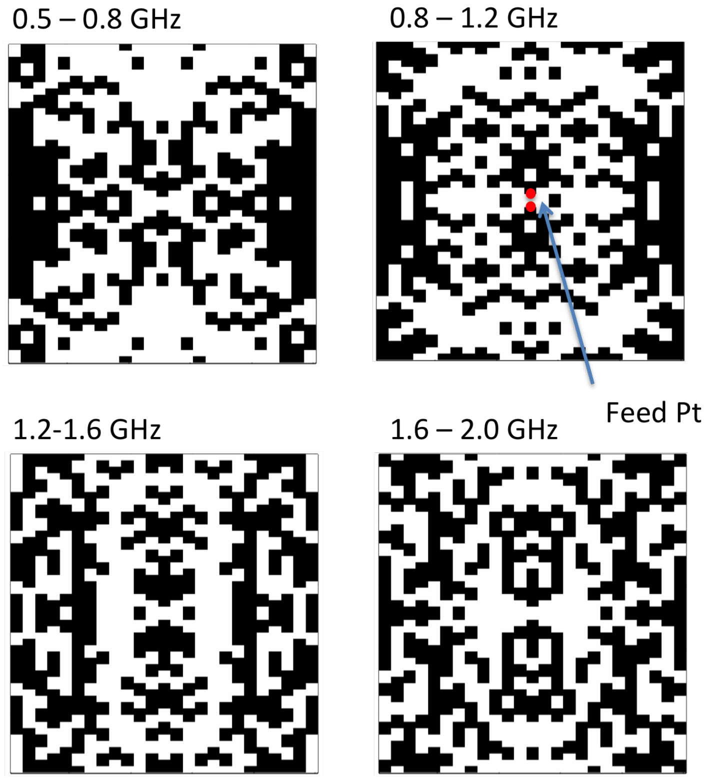

Dr. James G. Maloney
Inventor of the Fragmented Aperture Antenna

Copyright Notice and Fair Use Statement

Draft Manuscript Notice

This is a draft manuscript in active development. Formal permissions are being sought from IEEE and other copyright holders for specific figures reproduced from published papers. The manuscript may be revised as permissions are granted, denied, or figures are replaced. Readers should expect the final version to differ from this draft.

Copyright and Permissions

This book, *Fragmented Aperture Antennas*, is provided freely for educational and research purposes. It is not sold commercially and is distributed as an open educational resource to advance knowledge in the field of computational antenna design.

Use of Published Figures and Data

This work includes figures, data, and results from previously published scientific papers to provide comprehensive documentation of the historical development and current state of fragmented aperture antenna technology. All such materials are used in accordance with established principles of fair use under U.S. Copyright Law (17 U.S.C. § 107) and international copyright conventions.

Fair Use Rationale

The use of published materials in this work satisfies the four-factor test for fair use:

1. **Purpose and Character:** This book is a non-commercial, educational work that provides scholarly analysis and historical documentation of fragmented aperture antenna technology. Materials are used to illustrate technical concepts and validate scientific claims within a transformative educational context.
2. **Nature of the Work:** Materials used are factual, scientific, and technical in nature, consisting primarily of measurement data, simulation results, and engineer-

ing diagrams from published research papers.

3. **Amount and Substantiality:** Only a small number of figures (typically 2–4) are reproduced from any single publication, representing a minor portion of the original works and only what is necessary for educational purposes.

4. **Market Effect:** This non-commercial educational work does not compete with or substitute for the original publications. Indeed, proper citation and discussion are intended to increase awareness of and citations to the original research.

Good Faith Permission Efforts

The author has made good faith efforts to contact authors and publishers of all referenced works to request permission for figure reproduction. Where permission has been explicitly granted, this is noted in the figure caption. Where permission could not be obtained after reasonable attempts, materials are included under fair use provisions as described above.

Attributions and Citations

All reproduced figures and data are attributed to their original sources directly in the figure caption, with complete bibliographic citations in the chapter references. Where applicable, copyright notices specified by publishers are included. These attributions serve both to comply with academic standards and to direct readers to the original publications for complete context.

Compliance and Removal Requests

The author respects the intellectual property rights of all researchers and publishers. If any copyright holder believes that material has been used inappropriately or wishes to request removal:

Contact: Dr. James G. Maloney
Email: jmaloney65@gmail.com

Upon receiving a substantiated request, the author will promptly:

1. Review the concern in good faith

2. Remove or replace the material if appropriate

3. Provide revised versions of the book as necessary

This book is hosted on GitHub and other platforms to facilitate rapid updates in response to any concerns.

Open Educational Resource

This book is provided as an open educational resource to:

- Document the historical development of fragmented aperture technology
- Provide educational materials for students and researchers
- Advance scientific knowledge in computational antenna design
- Preserve technical knowledge for future generations

The work is distributed freely without charge and without commercial intent.

No Warranty

Acknowledgment of Copyright Holders

The author gratefully acknowledges the following publishers and their contributions to scientific knowledge:

- **IEEE** (Institute of Electrical and Electronics Engineers)
- **IET** (Institution of Engineering and Technology)
- **Electromagnetics Academy**
- **AMTA** (Antenna Measurement Techniques Association)

And the many researchers whose work is cited throughout this book. Their contributions to the field of antenna engineering have made this comprehensive reference possible.

Version: 1.0
Last Updated: March 6, 2026

This document will be updated to reflect any permission grants received after publication.

Acknowledgments: Permissions Granted

Permissions Granted

The author gratefully acknowledges the following researchers and institutions who graciously granted permission to reproduce figures from their published work:

Permissions Received

[This section will be updated as permissions are received from external researchers.]

Materials Used Under Fair Use

The following materials are used under fair use provisions (17 U.S.C. § 107) where permission could not be obtained after good faith attempts to contact authors. If any copyright holder listed below wishes to grant explicit permission retroactively, please contact the author.

[This section will list specific figures and papers used under fair use after permission attempts.]

Collaborative Spirit

These permissions, whether explicitly granted or used under fair use provisions, demonstrate the collaborative spirit of the scientific community. The author deeply appreciates the willingness of researchers to share their work for educational purposes, and hopes this book will increase awareness of and citations to their important contributions.

Contents

List of Figures

List of Tables

Dedicated to my children Kelsey, Emily, Grace and Sam.

Acknowledgements

Over the years, I have had the pleasure to work with many smart individuals who each contributed to the development of Fragmented Aperture Antennas.

For my whole career, Prof. Glenn Smith has always be a major supporter of my research efforts. Starting with teaching me how to do research during my Ph.D. thesis, to discussing many research issues over coffee during my university lab years, to co-authoring many book chapters with me, to helping invent the Fragmented Aperture, Dr Smith became a treasured collaborator and friend.

In the early years, I had the good fortune to work with one of the brightest minds, Dr. Morris Kesler. Morris was also one of the co-inventors of the Fragmented Aperture. Morris also assisted me in writing book chapters on Modeling Periodic Structures that are used in the analysis and design of phased array antennas and other periodic structures.

I had many conversations with Dr. Eric Kuster when stuck on a research topic, and his non-engineer view point was very helpful to me over the years.

I would like to thank Mr. Paul Friederich, Dr. Lon Pringle, Mr. Jim Acree for their dedicated support as project directors for both the research on Fragmented Apertures and for helping advocate for customer solutions based on Fragmented Apertures.

In the later years, the development of Fragmented Aperture solutions for many diverse applications were impacted by the assistance of Mr. Brad Baker, Mr. Kevin Cook, Dr. Doug Denison, Ms. Lynn Fountain, Mr. James Fraley, Mr. David Landgren, and Dr. Todd Lee.

The fabrication of many of the Fragmented Apertures relied heavily on the machining skills of the best machinist I ever met, Mr. Kurt Weismayer. Without Kurt's skills, many of the antennas certainly would not have been built exactly, and the measured RF performance would have been in worse agreement with the model predictions.

I also have greatly enjoyed working closely with Dr. John Schultz over the last 10+ years. Collaborating with John on many research projects has been rewarding and always a pleasure.

Lastly, I want to thank Ms. Rebecca Schultz and Dr. Kate Maloney for allowing me to assist Compass Technology Groups research efforts over the last few years. Also, I would like to thank them for their support in further developing the Fragment Aperture antenna.

Chapter 1

Introduction to Fragmented Aperture Antennas

1.1 Overview

This book describes a class of antennas called Fragmented Aperture Antennas. Unlike traditional antennas whose physical shapes are guided by analytical insight and engineering intuition, fragmented aperture antennas are designed computationally. A planar conducting surface is divided into many sub-wavelength regions, or pixels, each of which may be either conducting or non-conducting. A genetic algorithm, working in concert with a full-wave electromagnetic simulation, determines which pixels should be conducting and which should not, so as to best satisfy a given set of antenna performance requirements. The resulting antenna structures are complex, non-intuitive metallic patterns that often approach the theoretical limits of antenna performance for a given aperture size.

The fragmented aperture concept was invented in the late 1990s [1], and the term “Fragmented Aperture Antenna” was coined by the author upon visual inspection of the optimized designs, which consistently showed metallic pixels forming many connected and disconnected fragments across the aperture surface. The original concept was disclosed in U.S. Patent 6,323,809 [2]. Since then, the concept has been extended to reconfigurable antennas [3], ultra-wideband phased arrays with bandwidths exceeding 33:1 [4], and wide-scanning array designs [5]. Other research groups have successfully adopted the approach for broadband phased array element design using genetic algorithms [6] and fragmented antennas based on coupled small radiating elements [7]. Fragmented aperture antennas have been successfully designed, fabricated, and measured for a wide variety of applications spanning frequencies from UHF through millimeter wave.

This introductory chapter provides background on fundamental antenna concepts, motivates the need for a computational approach to antenna design, introduces the fragmented aperture concept, and concludes with a roadmap for the remainder of the book.

1.2 Antenna Fundamentals

An antenna is a transducer between guided electromagnetic waves, such as those on a transmission line or waveguide, and free-space electromagnetic waves that propagate away from the antenna. When used for transmission, an antenna converts a guided signal into radiation; when used for reception, it captures incident radiation and converts it into a guided signal. By the principle of reciprocity, the properties of an antenna are the same whether it is transmitting or receiving [8].

Several key parameters characterize the performance of an antenna:

1.2.1 Radiation Pattern

The radiation pattern describes the spatial distribution of electromagnetic energy radiated by an antenna as a function of direction. It is typically represented as a plot of radiated power (or field strength) versus angle, normalized to the direction of maximum radiation. Important features of the radiation pattern include the main beam (or main lobe), which is the angular region of strongest radiation; the sidelobes, which are regions of lesser radiation surrounding the main beam; and the back lobe, which is radiation in the direction opposite the main beam. The beamwidth, usually defined as the angular width between the half-power (-3 dB) points of the main beam, quantifies how directional the antenna is.

1.2.2 Directivity and Gain

Directivity is a measure of how effectively an antenna concentrates radiated energy in a particular direction compared to an isotropic radiator (a hypothetical antenna that radiates equally in all directions). The directivity D in a given direction is defined as the ratio of the radiation intensity in that direction to the radiation intensity averaged over all directions:

$$D = \frac{U(\theta, \phi)}{U_{\text{avg}}} = \frac{4\pi U(\theta, \phi)}{P_{\text{rad}}} \tag{1.1}$$

where $U(\theta, \phi)$ is the radiation intensity (power per unit solid angle) and P_{rad} is the total radiated power.

Gain is closely related to directivity but also accounts for losses within the antenna. The gain G is related to the directivity D by the radiation efficiency η:

$$G = \eta\, D \tag{1.2}$$

where η accounts for ohmic and dielectric losses in the antenna structure.

In practice, it is often useful to work with the *realized gain*, which further accounts for impedance mismatch between the antenna and its feed:

$$G_{\text{realized}} = (1 - |\Gamma|^2)\, G \tag{1.3}$$

where Γ is the voltage reflection coefficient at the antenna terminals. The realized gain captures the overall effectiveness of the antenna in converting guided-wave power into radiation in a given direction.

1.2.3 Aperture and Aperture Efficiency

A fundamental result in antenna theory relates the maximum achievable gain of an antenna to its physical aperture area A:

$$G_{\text{max}} = \frac{4\pi A}{\lambda^2} \tag{1.4}$$

where λ is the free-space wavelength. This result applies to a uniformly illuminated aperture radiating into one hemisphere (i.e., with a ground plane or reflector behind it). For an aperture that radiates equally into both hemispheres (no ground plane), the limit becomes $2\pi A/\lambda^2$.

The aperture efficiency η_a describes how closely an antenna approaches this theoretical limit:

$$\eta_a = \frac{G}{G_{\text{max}}} = \frac{G\lambda^2}{4\pi A} \tag{1.5}$$

Traditional antenna designs rarely achieve aperture efficiencies above 50–70%. As will be shown throughout this book, fragmented aperture antennas routinely approach the theoretical aperture gain limit, often achieving efficiencies that exceed those of conventional designs.

1.2.4 Bandwidth

Every antenna has a finite bandwidth over which it operates satisfactorily. Bandwidth may be defined in terms of several criteria, but the most common is the impedance bandwidth: the range of frequencies over which the antenna maintains an acceptable impedance match to its feed line. A common threshold is a voltage standing wave ratio (VSWR) of 2:1, corresponding to a return loss of approximately 10 dB, meaning that no more than 10% of the incident power is reflected back to the source. More demanding applications may require a VSWR below 1.5:1 (return loss better than 14 dB) or even 1.3:1.

Bandwidth can be expressed as a ratio of the upper to lower frequency limits (e.g., 10:1 bandwidth for an antenna operating from 1 to 10 GHz) or as a fractional bandwidth:

$$\text{BW}_{\text{frac}} = \frac{f_H - f_L}{f_c} \tag{1.6}$$

where f_H and f_L are the upper and lower frequency limits and f_c is the center frequency. Antennas with bandwidths of 2:1 or greater are often called wideband, while those exceeding roughly 10:1 are called ultra-wideband.

Achieving wide bandwidth while maintaining high gain and an acceptable impedance match is one of the central challenges in antenna design and a particular strength of the fragmented aperture approach.

1.2.5 Polarization

The polarization of an antenna describes the orientation of the electric field vector of the radiated wave. Common polarizations include linear (vertical or horizontal), circular (right-hand or left-hand), and elliptical. The polarization of the radiated field is determined by the currents flowing on the antenna structure, and achieving a desired polarization is an important design goal. Fragmented aperture antennas can be designed for any of these polarizations, including cases where the polarization varies with beam direction.

1.3 Antenna Arrays

A single antenna element has a radiation pattern determined by its geometry and size. To achieve higher gain, narrower beams, or the ability to steer the beam electronically, multiple antenna elements are arranged in an array. In an array, the signals from the individual elements combine coherently, and the resulting radiation pattern is the product of the individual element pattern and the array factor, which depends on the element spacing, number of elements, and the relative amplitude and phase of the excitation at each element.

Electronic beam steering is accomplished by adjusting the relative phases of the signals at each element. This is the basis of the phased array, which can rapidly redirect its beam without physically moving the antenna. Phased arrays are essential in modern radar, communications, and electronic warfare systems.

However, the design of wideband phased arrays presents significant challenges. Mutual coupling between array elements—the electromagnetic interaction between neighboring elements—can cause scan blindness, a condition where the array is poorly matched at certain combinations of frequency and scan angle. Traditional array design approaches attempt to minimize mutual coupling, but as will be shown in this book, the fragmented aperture approach embraces mutual coupling, and in some cases exploits direct electrical connections between elements to achieve bandwidths that far exceed those of conventional array elements.

1.4 Limitations of Traditional Antenna Design

Traditional antenna design relies on a library of known antenna types—dipoles, patches, horns, spirals, log-periodic structures, and others—each with well-understood behavior that can be predicted analytically or with simple numerical models. The designer selects an antenna type appropriate for the application and then adjusts a relatively small number of geometric parameters (lengths, widths, feed positions, spacings) to optimize performance.

This approach has been enormously successful and has produced the antenna designs in widespread use today. However, it is inherently constrained by the set of geometries that have been studied and understood. The designer is limited to exploring variations within known antenna topologies. The number of degrees of freedom available for optimization is small—typically fewer than a dozen parameters—and the design space is correspondingly limited.

Consider, by contrast, an antenna aperture divided into a grid of 200 sub-wavelength pixels, each of which may be independently set to conducting or non-conducting. This seemingly simple description defines a design space of $2^{200} \approx 10^{60}$ possible antenna geometries. The vast majority of these configurations have never been conceived by any antenna designer, and many of them produce antenna characteristics that are unlike any known antenna type. The challenge, of course, is finding the configurations that produce useful antennas among this enormous number of possibilities.

This is precisely the challenge that the fragmented aperture design approach addresses.

1.5 The Fragmented Aperture Concept

The fragmented aperture antenna design approach combines three essential elements:

1. **A pixelated aperture.** The antenna surface is divided into a grid of sub-wavelength regions, or pixels. Each pixel is assigned a binary state: conducting (metal) or non-conducting (absent). The set of all pixel states defines the antenna geometry. Early fragmented apertures used rectangular pixels on a rectilinear grid, but as described in Chapter 3, improved pixel shapes and lattice geometries have been developed to address fabrication challenges.

2. **A full-wave electromagnetic simulation.** A rigorous numerical solution of Maxwell's equations is used to predict the antenna performance for any given pixel configuration. The finite-difference time-domain (FDTD) method has been used exclusively in the author's work because a single time-domain simulation efficiently produces antenna characteristics across the entire frequency band of interest. A detailed description of the FDTD method as applied to antennas is provided in Appendix A.

3. **An evolutionary optimization algorithm.** Because the design space is far too large for exhaustive search, a genetic algorithm (GA) is used to efficiently explore the space of possible pixel configurations. The GA maintains a population of candidate antenna designs, evaluates each design using the FDTD simulation, and evolves the population over many generations using selection, crossover, and mutation operations. The algorithm converges toward designs that best satisfy the specified performance goals.

The result of this design process is an antenna whose physical structure has been computationally optimized to meet a particular set of performance requirements. The antenna shapes that emerge from this process are invariably complex and non-intuitive. Inspection of the metallic regions on the aperture reveals many interconnected and isolated fragments of conductor—hence the name *fragmented aperture*.

A critical advantage of this approach is that the full-wave simulation captures all of the relevant physics: mutual coupling, surface wave effects, feed interactions, dielectric loading, and diffraction from edges and discontinuities. The optimizer therefore has access to the true electromagnetic behavior of each candidate design, not an approximate or simplified model. This is what allows fragmented aperture designs to routinely approach theoretical performance limits.

1.6 Novelty and Significance

The fragmented aperture antenna represents a fundamentally different philosophy of antenna design. Rather than starting from an analytical understanding of how a particular geometric shape radiates and then perturbing that shape to improve performance, the fragmented aperture approach starts from a general description of the design space (the set of all possible pixel configurations) and uses computation to discover structures that meet the desired specifications. In this sense, the antenna structure itself is the output of the design process, not the input.

This computational approach to designing antenna structure has produced several notable results:

- Single-element fragmented aperture antennas that approach the theoretical aperture gain limit $2\pi A/\lambda^2$ for apertures without a ground plane, across bandwidths exceeding an octave.
- Reconfigurable fragmented aperture antennas (Agile Aperture Antennas) that can electronically switch between different operating modes—changing beam direction, bandwidth, or polarization—by opening and closing switched links between metallic pads.
- Ultra-wideband phased array elements based on the fragmented aperture concept that achieve bandwidths of 33:1, with preliminary work suggesting that 100:1 bandwidths are achievable. A key insight enabling these designs was that electrical connections between array elements should be exploited rather than avoided.
- Improved pixel geometries that eliminate the fabrication issue of "diagonal touching"—a problem that plagued early fragmented aperture designs and caused poor agreement between modeled and measured antenna performance.
- An improved mutation algorithm for the genetic algorithm that significantly accelerates convergence for designs with large numbers of pixels.

These results, and others, are described in detail in the chapters that follow.

1.7 Organization of the Book

The remainder of this book is organized as follows:

Chapter 2: Original Approach to Design Fragmented Apertures. This chapter describes the original fragmented aperture concept as disclosed in U.S. Patent 6,323,809. The genetic algorithm design approach is presented, along with early design results that demonstrated the viability of the concept.

Chapter 3: Improved Approach to Design Fragmented Apertures. The original fragmented aperture approach suffered from the problem of diagonal touching, where pixels that touch only at corners lead to fabrication difficulties and poor model-measurement agreement. This chapter presents three improved pixel geometries that inherently avoid diagonal touching, along with an improved mutation algorithm that accelerates the convergence of the genetic algorithm for designs with many pixels.

Chapter 4: Advanced Fragmented Aperture Antennas. This chapter presents a comprehensive survey of fragmented aperture antenna designs that illustrate the versatility of the approach. Topics include fragmented ground planes, fragmented superstrates for enhanced forward gain, various feed strategies, bandwidth tailoring, fixed beam steering, polarization control (linear and circular), beamwidth tailoring, out-of-band rejection, and the design of array elements including unit cell optimization for phased arrays.

Chapter 5: Reconfigurable Fragmented Aperture Antennas. This chapter describes the Agile Aperture Antenna, a reconfigurable antenna in which switched links between metallic pads allow the antenna to be electronically reconfigured to meet different performance specifications. Static and reconfigurable proof-of-concept designs are presented with measured results.

Chapter 6: Wideband Antenna Arrays. This chapter describes the development of ultra-wideband phased arrays using fragmented aperture design principles. Key innovations include connected arrays, broadband screen backplanes using resistive card layers to mitigate ground-plane nulls, and multi-layer radiators for improved front-to-back ratio. Measured results for arrays with bandwidths up to 33:1 are presented.

Chapter 7: Designing Wide Scan Fragmented Array Antennas. This chapter describes techniques for designing fragmented aperture array elements with wide scan volumes ($\pm 60^\circ$ and beyond) using spectral-domain FDTD simulation within the genetic algorithm design process. A laminated printed circuit board fabrication approach is presented, and results for a whole X-band (8–12 GHz) array element are shown.

Chapter 8: Reconfigurable Fragmented Aperture Arrays. This chapter describes a reconfigurable phased array concept in which the fragmented aperture element is electronically reconfigured as the beam is steered, reducing scan loss from $\cos^n \theta$ ($n > 1$) to the theoretical $\cos \theta$ projected-area limit. The connection to the DARPA Arrays at Commercial Timescales (ACT) program is described.

Chapter 9: Recent Fragmented Aperture Innovations. This chapter surveys recent developments that extend the fragmented aperture concept in new directions, including topology optimization using level set methods, UAV swarm antennas, and the application of machine learning and deep learning techniques to accelerate the design process.

Chapter 10: Fragmented Apertures Applied to Other Electromagnetic Structures. The fragmented aperture design methodology is not limited to antennas. This chapter describes applications of the same pixelated optimization approach to non-antenna electromagnetic structures, including broadband phase surfaces, RF power combining networks, pixelated absorbers, pixelated waveguide components, radomes and RCS reduction surfaces, and metamaterials.

Appendix A: Computational Modeling of Antennas. This appendix provides a self-contained introduction to the finite-difference time-domain (FDTD) method as applied to antenna analysis. The basic algorithm is described, the formulation for both transmitting and receiving antennas is presented, and several examples are provided to illustrate the accuracy and utility of the method.

References

[1] J. G. Maloney, M. P. Kesler, P. H. Harms, T. L. Fountain, and G. S. Smith, “The fragmented aperture antenna: FDTD analysis and measurement,” in *Millennium Conference on Antennas and Propagation (AP 2000)*, 2000, p. 93.

[2] J. G. Maloney, M. P. Kesler, P. H. Harms, and G. S. Smith, “Fragmented aperture antennas and broadband ground planes,” U.S. Patent No. 6,323,809 B1, Nov. 2001.

[3] L. N. Pringle, P. H. Harms, S. P. Blalock, G. N. Kiesel, E. J. Kuster, P. G. Friederich, R. J. Prado, J. M. Morris, and G. S. Smith, “A reconfigurable aperture antenna based on switched links between electrically small metallic patches,” *IEEE Transactions on Antennas and Propagation*, vol. 52, no. 6, pp. 1434–1445, Jun. 2004.

[4] D. Landgren, T. Brunasso, K. Allen, D. Dykes, J. Kovitz, J. Perez, J. Dee, J. Marsh, C. Hunter, and G. Smith, “A broadband array with unbalanced feeds : Elements and power combiners based on the fragmented aperture principle,” in *2019 IEEE International Symposium on Antennas and Propagation and USNC-URSI Radio Science Meeting*, 2019, pp. 1223–1224.

[5] J. G. Maloney, B. N. Baker, R. T. Lee, G. N. Kiesel, and J. J. Acree, “Wide scan, integrated printed circuit board, fragmented aperture array antennas,” in *2011 IEEE International Symposium on Antennas and Propagation (APSURSI)*, 2011, pp. 1965–1968.

[6] B. Thors, H. Steyskal, and H. Holter, “Broad-band fragmented aperture phased array element design using genetic algorithms,” *IEEE Transactions on Antennas and Propagation*, vol. 53, no. 10, pp. 3280–3287, 2005.

[7] N. Barani, J. F. Harvey, and K. Sarabandi, “Fragmented antenna realization using coupled small radiating elements,” *IEEE Transactions on Antennas and Propagation*, vol. 66, no. 4, pp. 1725–1735, 2018.

[8] IEEE, “Ieee standard for definitions of terms for antennas,” Institute of Electrical and Electronics Engineers, Tech. Rep. IEEE Std 145-2013, 2013.

Chapter 2

Original Approach to Design Fragmented Apertures

2.1 Aperture Utilization

A central goal in antenna design is to make effective use of the available aperture area. As discussed in Chapter 1, the theoretical maximum gain for a uniformly illuminated planar aperture of area A radiating into one hemisphere is $4\pi A/\lambda^2$, and for an aperture radiating into both hemispheres (no ground plane), the limit is $2\pi A/\lambda^2$. Traditional antenna designs—dipoles, patches, spirals, and the like—typically utilize only a fraction of the available aperture area at any given frequency. For example, a spiral antenna uses an "active region" whose size scales with frequency; at any given operating frequency, much of the physical aperture is not contributing to the radiation.

The original fragmented aperture concept was motivated by a simple question: *can one design a planar antenna that utilizes the entire aperture area across a wide frequency band, thereby approaching the theoretical gain limit?* The answer, as demonstrated in this chapter, is yes—provided one is willing to abandon traditional antenna geometries in favor of computationally optimized structures.

2.2 Original Genetic Design Approach

2.2.1 Binary Encoding of Antenna Geometry

The fundamental idea behind the fragmented aperture antenna is to represent the antenna geometry as a binary string that can be manipulated by an evolutionary optimization algorithm. The antenna surface is divided into a grid of sub-wavelength rectangular pixels, as illustrated in Figure 2.1. Each pixel is assigned a single binary value: 1 for conducting (metal present) and 0 for non-conducting (metal absent). The collection of all pixel states defines the antenna geometry and constitutes the "genetic code" of the antenna.

This binary representation maps naturally onto a genetic algorithm (GA). The

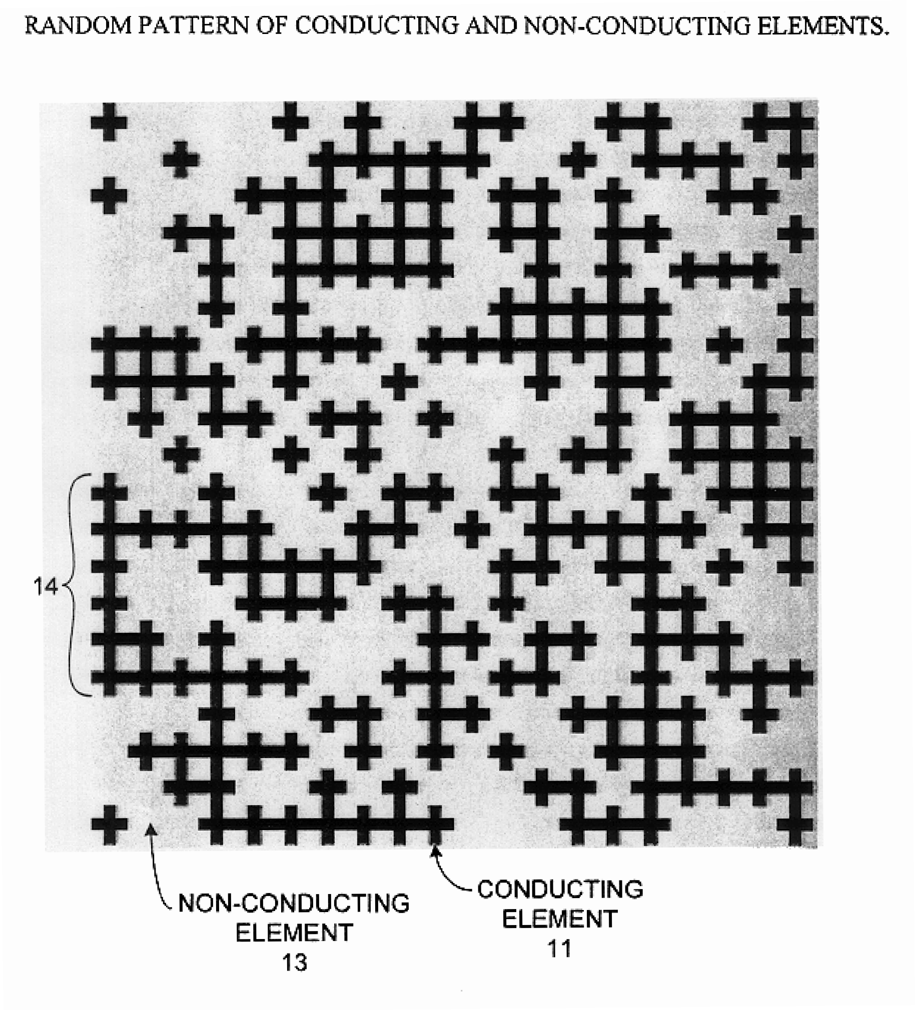

Figure 2.1: The fragmented aperture concept: a planar surface divided into a grid of sub-wavelength pixels, each either conducting (black) or non-conducting (white). The pattern of conducting and non-conducting elements defines the antenna geometry [1].

GA maintains a population of candidate antenna designs, each represented by a binary string. Over successive generations, the population evolves toward better antenna designs through the standard genetic operations of selection, crossover, and mutation.

2.2.2 Two-Stage Optimization

The original design process employed a two-stage optimization approach, as illustrated in Figure 2.2. In the first stage, the aperture area is described using a relatively small number of trapezoidal conducting strips arranged symmetrically about a coaxial feed point. Each strip has a variable length that is encoded in the binary representation. This coarse description of the antenna geometry allows the GA to quickly explore the design space and identify promising regions.

In the second stage, the best design from the first stage is converted to the full pixel representation and the GA continues to optimize at the pixel level, refining the antenna geometry to improve performance. The flowchart for this second stage is shown in Figure 2.3.

2.2.3 Fitness Evaluation with FDTD

At each generation of the GA, every candidate antenna in the population must be evaluated to determine how well it meets the design objectives. This evaluation requires a full-wave electromagnetic simulation of each candidate antenna. The finite-difference time-domain (FDTD) method was used exclusively for this purpose because a single time-domain simulation produces the antenna response across the entire frequency band of interest via Fourier transformation (see Appendix A for details).

The fitness function used to evaluate each candidate antenna was typically based on the broadside realized gain across the design bandwidth. Designs that achieved good impedance match (low VSWR) and high broadside gain over the specified frequency range received higher fitness scores. The GA then preferentially selected high-fitness individuals for reproduction, driving the population toward better antenna designs over successive generations.

Even with the efficiency of the FDTD method, the computational cost of evaluating hundreds or thousands of candidate antennas over many GA generations was substantial. This was one of the earliest applications of large-scale parallel computing to antenna design, with populations of antennas evaluated simultaneously on clusters of workstations.

2.2.4 Symmetry Constraints

To reduce the size of the design space and to ensure that the resulting antenna designs had desirable radiation characteristics, symmetry constraints were typically imposed during the optimization. For a vertically polarized broadside antenna, left-right and top-bottom symmetry were enforced, reducing the number of independent pixels (and hence the length of the binary string) by a factor of four. For example, an aperture with 400 pixels and both symmetries enforced has only 100 independent degrees of freedom, corresponding to a design space of 2^{100} possible configurations—still enormous, but

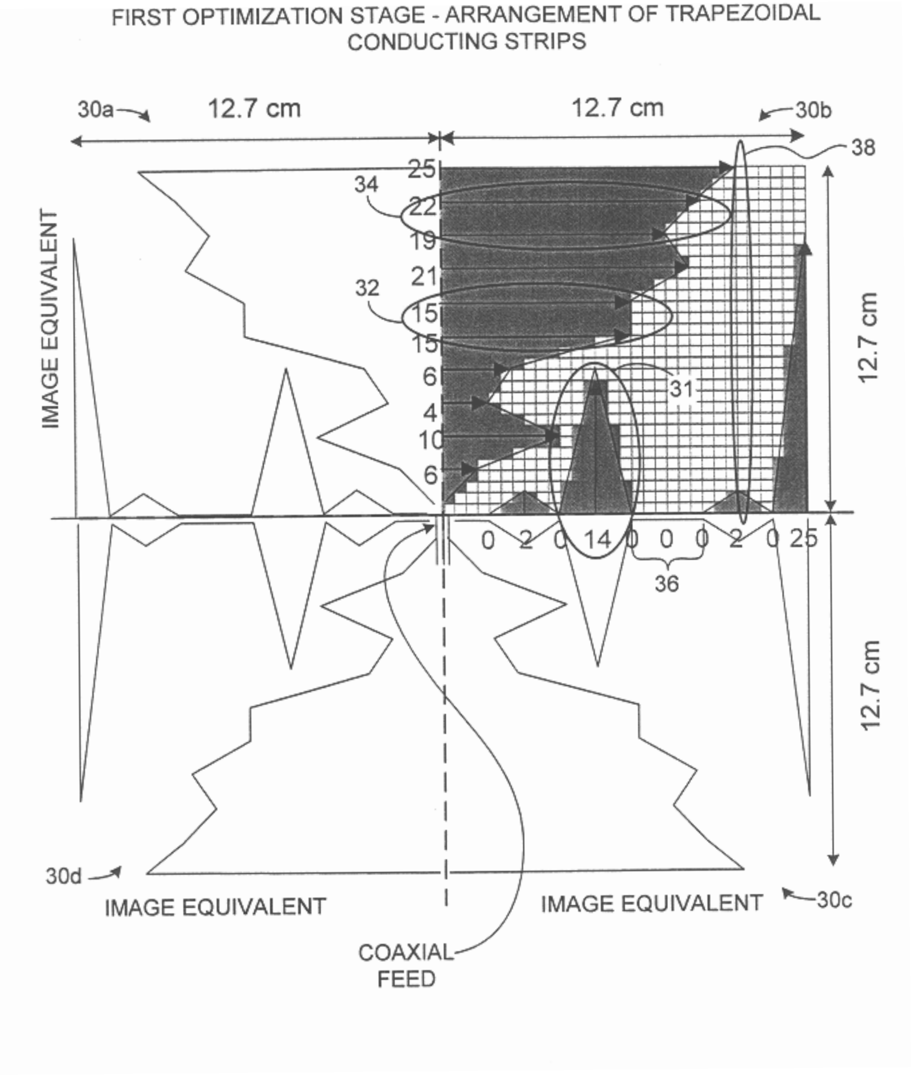

Figure 2.2: First optimization stage: the aperture is described using trapezoidal conducting strips of variable length arranged about a coaxial feed. This coarse parameterization enables rapid exploration of the design space [1].

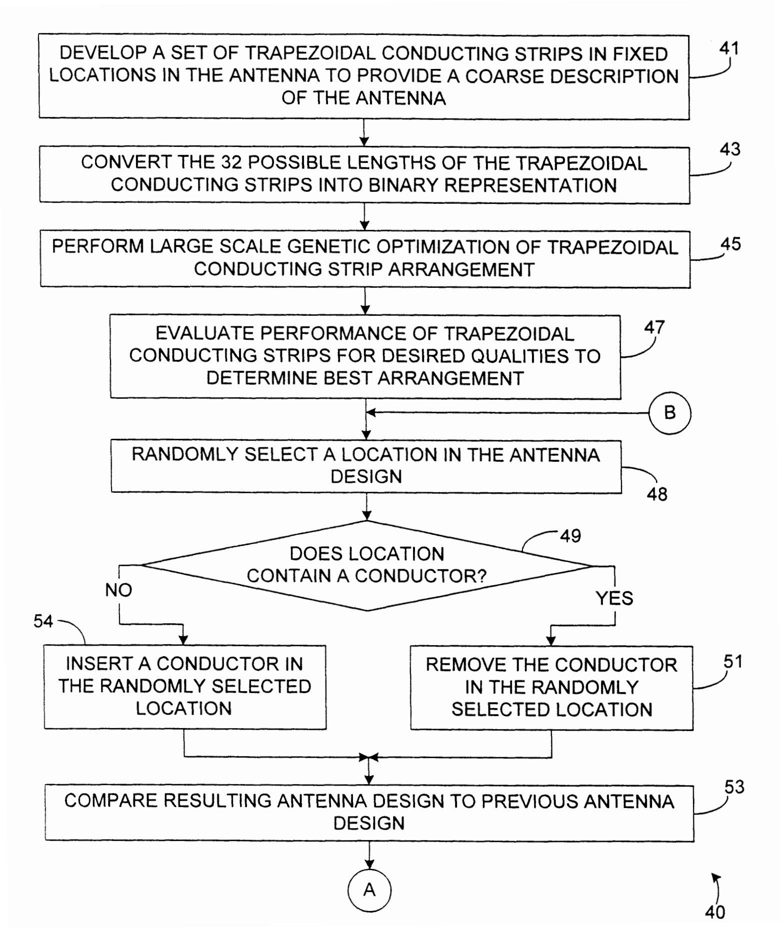

Figure 2.3: Flowchart of the genetic optimization process for fragmented aperture design. The algorithm iteratively toggles pixels between conducting and non-conducting states, evaluating the antenna performance at each step using full-wave electromagnetic simulation [1].

significantly more tractable for the GA.

2.3 First Success

The first successful fragmented aperture antenna design was a planar aperture optimized to operate from 800 MHz to 2.5 GHz (a bandwidth of approximately 3:1). The aperture was 10 inches × 10 inches (25.4 cm × 25.4 cm) and was excited at a feed point near the center of the aperture. The optimized design is shown in Figure 2.4.

The visual complexity of the design in Figure 2.4 is striking. The conducting regions form an intricate pattern of connected and disconnected fragments that bears no resemblance to any traditional antenna geometry. It was this visual character—the many fragments of conductor scattered across the aperture—that led to the name "Fragmented Aperture Antenna."

Despite the non-intuitive appearance of the design, the measured performance was excellent. Figure 2.5 compares the measured broadside gain with the FDTD prediction and with two reference curves: the uniform aperture gain limit ($2\pi A/\lambda^2$, since there is no ground plane) and the gain of a spiral antenna of the same aperture size.

Several important observations can be drawn from Figure 2.5:

- Within the optimization range of 800 MHz to 2.5 GHz, the fragmented aperture closely approaches the uniform aperture gain limit. This demonstrates that the GA/FDTD design process is effective at utilizing the full aperture area.
- The measured and FDTD-predicted gains are in excellent agreement across the entire frequency range, validating the accuracy of the FDTD model used in the design process.
- The fragmented aperture significantly outperforms a spiral antenna of the same physical aperture size. The spiral, being a traveling-wave antenna with a frequency-dependent active region, does not utilize the full aperture at any given frequency.
- Outside the optimization range, the antenna performance degrades, as expected. The GA optimized the design specifically for the 800 MHz to 2.5 GHz band, and performance outside this band was not part of the fitness function.

2.4 Bidirectional Radiation

Because the first fragmented aperture antennas were single-layer planar structures with no ground plane, they radiated into both hemispheres. Figure 2.6 shows the H-plane radiation pattern of the first successful design, comparing the FDTD prediction with the measured pattern.

The bidirectional radiation pattern is clearly visible in Figure 2.6, with the antenna producing roughly equal radiation in the forward and backward directions. The model-measurement agreement is again excellent. This bidirectional behavior is a natural consequence of the single-layer planar geometry: since the antenna structure is symmetric about the plane of the aperture (to within the thickness of the conductor), there is no physical mechanism to preferentially direct radiation into one hemisphere.

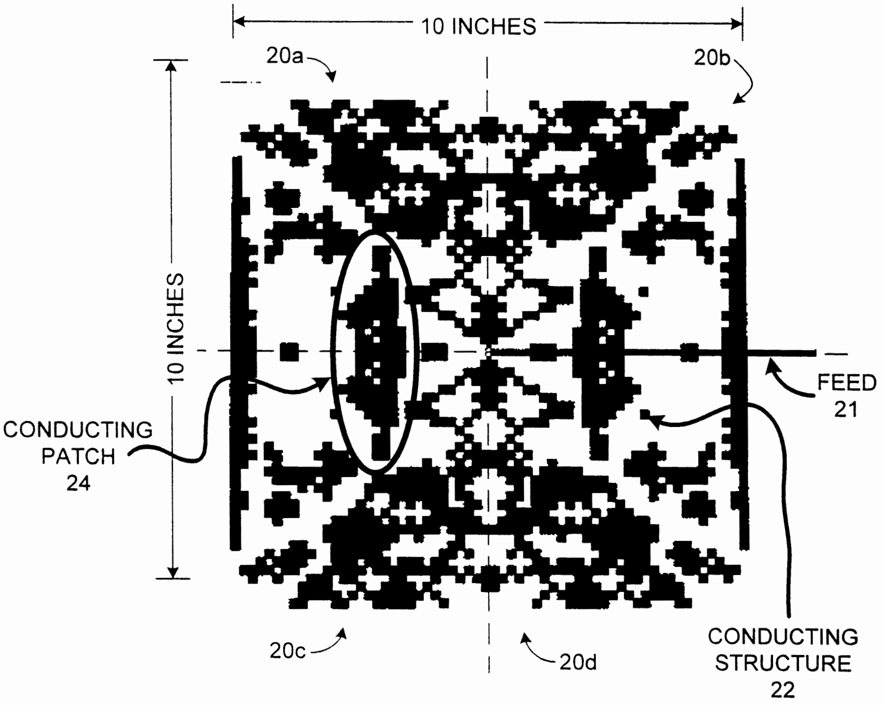

Figure 2.4: The first successful fragmented aperture antenna: a 10-inch × 10-inch aperture optimized for 800 MHz to 2.5 GHz. The complex pattern of conducting (black) and non-conducting (white) regions was determined entirely by the genetic algorithm and FDTD simulation. The feed is located at the right side of the aperture. Left-right and top-bottom symmetry lines are indicated by the dashed lines [1].

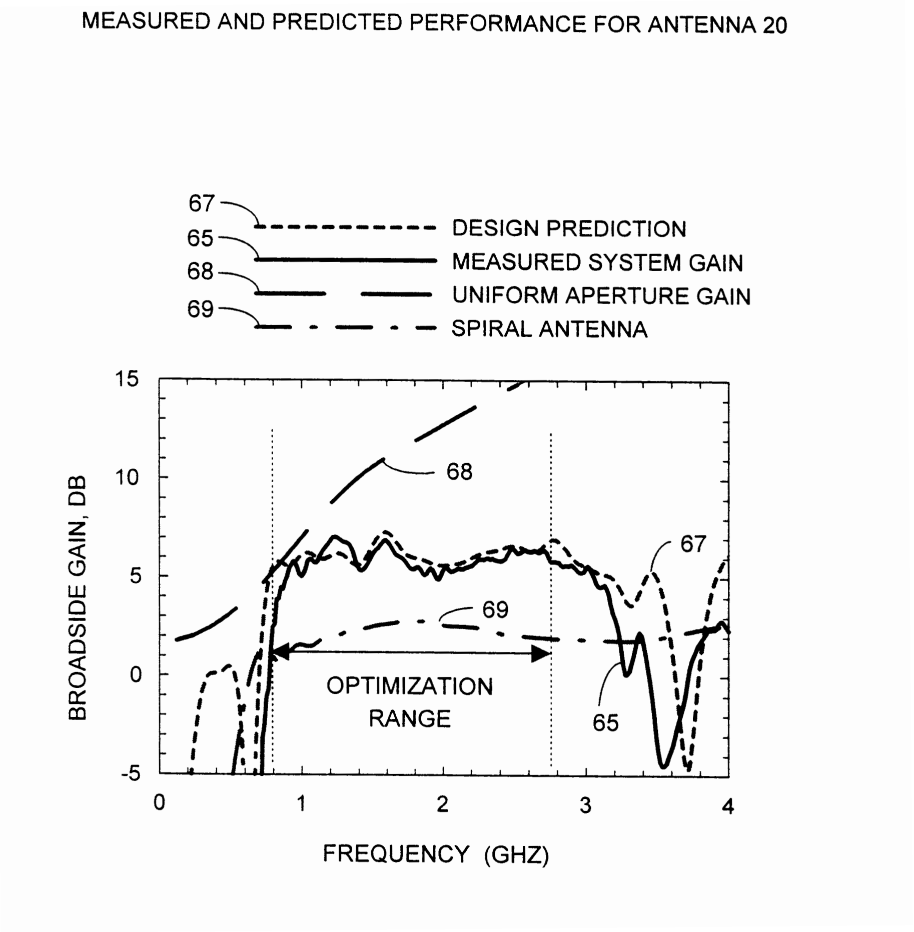

Figure 2.5: Measured and predicted broadside gain for the first fragmented aperture antenna (Figure 2.4). The fragmented design closely approaches the uniform aperture gain limit across the 800 MHz to 2.5 GHz optimization range, and significantly outperforms a spiral antenna of the same aperture size. The measured and FDTD-predicted gains are in excellent agreement [1].

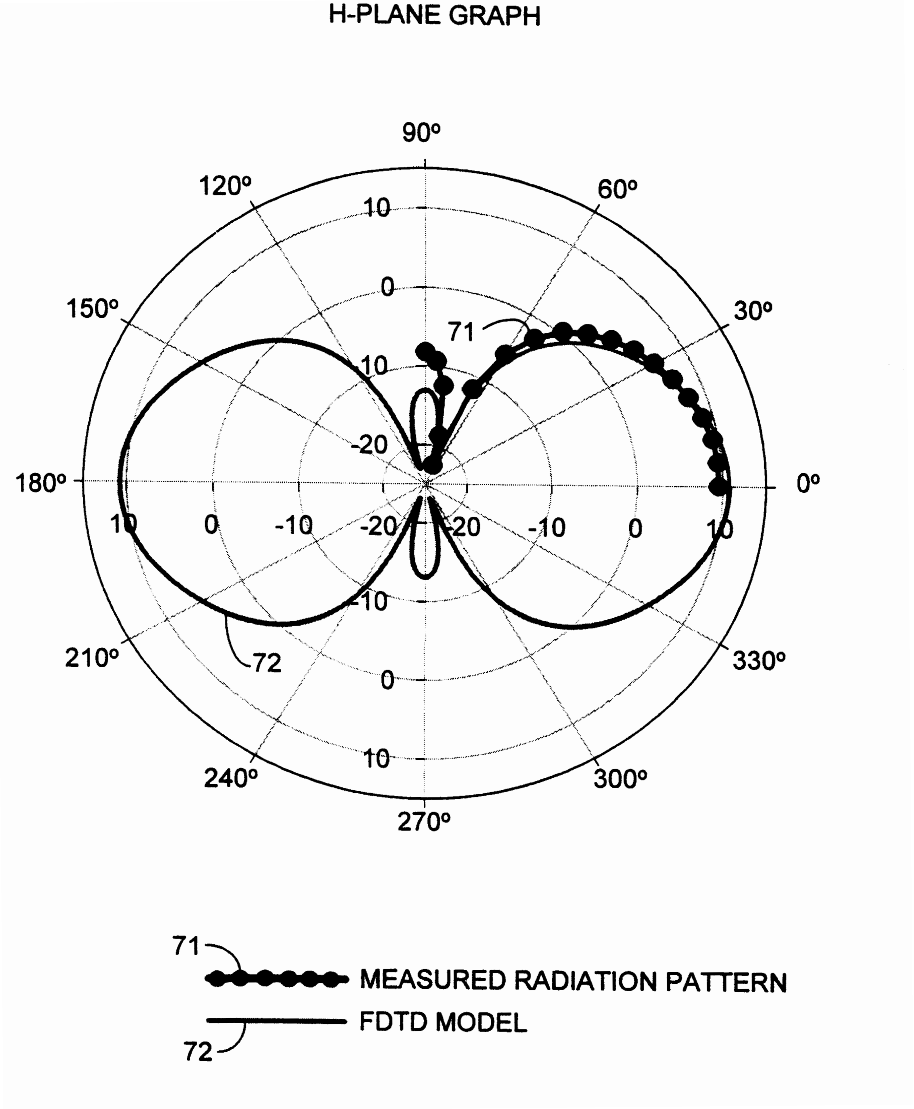

Figure 2.6: H-plane radiation pattern of the first fragmented aperture antenna, comparing the measured pattern with the FDTD model prediction. The pattern is clearly bidirectional, with roughly equal radiation into the forward and backward hemispheres [1].

For many applications, bidirectional radiation is undesirable—half of the radiated power is directed away from the intended coverage area. This motivates the use of a ground plane behind the aperture. However, as will be discussed in detail in Chapter 6, a simple conducting ground plane introduces half-wave nulls at frequencies where the aperture-to-ground-plane spacing is an integer multiple of $\lambda/2$. Addressing this challenge led to the development of broadband screen backplanes and multi-layer radiating structures that are key features of the wideband fragmented array designs.

2.5 Fragmented Broadband Ground Planes

An interesting early application of the fragmented aperture concept was the design of broadband ground planes. Just as the pixel pattern on the radiating aperture can be optimized to achieve desired antenna characteristics, the pixel pattern on a surface behind the aperture can be optimized to function as a broadband ground plane.

A conventional conducting ground plane placed a quarter wavelength behind a radiating aperture provides constructive interference at the design frequency: the backward-radiated wave reflects off the ground plane and, after traveling an additional half wavelength (round trip), arrives back at the aperture in phase with the forward-radiated wave. However, this constructive interference is inherently narrowband.

By replacing the solid conducting ground plane with a fragmented surface—a pixelated pattern of conducting and non-conducting regions—it is possible to design a reflector that provides a more uniform phase response over a wider bandwidth. The original patent demonstrated this by measuring the transmission phase through a fragmented surface, showing that the fragmented pattern maintains a substantially flatter phase response than a solid conducting reference across a wide frequency range (see Chapter 10 for details and the transmission phase comparison figure).

This early exploration of broadband fragmented surfaces was significant for two reasons. First, it demonstrated that the fragmented aperture concept extends beyond antenna design to the engineering of electromagnetic surfaces with tailored properties—a theme developed further in Chapter 10. Second, it laid the groundwork for the broadband screen backplane designs described in Chapter 6, which use fragmented conducting layers in combination with resistive card (r-card) layers to achieve ultra-wideband ground plane performance for phased array antennas.

2.6 The Original Patent and Early Publications

The original fragmented aperture antenna concept, including both the radiating aperture and the broadband ground plane, was disclosed in U.S. Patent 6,323,809, "Fragmented Aperture Antennas and Broadband Ground Planes," granted November 27, 2001 [1]. The inventors were J. G. Maloney, M. P. Kesler, P. H. Harms, and G. S. Smith.

The first public presentation of the fragmented aperture concept occurred at the ICAP/JINA Conference on Antennas and Propagation in 2000 [2]. The reconfigurable version of the concept (switched fragmented apertures) was presented at the IEEE Antennas and Propagation Symposium later that same year [3]. The concept was subsequently described in a number of conference papers and symposium presentations

[4], and was included as part of a chapter on wideband arrays in the Modern Antenna Handbook [5].

Since the original publications, several other research groups have independently adopted the fragmented aperture design approach for their own applications. Herscovici et al. applied the concept to aperture-coupled microstrip antennas [6]. Thors et al. used genetic algorithms for broadband fragmented aperture phased array element design [7]. Ellgardt and Persson investigated wide-angle scanning fragmented aperture arrays [8]. More recent work has explored fragmented antennas based on coupled small radiating elements [9] and optimized designs with integrated baluns [10]. These and other efforts confirm the broad applicability of the fragmented aperture design philosophy.

2.7 Lessons Learned

The success of the original fragmented aperture antenna validated the fundamental premise that computational optimization could discover antenna geometries far beyond those accessible through traditional design approaches. However, the early work also revealed important limitations that would drive subsequent research:

- **Diagonal touching.** The original rectangular pixel geometry led to situations where conducting pixels touched only at their corners. In the FDTD simulation, these diagonally touching pixels are always electrically connected, but when fabricated (e.g., by printed circuit board etching), the connection is unreliable. This issue, and the solutions to it, are the subject of Chapter 3.

- **Convergence for large pixel counts.** As the number of pixels increased beyond approximately 100, the standard GA mutation operator became increasingly ineffective at exploring the design space. An improved mutation strategy tailored for fragmented apertures is described in Chapter 3.

- **Bidirectional radiation.** Single-layer fragmented apertures without a ground plane radiate equally into both hemispheres, limiting the achievable gain to $2\pi A/\lambda^2$. Addressing this limitation motivated the development of broadband backplanes (Chapter 6) and multi-layer radiating structures (Chapter 6).

- **Fixed designs.** Once fabricated, a fragmented aperture antenna operates with a single set of characteristics. The desire for antennas that could dynamically change their operating characteristics led to the development of reconfigurable fragmented apertures (Chapter 5).

Despite these limitations, the original fragmented aperture concept established a powerful new paradigm for antenna design: one in which the physical structure of the antenna is determined by computation rather than by analytical insight alone. The remaining chapters of this book describe how this paradigm has been extended and refined to address an increasingly wide range of antenna design challenges.

References

[1] J. G. Maloney, M. P. Kesler, P. H. Harms, and G. S. Smith, "Fragmented aperture antennas and broadband ground planes," U.S. Patent No. 6,323,809 B1, Nov. 2001.

[2] J. G. Maloney, M. P. Kesler, P. H. Harms, T. L. Fountain, and G. S. Smith, "The fragmented aperture antenna: FDTD analysis and measurement," in *Millennium Conference on Antennas and Propagation (AP 2000)*, 2000, p. 93.

[3] J. G. Maloney, M. P. Kesler, L. M. Lust, L. N. Pringle, T. L. Fountain, and P. H. Harms, "Switched fragmented aperture antennas," in *IEEE Antennas and Propagation Society International Symposium*, Salt Lake City, UT, Jul. 2000, pp. 310–313.

[4] P. Friederich, L. Pringle, L. Fountain, P. Harms, D. Denison, E. Kuster, S. Blalock, G. Smith, J. Maloney, and M. Kesler, "A new class of broadband planar apertures," in *Antenna Applications Symposium*, Sep. 2001, pp. 561–587.

[5] W. Croswell, T. Durham, M. Jones, D. Schaubert, P. G. Friederich, and J. G. Maloney, "Wideband arrays," in *Modern Antenna Handbook*, C. A. Balanis, Ed. John Wiley & Sons, 2011, ch. 12.

[6] N. Herscovici, J. Ginn, T. Donisi, and B. Tomasic, "A fragmented aperture-coupled microstrip antenna," in *IEEE Antennas and Propagation Society International Symposium*, Jul. 2008, pp. 1–4.

[7] B. Thors, H. Steyskal, and H. Holter, "Broad-band fragmented aperture phased array element design using genetic algorithms," *IEEE Transactions on Antennas and Propagation*, vol. 53, no. 10, pp. 3280–3287, 2005.

[8] A. Ellgardt and P. Persson, "Characteristics of a broad-band wide-scan fragmented aperture phased array antenna," in *2006 First European Conference on Antennas and Propagation*, 2006, pp. 1–5.

[9] N. Barani, J. F. Harvey, and K. Sarabandi, "Fragmented antenna realization using coupled small radiating elements," *IEEE Transactions on Antennas and Propagation*, vol. 66, no. 4, pp. 1725–1735, 2018.

[10] Y. Zang, M. Jin, and X. Jiao, "The optimum design of a 3-10ghz linear-polarized fragmented aperture array with integrated balun," in *2019 International Symposium on Antennas and Propagation (ISAP)*, 2019, pp. 1–3.

Chapter 3

Improved Approach to Design Fragmented Apertures

3.1 Overview

In the late 1990s, Maloney et al. began investigating the design of highly pixelated apertures whose physical shape and structure are optimized using genetic algorithms (GA) and full-wave computational electromagnetic simulation (FDTD) to best meet a required antenna performance specification—gain, bandwidth, polarization, pattern, and so on [1]–[2]. Visual inspection of the optimized designs revealed that the metallic pixels formed many connected and disconnected fragments across the aperture, which led to the name *Fragmented Aperture Antennas* for this new class of antennas. A detailed description of the original design approach is disclosed in the original patent [3]. Since the original publications, other research groups have successfully applied the fragmented aperture design approach to their own applications [4]–[5], including the use of genetic algorithms for broadband fragmented aperture phased array design [6] and the development of fragmented antennas based on coupled small radiating elements [7].

However, the original fragmented design approach suffers from two significant deficiencies. First, the placement of pixels on a generalized rectilinear grid leads to the problem of *diagonal touching*—pixels that share only a corner vertex are electrically connected in the numerical model but may be disconnected when fabricated. Other research groups have also encountered this diagonal touching problem [8]. Second, the convergence of the GA becomes increasingly poor as the pixel count grows large ($\gg$ 100). Recent work has explored various optimization strategies to address convergence challenges, including the use of integrated baluns to simplify the design space [9] and automated optimization techniques [10].

This chapter presents solutions to both of these shortcomings. First, alternate approaches to the discretization of the aperture area that inherently avoid diagonal touching are presented. Second, an improved mutation operator tailored for fragmented aperture design that significantly improves convergence for large pixel counts is introduced.

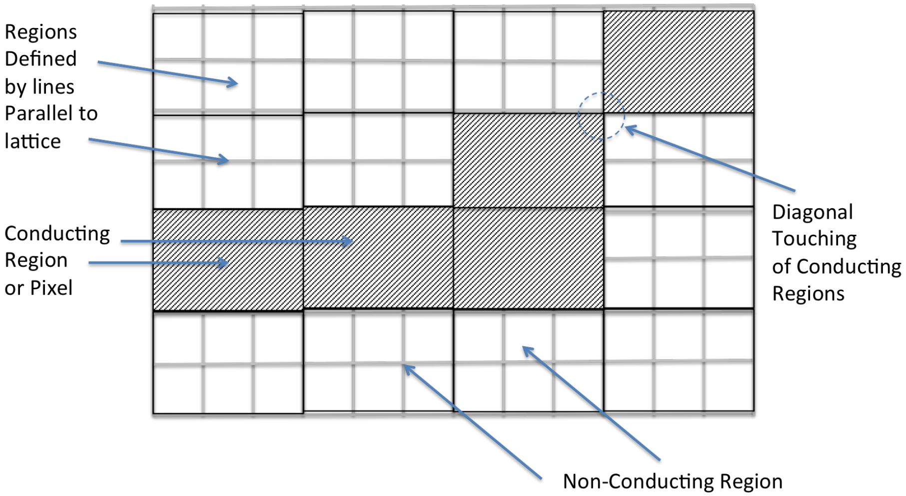

Figure 3.1: Original fragmented aperture approach based on a lattice of rectangular pixels. An example of diagonal touching is shown in the top right of the figure.

3.2 The Diagonal Touching Problem

Originally, fragmented aperture antennas were envisioned as a planar surface partitioned into a grid of rectangular pixels, each either conducting or non-conducting, as shown in Figure 3.1. A genetic algorithm and a computational electromagnetic model determined which pixels should be conducting and which should be non-conducting to form an antenna surface suitable for a given application. This concept was generalized to parallelogram-shaped pixels, as shown in Figure 3.2, in the original fragmented aperture patent [3].

As discussed in Chapter 2, the rectangular pixel approach was very successfully used to design novel antennas [1]–[2]. However, many of these designs proved troublesome to fabricate and measure. The primary problem is *diagonal touching* of pixels, as illustrated in the top right of Figures 3.1 and 3.2.

Diagonal touching is not a problem during the design phase because in the FDTD numerical model, diagonally adjacent conducting pixels are always electrically connected. However, when fabricated using processes such as printed circuit board etching, the diagonal contact is often broken due to over-etching, as illustrated in Figure 3.3(a). Disconnecting metal that should be connected can seriously degrade the antenna's impedance match and gain characteristics.

Other researchers have also observed the difficulties caused by diagonal touching. A close-up photograph of an etched copper fragmented surface is shown in Figure 3.3(b), where the disconnection of diagonally adjacent pixels is clearly visible [11].

In fact, nearly every antenna design included in the original fragmented aperture patent suffers from the diagonal touching problem. Figure 3.4 shows a few examples from U.S. Patent 6,323,809 [3], with the most troublesome diagonal-touching locations near the antenna feed circled.

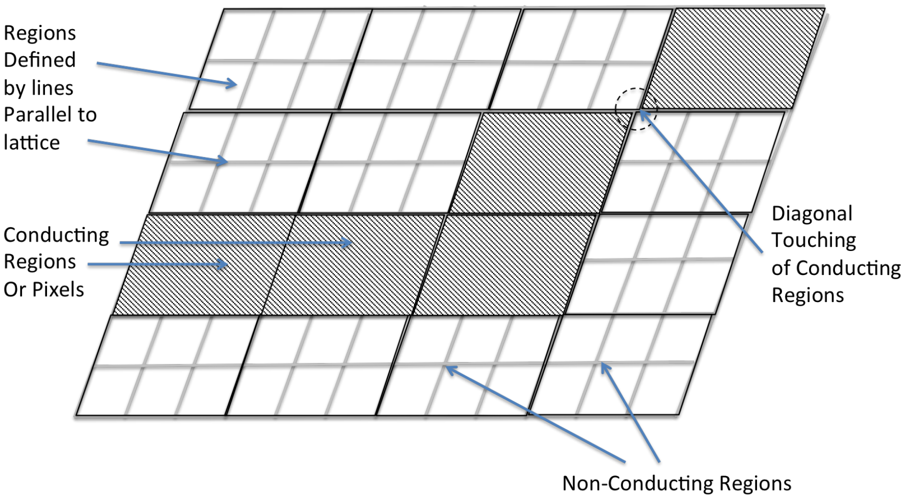

Figure 3.2: Generalized fragmented aperture approach based on parallelogram-shaped pixels. Again, an example of diagonal touching is shown in the top right of the figure.

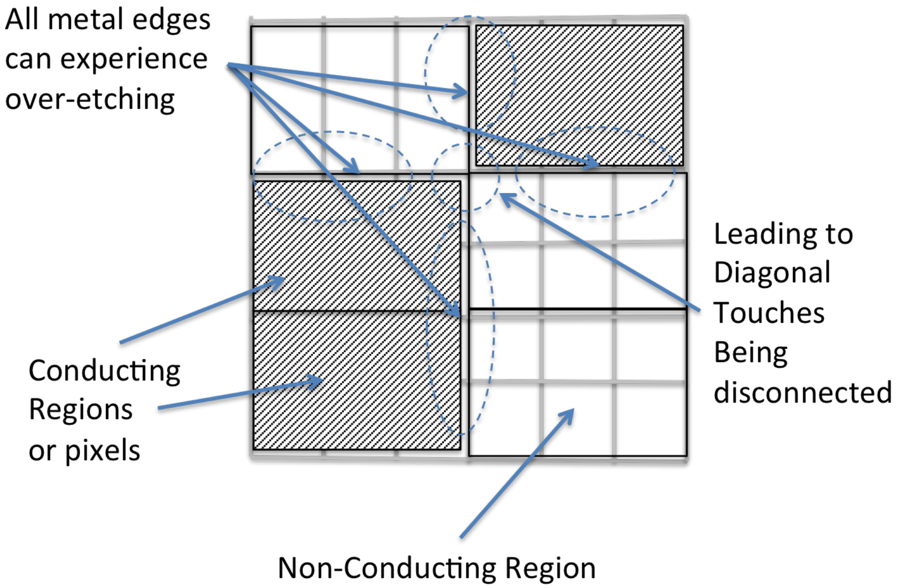

Figure 3.3: (a) Over-etching causing diagonal elements not to touch, as shown in the top center. (b) Close-up photograph of an etched copper fragmented antenna showing over-etch disconnecting diagonal fragments.

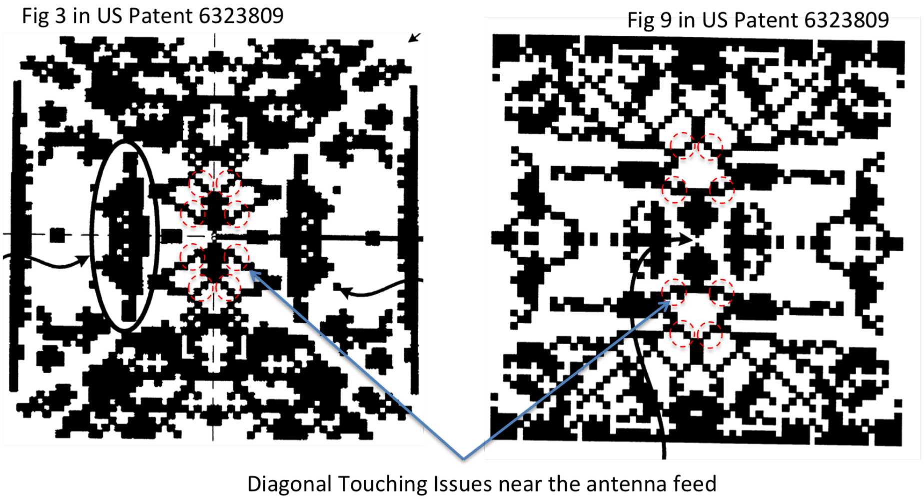

Figure 3.4: Two sample designs from the original fragmented aperture patent exhibiting diagonal touching [3]. The most troublesome examples of diagonal touching near the antenna feed are circled.

The root cause of the problem lies in the fundamental approach to area partitioning. When the pixel edges are parallel to the lattice forming vectors, as in Figures 3.1 and 3.2, the issue of diagonal touching is unavoidable. The next two sections present solutions: Section 3.3 describes several practical mitigation strategies, while Section 3.4 presents three improved pixel geometries that inherently eliminate diagonal touching.

3.3 Mitigation Strategies for Diagonal Touching

Before presenting the improved pixel geometries, it is instructive to review several practical strategies that have been used over the years to mitigate diagonal touching in designs based on the original rectangular pixel approach. Four such strategies are illustrated in Figure 3.5.

3.3.1 Super-Cell Approach

One approach that was successfully exploited is the super-cell strategy shown in Figure 3.5(a). A super-cell is a collection of smaller sub-elements—for example, a 3×3 grid of sub-pixels. To avoid diagonal touching, the conducting area is defined as the five sub-elements that form a plus sign, leaving the four corner sub-elements always non-conducting. This guarantees that no diagonal touching can occur.

The super-cell approach successfully produced antennas with good correlation between measurement and model. However, restricting the conducting area to plus-sign shapes forces electrical currents to flow only in directions aligned with the grid, which over-constrains the design and can lead to suboptimal antenna performance.

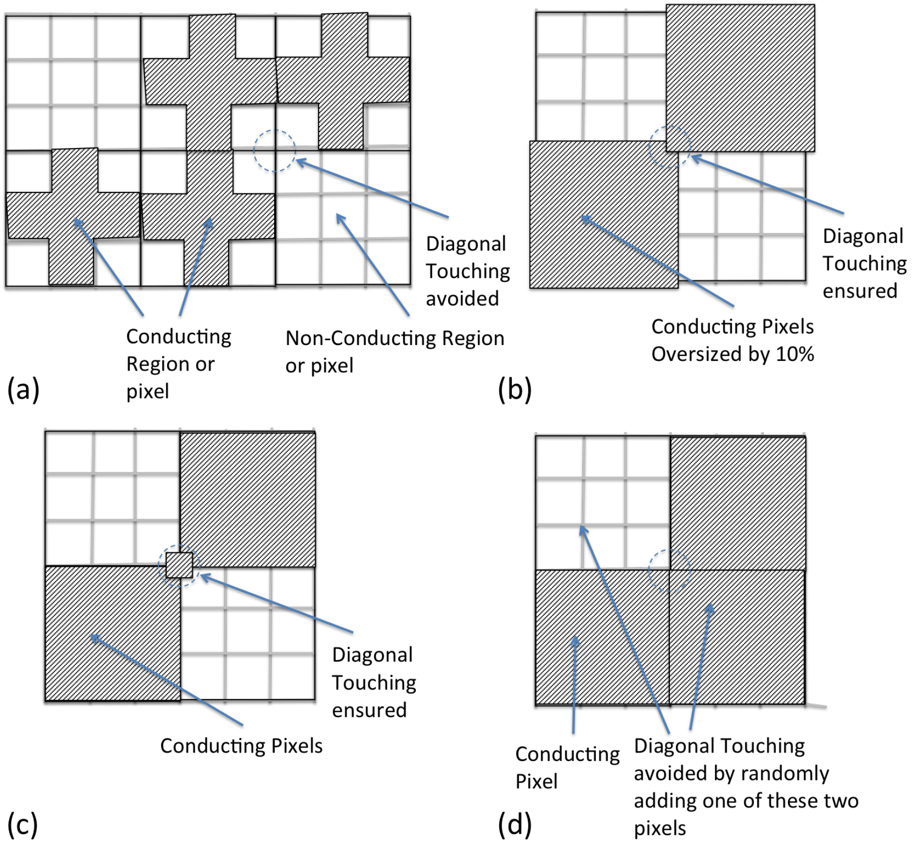

Figure 3.5: Four approaches to mitigating diagonal touching: (a) super-cell approach using 3 × 3 plus signs, (b) fabricating each pixel approximately 10% larger than designed, (c) placing a small metal square at diagonal contact points to ensure connection, and (d) random coin-flip approach to resolve diagonal ambiguity.

3.3.2 Oversized Fabrication

Another successful approach was to intentionally fabricate every pixel approximately 10% larger than designed, as illustrated in Figure 3.5(b). This enlargement ensures that diagonally adjacent pixels overlap slightly, guaranteeing electrical contact. This strategy was found to yield a high percentage of successfully fabricated antennas.

However, oversized fabrication results in the antenna having roughly 10–20% more conductor than originally designed, which can alter the antenna characteristics from the design predictions. It is worth noting that fabricating pixels 10% *smaller* would guarantee that diagonal pixels never touch, but this would mean that conducting regions could never extend beyond a single pixel—a condition that would render the antenna virtually useless. Moreover, smaller fabrication would be inconsistent with the FDTD model used during design, in which diagonally adjacent conducting pixels are always connected.

3.3.3 Metal Bridge and Coin-Flip Approaches

Other research groups have developed additional strategies. Ellgardt and Persson [5] considered both the oversized pixel strategy of Figure 3.5(b) and a variant in which a small square of metal is placed at each diagonal contact point to ensure connection, as shown in Figure 3.5(c). Rahmat-Samii and colleagues at UCLA have used a random coin-flip process to resolve diagonal ambiguity: when two non-conducting pixels are diagonally adjacent to two conducting pixels, a random selection determines which non-conducting pixel is made conducting to complete the connection, as illustrated in Figure 3.5(d).

While each of these mitigation strategies can be effective, they all represent workarounds for a fundamental problem. The proper solution is to change the pixel geometry itself so that diagonal touching cannot occur, as described in the next section.

3.4 Four Improved Pixel Geometries

The proper approach to eliminating diagonal touching is to break the dependence between pixel edges and lattice directions that is implicit in the rectangular and parallelogram geometries of Figures 3.1 and 3.2. The following three subsections present three different pixel geometries that accomplish this, each leading to improved fragmented aperture antennas. Recent studies have examined important design considerations such as pixel size, symmetry constraints, and their effects on antenna performance [12].

3.4.1 First Approach: Skewed Lattice

In the first approach, the individual conducting/non-conducting elements are defined using lattice vectors that are not both parallel to the element edges, as illustrated in Figure 3.6. The example shown uses square elements arranged on a skewed lattice with a skew angle of $\psi \approx 63.4°$.

Notice that skewing the lattice vector $\vec{V}_2$ completely eliminates the possibility of diagonal touching. Every adjacent pixel pair shares a full edge, so the electrical con-

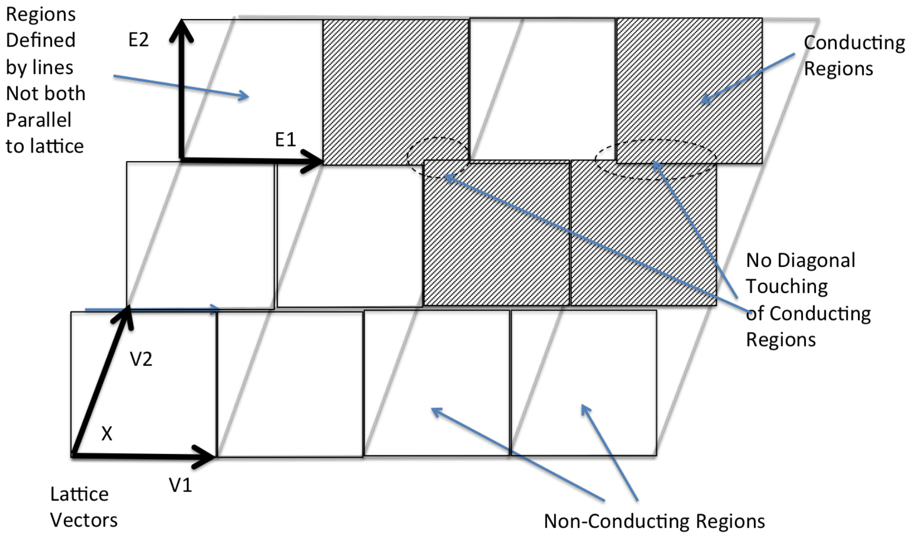

Figure 3.6: First approach to improved fragmented aperture antennas: square elements on a skewed lattice. Skewing the lattice vector $\vec{V}_2$ eliminates the possibility of diagonal touching.

nection between adjacent conducting pixels is always robust and unambiguous.

3.4.2 Second Approach: Alternating Pixel Shapes

In the second approach, two complementary pixel shapes are used that alternate across the aperture, as illustrated in Figure 3.7. The shapes are chosen so that adjacent pixels always share a definite edge rather than merely a corner point.

The key requirement is that the two shapes together tessellate the plane—that is, they tile the aperture surface without gaps or overlaps. When this condition is met and the shapes are designed so that adjacency always involves a shared edge, diagonal touching is inherently impossible.

3.4.3 Third Approach: Single Self-Tessellating Shape

In the third approach, a single pixel shape is chosen that tessellates the plane by itself while ensuring that adjacent pixels share edges rather than corner points. Figure 3.8 shows one example of such a shape, although many other shapes satisfying these requirements exist.

The advantage of a single-shape tessellation is simplicity of implementation: only one pixel geometry needs to be defined and manufactured. However, depending on the chosen shape, this approach may not naturally support the left-right and top-bottom symmetry constraints that are commonly imposed for broadside, linearly polarized antenna designs. This makes the third approach particularly well suited for designs where symmetry is not required, such as beam-steered or circularly polarized antennas.

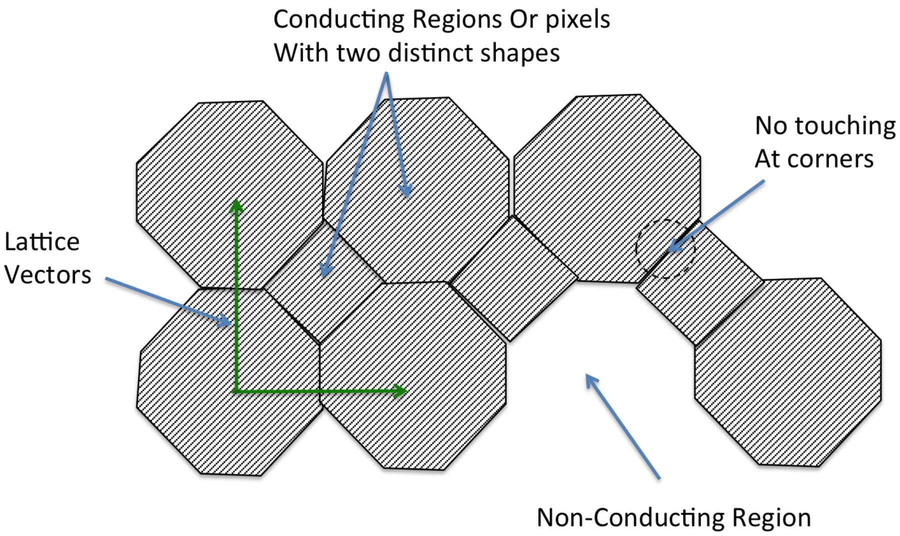

Figure 3.7: Second approach to improved fragmented aperture antennas: alternating pixel shapes that tessellate the plane while ensuring definite edge contact between adjacent pixels.

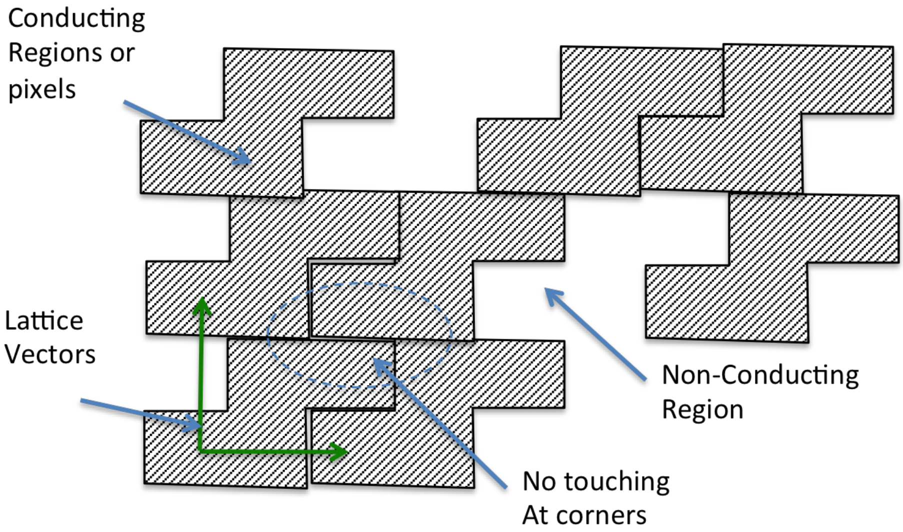

Figure 3.8: Third approach to improved fragmented aperture antennas: a single self-tessellating pixel shape that tiles the aperture surface while ensuring definite edge contact between all adjacent pixels.

3.4.4 Fourth Approach: Metal Patches with Switchable Links

The fourth approach to eliminating diagonal touching was inspired by the reconfigurable fragmented aperture concept described in Chapter 5. In the reconfigurable antenna, the aperture consists of fixed metal patches connected by switchable links—RF switches that can be opened or closed to change the effective conducting pattern. Each switch explicitly connects two adjacent patches along a shared edge, so the connection topology is unambiguous: every electrical connection is a deliberate, edge-shared link rather than a corner contact.

This observation led to a new class of fixed (non-reconfigurable) fragmented aperture designs in which the aperture is constructed as a fine grid of metal patches with narrow conducting links between them. The metal structure resembles a maze or labyrinth, with a much finer level of detail than the original rectangular pixel designs. Crucially, because every conducting connection passes through an explicit link between edge-adjacent patches, diagonal touching is inherently impossible.

Figure 3.9 shows the switched aperture concept from the original patent. The aperture consists of metal patches (145) arranged on a grid, with switch locations (147) between adjacent patches. Each switch can be open (147a, non-conducting) or closed (147b, conducting). The feed patches (149) connect to the antenna terminals. When a particular set of switches is closed, the resulting conducting pattern forms a fragmented aperture antenna optimized for a specific frequency band and beam direction.

For a fixed antenna design, the switches are replaced by permanent conducting links (closed) or permanent gaps (open), but the underlying metal geometry is the same. The key advantage over the original rectangular pixel approach is that the finer grid of patches and links provides more degrees of freedom per unit area, enabling more detailed control of the current distribution across the aperture.

Figure 3.10 shows a broadside design optimized for 1.4–1.8 GHz using this approach. The resulting pattern has a characteristic maze-like appearance, with conducting paths winding through the aperture in complex patterns. The conducting regions (152), non-conducting gaps (154), and feed location (155) are visible, along with a detail callout (156) showing the fine patch-and-link structure. Compared to the original rectangular pixel designs of Chapter 2, this pattern has significantly finer spatial detail and no instances of diagonal touching.

Figure 3.11 shows the predicted and measured performance of this broadside design. The predicted system gain (166) approaches the uniform aperture gain limit (164) across the 1.4–1.8 GHz design band, and the measured system gain (162) confirms the predicted performance with good agreement.

Figure 3.12 shows the H-plane radiation pattern at 1.8 GHz, comparing the FDTD model prediction (174) with measured data (172). The excellent agreement between model and measurement demonstrates that the fine patch-and-link structure is accurately captured by the FDTD simulation and reliably reproduced in fabrication—a significant improvement over the original rectangular pixel designs, where diagonal touching could cause large discrepancies between model and measurement.

The same aperture hardware can produce different antenna designs simply by changing which links are conducting. Figure 3.13 shows a design on the same aperture optimized for a beam steered 30° from broadside at 1.4–1.8 GHz. The pixel pattern is visibly asymmetric—the left-right symmetry present in the broadside design of

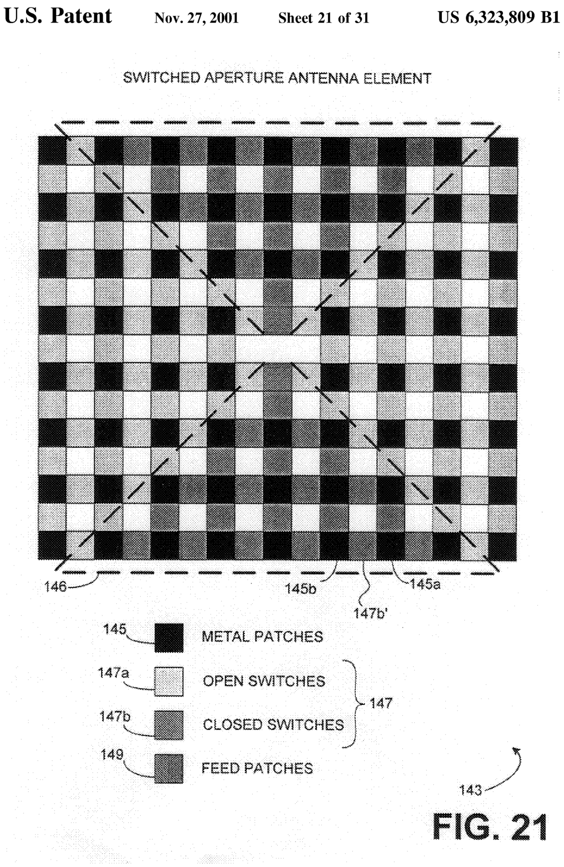

Figure 3.9: The switched aperture antenna concept: metal patches (145) connected by switchable links (147). Closed switches (147b) create conducting paths; open switches (147a) create gaps. This structure inherently avoids diagonal touching because every connection is an explicit edge-shared link [3].

U.S. Patent Nov. 27, 2001 Sheet 22 of 31 US 6,323,809 B1

1.4 - 1.8 GHZ BROADSIDE SWITCHED APERTURE ANTENNA

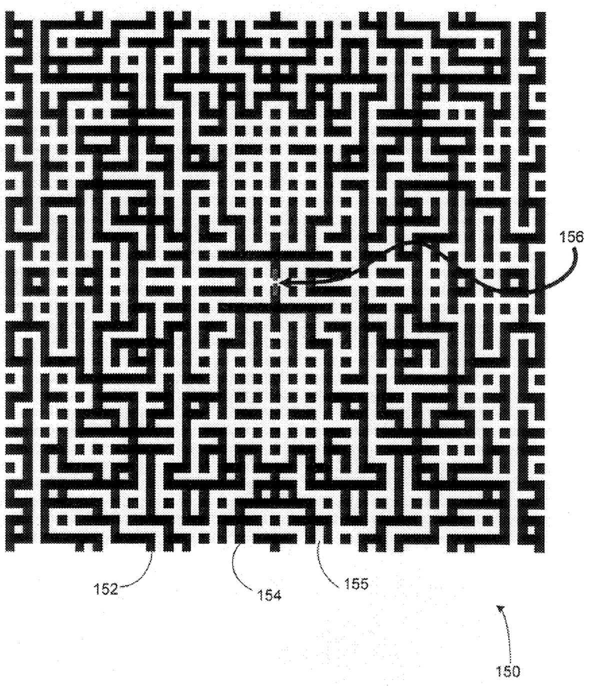

FIG. 22

Figure 3.10: A 1.4–1.8 GHz broadside fragmented aperture antenna designed using the metal patch and link approach (Fourth Approach). The maze-like conducting pattern (152) has much finer spatial detail than the original rectangular pixel designs and inherently avoids diagonal touching. The feed is at location 155 [3].

U.S. Patent Nov. 27, 2001 Sheet 23 of 31 US 6,323,809 B1

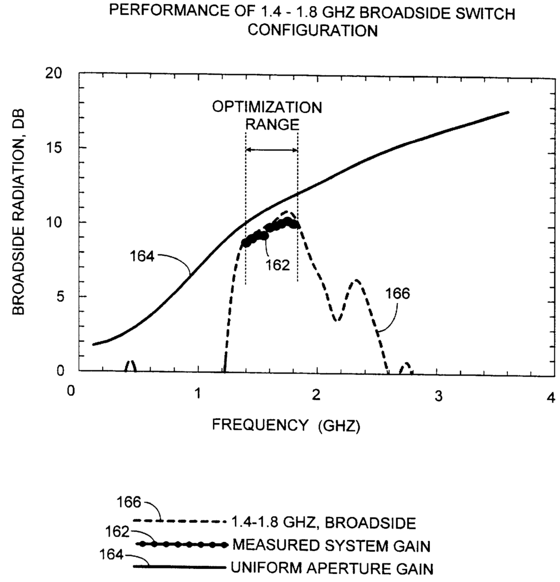

FIG. 23

Figure 3.11: Performance of the 1.4–1.8 GHz broadside switched aperture design: predicted gain (166), measured system gain (162), and uniform aperture gain limit (164). The measured results confirm that the design approaches the aperture limit within the optimization range [3].

U.S. Patent Nov. 27, 2001 Sheet 24 of 31 US 6,323,809 B1

H-PLANE RADIATION PATTERN AT 1.8 GHZ

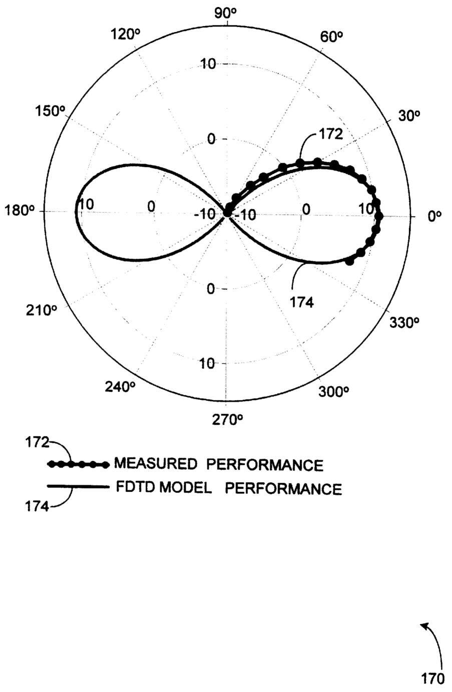

FIG. 24

Figure 3.12: H-plane radiation pattern at 1.8 GHz for the broadside switched aperture design: FDTD model (174) and measured (172). The close agreement confirms that the patch-and-link metal structure is accurately modeled and reliably fabricated [3].

Figure 3.10 is broken to create the phase gradient needed for beam steering.

Figure 3.14 shows the performance of the 30°-steered design. The predicted gain (192) and measured system gain (190) are consistent, with the gain in the steered direction reduced relative to broadside by the expected $\cos\theta$ projection factor.

The H-plane radiation pattern at 1.8 GHz for the steered design is shown in Figure 3.15. The main beam is clearly steered to approximately 30° from broadside, and the measured pattern (197) agrees closely with the FDTD model prediction (198). The bidirectional pattern shape (forward and backward lobes of comparable magnitude) is characteristic of a planar aperture without a ground plane, as discussed in Chapter 4.

Figure 3.16 summarizes the system gain for three different switch configurations on the same aperture: the 1.4–1.8 GHz broadside design of Figure 3.10 (curve 202), the 1.4–1.8 GHz 30°-steered design of Figure 3.13 (curve 206), and a 2.4–3.0 GHz broadside design (curve 208, antenna not shown). All three configurations approach the uniform aperture gain limit (204) within their respective design bands. This summary demonstrates that the metal patch and link approach is versatile: the same physical aperture hardware can support multiple frequency bands and beam directions simply by changing the link pattern.

The metal patch and link approach thus serves a dual purpose. As a fixed antenna design strategy, it inherently eliminates diagonal touching and provides finer spatial control of the aperture conducting pattern. As a reconfigurable antenna concept, it enables the same hardware to support multiple antenna configurations through electronic switching. The reconfigurable aspects are developed in detail in Chapter 5.

3.5 Improved Mutation Algorithm for Better Convergence

In addition to the diagonal touching problem, the original fragmented aperture design approach suffered from poor convergence of the genetic algorithm when the number of pixels became large. This section describes an improved mutation operator that addresses this limitation. More recent work has explored alternative optimization approaches including topology optimization with level set methods [13], machine learning and neural network techniques [14, 15, 16], and reinforcement learning [17]; however, genetic algorithms remain popular due to their simplicity and effectiveness for pixelated antenna design [18, 19].

In a standard genetic algorithm, mutation is a random process in which a small number of genes are changed each generation to help the algorithm avoid convergence to suboptimal solutions. For a fragmented aperture antenna, mutation randomly toggles a few pixels between conducting and non-conducting states. However, many of these random mutations produce only an isolated metal pixel in a non-conducting region or a small hole in an otherwise solid metal area. Such changes have negligible effect on the antenna performance, and the mutation step is effectively wasted.

The improved mutation algorithm is biased so that mutations preferentially extend the boundaries of existing conducting fragments into empty regions, or enlarge holes within large metal regions. This is accomplished using an adjacency matrix that describes which pixels are in contact with each other. By analyzing the local neighbor-

U.S. Patent Nov. 27, 2001 Sheet 25 of 31 US 6,323,809 B1

1.4 - 1.8 GHZ ANTENNA FOR 30 DEGREE STEERING

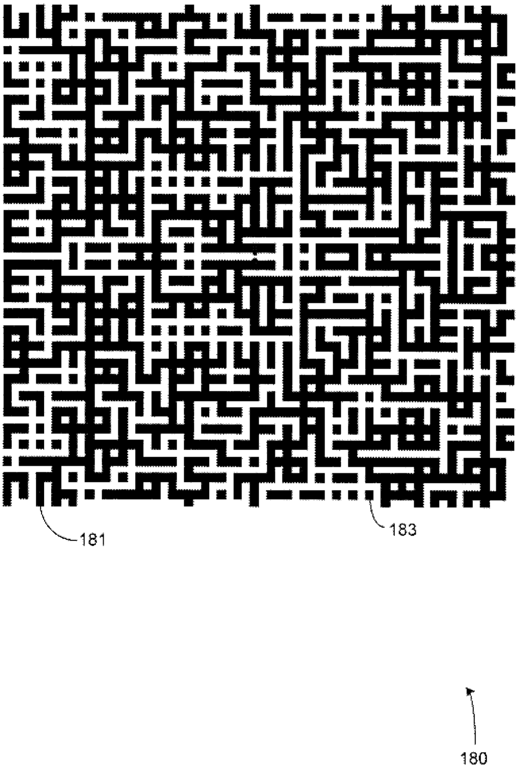

FIG. 25

Figure 3.13: A 1.4–1.8 GHz switched aperture antenna optimized for 30° beam steering. The asymmetric conducting pattern (181, 183) breaks the left-right symmetry of the broadside design to create the phase gradient for off-broadside radiation [3].

U.S. Patent Nov. 27, 2001 Sheet 26 of 31 US 6,323,809 B1

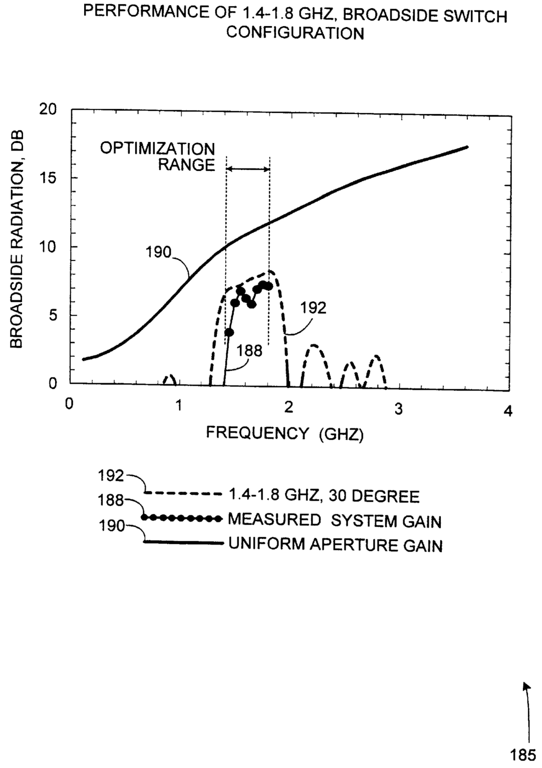

FIG. 26

Figure 3.14: Performance of the 30°-steered switched aperture design: predicted gain (192), measured system gain (190), and uniform aperture gain limit (188) [3].

U.S. Patent Nov. 27, 2001 Sheet 27 of 31 US 6,323,809 B1

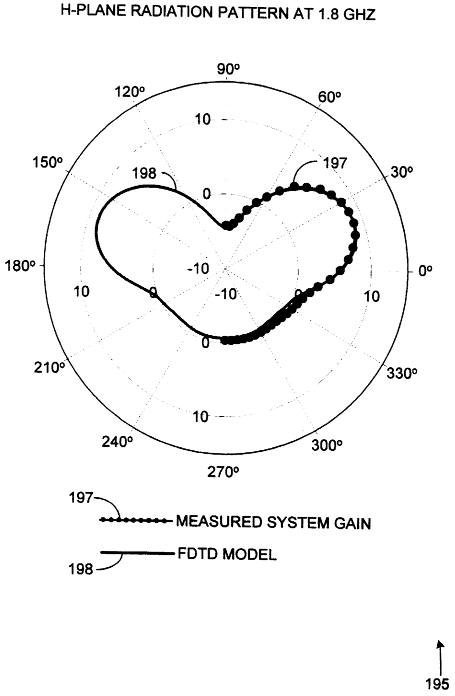

FIG. 27

Figure 3.15: H-plane radiation pattern at 1.8 GHz for the 30°-steered design: measured (197) and FDTD model (198). The beam is steered 30° from broadside with good model-measurement agreement [3].

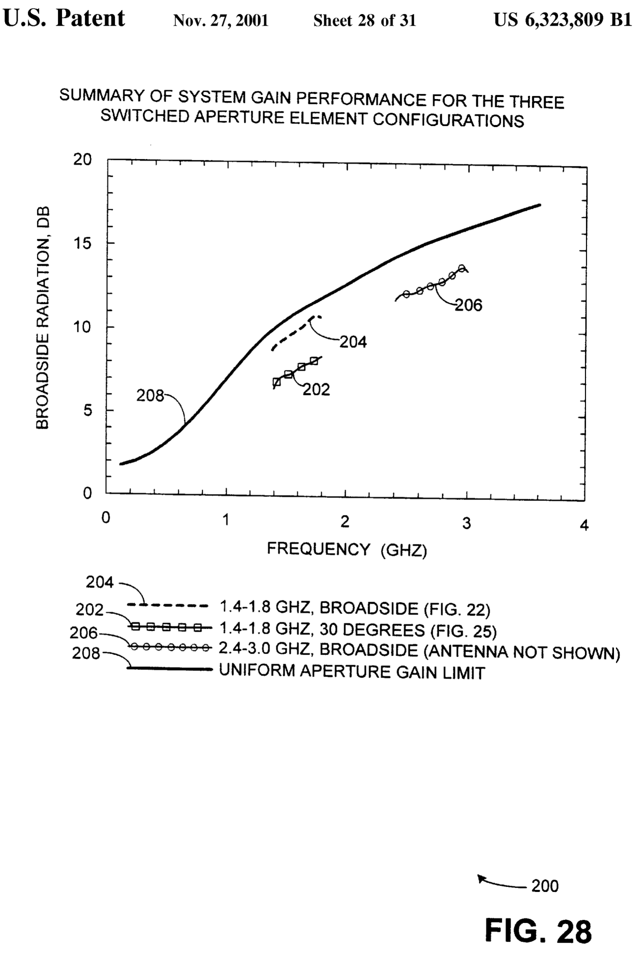

Figure 3.16: Summary of system gain for three switched aperture configurations on the same hardware: 1.4–1.8 GHz broadside (202), 1.4–1.8 GHz 30° steered (206), and 2.4–3.0 GHz broadside (208). The uniform aperture gain limit is shown as curve 204. All configurations approach the aperture limit within their design bands [3].

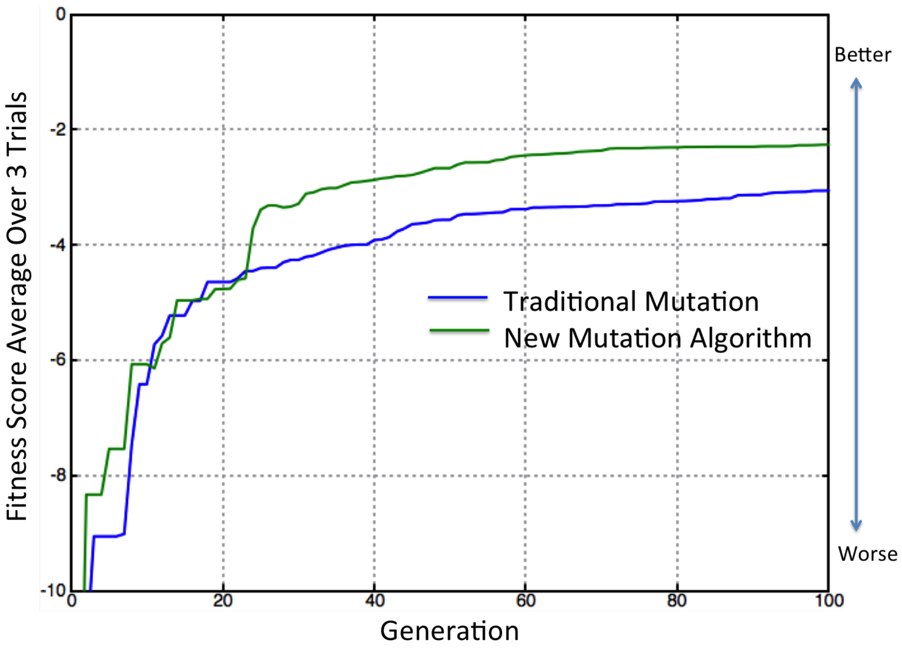

Figure 3.17: Convergence comparison between the traditional mutation algorithm (blue) and the improved adjacency-based mutation algorithm (green), averaged over three independent design trials. The improved algorithm converges to a better fitness score in fewer generations.

hood of each pixel, the algorithm identifies pixels at the boundaries between conducting and non-conducting regions and preferentially selects these boundary pixels for mutation.

To demonstrate the effectiveness of this adjacency-based mutation strategy, three independent design trials were conducted with the traditional mutation algorithm and three with the improved mutation algorithm. Figure 3.17 shows the convergence of the fitness score as a function of generation count, averaged over the three trials for each algorithm. The improved mutation algorithm (green line) converges to a better fitness score in fewer generations than the traditional approach (blue line).

As shown in Table 3.1, the improved mutation algorithm produced a better result than the traditional algorithm in every one of the three trials. The best trial with the improved algorithm achieved a fitness score of -1.684, compared to -2.238 for the best trial with the traditional algorithm—an improvement of more than 0.5 dB.

The results in Table 3.1 also illustrate an important practical point: when using an evolutionary algorithm to design an antenna, more than one design trial should always be executed. As these results show, the variation between trials can exceed 1 dB, so running multiple trials and selecting the best result is essential for obtaining high-quality designs.

Table 3.1: Fitness score comparison across three convergence trials for the traditional and improved mutation algorithms (higher score is better).

Fitness Score Comparison	Tradiational Mutation Algorithm	New Mutation Algorithm
Best of 3 Trials	-2.238	-1.684
Middle	-3.208	-2.461
Worst	-3.727	-2.850

3.6 Sample Improved Fragmented Aperture Designs

This section presents sample antenna designs produced using the improved pixel geometries described in Section 3.4. All designs use the improved mutation algorithm of Section 3.5.

3.6.1 First Approach Designs

The skewed-lattice approach of Figure 3.6 was used to design a series of fragmented aperture antennas spanning from 500 MHz to 2.0 GHz. The lattice skew angle was chosen to be $\psi = \tan^{-1}(2) \approx 63.4°$, which provides the left-right physical symmetry needed for linearly polarized broadside designs. The square pixels were 10.8 mm on a side, and the total aperture area was 25.4 cm × 25.4 cm. Each antenna was excited at a terminal pair at the center of the aperture with a 100 Ω transmission line.

The aperture designs were performed using a genetic algorithm with FDTD evaluation of each candidate antenna (see Appendix A for details on FDTD modeling of antennas). For these designs, the 25.4 cm × 25.4 cm aperture contained 663 individual pixels. Enforcing left-right and top-bottom symmetry reduced the number of independent degrees of freedom to 169. With a single bit representing the state of each pixel (1 = conducting, 0 = non-conducting), this yields a 169-bit genetic code. Using a population size of 32 antennas, approximately 100 GA generations were required to produce each design. The fitness function rewarded good impedance match (return loss better than 15 dB) and maximum broadside realized gain.

Four representative aperture designs are shown in Figure 3.18. The physical shapes clearly demonstrate that none of the designs suffer from diagonal touching—every connection between adjacent conducting pixels involves a full shared edge.

Figure 3.19 shows the broadside realized gain of each design as a function of frequency. The gains are compared with the aperture gain limit (black line), which for these ground-plane-free apertures is $2\pi A/\lambda^2$. All four designs approach the aperture gain limit within their respective design bands.

Figure 3.20 shows the VSWR of each design. The VSWR remains below 1.5

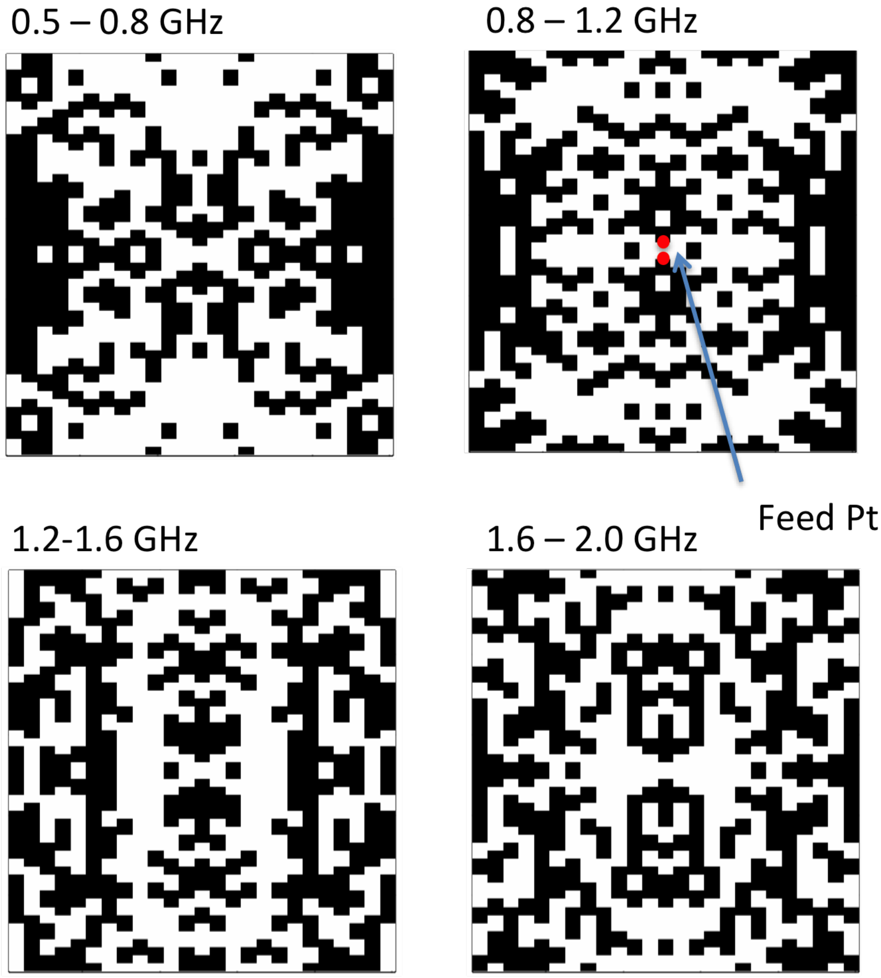

Figure 3.18: Four sample fragmented aperture designs produced using the skewed-lattice (First Approach) pixel geometry. None of the designs exhibit diagonal touching.

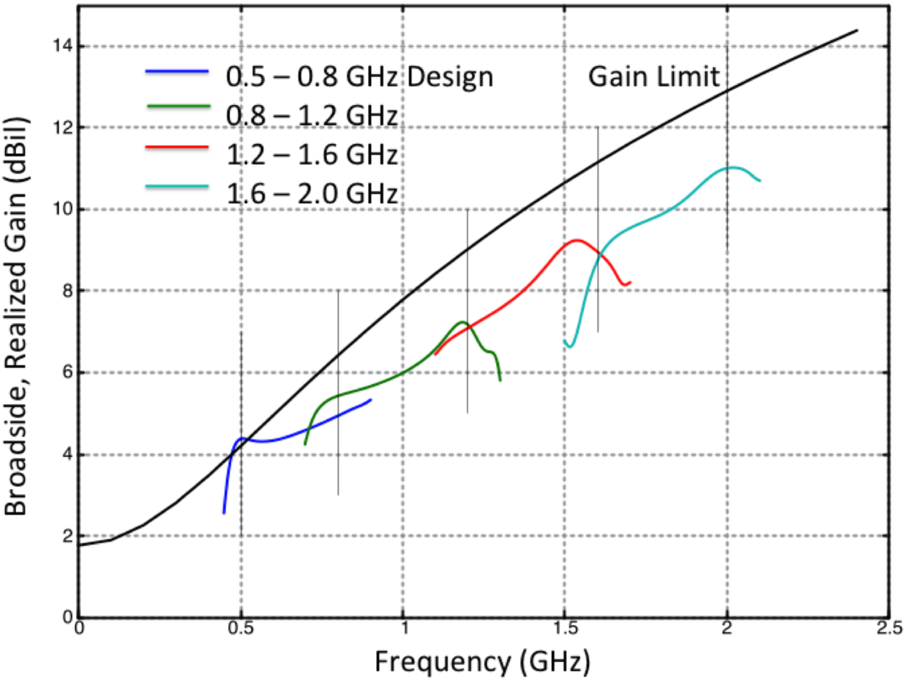

Figure 3.19: Broadside realized gain for the four skewed-lattice designs shown in Figure 3.18. The black line indicates the aperture gain limit $2\pi A/\lambda^2$.

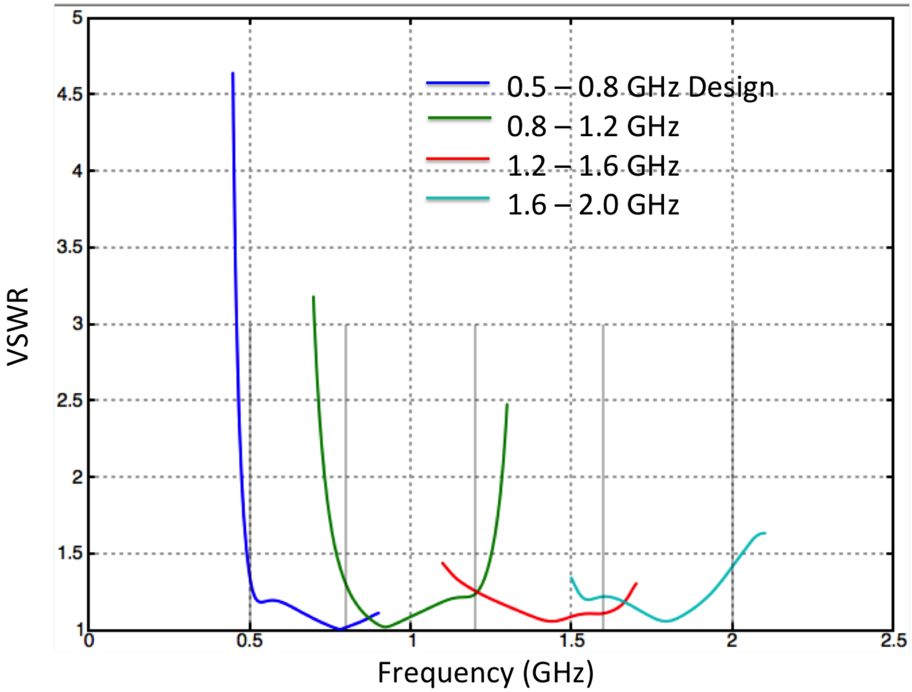

Figure 3.20: VSWR for the four skewed-lattice designs shown in Figure 3.18.

across the respective design bands, consistent with the fitness function requirement of return loss better than 15 dB.

3.6.2 Second Approach Designs

The alternating-shape approach of Figure 3.7 was also used to design fragmented aperture antennas. This pixel geometry naturally supports both left-right and top-bottom symmetry when required. The aperture area was again 25.4 cm × 25.4 cm, excited at the center with a 100 Ω feed. The aperture contained 841 shaped pixels, and with both symmetries enforced, the number of independent degrees of freedom was 221.

[Note: The Second Approach currently has two sample designs. Four designs are planned to match the First Approach presentation. Figures and text to be updated.]

Figure 3.21 shows two sample designs for the 0.5–0.8 GHz and 0.8–1.2 GHz bands. As with the first approach designs, no diagonal touching is present in the physical structures.

Figures 3.22 and 3.23 summarize the broadside gain and VSWR for these two designs. The performance is consistent with the design objectives, with gain approaching the aperture limit within each design band and VSWR remaining below 1.5.

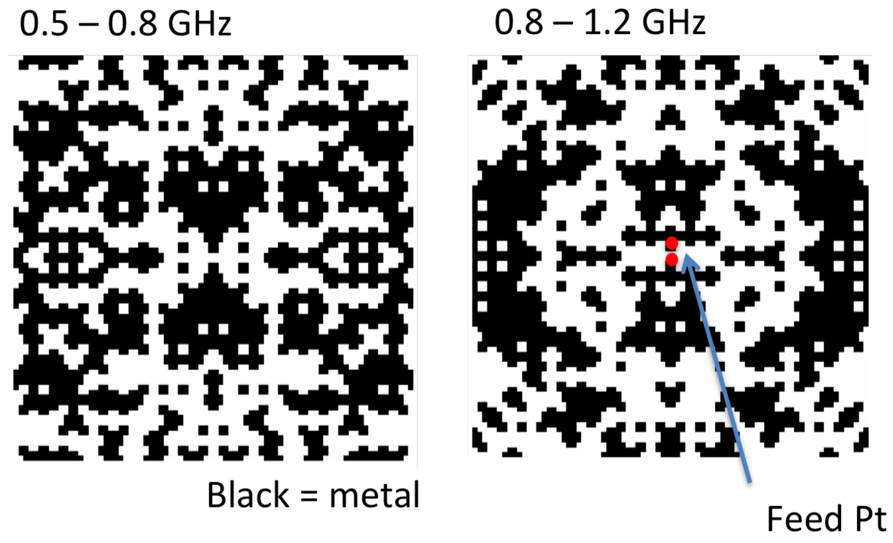

Figure 3.21: Two sample fragmented aperture designs produced using the alternating-shape (Second Approach) pixel geometry for the 0.5–0.8 GHz and 0.8–1.2 GHz bands.

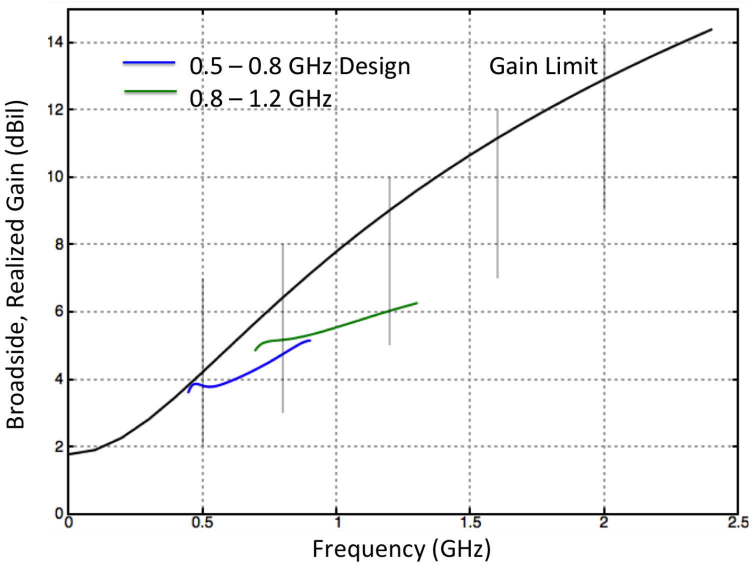

Figure 3.22: Broadside realized gain for the two alternating-shape designs shown in Figure 3.21.

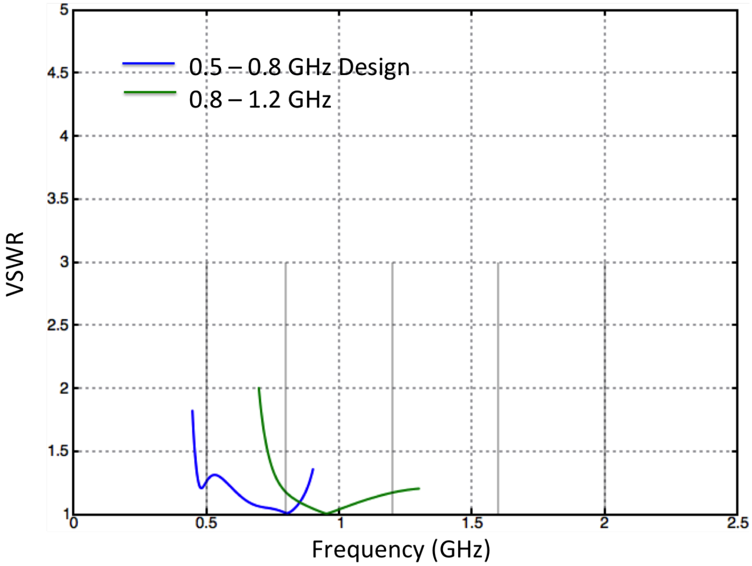

Figure 3.23: VSWR for the two alternating-shape designs shown in Figure 3.21.

3.6.3 Third Approach Designs

The self-tessellating shape approach of Figure 3.8 can also be used to design fragmented aperture antennas. As noted earlier, for vertically or horizontally polarized elements with a broadside beam, the lack of inherent left-right and top-bottom symmetry in many self-tessellating shapes is a drawback. However, for applications where the desired beam direction is not broadside or the desired polarization is circular or slant-linear, symmetry constraints are not needed and the third approach is fully competitive with the first and second.

[Missing content: Third Approach sample designs are needed. Planned designs include: (a) broadside vertically polarized, (b) broadside horizontally polarized, (c) broadside slant-linear polarized, and (d) vertically polarized beam steered 45° from broadside. Corresponding gain, VSWR, and azimuth pattern figures are also needed.]

References

[1] J. G. Maloney, M. P. Kesler, P. H. Harms, T. L. Fountain, and G. S. Smith, "The fragmented aperture antenna: FDTD analysis and measurement," in *Millennium Conference on Antennas and Propagation (AP 2000)*, 2000, p. 93.

[2] W. Croswell, T. Durham, M. Jones, D. Schaubert, P. G. Friederich, and J. G. Maloney, "Wideband arrays," in *Modern Antenna Handbook*, C. A. Balanis, Ed. John Wiley & Sons, 2011, ch. 12.

[3] J. G. Maloney, M. P. Kesler, P. H. Harms, and G. S. Smith, “Fragmented aperture antennas and broadband ground planes,” U.S. Patent No. 6,323,809 B1, Nov. 2001.

[4] N. Herscovici, J. Ginn, T. Donisi, and B. Tomasic, “A fragmented aperture-coupled microstrip antenna,” in *IEEE Antennas and Propagation Society International Symposium*, Jul. 2008, pp. 1–4.

[5] A. Ellgardt and P. Persson, “Characteristics of a broad-band wide-scan fragmented aperture phased array antenna,” in *European Conference on Antennas and Propagation (EuCAP)*, Nov. 2006, pp. 1–5.

[6] B. Thors, H. Steyskal, and H. Holter, “Broad-band fragmented aperture phased array element design using genetic algorithms,” *IEEE Transactions on Antennas and Propagation*, vol. 53, no. 10, pp. 3280–3287, 2005.

[7] N. Barani, J. F. Harvey, and K. Sarabandi, “Fragmented antenna realization using coupled small radiating elements,” *IEEE Transactions on Antennas and Propagation*, vol. 66, no. 4, pp. 1725–1735, 2018.

[8] A. Ellgardt, “Wide-angle scanning wide-band phased array antennas,” Ph.D. dissertation, KTH School of Electrical Engineering, Stockholm, Sweden, 2009, page 21 discusses diagonal touching issues.

[9] Y. Zang, M. Jin, and X. Jiao, “The optimum design of a 3-10ghz linear-polarized fragmented aperture array with integrated balun,” in *2019 International Symposium on Antennas and Propagation (ISAP)*, 2019, pp. 1–3.

[10] Y. Li, J. Dong, S. Wang, Y. Wu, B. Xiong, Q. Li, K. Wang, and Y. Zhang, “An automated approach for pixelated antenna topology design incorporating multi-objective optimization algorithms,” in *2019 International Conference on Microwave and Millimeter Wave Technology (ICMMT)*, 2019, pp. 1–3.

[11] A. Ellgardt and P. Persson, “Characteristics of a broad-band wide-scan fragmented aperture phased array antenna,” in *2006 First European Conference on Antennas and Propagation*, 2006, pp. 1–5.

[12] D. Mair, M. Renzler, and R. Rueland, “Design considerations for pixelated antennas regarding pixel size and symmetry,” in *2024 International Symposium on Electromagnetic Compatibility – EMC Europe*, 2024, pp. 226–231.

[13] C. T. Howard, A. Saad-Falcon, D. W. Landgren, and K. W. Allen, “Topology optimization of a wideband planar phased array element using periodic level set functions,” in *2024 IEEE International Symposium on Phased Array Systems and Technology (ARRAY)*, 2024, pp. 1–7.

[14] M. Li, Y. Wang, and M. Zhu, “Inverse design of pixelated antenna based on residual neural network,” in *2025 International Applied Computational Electromagnetics Society Symposium (ACES-China)*, 2025, pp. 1–3.

[15] Q. Wang, Z. Pang, D. Gao, P. Liu, X. Pang, and X. Yin, “Machine learning-assisted quasi-bisection method for pixelated patch antenna bandwidth optimization,” *IEEE Antennas and Wireless Propagation Letters*, vol. 23, no. 12, pp. 4807–4811, 2024.

[16] J. P. Jacobs, “Accurate and efficient modeling of gain patterns of multiband pixelated antenna by deep neural networks,” in *2022 International Conference on Electromagnetics in Advanced Applications (ICEAA)*, 2022, pp. 306–306.

[17] Q. Wang, Z. Pang, D. Gao, P. Liu, X. Zhang, X. Pang, and X. Yin, “Bandwidth enhancement of pixelated patch antennas based on localized reinforcement learning,” in *2024 14th International Symposium on Antennas, Propagation and EM Theory (ISAPE)*, 2024, pp. 1–4.

[18] D. Mair, M. Unterladstaetter, M. Renzler, and T. Ussmueller, “Evolutionary optimized pixelated antennas for 5g iot communication,” in *2022 52nd European Microwave Conference (EuMC)*, 2022, pp. 548–551.

[19] A. Zeghdoud, M. C. Derbal, and M. Nedil, “Accelerated convergence in ga-based patch antenna optimization using fuzzy logic and machine learning,” in *2025 IEEE International Symposium on Antennas and Propagation and North American Radio Science Meeting (AP-S/CNC-USNC-URSI)*, 2025, pp. 1829–1831.

Chapter 4

Advanced Fragmented Aperture Antennas

4.1 Introduction

Chapters 2 and 3 described the fragmented aperture design methodology and demonstrated its effectiveness for broadside, linearly polarized antennas without ground planes. Those early designs validated the core concept: a genetic algorithm working with a full-wave electromagnetic simulation can produce antenna geometries that approach the theoretical aperture gain limit across multi-octave bandwidths. This chapter broadens the picture by surveying the many ways the fragmented aperture approach can be applied to meet diverse antenna requirements.

The designs in this chapter illustrate that once the fundamental design machinery is in place—a pixelated aperture representation, a genetic algorithm, and a full-wave solver—the same process can be directed toward a remarkably wide range of performance objectives simply by changing the fitness function and the physical configuration. Topics include fragmented ground planes, fragmented superstrates for enhanced forward gain, various feed strategies, bandwidth tailoring, fixed beam steering, polarization control (including circular polarization), beamwidth shaping, out-of-band rejection, and array element design including unit cell optimization for phased arrays.

Several of the sections below include designs by other research groups who have adopted the fragmented aperture or closely related pixelated antenna approaches. Their work demonstrates that the concept has broad applicability and has been successfully implemented by independent teams worldwide.

4.2 Fragmented Ground Planes

Chapter 2 introduced the concept of fragmented broadband ground planes, in which the pixel pattern on a surface behind the radiating aperture is optimized to enhance the antenna's forward radiation. The original fragmented aperture patent [1] disclosed this concept alongside the radiating aperture itself, recognizing that the same binary pixel optimization could be applied to any conducting surface in the antenna structure.

The fragmented ground plane concept is closely related to the *defected ground structure* (DGS) technique that has been widely studied in the microwave engineering community. In the DGS approach, deliberate patterns of slots or removed conductor regions are introduced into the ground plane of a microstrip or stripline circuit to modify its electromagnetic behavior. DGS techniques have been used to improve antenna bandwidth, suppress harmonics, reduce mutual coupling between array elements, and create stopband filtering characteristics.

Early work by Sung, Kim, and Kim [2] demonstrated that a defected ground structure beneath a microstrip patch antenna could suppress higher-order harmonics, creating a stopband in the ground plane that prevented radiation at harmonic frequencies. Liu et al. [3] combined photonic bandgap structures with DGS to achieve similar harmonic suppression. Biswas et al. [4] used dumbbell-shaped DGS geometries with equivalent LC circuit models to build a low-pass filter directly into the microstrip feed line.

An important electromagnetic consequence of introducing defects into the ground plane is that the modified ground plane allows energy to radiate through it, increasing the backward radiation of the antenna. This effect is clearly visible in the radiation patterns reported in several DGS studies, where the back lobe is noticeably larger than that of an antenna with an intact ground plane. In this respect, DGS antennas share a characteristic with the fragmented aperture designs discussed throughout this book: the early fragmented aperture antennas of Chapters 2 and 3, which had no ground plane at all, radiated equally into both hemispheres. The fragmented ground planes disclosed in the original patent [1] represent a middle ground—a ground surface whose pixel pattern is optimized to balance forward gain enhancement against the backward radiation that inevitably accompanies any disruption of the conducting ground.

The distinction between the fragmented aperture approach and conventional DGS is primarily one of design methodology. DGS designs typically use simple, analytically motivated geometries—dumbbell shapes, spirals, or periodic slot patterns—whose dimensions are tuned by parametric sweeps. The fragmented aperture approach, by contrast, treats every sub-wavelength pixel of the ground plane as a free variable and uses a genetic algorithm to determine the optimal pattern. This allows the optimizer to discover complex, non-intuitive geometries that may outperform hand-designed DGS patterns, particularly when broadband performance is required.

As shown in Chapter 10 (Figure 10.1), the original patent demonstrated that a fragmented surface maintains a more uniform transmission phase across frequency than a solid conducting surface, demonstrating its potential as a broadband reflector. This concept was later developed into the broadband screen backplane described in Chapter 6, which uses resistive card layers in conjunction with a conducting ground plane to achieve ultra-wideband operation.

Figure 4.1 shows the fragmented ground plane concept as disclosed in the original patent. A radiating aperture (100) is placed in front of a fragmented ground plane layer (99), separated by approximately $\lambda_0/8$. Unlike a conventional solid ground plane, the ground plane layer itself has a pixelated pattern that is optimized to enhance the antenna's forward radiation.

Figure 4.2 illustrates that the ground plane pattern depends on the design approach. Two fragmented ground plane designs are shown: one optimized starting from the ac-

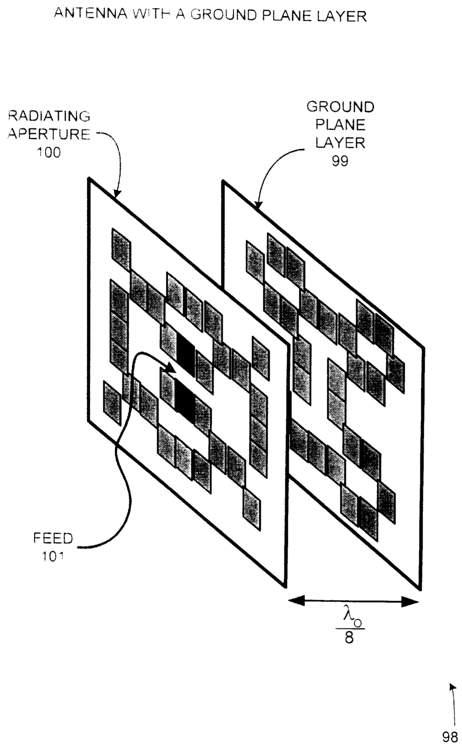

FIG. 15

Figure 4.1: The fragmented ground plane concept: a radiating aperture (100) is placed in front of a pixelated ground plane layer (99), separated by approximately $\lambda_0/8$. Both the radiating surface and the ground plane are optimized using the genetic algorithm [1].

tual patterned radiating aperture (105), and one optimized starting from a uniform conducting sheet (106). The two ground plane patterns differ significantly, demonstrating that the optimizer tailors the ground plane to the specific radiating surface it supports.

Figure 4.3 compares the performance of the fragmented aperture with and without the optimized ground plane. The solid curve (111) shows the uniform aperture gain limit. Without a reflector, the antenna radiates into both hemispheres and achieves approximately half the aperture limit (curve 112). With an optimized fragmented reflector, the forward gain is substantially increased (curves 114, 116), approaching the full aperture limit over the design band. However, Figure 4.4 reveals an important detail: the H-plane radiation pattern of the antenna with the fragmented ground plane (125) still shows appreciable backward radiation compared to what a solid ground plane would produce. The antenna alone (126) is nearly symmetric front-to-back, and the fragmented ground plane redirects a significant portion—but not all—of the backward energy into the forward hemisphere. This residual backward radiation through the fragmented ground plane is a direct consequence of the non-conducting pixels in the ground surface, and it is the same phenomenon observed in defected ground structures.

More recently, researchers have explored the physical bounds on antenna performance above a ground plane. Tayli and Gustafsson [5] derived fundamental limits on the gain and bandwidth achievable by antennas above ground planes, providing a theoretical benchmark against which fragmented ground plane designs can be evaluated. Ehrenborg and Gustafsson [6] extended this work to automatic design methods, demonstrating that optimization-based approaches can approach these physical bounds.

4.3 Fragmented Superstrates

The preceding section described the use of a fragmented surface *behind* the radiating aperture—a fragmented ground plane—to enhance forward gain. A complementary technique is to place a fragmented surface *in front of* the radiating aperture as a superstrate. Just as the fragmented ground plane acts as an optimized reflector, a fragmented superstrate acts as an optimized director, and the combination of reflector, driven element, and one or more directors is directly analogous to the classic Yagi-Uda antenna.

4.3.1 Yagi-Uda Analogy

In a Yagi-Uda antenna, a single driven element is surrounded by parasitic elements: a reflector behind the driven element and one or more directors in front of it. The reflector is slightly longer than resonant and presents an inductive impedance that causes it to re-radiate with a phase that reinforces the forward direction. The directors are slightly shorter than resonant and present capacitive impedances that produce a traveling-wave-like excitation across the array of parasitic elements, concentrating the radiation in the forward direction. Adding more directors increases the electrical length of the antenna and narrows the beam, increasing the forward gain.

The fragmented aperture antenna with a ground plane and one or more superstrate layers follows exactly this paradigm:

- The **fragmented ground plane** (Section 4.2) serves as the reflector, redirecting

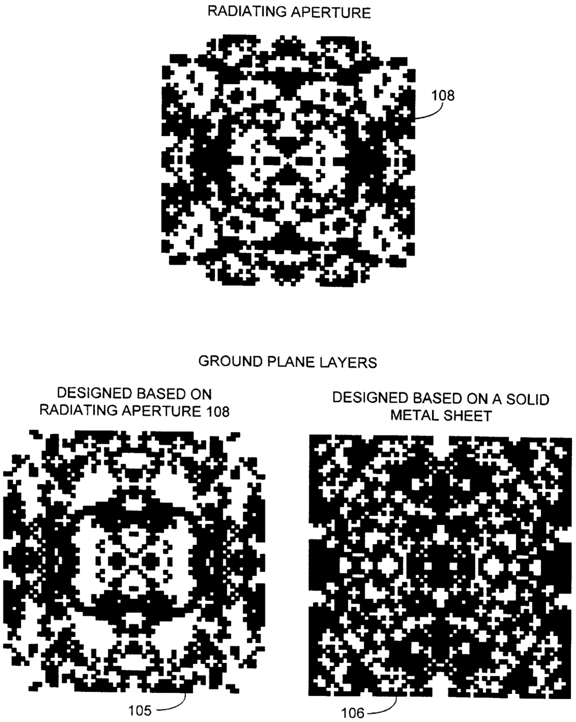

FIG. 16

Figure 4.2: A radiating aperture (108, top) and two fragmented ground plane designs optimized for it: one designed starting from the patterned radiating aperture (105, bottom left) and one starting from a solid metal sheet (106, bottom right). The optimizer produces different ground plane patterns depending on the initial condition [1].

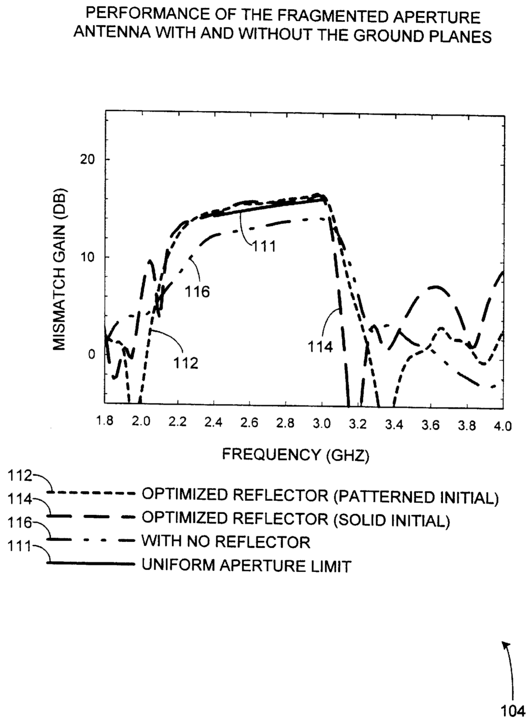

FIG. 17

Figure 4.3: Performance comparison of the fragmented aperture with optimized reflector (patterned initial, 114; solid initial, 116), without reflector (112), and the uniform aperture limit (111). The optimized ground plane substantially increases the forward gain [1].

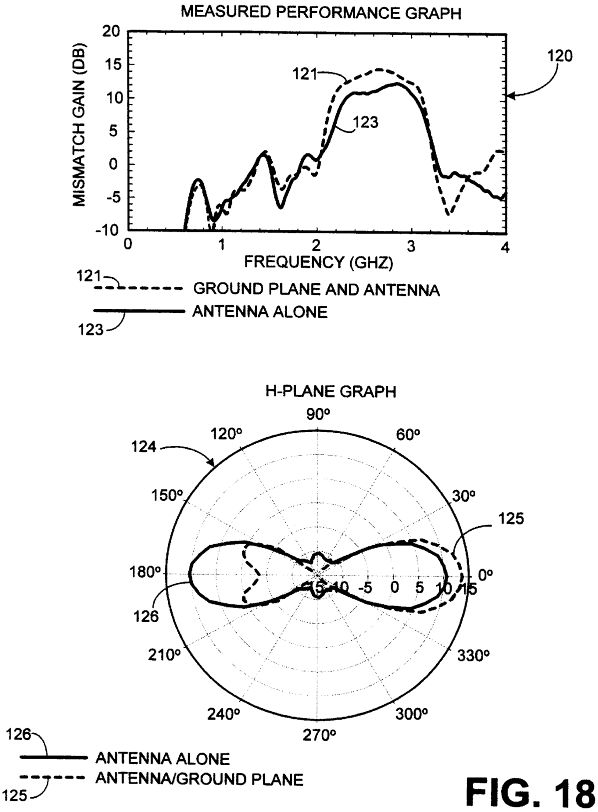

FIG. 18

Figure 4.4: Top: measured gain with (121) and without (123) the fragmented ground plane. Bottom: H-plane radiation pattern showing the antenna alone (126, bidirectional) and with the fragmented ground plane (125, predominantly forward but with residual backward radiation). The non-conducting pixels in the ground plane allow some energy to radiate through it [1].

backward radiation into the forward hemisphere.

- The **radiating aperture** is the driven element, excited by one of the feed strategies described in Section 4.4.
- One or more **fragmented superstrate layers**, placed at optimized distances in front of the radiating aperture, serve as directors. Each superstrate is a pixelated conducting surface whose pattern is optimized by the genetic algorithm to maximize the forward gain of the composite structure.

The key advantage of the fragmented aperture approach over a conventional Yagi-Uda is the same advantage that applies throughout this book: rather than using simple dipole-like elements whose lengths are tuned by hand, each surface is a pixelated aperture with hundreds or thousands of binary design variables, and the genetic algorithm is free to discover complex patterns that provide broadband directive behavior far beyond what analytical parasitic element design can achieve.

4.3.2 Single Superstrate Layer

The simplest superstrate configuration places a single fragmented surface at a distance of approximately $\lambda_0/4$ to $\lambda_0/2$ in front of the radiating aperture. The spacing and the pixel pattern of the superstrate are both design variables that the genetic algorithm optimizes simultaneously. The superstrate modifies the aperture field distribution, and when properly designed, it narrows the beam in one or both principal planes, increasing the peak directivity without increasing the physical aperture area.

[TODO: Author to create a single-superstrate design example. Suggested approach: use the same radiating aperture and fragmented ground plane from Section 4.2 (Figures 4.1–4.4), add a superstrate layer, and optimize. Show: (a) the superstrate pixel pattern, (b) gain comparison with and without the superstrate, and (c) radiation pattern showing the narrower beam.]

The gain enhancement from a single superstrate is analogous to adding a single director to a Yagi-Uda antenna. The improvement is modest—typically 1 to 3 dB—but it comes at virtually no cost in aperture area, requiring only an additional planar surface and the associated mechanical support.

4.3.3 Multiple Superstrate Layers

Just as adding more directors to a Yagi-Uda increases the gain, stacking multiple fragmented superstrate layers in front of the radiating aperture can provide additional gain enhancement. Each successive layer acts as an additional director, further shaping the aperture field and narrowing the beam. The spacings between layers, as well as the pixel patterns of all layers, are jointly optimized by the genetic algorithm.

The design complexity grows with each additional layer—two superstrate layers double the number of pixel variables to be optimized—but the genetic algorithm handles this naturally by concatenating the pixel chromosomes of all layers into a single design vector. The full-wave FDTD simulation inherently accounts for all inter-layer coupling, so no approximate coupling models are needed.

[TODO: Author to create a multi-superstrate design example. Suggested approach: use the same base design as the single-superstrate case, add two or three superstrate layers, and optimize. Show: (a) the pixel patterns of all layers, (b) gain versus number of superstrate layers (0, 1, 2, 3), demonstrating diminishing returns, and (c) radiation patterns showing progressive beam narrowing.]

There is, of course, a point of diminishing returns. Each additional superstrate layer adds a small amount of ohmic and dielectric loss, increases the physical depth of the antenna, and expands the design space that the genetic algorithm must search. In practice, one or two superstrate layers provide the most favorable trade-off between gain improvement and structural complexity.

4.3.4 Design Considerations

Several practical considerations arise in fragmented superstrate design:

- **Bandwidth.** The Yagi-Uda analogy suggests that superstrate-enhanced designs will be inherently narrower in bandwidth than the driven aperture alone, because the director behavior depends on the electrical spacing between layers, which changes with frequency. However, the fragmented aperture optimizer can produce superstrate patterns that maintain directive behavior over a wider bandwidth than would be possible with simple resonant parasitic elements, just as fragmented ground planes outperform simple solid reflectors.

- **Scan compatibility.** For phased array applications, the superstrate must not degrade the scan performance of the array. The superstrate pixel pattern should be optimized jointly with scan angle performance, using the periodic boundary condition techniques described in Section 4.10.

- **Fabrication.** Superstrate layers can be fabricated using the same printed circuit board techniques used for the radiating aperture and ground plane, with dielectric spacer layers providing the required inter-layer separations. This is particularly straightforward in the laminated PCB construction described in Chapter 7.

4.4 Feed Strategies

A critical aspect of any practical antenna design is how the antenna is connected to the transmitter or receiver electronics. The choice of feed strategy affects impedance matching, bandwidth, polarization purity, radiation pattern symmetry, and manufacturing complexity. The fragmented aperture design process can accommodate a wide range of feed configurations, since the full-wave simulation naturally captures the electromagnetic interaction between the feed structure and the radiating aperture.

This section surveys the principal feed strategies that have been used with fragmented and pixelated aperture antennas. The categorization follows two axes: whether the feed approaches the radiating surface from the same plane (*in-plane*) or passes through a ground plane (*through ground plane*), and whether the feed is single-ended (unbalanced) or balanced.

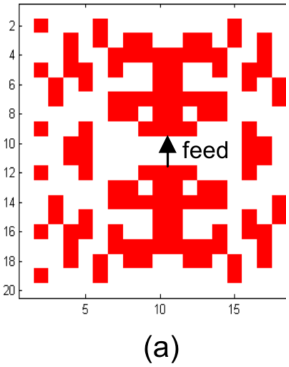

Figure 4.5: GA-optimized 20×20 fragmented patch element for a phased array, designed by Steyskal and Hanna at AFRL. Red pixels are conducting; white pixels are non-conducting. The feed point is at the center of the patch [7].

4.4.1 In-Plane, Single-Ended Feeds

The simplest feed configuration for a planar fragmented antenna is an in-plane microstrip feed, analogous to the way a conventional microstrip patch antenna is excited by a 50 Ω microstrip transmission line. In this approach, the fragmented conducting pattern and the feed line exist on the same substrate layer, and the feed connects directly to the edge or interior of the pixelated region.

This feed strategy has been adopted by several research groups working with fragmented or pixelated patch antennas. Steyskal and Hanna [7] at the Air Force Research Laboratory (AFRL) investigated the design of fragmented patch elements for phased arrays, studying how the pixel pattern on a patch element could be optimized while maintaining compatibility with a standard microstrip feed. Figure 4.5 shows the GA-optimized 20×20 pixel pattern from Steyskal and Hanna, and Figure 4.6 shows a 3-D perspective view of the fragmented patch with a custom feed structure consisting of vertical strips connecting the coaxial feed through the ground plane to the radiating surface. O'Donnell et al. [8] extended this work using a hybrid chromosome representation in the genetic algorithm to jointly optimize the pixel pattern and the feed location.

Barani, Harvey, and Sarabandi [9] demonstrated a fragmented antenna realized using coupled small radiating elements, each individually fed, showing that the fragmented concept can be implemented with direct microstrip excitation of sub-wavelength metallic patches. Their approach is particularly interesting because it demonstrates that the fragmented aperture concept is not limited to a single monolithic conducting surface; it can also be realized through the electromagnetic coupling between discrete conducting elements.

In the microstrip-fed configuration, the feed line itself becomes part of the electromagnetic environment that the optimizer must account for. The genetic algorithm

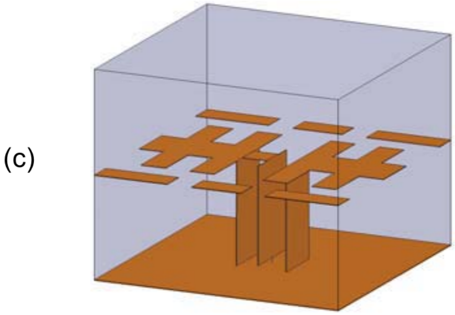

Figure 4.6: 3-D perspective of a fragmented patch element with a custom feed structure. Vertical conducting strips connect the coaxial feed through the ground plane to the pixelated radiating surface [7].

naturally handles this: the FDTD simulation includes the feed line geometry, and the optimizer adjusts the pixel pattern to achieve a good impedance match at the feed point.

Wright et al. [10] demonstrated a MEMS reconfigurable broadband patch antenna for conformal applications in which the pixelated conducting surface was fed from a microstrip line. The MEMS switches allowed dynamic reconfiguration of the pixel pattern, and the in-plane feed remained effective across multiple configurations. Figure 4.7 shows the fabricated Prototype 2 antenna with graphite dc bias lines and 36 installed MEMS switches, and Figure 4.8 shows the measured and simulated S11 for the three reconfiguration states (Highband, Midband, Lowband), demonstrating excellent agreement between model and measurement across a 1.1–1.7 GHz tuning range. Ali et al. [11] presented a related MEMS reconfigurable pixel microstrip patch for conformal load-bearing antenna structures (CLAS), further demonstrating the compatibility of in-plane feeds with pixelated apertures.

Figure 4.9 shows the fabricated coupled fragmented antenna elements from Barani et al. [9], photographed inside an anechoic chamber. The three inductively end-loaded folded dipole antennas are arranged in a linear formation, with electromagnetic coupling between adjacent elements creating the fragmented aperture effect. Figures 4.10 and 4.11 show the measured and simulated performance: the return loss (Figure 4.10) and peak gain (Figure 4.11) for three separation distances, confirming that the coupled fragmented concept provides bandwidth enhancement and gain improvement over a single element.

4.4.2 In-Plane, Other Strategies

Beyond simple microstrip feeds, several other in-plane excitation strategies have been applied to fragmented and pixelated antennas.

Aperture-coupled feeds. Herscovici et al. [12] demonstrated a fragmented aperture-

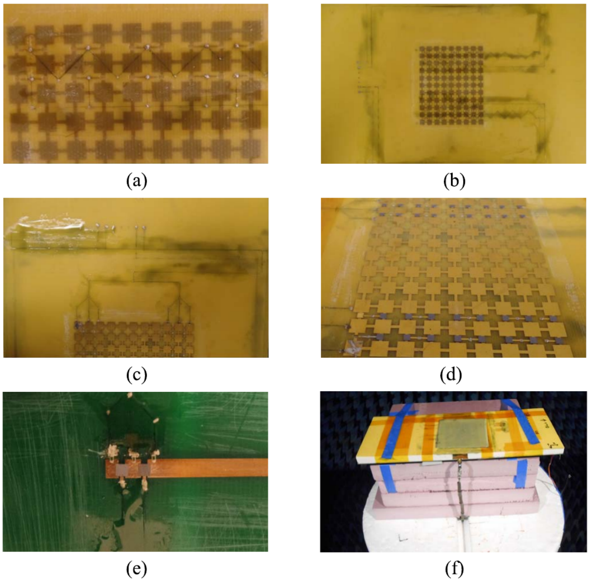

(a) (b)

(c) (d)

(e) (f)

Fig. 13. Photographs of Prototype 2 with high-impedance sawtooth-shape graphite dc bias lines. (a) Section of graphite lines on underside of patc substrate before protective coat of epoxy. (b) Underside of patch substrate wit graphite lines coated in epoxy. (c) Patch ground connection with protectiv coat of epoxy. (d) Pixel patch with 36 MEMS installed. (e) Feedline with bot MEMS installed. (f) Completed antenna on testing pedestal at WRCNC [41

Figure 4.7: Fabricated MEMS reconfigurable broadband patch antenna (Prototype 2): (a) graphite dc bias lines, (b) underside coated in epoxy, (c) ground connection, (d) pixel patch with 36 MEMS switches, (e) feedline with MEMS, (f) completed antenna on measurement pedestal [10].

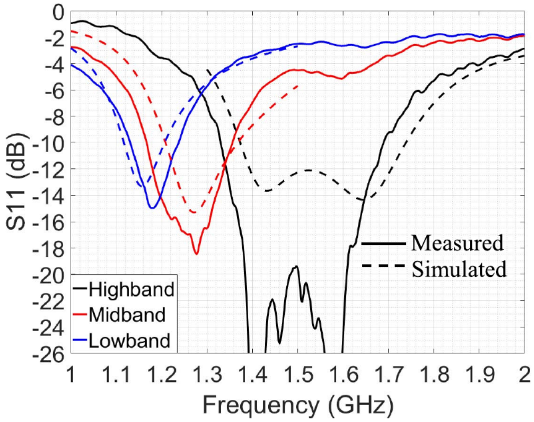

Figure 4.8: Measured (solid) and simulated (dashed) S11 for the three reconfiguration states of the MEMS pixelated patch antenna. The MEMS switches allow the antenna to be reconfigured between Highband, Midband, and Lowband operation [10].

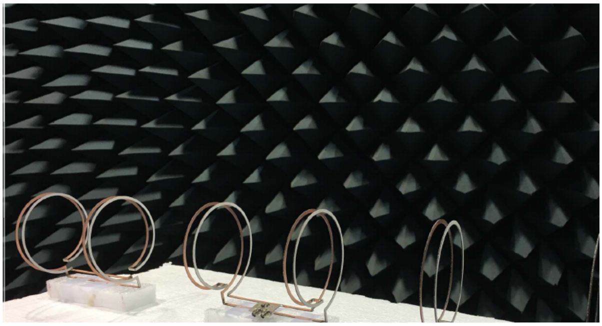

Figure 4.9: Fabricated coupled fragmented antenna elements in the anechoic chamber. Three inductively end-loaded folded dipole antennas form a fragmented aperture through electromagnetic coupling between adjacent elements [9].

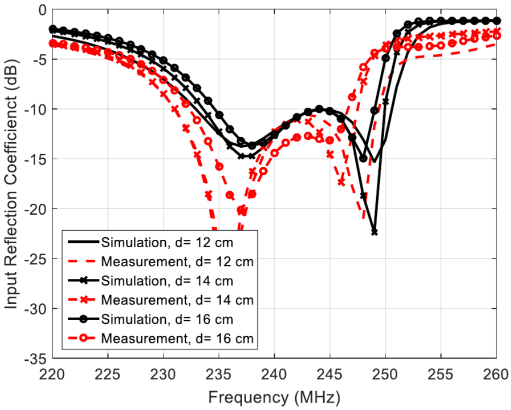

Figure 4.10: Measured (solid) and simulated (dashed) return loss for the coupled fragmented antenna at three separation distances ($d = 12$, 14, and 16 cm), showing good agreement between model and measurement [9].

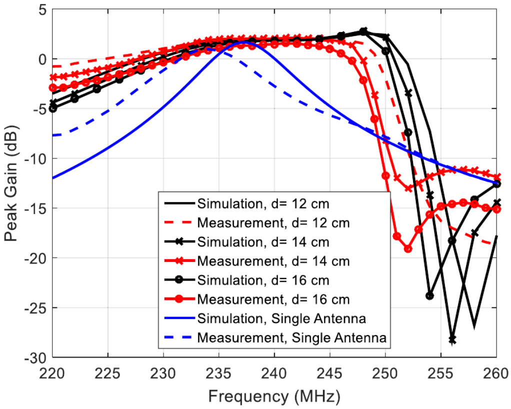

Figure 4.11: Measured and simulated peak gain for the coupled fragmented antenna at three separation distances compared to a single element. The coupled configuration provides approximately 1 dB gain improvement over the single element [9].

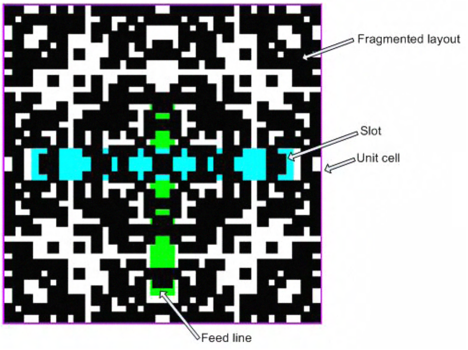

Figure 1 - The antenna layout shown as a unit cell in the infinite array environment.

Figure 4.12: Unit cell of the aperture-coupled fragmented microstrip array, showing the fragmented pixel pattern (top), coupling slot (center), and microstrip feed line (bottom) in the infinite array environment [13].

coupled microstrip antenna in which the feed energy is coupled to the radiating surface through a slot in the ground plane, rather than through a direct galvanic connection. This approach offers several advantages: the feed network is isolated on the opposite side of the ground plane from the radiating aperture, reducing spurious radiation from the feed lines; the coupling slot provides an additional degree of freedom for impedance matching; and the feed and radiating layers can be independently optimized. In a companion study, Herscovici et al. [13] extended the aperture-coupled fragmented concept to array configurations, investigating the scanning characteristics of aperture-coupled fed fragmented microstrip arrays. Their unit cell element, optimized using Ansoft Designer's genetic algorithm and validated with HFSS and CST, achieved greater than 70% bandwidth (VSWR $<$ 2:1) at broadside and maintained scan performance to 30° across the full operating band. This work at the Air Force Research Laboratory demonstrated that the aperture-coupled feed is compatible with phased array scanning, an important practical consideration for array applications. Figure 4.12 shows the unit cell layout from Herscovici et al. [13], illustrating the fragmented pixel pattern on the radiating layer, the coupling slot, and the microstrip feed line on the opposite side of the ground plane. Bishop et al. [14] further extended aperture-coupled feeding to a MEMS reconfigurable pixelated patch antenna for conformal load-bearing antenna structures (CLAS).

Integrated balun feeds. For balanced radiating structures, an integrated balun can convert a single-ended transmission line to a balanced excitation at the antenna terminals without requiring a separate balun component. Zang, Jin, and Jiao [15] demonstrated a 3–10 GHz linearly polarized fragmented aperture array with an integrated balun feed, achieving broadband performance with a compact, manufacturable feed structure. Figure 4.13 shows the cross-section of their multilayer array topology, illustrating the integrated balun formed by loaded vias and feed vias passing through the ground plane. Figure 4.14 shows the optimized fragmented patch geometry—a 20×20

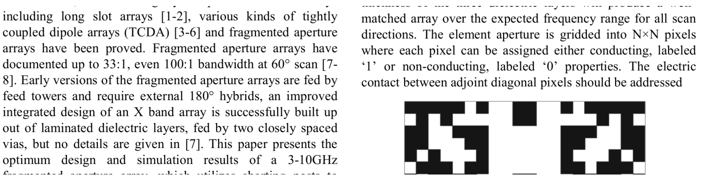

including long slot arrays [1-2], various kinds of tightly coupled dipole arrays (TCDA) [3-6] and fragmented aperture arrays have been proved. Fragmented aperture arrays have documented up to 33:1, even 100:1 bandwidth at 60° scan [7-8]. Early versions of the fragmented aperture arrays are fed by feed towers and require external 180° hybrids, an improved integrated design of an X band array is successfully built up out of laminated dielectric layers, fed by two closely spaced vias, but no details are given in [7]. This paper presents the optimum design and simulation results of a 3-10GHz

matched array over the expected frequency range for all scan directions. The element aperture is gridded into N×N pixels where each pixel can be assigned either conducting, labeled '1' or non-conducting, labeled '0' properties. The electric contact between adjoint diagonal pixels should be addressed

Figure 4.13: Cross-section of the multilayer fragmented aperture array with integrated balun feed. The structure comprises a superstrate, radiation layer with the fragmented patch, and substrate with loaded vias and feed vias forming the unbalanced-to-balanced transition [15].

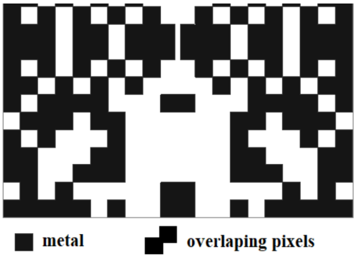

Figure 2. Geometry of the fragmented patch in the element aperture.

Figure 4.14: Optimized fragmented patch geometry for the 3–10 GHz array element. The binary pixel grid shows metal (black) and non-metal (white) regions, with overlapping pixels (grey) at diagonal corners to ensure electrical contact during fabrication [15].

binary pixel grid with overlapping diagonal pixels to ensure electrical contact at corners. This approach is related to the integrated balun designs used in tightly coupled dipole arrays [16].

Coplanar waveguide feeds. Coplanar waveguide (CPW) feeds offer another in-plane option that is particularly convenient for single-layer fabrication, since the signal conductor and ground conductors are on the same surface. CPW feeds have been used with pixelated antenna designs by several groups.

[TODO: Check literature for specific CPW-fed fragmented/pixelated antenna references. If none found in our .bib files, add a note or locate 1–2 references from IEEE Xplore.]

4.4.3 Through Ground Plane: Center Pin Feed

For fragmented aperture antennas backed by a ground plane, a common feed approach is to pass a coaxial transmission line through the ground plane, with the center conductor extending across the cavity to make contact with the radiating surface. This is analogous to a probe-fed microstrip patch antenna, but with the probe extending across a potentially thicker cavity that may contain dielectric layers or broadband screen backplane structures.

This feed configuration was used in the original wideband fragmented aperture arrays described in Chapter 6. As shown in Figure 7.2 in Chapter 7, the traditional construction uses machined aluminum feed towers that enclose the coaxial feed lines and provide structural support.

Landgren, Dykes, and Allen [17] at the Georgia Tech Research Institute (GTRI) developed an unbalanced feed design for wideband phased arrays that uses a single center pin extending from the coaxial connector through the cavity to the radiating layer. The unbalanced feed avoids the need for a balun or differential feed network, simplifying the antenna architecture and enabling compatibility with standard single-ended electronics. This work was significant because earlier fragmented aperture arrays had typically used balanced (differential) feeds, which require either a balun at each element or differential transmit/receive electronics.

Landgren et al. [18] demonstrated this unbalanced feed concept in a wideband millimeter-wave antenna element, showing that the fragmented aperture design process could optimize the pixel pattern to achieve good impedance matching with the unbalanced feed across a wide bandwidth. The FDTD simulation inherently captures the asymmetry introduced by the single-pin feed and optimizes the surrounding pixel pattern accordingly.

Figure 4.15 shows the fabricated mmWave fragmented aperture antenna element developed by Landgren et al. [18], including the antenna board, cable/connector assembly, measurement fixture, and a close-up of the fragmented aperture region near the feed and plated vias. The antenna aperture is approximately 5.0 mm × 2.0 mm on a 1.97 mm thick Rogers 5880LZ substrate, designed for 18–40 GHz operation with a single unbalanced coaxial feed. Figure 4.16 shows the measured and modeled performance: the reflection coefficient (left) and broadside realized gain (right) show close agreement between the FDTD model and measurements across the design band.

4.4.4 Through Ground Plane: Flanking Via Feed

A variation on the center pin feed uses a center conductor flanked by two (or more) closely spaced ground vias that extend from the ground plane to the radiating surface. This configuration creates a quasi-coaxial transmission line within the antenna cavity, providing better control of the feed impedance and reducing the excitation of unwanted cavity modes.

Landgren et al. [19] demonstrated a broadband array with unbalanced feeds in which the feed structure incorporated flanking vias alongside the center conductor. This design was part of a broader effort to develop fragmented aperture arrays with integrated power combiners, where the combiner networks were also designed using the fragmented aperture principle. The flanking via approach was also adopted in the laminated PCB construction described in Chapter 7 (see Figure 7.3), where the feed vias are manufactured using standard multi-layer PCB plating processes.

Landgren et al. [20] further developed this concept in a wideband phased array with fragmented combiner technology, demonstrating that the fragmented aperture optimiza-

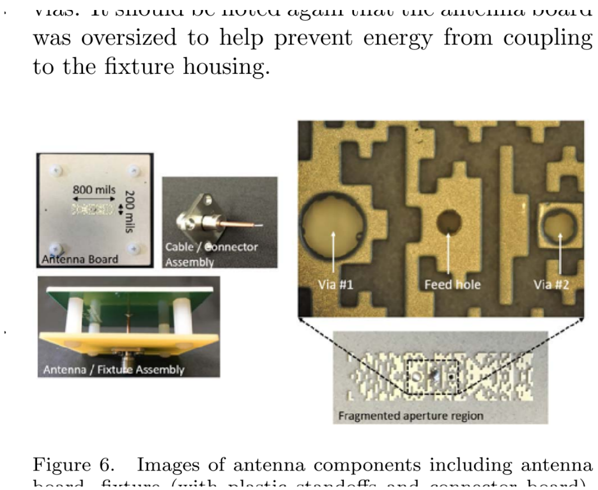

vias. It should be noted again that the antenna board was oversized to help prevent energy from coupling to the fixture housing.

Figure 6. Images of antenna components including antenna board, fixture (with plastic standoffs and connector board)

Figure 4.15: Fabricated mmWave fragmented aperture antenna element with unbalanced feed: antenna board, cable/connector assembly, measurement fixture (left), and close-up of the fragmented aperture region near the feed and plated vias (right) [18].

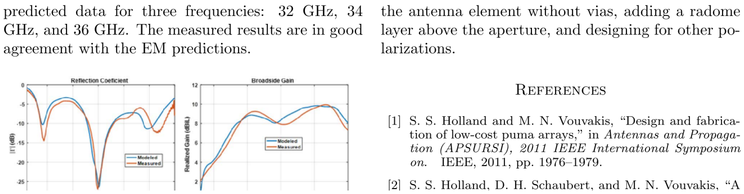

predicted data for three frequencies: 32 GHz, 34 GHz, and 36 GHz. The measured results are in good agreement with the EM predictions.

the antenna element without vias, adding a radome layer above the aperture, and designing for other polarizations.

REFERENCES

[1] S. S. Holland and M. N. Vouvakis, “Design and fabrication of low-cost puma arrays,” in *Antennas and Propagation (APSURSI), 2011 IEEE International Symposium on.* IEEE, 2011, pp. 1976–1979.

[2] S. S. Holland, D. H. Schaubert, and M. N. Vouvakis, “A

Figure 4.16: Measured vs. modeled performance of the mmWave fragmented aperture element: reflection coefficient (left) and broadside realized gain (right). The close agreement validates the unbalanced feed design approach at millimeter-wave frequencies [18].

tion could be applied not only to the radiating surface but also to the power combining networks behind the ground plane. The fragmented combiner concept—an important example of applying the fragmented aperture methodology to non-antenna electromagnetic structures—is described in detail in Chapter 10.

[TODO: Author to create an original flanking-via feed design example. Include figure showing the via geometry in cross-section and plan view, and a performance comparison with the center-pin-only feed.]

4.5 Bandwidth Tailoring

One of the most powerful aspects of the fragmented aperture design process is the ability to tailor the operating bandwidth by simply changing the fitness function presented to the genetic algorithm. The same physical aperture—the same substrate, the same pixel grid, the same feed—can be redesigned to cover different frequency bands by changing only the target frequencies in the optimization.

Chapter 3 demonstrated this directly: four different antenna designs were produced on identical 25.4 cm × 25.4 cm apertures with the same pixel grid, each covering a different portion of the 500 MHz to 2.0 GHz range. The pixel patterns differed significantly between designs, yet all achieved gain approaching the uniform aperture limit within their respective design bands.

This bandwidth tailoring capability has a natural extension: if the pixel pattern can be changed electronically rather than physically, the same antenna hardware could be reconfigured in real time to cover different frequency bands. This is precisely the concept behind the reconfigurable fragmented aperture antenna described in Chapter 5, where switched links between metallic pads allow the effective pixel pattern to be changed on the fly.

Several other research groups have explored bandwidth optimization of pixelated antennas. Wang et al. [21] developed a machine learning–assisted quasi-bisection method for optimizing the bandwidth of pixelated patch antennas, demonstrating that the design space for pixelated antennas is amenable to data-driven optimization techniques. Jayasinghe and Uduwawala [22] used genetic algorithms to design broadband patch antennas, and Jayasinghe, Anguera, and Uduwawala [23] extended the approach to multi-band designs for GSM, UMTS, LTE, and Bluetooth applications. Figure 4.17 shows the hexa-band design from Jayasinghe et al., including the optimized pixel pattern, 3-D model view, and photographs of the fabricated antenna. The measured and simulated reflection coefficients (Figure 4.18) show good agreement across all six operating bands, confirming that GA-optimized pixelated patches can achieve multi-band operation covering 880–960 MHz and 1700–2520 MHz.

Figures 4.19 and 4.20 illustrate this concept with two designs from the original patent, both on the same physical aperture. Figure 4.19 shows a broadband design optimized to cover a wide frequency range: the pixel pattern (left) was evolved by the genetic algorithm to maximize gain across the full design band, and the resulting performance (right) shows gain approaching the uniform aperture limit over approximately 2:1 bandwidth. Figure 4.21 shows a narrowband design optimized on the same aperture for a much narrower frequency range. The pixel pattern is visibly different—the narrowband design concentrates its conducting material differently to achieve high gain

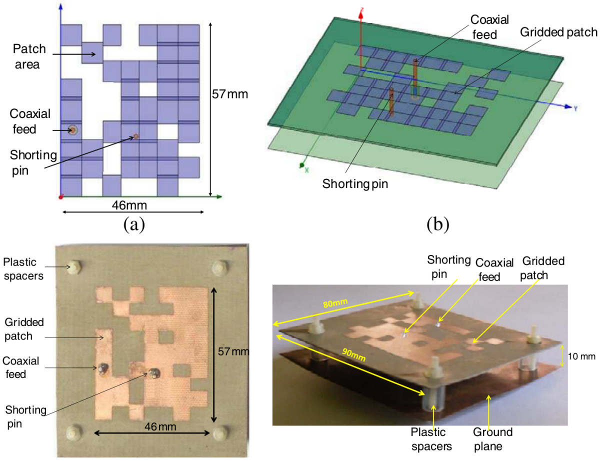

Figure 4.17: Hexa-band GA-optimized fragmented patch antenna: (a) pixel pattern, (b) 3-D model, (c) fabricated antenna top view, (d) fabricated antenna showing plastic spacers and coaxial feed. The design covers GSM900, GSM1800, GSM1900, UMTS, LTE2300, and Bluetooth bands [23].

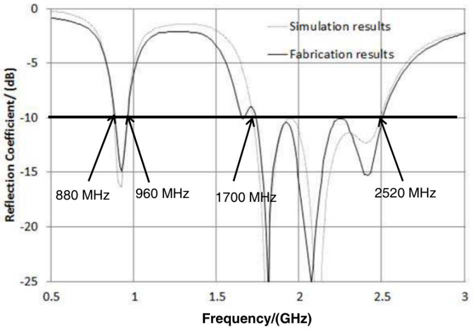

Figure 7. Reflection coefficient of the haxa band MPA.

Figure 4.18: Measured and simulated reflection coefficient of the hexa-band fragmented patch antenna, showing six operating bands below −10 dB across 880–960 MHz and 1700–2520 MHz [23].

over a limited band. Figure 4.22 confirms that the narrowband design achieves gain very close to the aperture limit within its target band.

The key insight for the reader is that the bandwidth is not an inherent property of the antenna hardware—it is a property of the pixel pattern. The hardware defines the *design space* (the set of possible pixel patterns), while the optimization determines which pattern within that space best meets the performance requirements. Changing the requirements produces a different optimal pattern on the same hardware.

4.6 Fixed Beam Steering

The fragmented aperture designs presented in Chapters 2 and 3 were all optimized for broadside radiation (perpendicular to the aperture plane). A broadside design with a centrally located feed naturally exhibits quadrant symmetry in its pixel pattern: the optimizer discovers patterns that are symmetric about both the horizontal and vertical axes through the feed point. This symmetry is a consequence of the broadside radiation requirement, which treats all four quadrants equivalently.

When the design objective is changed to steer the beam to a fixed angle away from broadside, this symmetry is broken. The optimizer must distribute conducting material asymmetrically across the aperture to create the phase gradient necessary for off-broadside radiation. The resulting pixel patterns are visually distinct from broadside designs and provide insight into how the fragmented aperture creates its radiation characteristics.

4.6.1 Broadside

For reference, a broadside design places the main beam perpendicular to the aperture plane. The pixel pattern exhibits the quadrant symmetry discussed above, and the design process exploits this symmetry to reduce the number of independent variables (as described in Chapter 3, where only one quadrant of pixels is optimized and the remaining three quadrants are generated by reflection).

4.6.2 Forward and Backward Steering

When the target beam direction is tilted to 45° from broadside (or any intermediate angle), the pixel pattern loses its left-right symmetry (for steering in the H-plane) or its top-bottom symmetry (for steering in the E-plane). The genetic algorithm must now optimize over a larger number of independent pixels, since symmetry can no longer be exploited to reduce the design space.

[TODO: Author to create example designs showing pixel patterns for broadside, $+45^\circ$, and -45° beam steering on the same aperture. A side-by-side comparison of the three pixel patterns would effectively illustrate how the symmetry changes. Include radiation pattern plots for each.]

The ability to design antennas with fixed beam steering has practical applications in conformal antennas, where the antenna must be mounted on a curved surface and the desired beam direction is not normal to the local surface. It also connects directly to the reconfigurable concept of Chapter 5: if the beam direction can be changed by

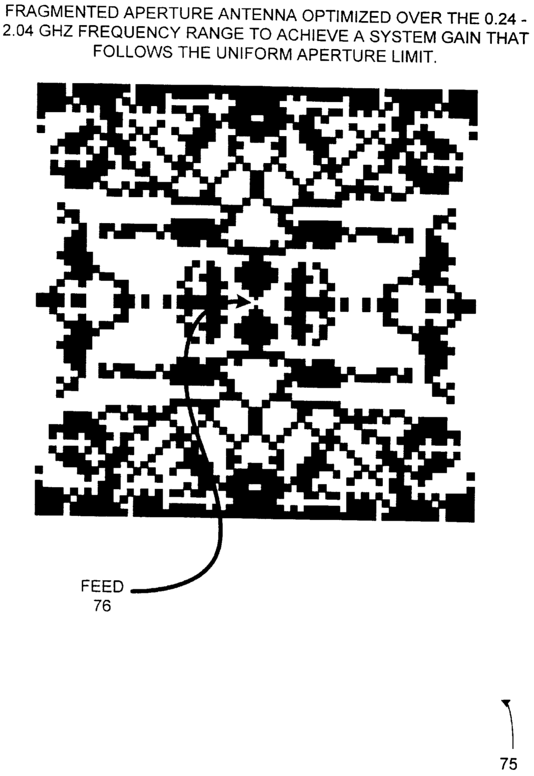

FIG. 9

Figure 4.19: Broadband fragmented aperture design: the pixel pattern (left) is optimized to maximize gain across a wide frequency range. The performance plot (right) shows gain approaching the uniform aperture limit over the full design band [1].

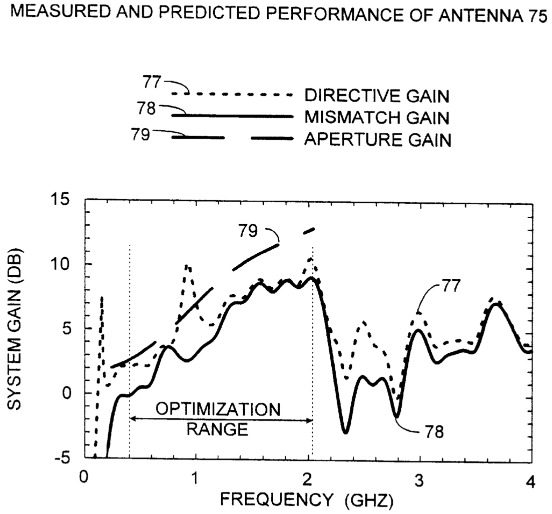

80

FIG. 10

Figure 4.20: Measured and simulated performance of the broadband fragmented aperture design. The realized gain tracks the uniform aperture limit across the design band [1].

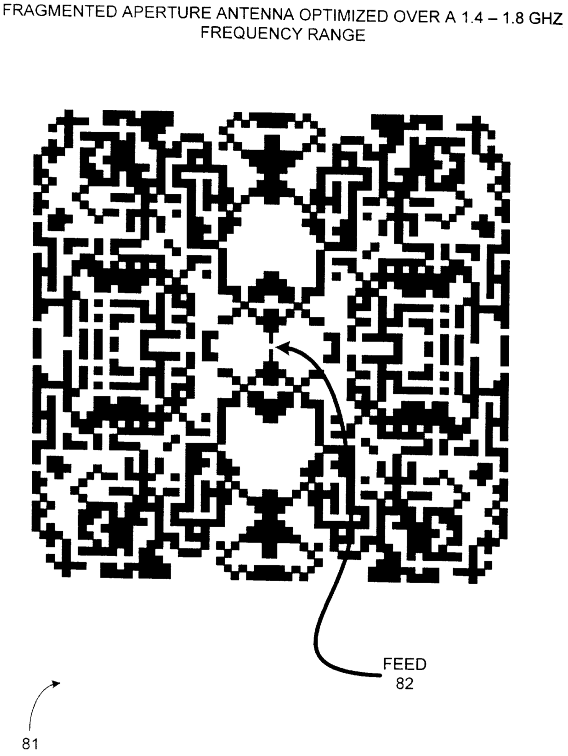

FIG. 11

Figure 4.21: Narrowband fragmented aperture design on the same physical aperture as the broadband design in Figure 4.19. The pixel pattern differs significantly, demonstrating that the bandwidth is a property of the pixel pattern, not the hardware [1].

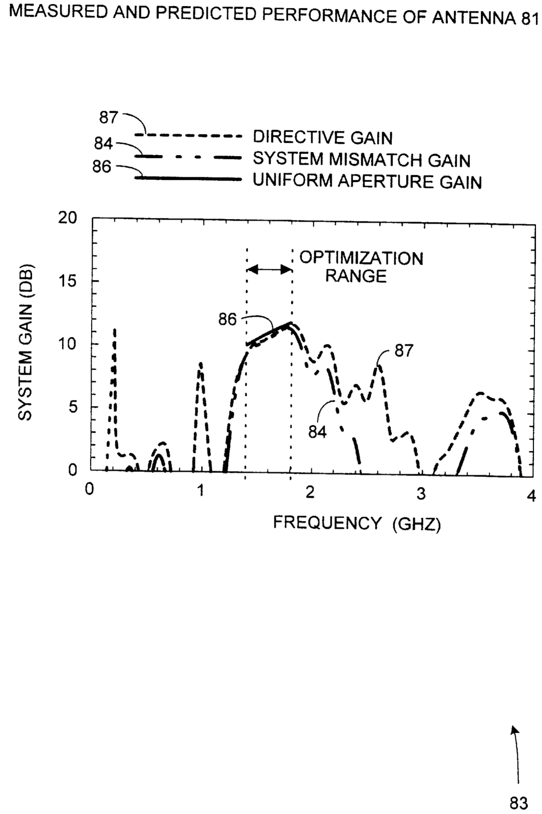

FIG. 12

Figure 4.22: Performance of the narrowband fragmented aperture design. The gain closely approaches the uniform aperture limit within the narrower target band [1].

changing the pixel pattern, then an electronically reconfigurable aperture can steer its beam without any mechanical motion.

4.6.3 Endfire

Endfire radiation (in the plane of the aperture) represents the extreme case of beam steering. As demonstrated in Chapter 5 (Figure 5.3), the reconfigurable fragmented aperture antenna was shown to produce endfire radiation when configured with an asymmetric pixel pattern. The endfire configuration exhibited no right-left symmetry, in contrast to the broadside configuration which maintained full quadrant symmetry.

Designing for endfire radiation is more challenging than broadside because the aperture is not oriented for maximum capture area in the endfire direction. Nevertheless, Tang, Zhang, and colleagues [24] demonstrated a dual-port endfire millimeter-wave reconfigurable antenna with an optimized pixel surface, showing that pixelated optimization can produce useful endfire patterns even at millimeter-wave frequencies.

[TODO: Author to create an endfire design example. Show the pixel pattern (which should be dramatically different from the broadside pattern) and the resulting radiation pattern. Reference the Ch 5 endfire result as a preview.]

4.7 Polarization

4.7.1 Linear Polarization

The designs presented in Chapters 2 and 3 were all linearly polarized. Linear polarization arises naturally when the pixel pattern and feed configuration have a preferred axis of symmetry. The designs in those chapters used a single feed point with quadrant symmetry enforced, producing a vertically polarized radiation pattern.

Linear polarization is the simplest case for the fragmented aperture design process, since the symmetry constraints reduce the number of independent pixels and the fitness function need only evaluate a single polarization component. The examples in Chapters 2 and 3 demonstrate that the approach achieves excellent linearly polarized performance, with realized gain approaching the aperture limit.

4.7.2 Circular Polarization

Circular polarization (CP) requires that the radiated electric field have two orthogonal components of equal amplitude with a 90° phase difference between them. For a fragmented aperture antenna with a single central feed point, achieving CP requires breaking the quadrant symmetry of the pixel pattern. Specifically, the pattern can have no lines of mirror symmetry passing through the feed point; if such a line existed, the radiated field would be linearly polarized along or perpendicular to that line.

This means that a CP design must optimize over a larger design space than a linearly polarized design: all four quadrants of the pixel pattern must be treated as independent variables, quadrupling the number of free parameters compared to a design that exploits quadrant symmetry. Despite this increase in design complexity, the genetic

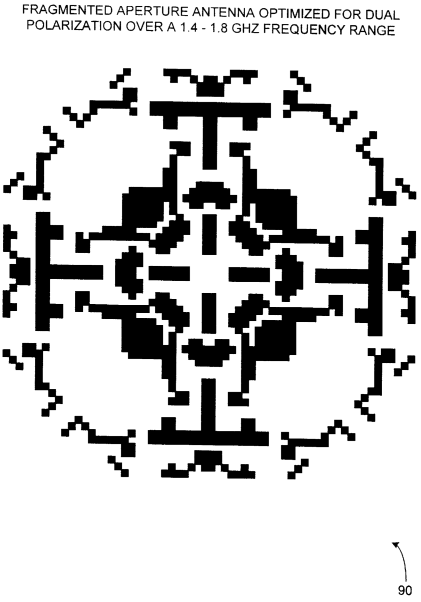

FIG. 13

Figure 4.23: Fragmented aperture antenna optimized for dual linear polarization over 1.4–1.8 GHz. The pixel pattern exhibits four-fold rotational symmetry, ensuring equal performance for both polarizations. Compare with the linearly polarized designs in Chapters 2 and 3, which have mirror symmetry [1].

algorithm can successfully discover pixel patterns that produce high-quality circular polarization.

An early example of polarization diversity is the dual-polarized fragmented aperture shown in Figure 4.23, from the original patent. This design was optimized over the 1.4–1.8 GHz frequency range to support two orthogonal linear polarizations simultaneously. The pixel pattern exhibits four-fold rotational symmetry (90° rotation maps the pattern onto itself) rather than the mirror symmetry of the single-polarization designs. This rotational symmetry ensures that the antenna performs identically for both polarizations. The associated performance data, shown in Figure 4.24, confirmed that the design approached the uniform aperture gain limit for both polarizations across the design band.

The transition from dual linear polarization to circular polarization is conceptually straightforward: the pixel pattern must support two orthogonal field components with a 90° phase difference, which requires breaking the four-fold rotational symmetry to

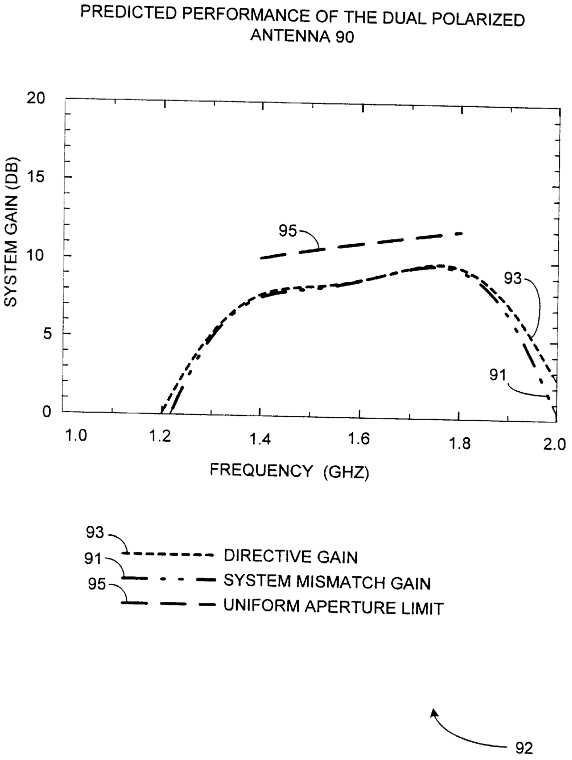

FIG. 14

Figure 4.24: Performance of the dual-polarized fragmented aperture antenna of Figure 4.23. The realized gain for both polarizations approaches the uniform aperture limit across the 1.4–1.8 GHz design band, confirming that the four-fold rotationally symmetric pixel pattern provides equal performance for orthogonal polarizations [1].

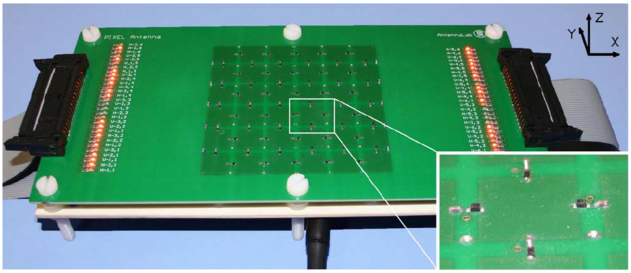

2. Picture of the pixel antenna prototype.

Figure 4.25: Fabricated reconfigurable parasitic pixel antenna prototype. The 6×6 pixel grid with PIN diode switches enables frequency, radiation pattern, and polarization reconfiguration from a single hardware platform [25].

introduce the necessary phase asymmetry.

[TODO: Author to create a circularly polarized fragmented aperture design. Show the pixel pattern (which should exhibit no mirror symmetry) and the axial ratio versus frequency. The dual-pol design above provides a starting point—the CP design should look qualitatively different, with the four-fold symmetry broken.]

Rodrigo, Jofre, and Cetiner [25] demonstrated a reconfigurable antenna using a parasitic pixel layer that could switch between frequency, radiation pattern, and polarization reconfiguration, including linear-to-circular polarization switching. Figure 4.25 shows the fabricated prototype with its 6×6 pixel grid and PIN diode switches, and Figure 4.26 shows the measured and simulated reflection coefficients for thousands of switch configurations, demonstrating the wide frequency tuning range achievable with the parasitic pixel layer.

Zechmeister and Lacik [26] designed a pixelated circularly polarized SIW horn antenna with nearly equal beamwidths in the principal planes, demonstrating that pixelated optimization can produce high-quality CP even in waveguide-fed configurations. Zechmeister, Lacik, and Kadlec [27] fabricated and measured both linearly polarized and circularly polarized versions of the pixelated SIW horn at 24 GHz. Figure 4.27 shows the fabricated LP prototype, and Figure 4.28 shows the measured and simulated radiation patterns, confirming nearly equal beamwidths in the E- and H-planes.

4.7.3 Non-Broadside Circular Polarization

The most challenging polarization design case is circular polarization at a steered beam angle. This combines the asymmetries required for both beam steering (Section 4.6) and circular polarization (requiring the absence of mirror symmetry), resulting in a pixel pattern with no exploitable symmetry whatsoever. Every pixel on the aperture is an independent variable.

Despite this being the most computationally demanding design scenario, it is also

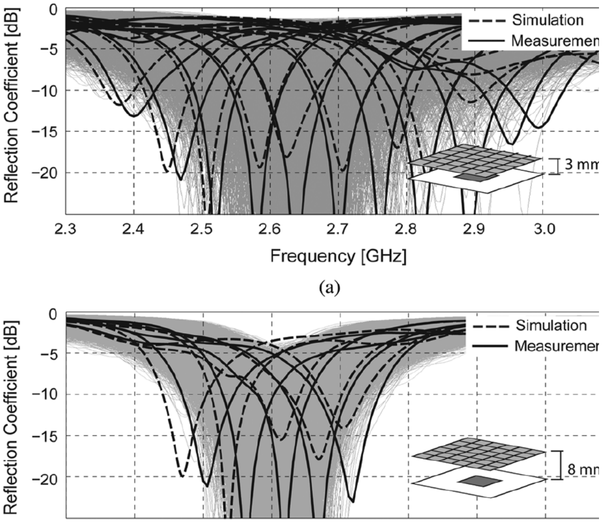

(a)

(b)

Fig. 3. Reflection coefficient of the different switch configurations, (a) mm, (b) $d = 8$ mm.

Figure 4.26: Measured (black) and simulated (grey) reflection coefficients for the parasitic pixel antenna across 20,000 switch configurations: (a) parasitic layer distance $d = 3$ mm, (b) $d = 8$ mm. The wide tuning range demonstrates the reconfiguration flexibility of the pixel layer approach [25].

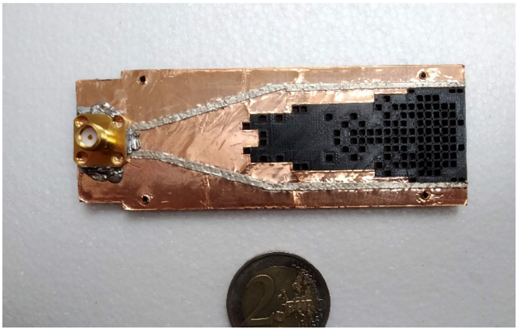

Figure 4.27: Fabricated linearly polarized pixelated SIW horn antenna prototype at 24 GHz. The 3D-printed substrate with optimized pixelated aperture is visible, with a coin for scale [27].

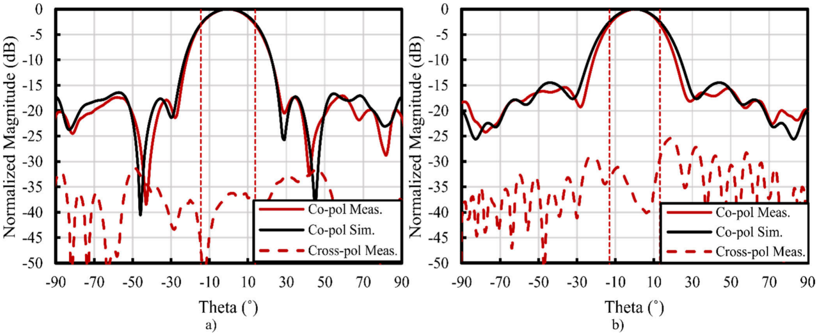

FIGURE 10. **Normalized measured and simulated radiation patterns of the linearly polarized antenna at 24.125 GHz a) E-plane and b) H-plane. Measured HPBW is indicated by vertical dashed lines.**

Figure 4.28: Measured and simulated radiation patterns of the pixelated SIW horn antenna at 24.125 GHz: (a) E-plane and (b) H-plane. The pixelated optimization achieves nearly equal beamwidths in both planes [27].

one of the most practically important. Satellite communication antennas, for example, often require CP at angles well away from broadside to maintain a link as the satellite moves across the sky.

[TODO: Author to create a non-broadside CP design example. This would be a flagship result for the chapter—showing that the fragmented aperture approach can simultaneously achieve beam steering and circular polarization from a single feed point, with no exploitable pixel symmetry. Show pixel pattern, radiation pattern, and axial ratio at the design angle.]

4.8 Beamwidth Tailoring

In addition to controlling the beam direction and polarization, the fragmented aperture design process can be used to tailor the beamwidth of the radiation pattern. The fitness function presented to the genetic algorithm can include requirements on the angular width of the main beam, the sidelobe levels, or the gain at specific angles relative to the main beam.

4.8.1 GPS CRPA Element Design

A compelling example of beamwidth tailoring is the design of miniaturized GPS Controlled Reception Pattern Antenna (CRPA) elements using the fragmented aperture approach. Maloney et al. [28] demonstrated that fragmented aperture optimization could produce compact GPS antenna elements with radiation patterns tailored to the requirements of CRPA null-steering algorithms.

A CRPA system uses an array of antenna elements and adaptive signal processing to steer nulls in the direction of jamming signals while maintaining reception of the desired GPS satellite signals. The performance of the CRPA system depends on the radiation characteristics of the individual elements, including the element beamwidth and the gain roll-off toward the horizon. The fragmented aperture approach allows these element-level pattern characteristics to be optimized directly, producing elements that are well suited for integration into the CRPA array.

Maloney and Baker [29] further developed this concept, presenting model and measurement results for a miniaturized GPS CRPA element designed using the fragmented aperture approach. The measured results confirmed that the element met the beamwidth and gain specifications required by the CRPA processor.

Figure 4.29 illustrates the miniaturization advantage: a conventional 7-element CRPA uses approximately 4-inch patch elements in a 16-inch array, while the fragmented aperture approach produces a notional 6-inch array with 1.5-inch dual-frequency elements. Figure 4.30 shows the FDTD model of the 7-element miniaturized CRPA with 2-inch fragmented aperture elements on a finite ground plane. Figure 4.31 shows the fabricated array and the measured versus modeled S11, demonstrating operation at both the L1 and L2 GPS bands.

Beamwidth tailoring has also been explored by other groups. Towfiq et al. [30] demonstrated a reconfigurable antenna with independent beam steering and beamwidth variability, using pixelated elements to achieve a range of beamwidths for wireless communication applications. Figure 4.32 shows the fabricated reconfigurable antenna

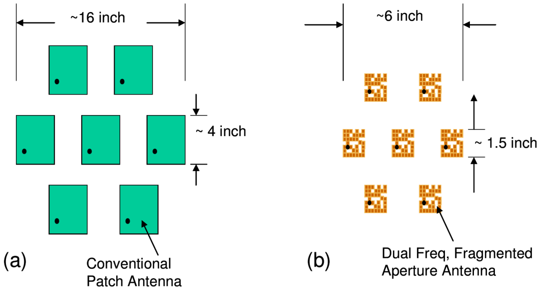

Figure 4.29: Size comparison: (a) conventional 7-element GPS CRPA with ∼4-inch patch elements in a ∼16-inch array, and (b) notional miniaturized CRPA with ∼1.5-inch dual-frequency fragmented aperture elements in a ∼6-inch array [29].

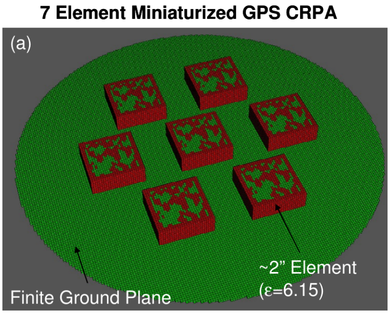

Figure 4.30: FDTD model of the 7-element miniaturized GPS CRPA array. Each element is a ∼2-inch fragmented aperture antenna on a dielectric substrate ($\varepsilon_r = 6.15$), with 4-inch element spacing on a finite ground plane [29].

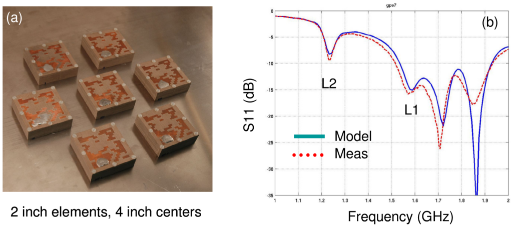

2 inch elements, 4 inch centers

Figure 4.31: (a) Fabricated 7-element miniaturized GPS CRPA array with 2-inch fragmented aperture elements on 4-inch centers. (b) Measured (dotted) and modeled (solid) S11, showing dual-band operation at the L1 and L2 GPS frequencies [29].

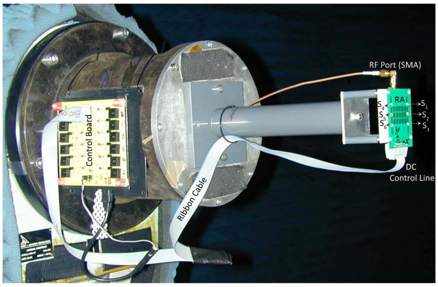

Fig. 5. Photograph of the RA measurement setup showing numbered interpixel p-i-n diode switches.

Figure 4.32: Fabricated reconfigurable antenna with beam steering and beamwidth variability. The p-i-n diode switches (S1–S6) are controlled via the ribbon cable from the switch control board, enabling 12 different beam configurations [30].

from Towfiq et al., with labeled p-i-n diode switches and the control board used to select among 12 different beam configurations. Figure 4.33 shows the measured and simulated performance for the broadside mode, confirming good agreement in both the reflection coefficient and the realized gain pattern. Zechmeister, Lacik, and Kadlec [27] optimized the beamwidth of pixelated SIW horn antennas to achieve nearly equal beamwidths in the principal planes.

4.9 Out-of-Band Rejection

In many practical scenarios, an antenna must operate in a specific frequency band while coexisting with strong emitters in nearby bands. If the antenna has significant gain at the interfering frequency, the received interference can saturate the front-end electronics and degrade system performance. Conventional approaches to this problem include

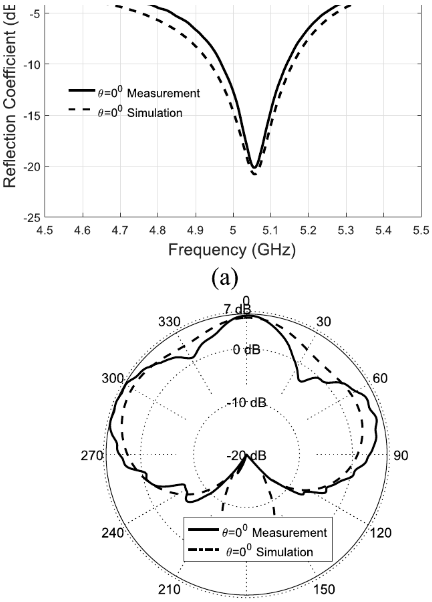

(a)

(b)

Fig. 6. Simulated and measured (a) reflection coefficients and (b) realized gain patterns of the RA for θ =0° on ϕ =0° plane (mode 1).

Figure 4.33: Measured and simulated performance of the reconfigurable antenna in broadside mode: (a) reflection coefficient and (b) realized gain pattern, showing good agreement between model and measurement [30].

external bandpass or bandstop filters in the receive chain. The fragmented aperture approach offers an alternative: the fitness function can include a requirement that the antenna gain be minimized at the interfering frequency, effectively building the filtering function into the antenna itself.

This is accomplished by adding a penalty term to the genetic algorithm fitness function. In addition to maximizing gain within the desired operating band, the fitness function penalizes designs that exhibit significant gain at the rejection frequency. The optimizer then searches for pixel patterns that satisfy both objectives simultaneously: high gain in-band and low gain at the rejection frequency.

[TODO: Author to create an example design demonstrating out-of-band rejection. Suggested scenario: an antenna operating in the 3.4–3.8 GHz 5G n78 band with a rejection notch at 5.8 GHz (C-V2X/DSRC band), representing a practical coexistence problem between 5G base station equipment and vehicular communication systems. Alternative scenario: a military S-band communications antenna (2.2–2.4 GHz) with rejection of a co-located S-band radar at 2.7–2.9 GHz (airport surveillance radar). Show gain vs. frequency with the notch clearly visible.]

The out-of-band rejection capability is related to the broader concept of frequency-selective surfaces (FSS), which have been extensively studied using pixelated and optimization-based design approaches. Zhao et al. [31] designed pixelated frequency-selective surfaces using an estimation of distribution algorithm, demonstrating that optimization-driven design can achieve sharp frequency selectivity from pixelated conducting patterns. While FSS designs are typically passive filtering structures rather than antennas, the underlying principle—that a pixelated conducting pattern can exhibit frequency-selective behavior—is the same.

This capability is another illustration of the versatility of the fragmented aperture design process: by changing the fitness function, the same design machinery that produces broadband antennas can also produce antennas with deliberately shaped frequency responses.

4.10 Array Elements

The preceding sections of this chapter have focused on single-element antenna designs in which the fragmented aperture operates as a standalone antenna. The fragmented aperture concept extends naturally to the design of elements for phased array antennas, where the optimization must account for mutual coupling between adjacent elements and the impedance behavior as the array beam is scanned.

4.10.1 From Standalone Antenna to Array Element

A standalone fragmented aperture antenna is designed in free space (or above a ground plane) with radiation boundaries on all sides. When the same antenna is placed into a phased array, its performance changes dramatically. Mutual coupling between adjacent elements modifies the input impedance, the radiation pattern is replaced by the embedded element pattern, and the array beam steering introduces scan-dependent impedance variations. An element designed in isolation will generally perform poorly in an array environment because the optimizer had no knowledge of these coupling effects during the design process.

The solution is *direct element design*: the unit cell is designed from the outset as an array element, with the full-wave simulation incorporating the array environment. The FDTD simulation models a single unit cell with periodic boundary conditions (PBC) on the lateral faces, so that the element behaves as though it is embedded in an infinite array. The genetic algorithm optimizes the pixel pattern of this unit cell, and the fitness function evaluates the embedded element performance—typically the embedded element realized gain (EERG) or the active reflection coefficient as a function of frequency and scan angle.

4.10.2 Unit Cell Design

The unit cell for a fragmented aperture array element is defined by the element lattice (usually square or triangular) and the element spacing, which is constrained by the grating lobe condition $d < \lambda_{\min}/(1 + \sin\theta_{\max})$ where d is the element spacing, $\lambda_{\min}$ is the wavelength at the highest operating frequency, and $\theta_{\max}$ is the maximum scan angle.

Within the unit cell, the pixel grid is defined in the same way as for standalone antennas: the conducting surface is divided into sub-wavelength pixels, each of which is either conducting or non-conducting. The key difference is that the pixel pattern at the edges of the unit cell must be compatible with the periodic boundary conditions. In the connected array approach, the pixel pattern extends continuously across element boundaries—there is no enforced gap between adjacent elements. These inter-element connections allow currents to flow across multiple unit cells, which is critical for maintaining a good impedance match at low frequencies where the wavelength is much larger than a single element.

Figure 4.34 shows an early example from the original patent: a linear array of three connected fragmented aperture elements, each 10 inches square, with feed points at the center of each element. This connected array concept proved essential for achieving wideband array performance.

The fragmented aperture array element has a strong conceptual connection to the *current sheet array* concept developed by Munk [32] and further explored by Harris and others. Munk showed that an ideal current sheet—a continuous distribution of electric current over a planar surface backed by a ground plane—can achieve a theoretical impedance bandwidth of approximately π:1 (about 3.14:1) for scan volumes up to $\pm 45^\circ$. The fragmented aperture array element can be viewed as a practical realization of this concept: the connected pixel pattern approximates a current sheet, and the genetic algorithm finds the specific pattern that best approaches the current sheet performance within the constraints of the binary pixel representation and the physical feed structure.

4.10.3 Incorporating Scan Performance

For a fixed-beam array or a broadside-only design, the fitness function can evaluate the embedded element performance at broadside alone. For phased arrays that must scan,

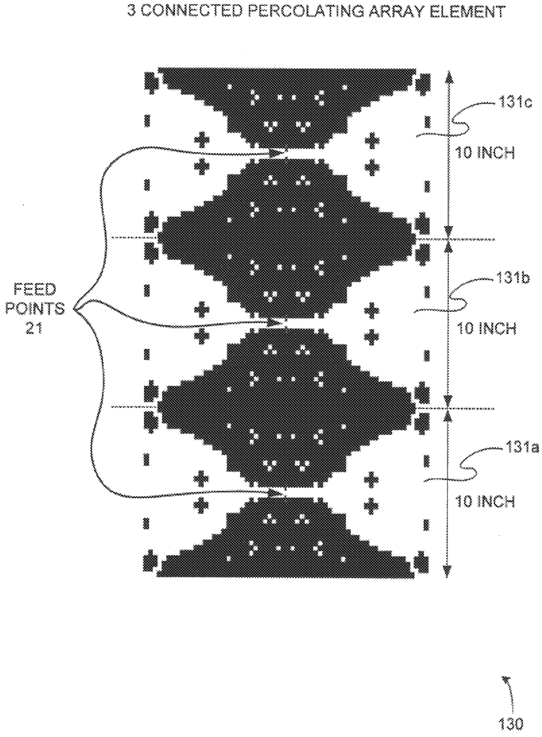

FIG. 19

Figure 4.34: Three connected fragmented aperture array elements from the original patent, each 10 inches square with a central feed point. The pixel pattern extends continuously across element boundaries, allowing inter-element current flow. This connected array concept proved essential for achieving wideband array performance, as discussed in Chapter 6 [1].

the fitness function must sample the scan volume. There are two principal approaches:

1. **Multi-angle optimization.** The FDTD simulation is run at several scan angles (e.g., broadside, 30°, 45°, 60° in the principal planes), and the fitness function combines the performance at all sampled angles. This approach was used in the early fragmented array designs and produces a single pixel pattern that is a compromise across the scan volume. The technique is described in detail in Chapter 7.

2. **Spectral-domain FDTD.** A single broadband FDTD simulation with a spectral-domain excitation provides the embedded element response at all frequencies and all scan angles simultaneously, dramatically reducing the computational cost compared to separate simulations at each angle. This approach is described in Chapter 7.

The multi-angle approach is straightforward but computationally expensive, since each fitness evaluation requires multiple FDTD simulations. The spectral-domain approach is more efficient but requires specialized FDTD formulations. Both approaches have been used successfully to design fragmented aperture array elements with bandwidths spanning multiple octaves.

4.10.4 Example Results

Thors, Steyskal, and Holter [33] at the Swedish Defence Research Agency (FOI) and the US Air Force Research Laboratory demonstrated broad-band fragmented aperture phased array element design using genetic algorithms, confirming that the fragmented aperture concept could be successfully applied to array element design by independent research groups. Figure 4.35 shows the canonical unit cell geometry from Thors et al.: (a) the side view showing the fragmented surface, dielectric substrate, and ground plane, and (b) the top view showing the 20×20 pixel grid with the GA-optimized metal pattern. Figure 4.36 shows their best design result, in which the GA was allowed to optimize the substrate thickness along with the pixel pattern, achieving a 2.23:1 bandwidth (1.5–5.0 GHz design band) with reflection coefficients below -10 dB (SWR < 2) at broadside and 45° scan in all principal planes. Ellgardt and Persson [34] characterized the broadband, wide-scan performance of fragmented aperture phased array elements, and Ellgardt's doctoral thesis [35] provided a comprehensive treatment of wide-angle scanning with fragmented aperture array elements.

These early results demonstrated that 2:1 to 4:1 bandwidth is achievable with single-layer fragmented aperture array elements. Achieving wider bandwidths requires the multi-layer structures and broadband backplane techniques described in Chapter 6. Achieving wide scan volumes (±60° and beyond) across the full bandwidth requires the spectral-domain design approach described in Chapter 7, which also presents a laminated printed circuit board fabrication method that enables practical, low-cost manufacturing of fragmented aperture arrays. The array elements are usually balanced-fed with differential feeds and electronics; unbalanced feed approaches are also discussed in Chapter 6.

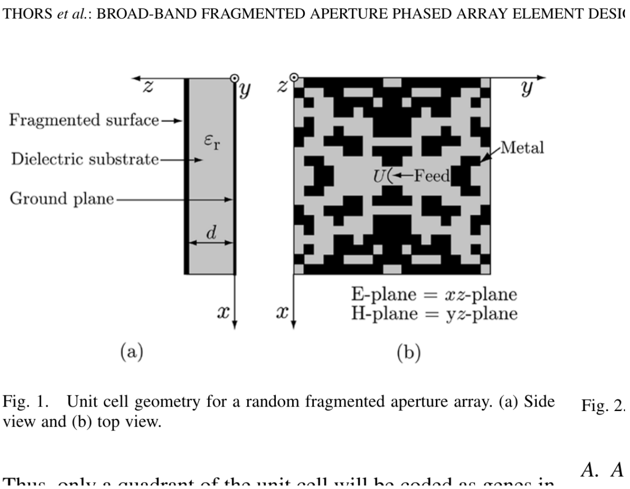

THORS *et al.*: BROAD-BAND FRAGMENTED APERTURE PHASED ARRAY ELEMENT DESI

Fig. 1. Unit cell geometry for a random fragmented aperture array. (a) Side view and (b) top view.

Fig. 2.

A. A

Figure 4.35: Unit cell geometry for a fragmented aperture phased array element: (a) side view showing the fragmented surface, dielectric substrate, and ground plane, and (b) top view showing the 20×20 pixel grid with the GA-optimized metal (black) and non-metal (grey) distribution [33].

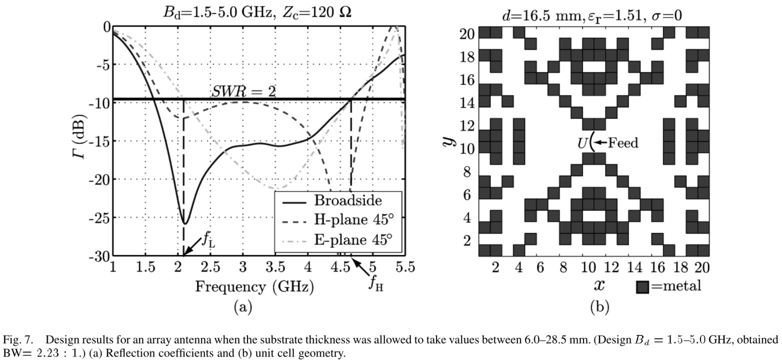

Fig. 7. Design results for an array antenna when the substrate thickness was allowed to take values between 6.0–28.5 mm. (Design $B_d = 1.5$–5.0 GHz, obtained BW= $2.23 : 1$.) (a) Reflection coefficients and (b) unit cell geometry.

Figure 4.36: Best-performing GA-designed fragmented aperture array element from Thors et al.: (a) reflection coefficients at broadside, H-plane 45°, and E-plane 45° scan, and (b) the optimized unit cell geometry. The GA optimized both the pixel pattern and the substrate thickness (d = 16.5 mm), achieving a 2.23:1 bandwidth [33].

4.11 Summary

This chapter has surveyed the versatility of the fragmented aperture antenna design approach through a range of design examples and applications. The key themes are:

1. **Fragmented ground planes** extend the pixel optimization concept from the radiating aperture to the ground structure, connecting to the broader literature on defected ground structures.

2. **Fragmented superstrates** provide the complementary function: optimized director layers in front of the radiating aperture that enhance forward gain, analogous to adding directors to a Yagi-Uda antenna.

3. **Feed strategies** range from simple in-plane microstrip feeds to through-ground-plane configurations with center pins or flanking vias. Unbalanced feed designs simplify the antenna architecture by eliminating the need for baluns.

4. **Bandwidth tailoring** is achieved by changing the fitness function, not the hardware. The same aperture can cover different bands with different pixel patterns, motivating the reconfigurable designs of Chapter 5.

5. **Fixed beam steering** changes the symmetry of the pixel pattern. Broadside designs exhibit quadrant symmetry; steered designs progressively lose symmetry as the beam moves off broadside; endfire designs are fully asymmetric.

6. **Polarization control** including circular polarization is achievable from a single feed point by breaking the pixel symmetry. Non-broadside CP is the most general case, requiring optimization over all pixels independently.

7. **Beamwidth tailoring** has been demonstrated for GPS CRPA elements, where the element pattern must be optimized for compatibility with adaptive null-steering algorithms.

8. **Out-of-band rejection** is achieved by adding rejection penalties to the fitness function, building filtering into the antenna design.

9. **Array elements** extend the fragmented aperture concept to phased arrays using periodic boundary conditions and scan-aware fitness functions, as developed further in Chapters 6 and 7.

In every case, the same fundamental design machinery applies: a pixelated aperture, a genetic algorithm, and a full-wave electromagnetic simulation. The remarkable versatility of the approach arises not from changes to the design process itself, but from changes to the performance objectives encoded in the fitness function.

References

[1] J. G. Maloney, M. P. Kesler, P. H. Harms, and G. S. Smith, "Fragmented aperture antennas and broadband ground planes," U.S. Patent No. 6,323,809 B1, Nov. 2001.

[2] Y. J. Sung, M. Kim, and Y.-S. Kim, "Harmonics reduction with defected ground structure for a microstrip patch antenna," *IEEE Antennas and Wireless Propagation Letters*, vol. 2, pp. 111–113, 2003.

[3] H. Liu, Z. Li, X. Sun, and J. Mao, "Harmonic suppression with photonic bandgap and defected ground structure for a microstrip patch antenna," *IEEE Microwave and Wireless Components Letters*, vol. 15, no. 2, pp. 55–56, 2005.

[4] S. Biswas, C. K. Ghosh, A. Medda, and D. Mandal, "Harmonics suppression of microstrip patch antenna using defected ground structure," in *2016 IEEE International Conference*, 2016, pp. 1–4.

[5] D. Tayli and M. Gustafsson, "Physical bounds for antennas above a ground plane," *IEEE Antennas and Wireless Propagation Letters*, vol. 15, pp. 1281–1284, 2016.

[6] C. Ehrenborg and M. Gustafsson, "Physical bounds and automatic design of antennas above ground planes," in *2016 URSI International Symposium on Electromagnetic Theory (EMTS)*, 2016, pp. 353–356.

[7] H. Steyskal and D. Hanna, "Design aspects of fragmented patch elements for phased arrays," in *2007 IEEE Antennas and Propagation Society International Symposium*, Honolulu, HI, 2007, aFRL work on fragmented patch array elements.

[8] T. H. O'Donnell, S. Santarelli, H. Steyskal, and H. Southall, "Hybrid chromosome design for genetic optimization of a fragmented patch array antenna," in *Proc. SPIE 7347, Evolutionary and Bio-Inspired Computation: Theory and Applications III*, Apr. 2009, p. 73470R, aFRL/SPIE.

[9] N. Barani, J. F. Harvey, and K. Sarabandi, "Fragmented antenna realization using coupled small radiating elements," *IEEE Transactions on Antennas and Propagation*, vol. 66, no. 4, pp. 1725–1735, 2018.

[10] M. D. Wright, W. Baron, J. Miller, J. Tuss, D. Zeppettella, and M. Ali, "Mems reconfigurable broadband patch antenna for conformal applications," *IEEE Transactions on Antennas and Propagation*, vol. 66, no. 6, pp. 2770–2778, 2018.

[11] M. Ali, N. Bishop, W. Baron, B. Smyers, J. Tuss, and D. Zeppettella, "A mems reconfigurable pixel microstrip patch antenna for conformal load bearing antenna structures (clas) concept," in *2014 IEEE Antennas and Propagation Society International Symposium (APSURSI)*, 2014, pp. 1093–1094.

[12] N. Herscovici, J. Ginn, T. Donisi, and B. Tomasic, "A fragmented aperture-coupled microstrip antenna," in *2008 IEEE Antennas and Propagation Society International Symposium*, 2008, pp. 1–4.

[13] N. Herscovici, B. Tomasic, J. Ginn, and T. Donisi, "Scanning characteristics of aperture coupled fed fragmented microstrip arrays," in *2009 IEEE Antennas and Propagation Society International Symposium*, 2009, pp. 1–4.

[14] N. Bishop, M. Ali, W. Baron, J. Miller, J. Tuss, and D. Zeppettella, "Aperture coupled mems reconfigurable pixel patch antenna for conformal load bearing antenna structures (clas)," in *2014 IEEE Antennas and Propagation Society International Symposium (APSURSI)*, 2014, pp. 1091–1092.

[15] Y. Zang, M. Jin, and X. Jiao, "The optimum design of a 3-10ghz linear-polarized fragmented aperture array with integrated balun," in *2019 International Symposium on Antennas and Propagation (ISAP)*, 2019, pp. 1–3.

[16] J. P. Doane, K. Sertel, and J. L. Volakis, "A wideband, wide scanning tightly coupled dipole array with integrated balun (TCDA-IB)," *IEEE Transactions on Antennas and Propagation*, vol. 61, no. 9, pp. 4538–4548, 2013.

[17] D. W. Landgren, D. J. P. Dykes, and K. W. Allen, "An unbalanced feed design for wideband phased arrays," *arXiv preprint arXiv:1706.04658*, 2017, international Telemetry Conference. [Online]. Available: https://arxiv.org/abs/1706.04658

[18] D. W. Landgren, K. R. Cook, D. J. P. Dykes, J. Perez, P. R. Bowden, and K. W. Allen, "A wideband mmwave antenna element with an unbalanced feed," in *2017 IEEE National Aerospace and Electronics Conference (NAECON)*, 2017, pp. 209–212.

[19] D. Landgren, T. Brunasso, K. Allen, D. Dykes, J. Kovitz, J. Perez, J. Dee, J. Marsh, C. Hunter, and G. Smith, "A broadband array with unbalanced feeds : Elements and power combiners based on the fragmented aperture principle," in *2019 IEEE International Symposium on Antennas and Propagation and USNC-URSI Radio Science Meeting*, 2019, pp. 1223–1224.

[20] D. W. Landgren, T. Brunasso, J. B. Dee, J. Perez, D. J. P. Dykes, J. M. Marsh, C. P. Hunter, and K. W. Allen, "Wideband phased array antenna design with fragmented combiner technology," in *IEEE National Aerospace and Electronics Conference (NAECON)*, Jun. 2018, pp. 602–606.

[21] Q. Wang, Z. Pang, D. Gao, P. Liu, X. Pang, and X. Yin, "Machine learning-assisted quasi-bisection method for pixelated patch antenna bandwidth optimization," *IEEE Antennas and Wireless Propagation Letters*, vol. 23, no. 12, pp. 4807–4811, 2024.

[22] J. M. J. W. Jayasinghe and D. N. Uduwawala, "Design of broadband patch antennas using genetic algorithm optimization," in *2010 5th International Conference on Industrial and Information Systems (ICIIS)*, 2010, pp. 60–61.

[23] J. W. Jayasinghe, J. Anguera, and D. N. Uduwawala, "A simple design of multi band microstrip patch antennas robust to fabrication tolerances for GSM, UMTS, LTE, and bluetooth applications by using genetic algorithm optimization," *Progress In Electromagnetics Research M*, vol. 27, pp. 255–269, 2012.

[24] S. Tang, Y. Zhang, J. Rao, T. Qiao, C. Y. Chiu, and R. Murch, "Dual-port endfire millimeter wave reconfigurable antenna with optimized pixel surface," in *2023 IEEE International Symposium on Antennas and Propagation and USNC-URSI Radio Science Meeting (USNC-URSI)*, 2023, pp. 969–970.

[25] D. Rodrigo, L. Jofre, and B. A. Cetiner, “Frequency, radiation pattern and polarization reconfigurable antenna using a parasitic pixel layer,” *IEEE Transactions on Antennas and Propagation*, vol. 62, no. 6, pp. 3422–3427, 2014.

[26] J. Zechmeister and J. Lacik, “Pixelated circularly polarized siw horn antenna with nearly equal beamwidths in principal planes,” in *2022 24th International Microwave and Radar Conference (MIKON)*, 2022, pp. 1–4.

[27] J. Zechmeister, J. Lacik, and P. Kadlec, “The design of pixelated siw horn antennas with nearly equal beamwidths using binary ink stamp optimization,” *IEEE Access*, vol. 9, pp. 122 216–122 227, 2021.

[28] J. G. Maloney, B. N. Baker, J. J. Acree, J. W. Schultz, J. A. Little, and D. D. Reuster, “Fragmented aperture antenna design of miniaturized gps crpa: model and measurements,” in *2007 IEEE Antennas and Propagation Society International Symposium*, 2007, pp. 3784–3787.

[29] J. G. Maloney and G. P. Baker, “Fragmented aperture antenna design of miniaturized GPS CRPA: Model and measurements,” in *Proceedings of the Institute of Navigation GNSS Conference*, 2010.

[30] M. A. Towfiq, I. Bahceci, S. Blanch, J. Romeu, L. Jofre, and B. A. Cetiner, “A reconfigurable antenna with beam steering and beamwidth variability for wireless communications,” *IEEE Transactions on Antennas and Propagation*, vol. 66, no. 10, pp. 5052–5063, 2018.

[31] M. Zhao, X. Yu, Q. Wang, P. Kong, Y. He, L. Miao, and J. Jiang, “Novel absorber based on pixelated frequency selective surface using estimation of distribution algorithm,” *IEEE Antennas and Wireless Propagation Letters*, vol. 14, pp. 1467–1470, 2015.

[32] B. A. Munk, T. W. Taylor, T. Durharn, W. Croswell, B. Pigon, R. Boozer, S. Brown, M. Jones, J. Pryor, S. Ortiz, J. Rawnick, K. Krebs, M. Vanstrum, G. Gothard, and D. Wiebelt, “A low-profile broadband phased array antenna,” in *IEEE Antennas and Propagation Society International Symposium*, vol. 2, Columbus, OH, 2003, pp. 448–451.

[33] B. Thors, H. Steyskal, and H. Holter, “Broad-band fragmented aperture phased array element design using genetic algorithms,” *IEEE Transactions on Antennas and Propagation*, vol. 53, no. 10, pp. 3280–3287, 2005.

[34] A. Ellgardt and P. Persson, “Characteristics of a broad-band wide-scan fragmented aperture phased array antenna,” in *2006 First European Conference on Antennas and Propagation*, 2006, pp. 1–5.

[35] A. Ellgardt, “Wide-angle scanning wide-band phased array antennas,” Ph.D. dissertation, KTH School of Electrical Engineering, Stockholm, Sweden, 2009, page 21 discusses diagonal touching issues.

Chapter 5

Reconfigurable Fragmented Aperture Antennas

5.1 Introduction

In the preceding chapters, we have shown how the fragmented aperture concept can be used to design antennas that meet particular performance specifications. A planar sheet of conductor is divided into many sub-wavelength pixels, and a genetic algorithm working with an FDTD simulation determines which pixels should be conducting and which should not. Different designs can be obtained to meet different specifications: for example, one design might produce an antenna with a broadside beam optimized for a particular bandwidth, while a second design might produce an antenna with the beam steered to 45^o from broadside.

Of course, once a fragmented aperture antenna is fabricated, it can only meet one set of specifications—either the broadside design or the steered design, but not both. It would be enormously useful if a single fragmented aperture could be electronically switched between different configurations to meet different requirements on demand. This would require a mechanism for dynamically changing individual pixels from conducting to non-conducting and vice versa. Recent work has demonstrated various reconfigurable pixelated antenna implementations using MEMS switches [1, 2], phase transition materials [3], and magnetically actuated mechanisms [4].

One can imagine, for example, making the cladding on a circuit board from a photoconductive material and using a laser to selectively illuminate the pixels that need to be conducting for a particular design. Changing the illumination pattern would reconfigure the antenna. While this particular approach remains impractical with current technology, the underlying idea—a reconfigurable fragmented aperture—motivated the development of the Agile Aperture Antenna described in this chapter.

5.2 The Agile Aperture Antenna Concept

The concept of a reconfigurable fragmented aperture antenna was first published in 2000 under the name “switched fragmented aperture antenna” [5]. Subsequently, DARPA funded a solicitation for “reconfigurable aperture” antennas and coined the acronym RECAP. To distinguish the fragmented aperture approach from other reconfigurable antenna concepts, we later adopted the term “Agile Aperture Antenna” (A3), emphasizing that the purpose of reconfiguration is to make the antenna *agile*—able to dynamically change its frequency of operation, beam direction, polarization, or other characteristics. The seminal IEEE paper on this work [6] and a comprehensive book chapter [7] provide detailed treatments of reconfigurable aperture antenna technology.

The Agile Aperture Antenna implementation that was successfully demonstrated is shown schematically in Figure 5.1 [8]. A thin dielectric substrate supports an array of square metallic pads. The pads are electrically small, with side length l satisfying $l/\lambda_o \ll 1$, where λ_o is the free-space wavelength at the operating frequency. Each pad is connected to its neighboring pads by switched links, indicated by the arrows in the figure. Each switch may be independently set to open or closed depending on the desired antenna configuration. A single feed point (pair of terminals) is located near the center of the antenna.

The Agile Aperture Antenna can be understood as a variant of the fragmented aperture antenna in which the fundamental unit is not a single pixel but a metallic pad composed of a group of pixels. The pads are not contiguous; they are separated by narrow dielectric gaps. The antenna structure for any given configuration consists of the conducting pads that are connected by closed switches, together with all of the unconnected pads that remain present on the substrate. This is an important distinction from a conventional fragmented aperture: in the Agile Aperture Antenna, the unconnected pads are always physically present and contribute to the electromagnetic behavior of the antenna through scattering, even when they are not part of the connected conducting structure.

5.3 Static Proof of Concept

INSERT: Description of the first two static (hard-wired) pixelated designs that demonstrated the unconnected pads did not prevent good antenna performance. Include figures showing the two designs and their measured performance.

5.4 Reconfigurable Proof of Concept

To prove the validity of the Agile Aperture Antenna concept, a detailed study was conducted using a prototype antenna with hard-wired switches—gaps that were either closed by a soldered wire or left open. This study not only validated the design approach but also identified areas where future research would be needed to extend the concept to practical, electronically reconfigurable antennas.

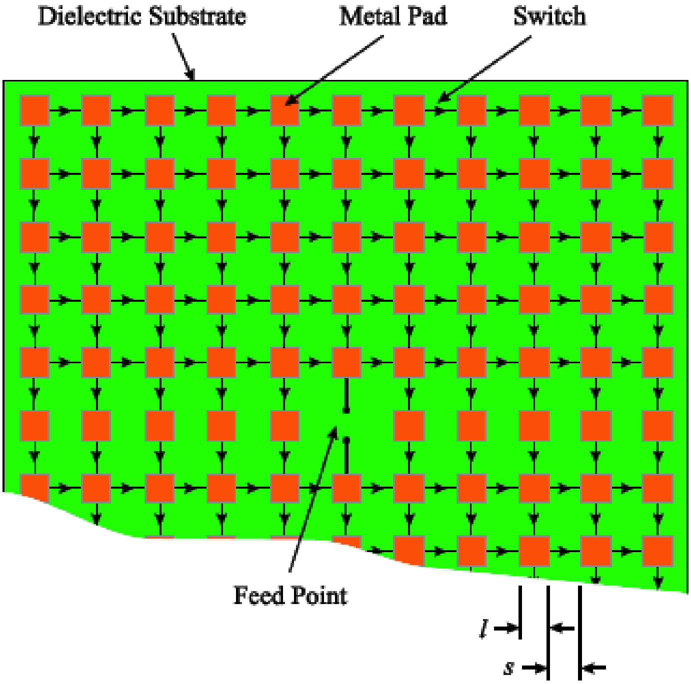

Figure 5.1: Schematic drawing of the Agile Aperture Antenna in dipole form. Square metallic pads are connected by switched links (arrows). The state of each switch (open or closed) determines the antenna configuration [8].

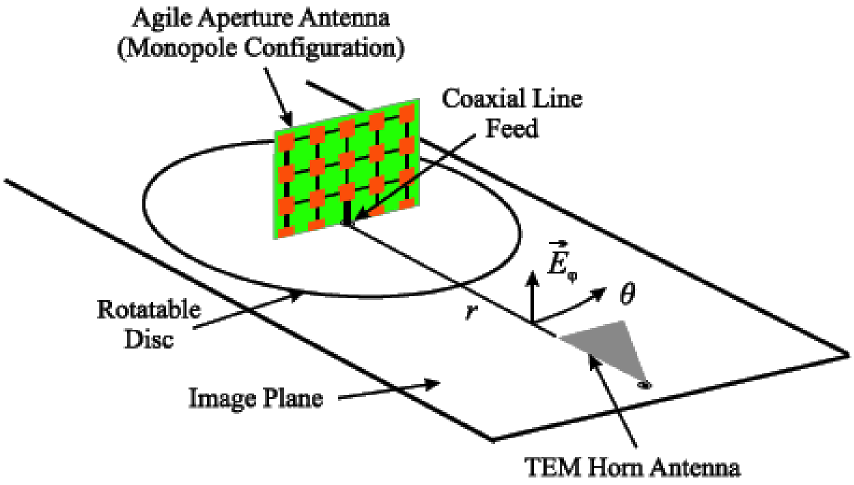

Figure 5.2: Experimental arrangement for measuring the Agile Aperture Antenna in monopole form. The antenna is mounted vertically on a rotatable disc centered in a large metallic image plane [8].

5.4.1 Prototype Description

For all of the antennas discussed in this section, the aperture was formed from a printed circuit board 22.5 cm × 22 cm in size, with the pads etched from the copper cladding on one side of the board. The pad side length and spacing were both $l = s = 1.0$ cm (see Figure 5.1). The board contained a total of 120 pads and 208 switches. The dielectric substrate was 1.7 mm thick FR4 circuit board with measured electrical properties $\varepsilon_r = 4.27$ and $\tan\delta = 0.07$ (verify loss tangent value).

The frequency of operation was in the range 0.85 GHz $\leq f \leq 1.45$ GHz, so the pads were electrically small: $0.028 \leq l/\lambda_o \leq 0.048$. All of the antenna designs described in this section have mirror symmetry about the horizontal line through the feed point, including the states of the switches. This symmetry allows the antennas to be analyzed and measured in either the "dipole form" shown in Figure 5.1 or the "monopole form" shown in Figure 5.2.

5.4.2 Measurement Setup

Figure 5.2 shows the experimental setup used for all of the measurements reported in this section. The monopole version of the Agile Aperture Antenna was mounted vertically on a rotatable disc centered in a large metallic image plane (insert image plane dimensions). The antenna was fed from below the image plane by a 50 Ω coaxial line, with the center conductor connected to the bottom pad in the center column of the antenna. A calibrated TEM horn antenna was located at a distance of (insert distance) from the antenna [8]. The scattering parameters for the two-port network formed by the Agile Aperture Antenna and the TEM horn were measured with a network analyzer and used to determine the absolute gain of the Agile Aperture Antenna [9]. The horizontal radiation pattern ($|E|$ versus azimuth angle ϕ) was obtained by rotating the disc while recording the output signal from the horn.

5.4.3 Design Procedure

The procedure for designing a switch configuration for the Agile Aperture Antenna is conceptually the same as for a conventional fragmented aperture: a rigorous FDTD simulation of the antenna is run in conjunction with a genetic algorithm optimizer (see Appendix A for an introduction to the FDTD method). In all of the FDTD simulations reported here, cubical Yee cells with a side length of 2.5 mm were used. More recent optimization approaches for reconfigurable pixelated antennas include beam steering techniques [10] and quantum genetic algorithms [11].

A performance goal is first established—for example, maximum broadside realized gain over a specified bandwidth. The GA then searches for the switch configuration (which switches should be open and which should be closed) that best meets this goal. Taking into account the mirror symmetry of the antenna, there are $2^{104} \approx 2 \times 10^{31}$ possible switch configurations—far too many to evaluate exhaustively. The GA provides an efficient, though approximate, method for searching this enormous design space.

5.4.4 Broadside Design

The design goal for the first example was to maximize the broadside realized gain over the frequency range 0.85 GHz $\leq f \leq 1.25$ GHz (a fractional bandwidth of 38%). The target was that the realized gain should equal or exceed the directivity of a uniform sheet of vertically directed current occupying the same aperture area.

Figure 5.3(a) shows the switch configuration obtained by the GA for this broadband, bidirectional, broadside design. Notice that this configuration has right-left symmetry in addition to the imposed top-bottom symmetry; all of the broadside designs discussed in this chapter are constrained to have this additional symmetry.

Figure 5.4(a) shows the realized gain versus frequency for this design. The dashed blue line is the design goal (uniform aperture directivity), the solid black line is the FDTD simulation, and the red line with markers is the measured result. All realized gain values are for the antenna in the dipole configuration. The simulated and measured realized gains are in good agreement over the design bandwidth, with a maximum difference of approximately 1 dB. The realized gain falls approximately 0.5–1.5 dB below the goal; a portion of this difference is attributable to impedance mismatch at the antenna feed.

Figure 5.4(b) shows the mismatch factor $(1 - |\Gamma_A|^2)$ as a function of frequency, where Γ_A is the voltage reflection coefficient at the antenna terminals. Within the design bandwidth, this factor ranges from 0.0 dB to -1.5 dB, confirming that mismatch accounts for a significant portion of the difference between the realized gain and the goal.

Figure 5.5 shows the horizontal radiation pattern at the center frequency $f =$

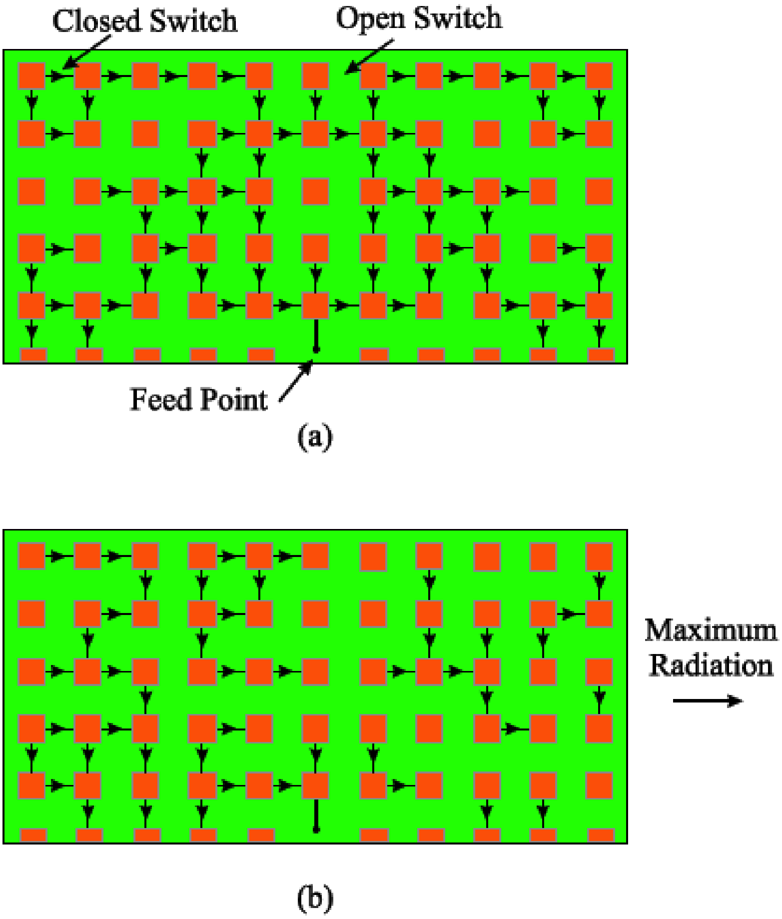

Figure 5.3: Switch configurations for the Agile Aperture Antenna (monopole form) with hard-wired switches. (a) Broadband, bidirectional, broadside design. (b) Narrowband, unidirectional, end-fire design. The two configurations are strikingly different, yet both are realized on the same physical antenna [8].

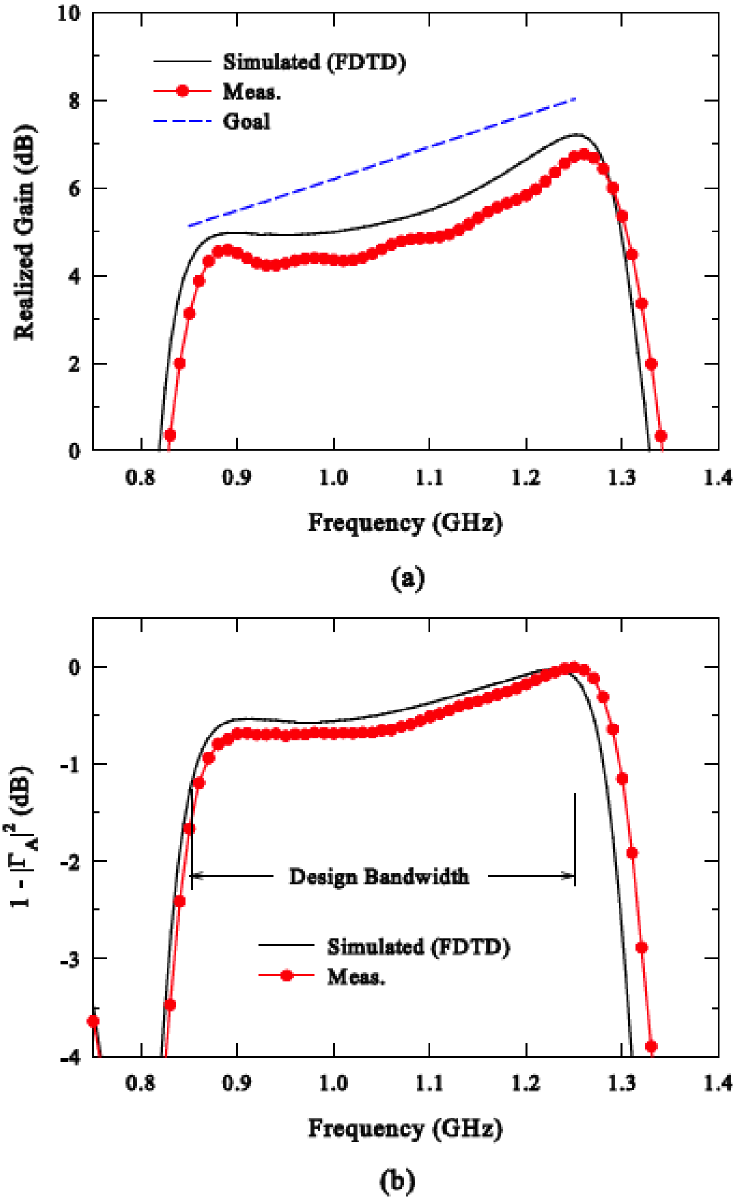

Figure 5.4: Results for the broadband, bidirectional, broadside design with hard-wired switches. (a) Realized gain versus frequency. (b) Gain reduction due to impedance mismatch: $(1 - |\Gamma_A|^2)$ [8].

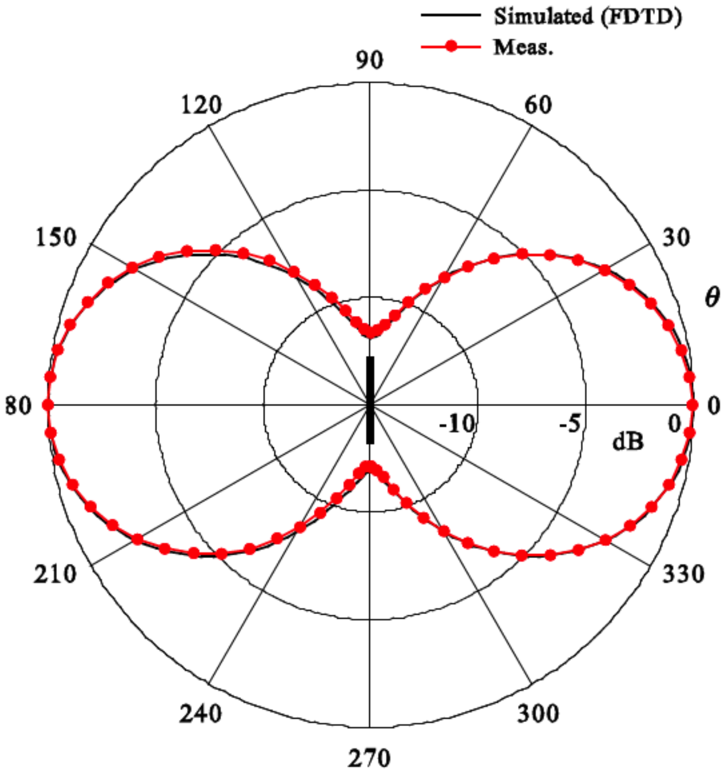

Figure 5.5: Horizontal radiation pattern at $f = 1.05$ GHz for the broadband, bidirectional, broadside design with hard-wired switches. Both patterns are normalized to 0 dB [8].

1.05 GHz. The simulated and measured patterns are nearly identical, with both normalized to a maximum of 0 dB. The heavy line at the center of the pattern indicates the orientation of the dielectric substrate.

5.4.5 End-Fire Design

To demonstrate the versatility of the Agile Aperture Antenna concept, a second design was produced for a completely different objective: a narrowband, unidirectional, end-fire beam over the frequency range $1.0\text{ GHz} \leq f \leq 1.1\text{ GHz}$ (a fractional bandwidth of 9.5%). The goal was again that the realized gain should equal or exceed the directivity of a uniform sheet of current, but now with the current phased to produce end-fire radiation.

Figure 5.3(b) shows the switch configuration for this end-fire design. It is immediately apparent that this configuration is strikingly different from the broadside configuration in Figure 5.3(a)—the end-fire design does not have right-left symmetry and produces a fundamentally different current distribution on the aperture. Yet both configurations are realized on the same physical hardware simply by changing which switches are open and which are closed.

Figure 5.6(a) shows the realized gain versus frequency for the end-fire design. The simulated and measured results are again in good agreement over the design bandwidth, with a maximum difference of approximately 1 dB. The realized gain falls approximately 1.0–2.0 dB below the goal. The mismatch factor shown in Figure 5.6(b) is within the range 0.0 dB to -0.8 dB over the design bandwidth.

Figure 5.7 shows the horizontal radiation pattern at $f = 1.05$ GHz. The simulated and measured patterns are in excellent agreement, and both clearly show the characteristic end-fire beam directed to one side of the antenna.

5.4.6 Observations on the Designed Configurations

In the configurations studied, approximately 30% to 60% of the switches were closed. One might expect that examination of the switch states for a particular design would reveal recognizable antenna structures—for example, the end-fire design might show strings of pads forming linear elements arranged like the driven element, reflector, and director of a Yagi-Uda array. However, as seen in Figure 5.3(b), this is not the case. In general, there is no simple, discernible relationship between the switch states and the design goal.

This lack of an obvious physical interpretation is consistent with the experience from conventional fragmented aperture design (Chapter 2): the GA discovers complex, non-intuitive structures that exploit the full electromagnetic physics of the problem. In the case of the Agile Aperture Antenna, the optimization is further complicated by the presence of the unconnected pads, which scatter electromagnetic energy and must be accounted for in the design. It is clear, however, that the switch connections near the feed point are often arranged to improve the impedance match between the antenna and the transmission line.

5.5 Discussion

The broadside and end-fire examples presented above, along with several other designs not shown, demonstrate that the Agile Aperture Antenna concept is viable: a single physical antenna can be reconfigured via its switch states to meet fundamentally different performance specifications. The excellent agreement between FDTD simulations and measurements further validates the design procedure.

However, for the Agile Aperture Antenna to transition from a laboratory concept to a practical technology, several challenges must be addressed. Most critically, a switch technology must be developed that can be electronically controlled without interfering with the electromagnetic performance of the antenna. The switches must introduce minimal insertion loss when closed, provide high isolation when open, and the control circuitry (bias lines, drivers) must not distort the antenna's radiation characteristics.

Subsequent research has explored several promising switch technologies for reconfigurable pixelated antennas. MEMS-based switches have been successfully demon-

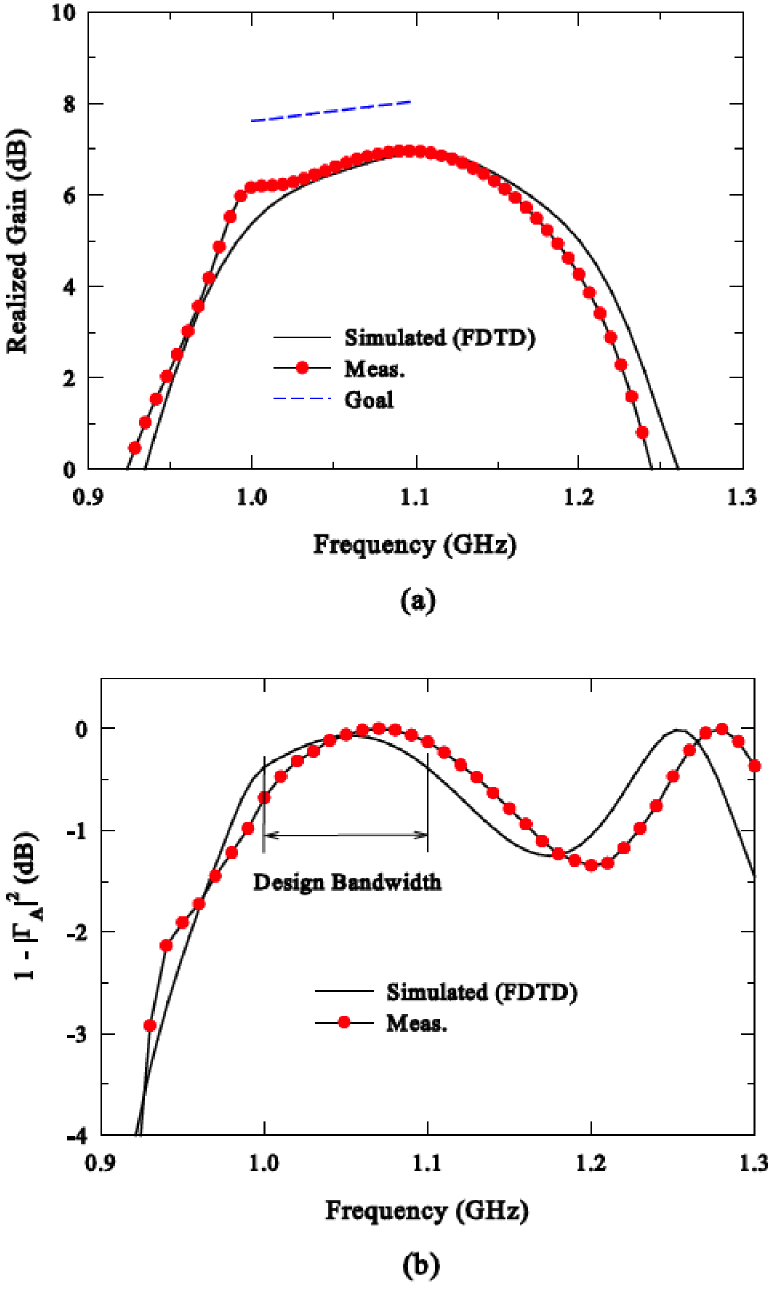

(a)

(b)

Figure 5.6: Results for the narrowband, unidirectional, end-fire design with hard-wired switches. (a) Realized gain versus frequency. (b) Gain reduction due to impedance mismatch: $(1 - |\Gamma_A|^2)$ [8].

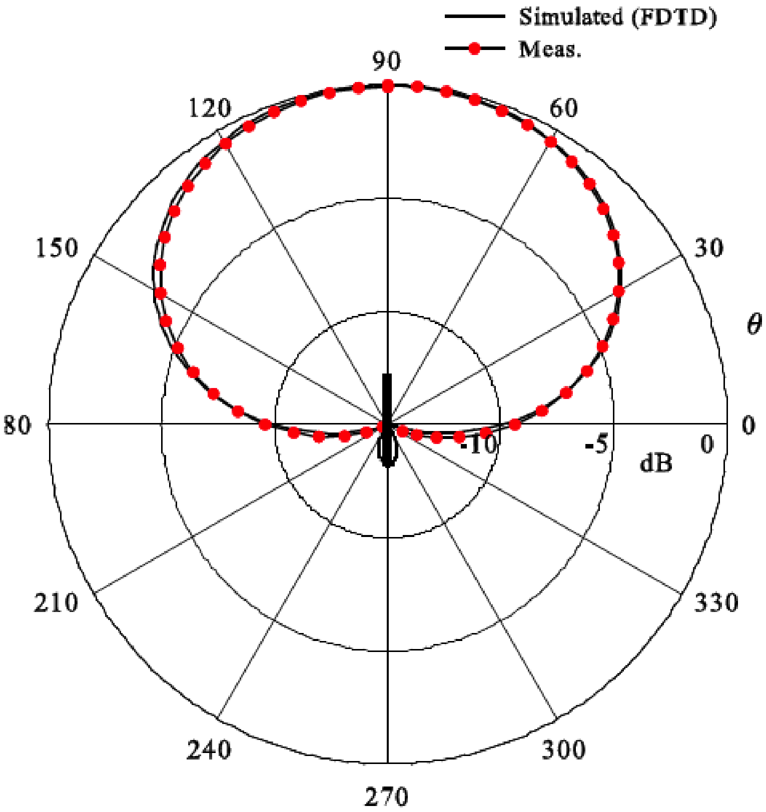

Figure 5.7: Horizontal radiation pattern at $f = 1.05$ GHz for the narrowband, unidirectional, end-fire design with hard-wired switches. Both patterns are normalized to 0 dB [8].

strated for reconfigurable patch antennas [12, 2, 1], offering excellent RF performance with low insertion loss and high isolation. Phase transition materials such as vanadium dioxide (VO2) provide another approach, enabling frequency reconfiguration through voltage-controlled phase changes [3]. Other techniques include magnetically actuated pixels [4] and tunable designs using varactors [13]. More recent work has focused on dual-port mmWave reconfigurable designs with optimized pixel configurations [14] and novel frequency reconfigurable implementations [15, 11].

5.6 Acknowledgement

The author would like to thank Professor Glenn Smith for his dedication in writing the original IEEE paper [8] on which much of this chapter is based. The author also acknowledges the contributions of the full research team as described in [16].

References

[1] M. D. Wright, W. Baron, J. Miller, J. Tuss, D. Zeppettella, and M. Ali, “Mems reconfigurable broadband patch antenna for conformal applications,” *IEEE Transactions on Antennas and Propagation*, vol. 66, no. 6, pp. 2770–2778, 2018.

[2] M. Ali, N. Bishop, W. Baron, B. Smyers, J. Tuss, and D. Zeppettella, “A mems reconfigurable pixel microstrip patch antenna for conformal load bearing antenna structures (clas) concept,” in *2014 IEEE Antennas and Propagation Society International Symposium (APSURSI)*, 2014, pp. 1093–1094.

[3] Z. Lou, L. Liao, Y. Wang, Y. Yang, J. Li, and S. Yan, “Frequency reconfigurable pixelated antenna using vo2 phase transition material,” in *2025 IEEE 8th International Symposium on Electromagnetic Compatibility (ISEMC)*, 2025, pp. 1–3.

[4] J. Pal, K. Deshpande, L. Chomas, S. Santhanam, F. Donzelli, D. Piazza, J. A. Bain, and G. Piazza, “Magnetically actuated reconfigurable pixelated antenna,” *2018 IEEE Micro Electro Mechanical Systems (MEMS)*, pp. 791–794, 2018.

[5] J. G. Maloney, M. P. Kesler, L. M. Lust, L. N. Pringle, T. L. Fountain, P. H. Harms, and G. S. Smith, “Switched fragmented aperture antennas,” in *IEEE Antennas and Propagation Society International Symposium*, Salt Lake City, UT, Jul. 2000, pp. 310–313.

[6] L. N. Pringle, P. H. Harms, S. P. Blalock, G. N. Kiesel, E. J. Kuster, P. G. Friederich, R. J. Prado, J. M. Morris, and G. S. Smith, “A reconfigurable aperture antenna based on switched links between electrically small metallic patches,” *IEEE Transactions on Antennas and Propagation*, vol. 52, no. 6, pp. 1434–1445, Jun. 2004.

[7] G. H. Huff and J. T. Bernhard, “Reconfigurable antennas,” in *Modern Antenna Handbook*, C. A. Balanis, Ed. Wiley, 2007, ch. 8.

[8] L. N. Pringle, P. H. Harms, S. P. Blalock, G. N. Kiesel, E. J. Kuster, P. G. Friederich, R. J. Prado, J. M. Morris, and G. S. Smith, “A reconfigurable aperture antenna based on switched links between electrically small metallic patches,” *IEEE Transactions on Antennas and Propagation*, vol. 52, no. 6, pp. 1434–1445, Jun. 2004.

[9] R. T. Lee and G. S. Smith, “A design study for the basic TEM horn antenna,” *IEEE Antennas and Propagation Magazine*, vol. 46, no. 1, pp. 86–92, Feb. 2004.

[10] M. A. Towfiq, I. Bahceci, S. Blanch, J. Romeu, L. Jofre, and B. A. Cetiner, “A reconfigurable antenna with beam steering and beamwidth variability for wireless communications,” *IEEE Transactions on Antennas and Propagation*, vol. 66, no. 10, pp. 5052–5063, 2018.

[11] R. M. Bichara, F. A. Z. Asadallah, M. Awad, and J. Costantine, “A miniaturized reconfigurable antenna using quantum genetic algorithm optimization,” in *2021 IEEE International Symposium on Antennas and Propagation and USNC-URSI Radio Science Meeting (APS/URSI)*, 2021, pp. 763–764.

[12] M. Wright, M. Ali, W. Baron, J. Miller, J. Tuss, and D. Zeppettella, “Effect of bias traces and wires on a mems reconfigurable pixelated patch antenna,” in *2016 IEEE International Symposium on Antennas and Propagation (APSURSI)*, 2016, pp. 1429–1430.

[13] R. O. Ouedraogo, J. Tang, K. Fuchi, E. J. Rothwell, A. R. Diaz, and P. Chahal, “A tunable dual-band miniaturized monopole antenna for compact wireless devices,” *IEEE Antennas and Wireless Propagation Letters*, vol. 13, pp. 1247–1250, 2014.

[14] S. Tang, Y. Zhang, J. Rao, T. Qiao, C. Y. Chiu, and R. Murch, “Dual-port endfire millimeter wave reconfigurable antenna with optimized pixel surface,” in *2023 IEEE International Symposium on Antennas and Propagation and USNC-URSI Radio Science Meeting (USNC-URSI)*, 2023, pp. 969–970.

[15] T. Qiao, S. Tang, J. Rao, Y. Zhang, C. Y. Chiu, Q. S. Cheng, and R. Murch, “A novel optimization technique for designing frequency reconfigurable pixelated planar antenna,” in *2023 IEEE International Symposium on Antennas and Propagation and USNC-URSI Radio Science Meeting (USNC-URSI)*, 2023, pp. 1757–1758.

[16] J. G. Maloney *et al.*, “Chapters on antennas and fdtd methods,” in *Modern Antenna Handbook*, C. A. Balanis, Ed. Wiley, 2007, see Chapters 8, 12, and 30.

Chapter 6

Wideband Antenna Arrays

6.1 Introduction

Students of antenna design are taught that the gain of an array antenna can be estimated by multiplying the pattern of a single element by the array factor. This approach ignores mutual coupling between elements, which has traditionally been a major challenge for designers of phased arrays. Mutual coupling introduces areas of scan blindness—combinations of frequency and scan angle for which the array is poorly matched—that can severely degrade array performance. As the sophistication of numerical modeling codes has increased in concert with the availability of inexpensive parallel computing power, antenna designers have developed the ability to include the effects of mutual coupling in their performance predictions. This capability, in turn, suggests the possibility of *exploiting* mutual coupling rather than merely avoiding it.

To appreciate why wideband arrays are challenging, consider the performance comparison in Figure 6.1. A $10'' \times 10''$ aperture is populated with three different antenna types: a uniform current sheet (the theoretical ideal), a spiral antenna, and a bowtie antenna. The uniform current sheet achieves the full aperture gain limit across frequency, but it is a theoretical construct, not a realizable antenna. The spiral produces useful gain only over a limited bandwidth, and the bowtie exhibits narrow resonant peaks. Neither conventional design approaches the broadband performance that the aperture could support.

The fragmented aperture design approach, applied to array elements, offers a path to achieving the broadband performance that conventional element designs cannot. By allowing a genetic algorithm to optimize the conducting pattern of each unit cell—including connections between adjacent elements—the design process can exploit mutual coupling to produce arrays with bandwidths far exceeding those of conventional designs.

This chapter traces the development of wideband fragmented aperture arrays, beginning with the discovery that electrical connections between elements are essential for wide bandwidth. It then describes the broadband screen backplane, a key innovation that mitigates the half-wave nulls introduced by a ground plane, enabling practical planar arrays with bandwidths of 10:1 and beyond. The chapter continues with multi-layer

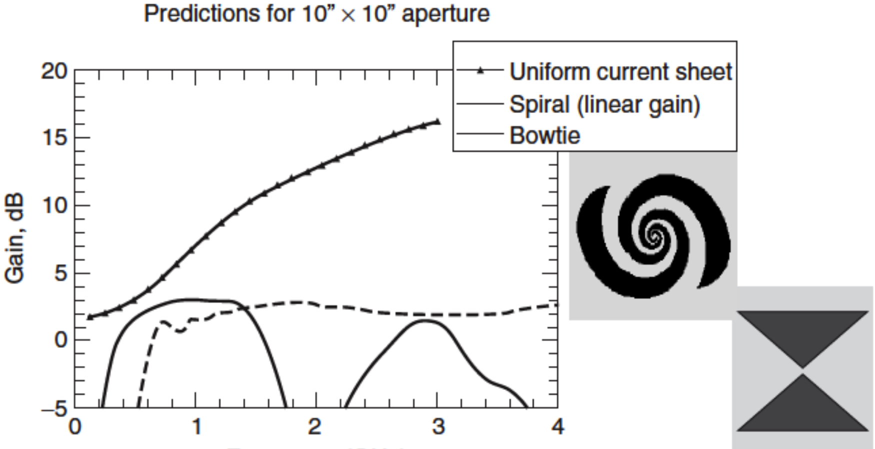

Figure 6.1: Predicted gain for three antenna types occupying a $10'' \times 10''$ aperture: a uniform current sheet (theoretical ideal), a spiral antenna, and a bowtie antenna. Neither the spiral nor the bowtie approaches the broadband aperture gain limit [1].

radiator designs that use parasitic face sheets to enhance front-to-back ratio, further extending achievable bandwidths to 33:1. Measured results from laboratory proof-of-concept arrays are presented throughout.

6.2 Connected Fragmented Array Elements

The fragmented aperture design approach extended naturally from single-element antennas to array elements. The key insight that led to a breakthrough in achievable bandwidths was the recognition that DC electrical connection between adjacent elements was not merely tolerable but actually beneficial and should be exploited. Subsequent multiple-octave array designs consistently featured these inter-element connections, which support continuous current paths spanning multiple elements.

The importance of connected arrays can be understood intuitively. In an array with an 8:1 bandwidth, the radiated wavelength changes from approximately two element widths at the highest frequency to 16 element widths at the lowest. For the array to radiate efficiently at the lowest frequencies, continuous conducting paths of sufficient length must be present on the aperture surface. With a connected array, such paths naturally exist.

To demonstrate the importance of inter-element connections, the 6-cm elements shown in Figure 6.2 were designed to operate from 0.25–2.5 GHz in an array with no ground plane. Two designs were compared: the first was optimized with electrical connections between elements permitted (a connected array), while the second was optimized with a boundary enforced around each element to prevent conducting pathways between elements. The realized gain achieved by an 8×8 finite array of each element

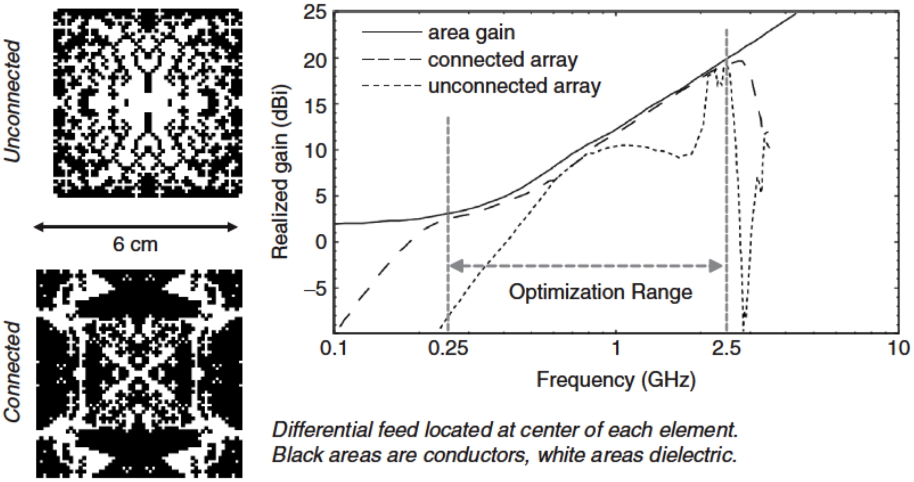

Differential feed located at center of each element.
Black areas are conductors, white areas dielectric.

Figure 6.2: Design experiment comparing two 8 × 8 arrays: (a) connected array element, (b) unconnected array element, (c) embedded element gain comparison for a central element. The connected array element far outperforms the unconnected element [1].

design is shown in Figure 6.2(c). Because of the continuous current paths across element boundaries, the connected design maintains a good impedance match over the full 10:1 bandwidth and achieves markedly superior performance.

Another key feature of the connected geometry is that the overall size of the array becomes a limiting factor on the lowest operating frequency. When the connected element design of Figure 6.2 was modeled in arrays of various sizes (again without a ground plane), the low-frequency performance scaled proportionally with array size, as shown in Figure 6.3. Arrays of 2×2, 4×4, 8×8, and 16×16 elements were simulated. In all cases, the upper frequency limit remained relatively constant, being limited by the element lattice spacing and the onset of grating lobes. The low-frequency limit, on the other hand, was approximately proportional to the overall array dimension.

To confirm the validity of these simulation predictions, a fragmented array with 3-cm elements was designed and measured in 1999. The metric used was the embedded element realized gain (EERG), obtained by driving one central element while terminating all surrounding elements in matched resistive loads. The EERG measures the performance of a single element in the array environment and is a powerful diagnostic because angle-pattern cuts of the EERG can be used to predict the scan performance of a fully driven array. This approach greatly reduces measurement cost since beam-forming electronics are not required. As shown in Figure 6.4, the array achieves near aperture-limited gain at broadside over a 10:1 bandwidth, with excellent model-measurement agreement.

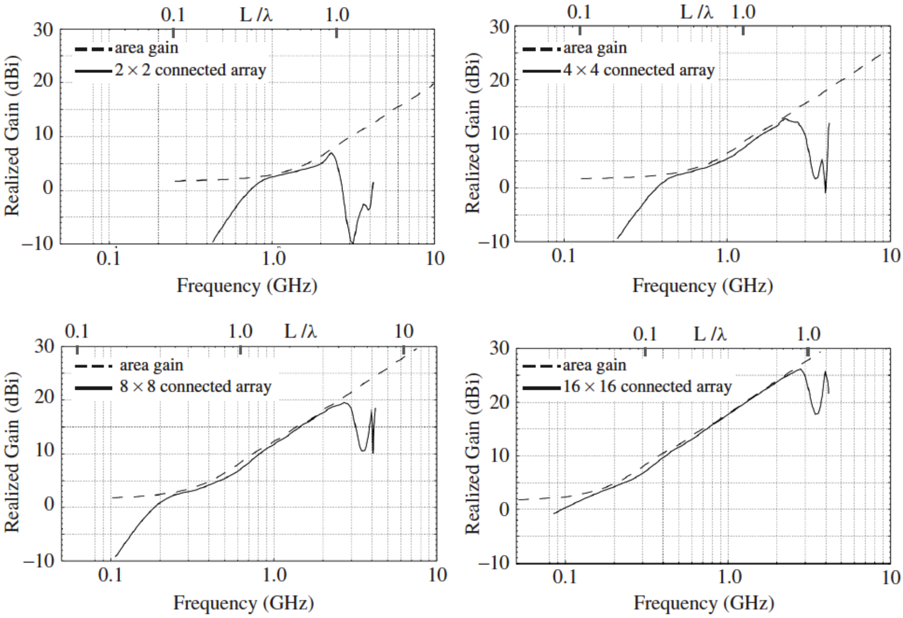

Figure 6.3: The connected element from Figure 6.2 simulated in arrays of various sizes. The low-frequency performance limit is approximately proportional to overall array size [1].

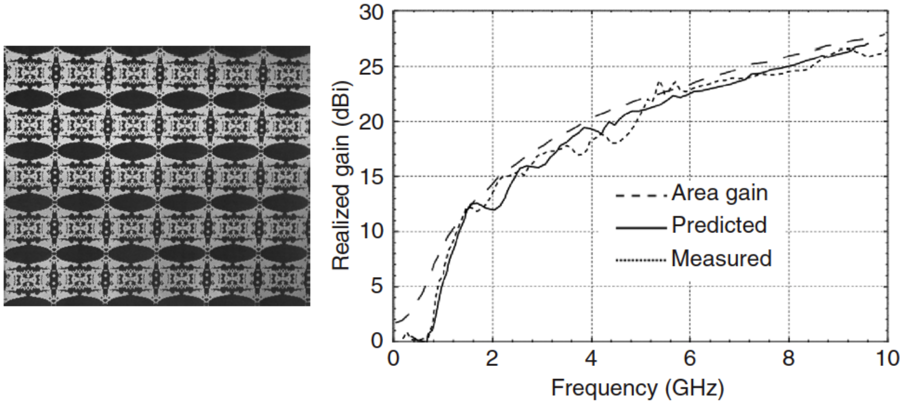

Figure 6.4: Embedded element realized gain (EERG) for a central element of a 10 × 17 array with 3-cm square unit cells, demonstrating 10:1 bandwidth with excellent model-measurement agreement [1].

6.3 Wideband Backplanes: Planar 10:1 Arrays

Early explorations of fragmented arrays (2000 and earlier) focused on fundamental questions of element connections, bandwidth limits, and natural impedance values [2]–[3]. These investigations typically either used no ground plane behind the radiating surface or accepted the limitations of simple ground planes. More recent work has demonstrated unbalanced feed designs for wideband phased arrays [4, 5] and broadband arrays with power combiners based on the fragmented aperture principle [6].

Ideally, a ground plane should be located $\lambda/4$ behind the radiating surface of a planar antenna. The backward-radiated energy travels a round-trip path of $\lambda/2$, accumulating 180° of phase, and the 180° phase inversion at the perfect electric conductor (PEC) surface of the ground plane causes the reflected energy to arrive in phase with the forward-going radiation. Wideband antennas pose a fundamental difficulty, however, since λ varies widely over the operating bandwidth. When the ground plane is $\lambda/2$ behind the radiating surface (or an integer multiple of $\lambda/2$), the backward-going radiation is reflected and arrives exactly out of phase with the forward radiation, producing a deep null in the gain.

This situation is illustrated in Figure 6.5, which shows the results of a simulation of a fragmented aperture radiator placed 2.5 cm in front of a PEC ground plane. The broadside gain is normalized to the area gain. Without the ground plane, the radiator is well matched across the band, but because it radiates in both directions, the forward radiation only approaches -3 dB, represented by the dashed line. With the ground plane, the gain approaches the maximum around 3 GHz, where 2.5 cm represents a quarter of the free-space wavelength and the ground plane provides nearly 3 dB of gain enhancement. At 6 GHz, however, the ground plane is a half wavelength behind the radiating surface, and a deep null appears. This null repeats at every integer multiple of $\lambda/2$ (12 GHz, 18 GHz, etc.). Practical experience indicates that fragmented aperture designs can be extended to approximately 8:1 bandwidths before the half-wave null must be addressed.

The problem is further complicated if the array is intended to scan over a significant volume, because the null frequency depends on the scan angle, as illustrated in Figure 6.6. As the scan angle moves away from broadside, the null frequency increases. The contour plot in the figure shows this trend clearly.

6.3.1 The Broadband Screen Backplane

Since the problem can be attributed to backward-radiated energy reflecting off the ground plane, one is tempted to address it with absorbing solutions. Interestingly, the Salisbury screen absorbing structure has the desirable characteristic that its tuned absorption frequency increases with incidence angle, exactly analogous to the scan angle–frequency dependence of the half-wave null. This was the inspiration for the *broadband screen backplane*, which was developed to extend the frequency performance of fragmented apertures over a ground plane.

The broadband screen backplane consists of one or more resistive card (r-card) layers placed between the radiating aperture and the PEC ground plane. Figure 6.7 shows the performance of a typical r-card layer placed halfway between the aperture layer

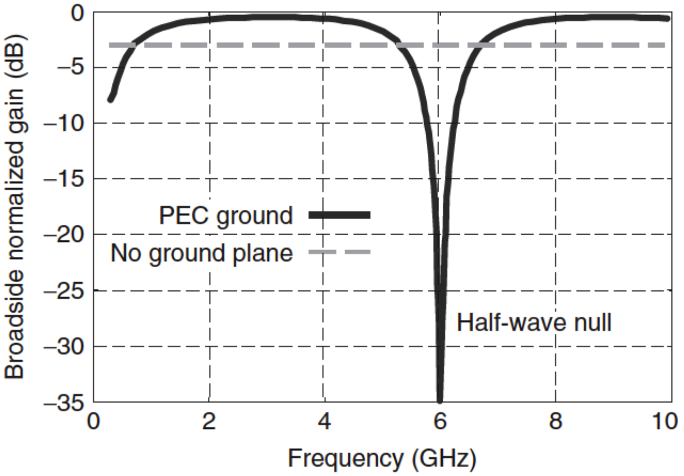

Figure 6.5: When a broadband radiating sheet is placed in front of a simple PEC ground plane, the resulting gain suffers nulls at frequencies where the separation distance is an integer multiple of $\lambda/2$ (in this case, 6 GHz for a 2.5-cm separation) [1].

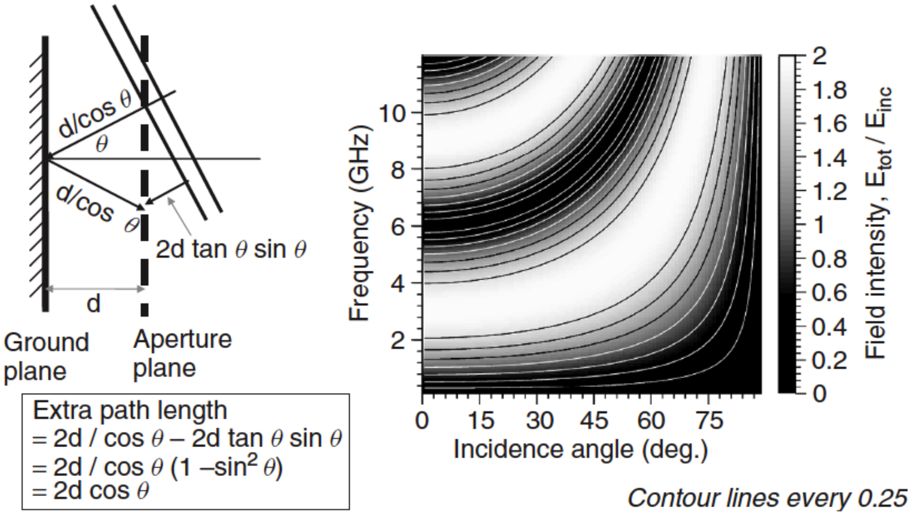

Figure 6.6: The half-wave null frequency depends on scan angle. Left: geometry illustration. Right: contour plot showing the relationship between field intensity at the radiating surface, frequency, and scan angle for a 2.5-cm separation [1].

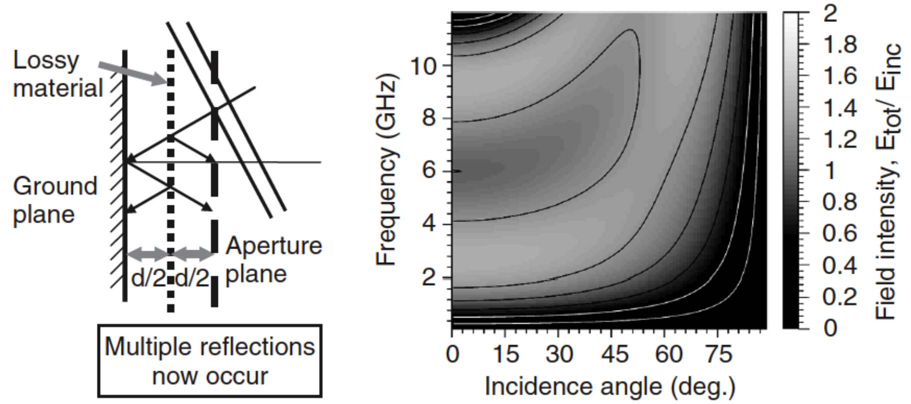

Contour lines every 0.25

Figure 6.7: A 377 Ω/square r-card layer placed halfway between the radiating surface and the PEC ground plane (2.5-cm separation) eliminates the deep null at $\lambda/2$ [1].

and the ground plane. The backplane is most absorptive at exactly the frequency/angle combinations where the half-wave null occurs (and at every odd multiple of half wavelengths).

Figure 6.8 shows the normalized realized gain at broadside with this first-generation broadband screen backplane. The aperture has recovered enough gain at the problem frequency to achieve near 50% efficiency. However, one can do better. For overall antenna performance, the impedance value, position, and even the number of r-card layers may be treated as free variables in the design. For example, if the 377 Ω r-card is replaced with a 225 Ω card, the realized gain is maintained within 2 dB of the aperture limit across the operating band.

6.3.2 A 10:1 Proof-of-Concept Array

Figure 6.9 shows a 10:1 bandwidth design that was developed as a proof of concept using a single r-card broadband screen. The array demonstrated better than 50% efficiency over the operating band of 1–10 GHz. The plot on the right shows normalized predictions of realized gain, or equivalently, insertion loss. The upper curve (normalized gain) shows the effects of resistive loss alone, while the lower curve (normalized realized gain) shows the combined effects of resistive and mismatch loss. The separation between the two curves is a measure of the impedance match quality.

6.3.3 Multi-Layer Broadband Screen Backplanes

With a simple conducting ground plane behind a planar radiating surface, a standing wave occurs when the separation distance is $\lambda/2$ (or an integer number of half wavelengths), placing a field null at the radiating surface. The resulting impedance mismatch

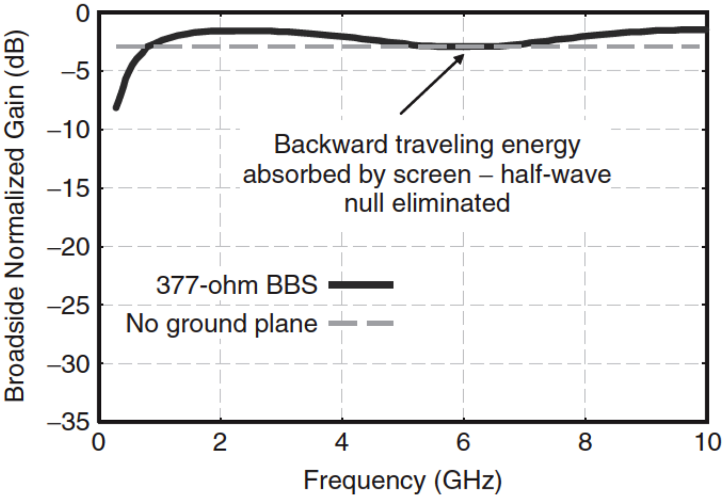

Figure 6.8: Normalized realized gain at broadside for the configuration of Figure 6.7, showing that the deep null at 6 GHz has been improved to approximately 3 dB insertion loss [1].

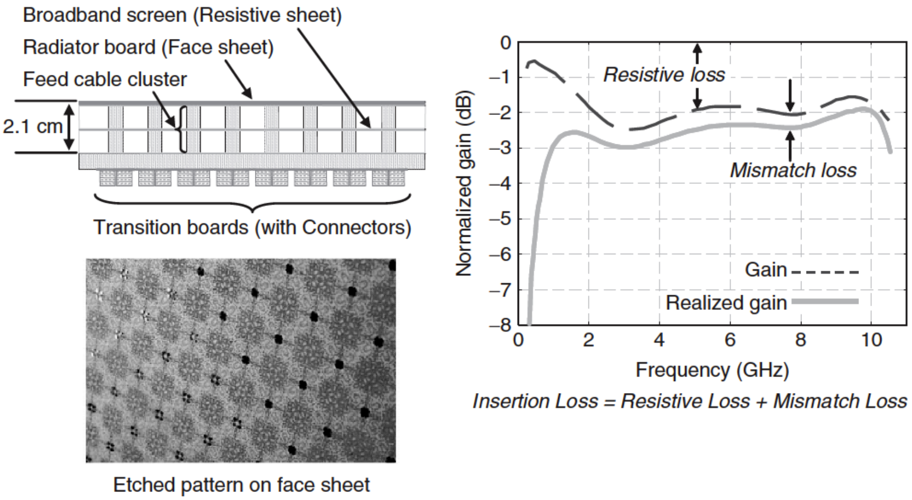

Figure 6.9: The first array built using the broadband screen backplane: a 10:1 design with efficiency better than 50% (< 3 dB insertion loss) from 1 to 10 GHz [1].

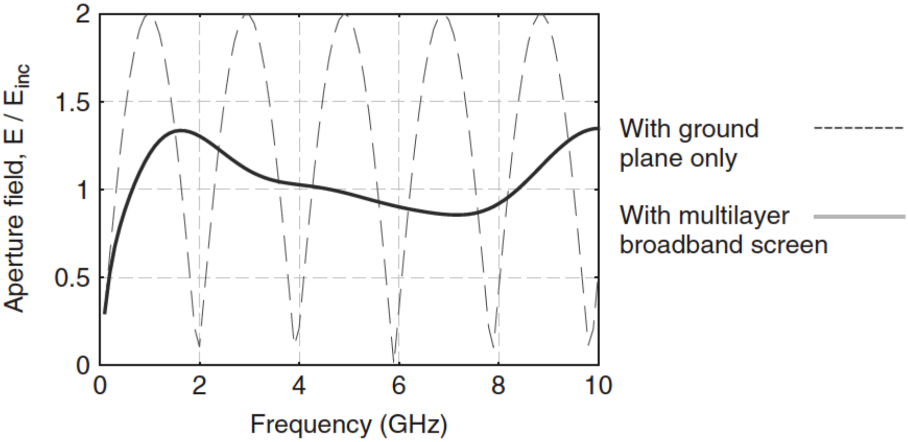

Figure 6.10: Aperture fields 3 inches in front of a PEC surface, with and without a broadband screen backplane [1].

causes the deep dropout in the gain curve. In addition to the energy they dissipate, r-cards inserted in the backplane stack introduce additional reflection boundaries that redistribute the standing wave to avoid field cancellation at the radiating surface.

As the operating bandwidth of the array spans more octaves, a simple ground plane introduces more half-wave nulls, and the problem of defeating the standing wave becomes more complex. Figure 6.10 shows an example of a radiating surface located three inches in front of a simple conducting ground plane. The resulting standing wave produces interference nulls approximately every 2 GHz. When the empty cavity is replaced by an optimized broadband screen with six r-card layers, the standing-wave nulls are eliminated. Figure 6.11 compares the performance of the empty cavity with the broadband screen over frequency and scan angle, demonstrating that the nulls are effectively controlled to scan angles of 60° or more.

6.4 Multi-Layer Radiators: 33:1 Bandwidth Arrays

A broadband screen backplane can control half-wave nulls, but it uses a loss mechanism to do so. While it is not necessary to attenuate all of the backward-radiated energy, some resistive loss is inevitable with this approach. A more desirable strategy would be to radiate energy preferentially into the forward hemisphere, thereby reducing the amount of backward-radiated energy that can reflect off the ground plane.

6.4.1 Directional Radiation from Thick Apertures

As a thought experiment, consider the ideal planar radiator with no thickness shown on the left in Figure 6.12. Radiation must occur equally into both hemispheres since nothing distinguishes one side from the other. However, if the radiating layer has some

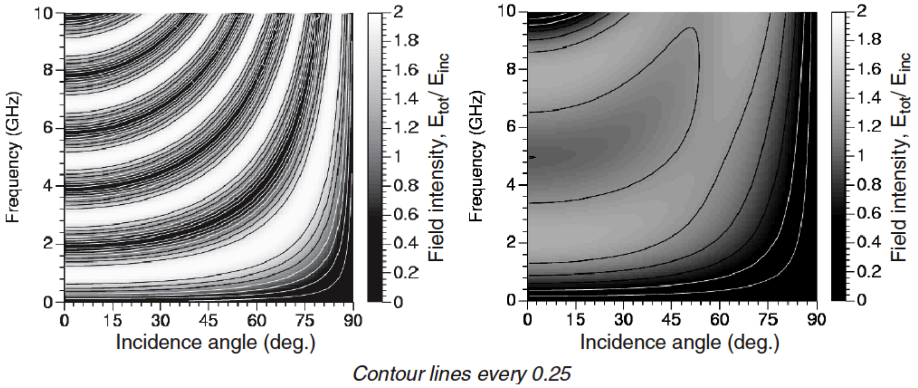

Figure 6.11: Contour plots comparing the configurations of Figure 6.10 over a range of scan angles. The broadband screen effectively eliminates standing-wave nulls to scan angles beyond 60° [1].

thickness, asymmetries may be introduced that cause the surface to radiate preferentially in one direction, as shown on the right in Figure 6.12. For example, if 90% of the energy is directed into the forward hemisphere, then even if the backward-radiated 10% is reflected and returns 180° out of phase, it will only reduce the transmitted power to 80% of the maximum value.

This principle can be exploited using multiple radiating layers in front of the ground plane. The additional layers may be actively driven or parasitic, analogous to the directors in a Yagi-Uda antenna.

6.4.2 Parasitic Layer Design Experiments

In Figure 6.13, two radiating layers approximately 8 mm apart with no ground plane were optimized using the fragmented aperture design process. The design goal was to maximize gain in the forward hemisphere. The plot shows the normalized forward-going and backward-going radiation, demonstrating good front-to-back ratio (F/B) over the upper octave of the design region (1–10 GHz). As the wavelength gets longer, the electrical separation between radiating layers becomes insufficient to direct the radiation.

The region of effectiveness for the parasitic-layer approach is sufficient to produce the 10:1 design of Figure 6.14, where the realized gain remains within 3 dB of the maximum across the band. This design is for illustrative purposes, as it does not include realistic feed structures or material loss.

The extent to which multiple radiating face-sheet layers improve the bandwidth depends on the number and spacing of the face sheets. Figure 6.15 shows designs using two and three face sheets, respectively. These simulations include realistic feed structures, but the ground planes have been replaced by perfectly matched absorbing layers. With two face sheets, the antenna exhibits enhanced gain over most of the upper

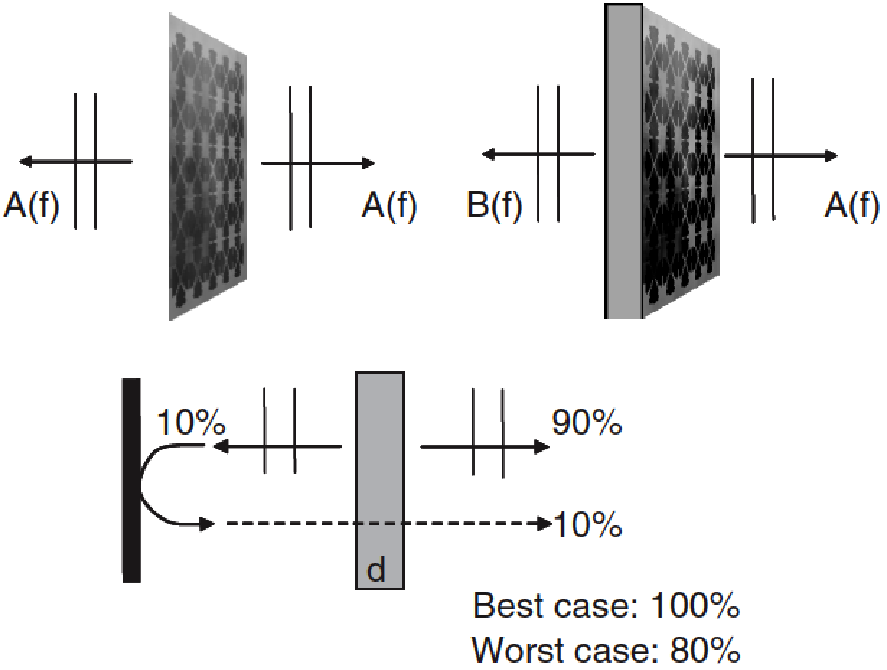

Figure 6.12: Thought experiment demonstrating the benefit of preferential forward radiation. A radiator with finite thickness can achieve asymmetric radiation (front-to-back ratio), mitigating the impact of ground plane reflections [1].

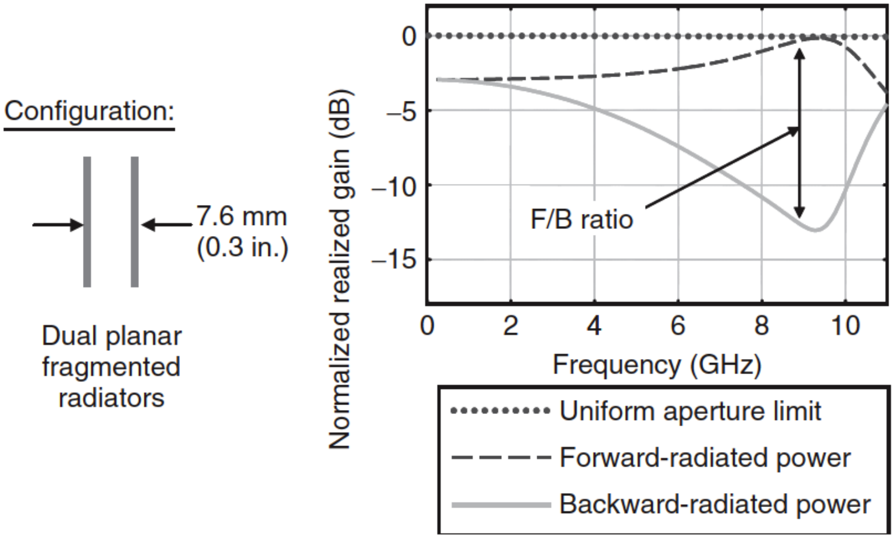

Figure 6.13: Idealized design with two simultaneously optimized radiating layers and no ground plane. The design goal was to maximize front-to-back ratio [1].

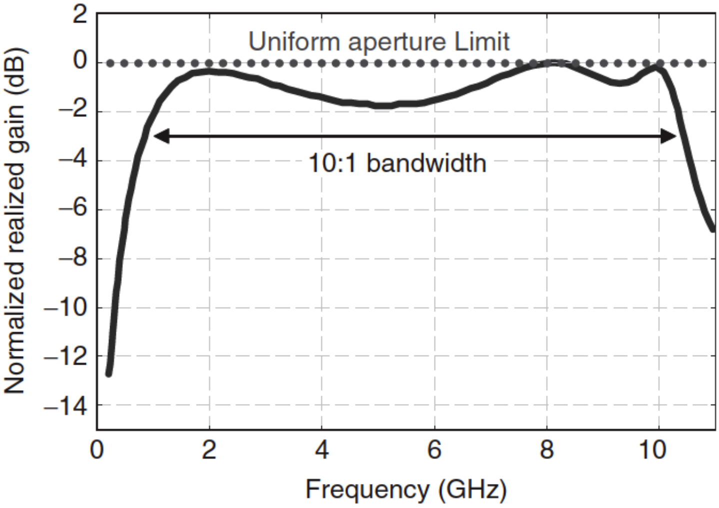

Figure 6.14: Parasitic layers directing radiation forward in the presence of a PEC backplane, keeping insertion loss below 2 dB over most of a 10:1 bandwidth [1].

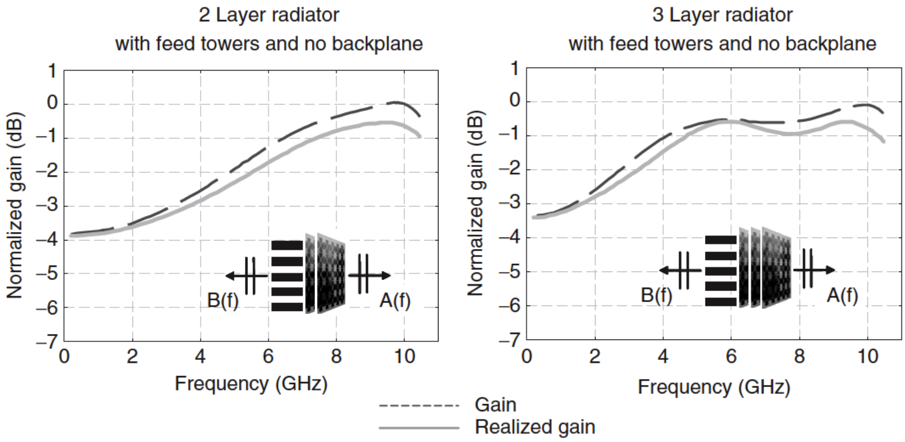

Figure 6.15: Design experiments with two and three radiating face sheets. The ground plane has been replaced in each simulation with a perfectly absorbing back boundary. Normalized gain levels above −3 dB indicate front-to-back ratio enhancement [1].

octave. With three, antenna gain is enhanced over the upper two octaves.

6.4.3 33:1 Proof-of-Concept Arrays

Design of fragmented elements for phased arrays with operating bandwidths beyond 10:1 requires a judicious combination of a multi-layer radiator with a broadband screen backplane. In partnership with Northrop Grumman Electronics Systems, the Georgia Tech Research Institute (GTRI) built and measured two laboratory proof-of-concept radiators with 33:1 bandwidths, each incorporating both design strategies. Each design consisted of a three-layer radiator stack over a six-r-card backplane stack. In the first design, two face sheets were driven by the feeds and the third was parasitic. To simplify the manufacturing process, the second design had only the innermost face sheet driven, with two parasitic outer layers.

Figure 6.16 shows the performance of the second design in a periodic simulation, which eliminates finite-array edge effects. The simulation includes realistic feed structures and material properties. Gain is normalized to the element area gain, so the 0 dB line represents ideal performance. The design achieves approximately 1 dB or better insertion loss over the upper octave, with better than 3 dB insertion loss over the entire 0.3–10 GHz design bandwidth.

6.4.4 33:1 Measured Results

The simulations were validated with measurements of a test piece on three different antenna ranges covering the entire operating bandwidth. The test antenna was a 23 × 23 element, dual-linear-polarized array with the center element actively driven and all surrounding elements terminated in matched 188 Ω impedances at the feed points. Fig-

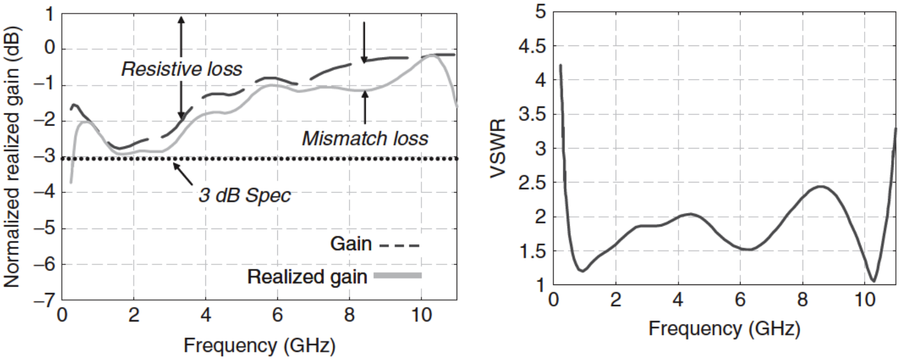

Figure 6.16: Predicted performance of the 33:1 antenna design in a periodic simulation, including realistic feed structures. Antenna efficiency is better than 50% over the entire 0.3–10 GHz bandwidth [1].

ure 6.17 illustrates the composition of one element of the array in cross section, with diagrams of the etched unit-cell pattern on each face sheet and a photograph of the test antenna.

Broadside frequency scans of the EERG are plotted in Figure 6.18. The figure compares measurement results at broadside to predictions. The element area gain (dashed line) represents the physical limit for antenna performance. The predicted EERG at broadside is shown as a solid line. Four measured data sets from three different antenna ranges are compared, including three different calibration horns spanning the 33:1 bandwidth. Data was measured on both V-pol and H-pol feeds (both should be equivalent at broadside for this symmetric design). The measured data show excellent consistency across ranges and at both sets of feed points, and excellent agreement with the predictions.

The measurements showed approximately 1 dB more insertion loss at the high end than predicted. The difference exceeds what can be attributed to resistive loss in the feed cables and on the metal radiating surfaces; it is likely due to slight imperfections in the assembly of the radiator. Performance at the high end is particularly sensitive to the position and planarity of the three face-sheet layers, and the planarity in the assembled test piece was affected by warping in the etched sheets.

This slight high-frequency offset is removed in Figure 6.19 to facilitate angle-pattern comparisons. These patterns allow detailed comparison of measured and modeled EERG over angle cuts at several discrete frequencies. Model-measurement agreement is excellent, with the models predicting features such as the ripple at 2 GHz due to finite-array edge effects and the narrowing of the scan volume above 8 GHz.

Figure 6.20 presents the measured EERG data from three overlapping data sets for H-plane scans and two for E-plane scans. The contour plots show angle cuts plotted horizontally at each frequency. Each angle cut has been normalized so that the maximum value at each frequency is zero (i.e., the frequency slope has been removed). The resulting image shows the achievable scan volume as a function of frequency for a fully

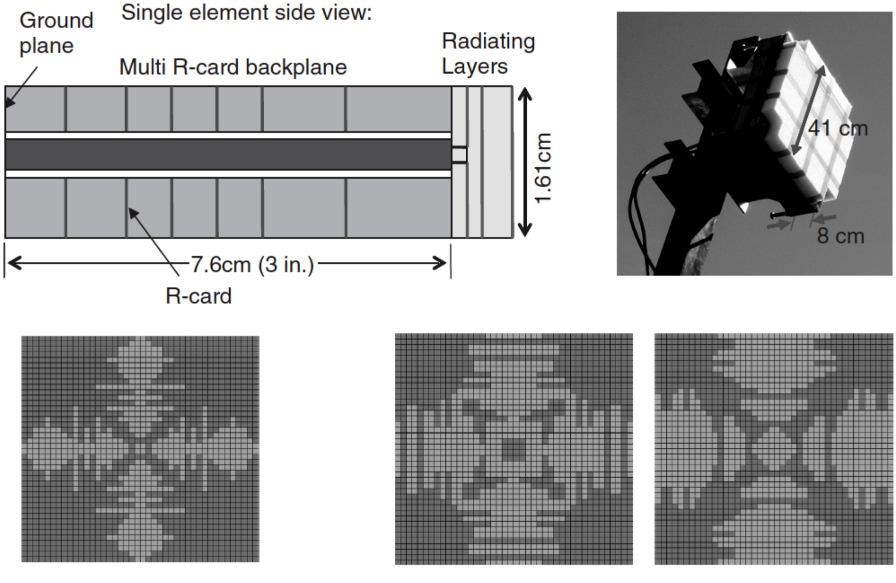

Face sheet 1: Driven layerF

Face sheets 2 & 3: Parasitic layers

Figure 6.17: Construction details of the 33:1 antenna design, including a photograph of the 23 × 23 element test piece used to measure embedded element realized gain [1].

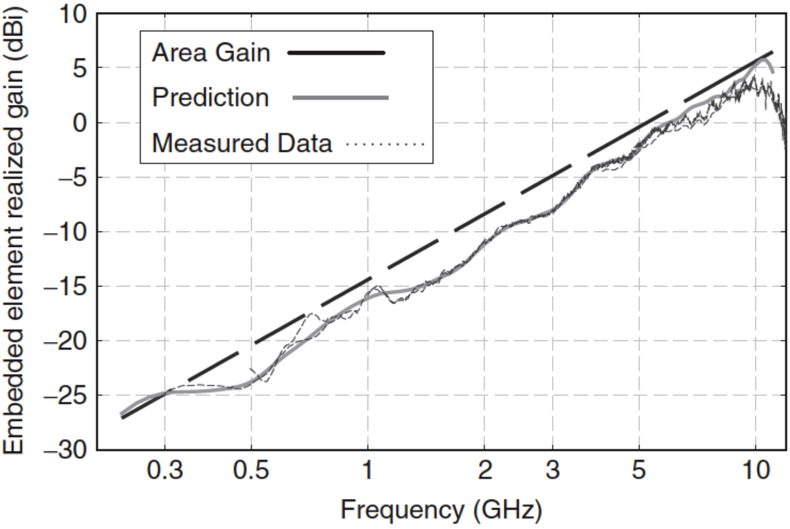

Figure 6.18: Compilation of measured EERG data at broadside for the 33:1 test antenna (three antenna ranges, two polarizations) compared with numerical predictions. The dashed line represents the element area gain [1].

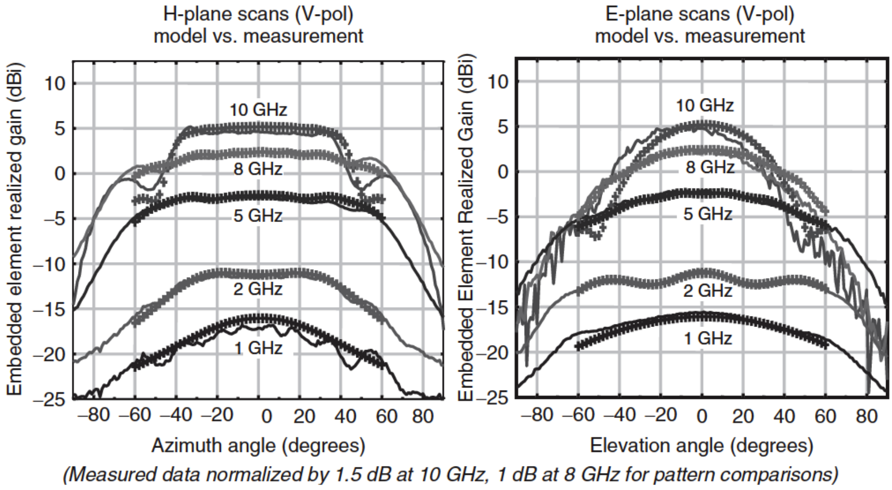

Figure 6.19: Comparison of modeled (solid lines) and measured (data markers) EERG pattern cuts at several discrete frequencies, showing excellent agreement [1].

driven array with this element design. The scan volume, as defined by the -3 dB points, is approximately ±60° over most of the band, with some narrowing above 9 GHz in the H-plane and above 7 GHz in the E-plane. Notably, the scan volume shows no evidence of scan blindness anywhere in the operating bandwidth.

6.5 Design Rules and Scaling

Experience with several wideband phased array designs has produced empirical evidence for a useful rule of thumb regarding the thickness of these wideband radiators. Figure 6.21 compiles results for five fragmented array designs with bandwidths greater than an octave. Designs with bandwidths less than 10:1 used simple ground planes; antennas with bandwidths of 10:1 or greater incorporated broadband screen backplanes. In each case, the overall thickness is dictated not by the bandwidth but by the lowest operating frequency. For cavities filled with air or low-dielectric foams, the antenna thickness is approximately $\lambda/12$ at the lowest operating frequency.

6.6 Unbalanced Feed Arrays

More recently, Landgren et al. at GTRI developed wideband phased arrays using a single unbalanced (single-ended) coaxial feed per element, eliminating the need for baluns or differential electronics [4]. The unit cell consists of multiple layers of low-permittivity materials, a coaxial feed, and one or two fragmented aperture layers (a driven layer and an optional parasitic director layer) with no vias. This all-planar construction significantly simplifies manufacturing compared to the machined aluminum

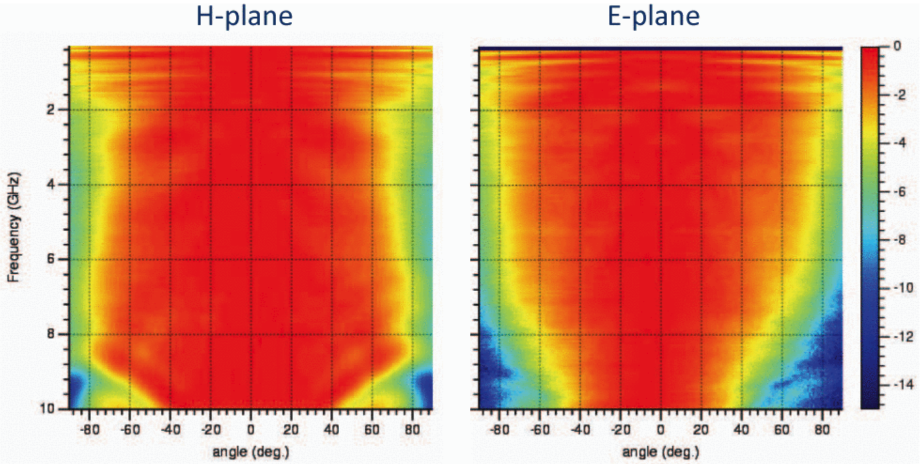

Figure 6.20: Compilation of measured EERG angle cuts normalized to the maximum at each frequency. The resulting contours indicate achievable scan volume. No scan blindness is observed within the operating bandwidth [7].

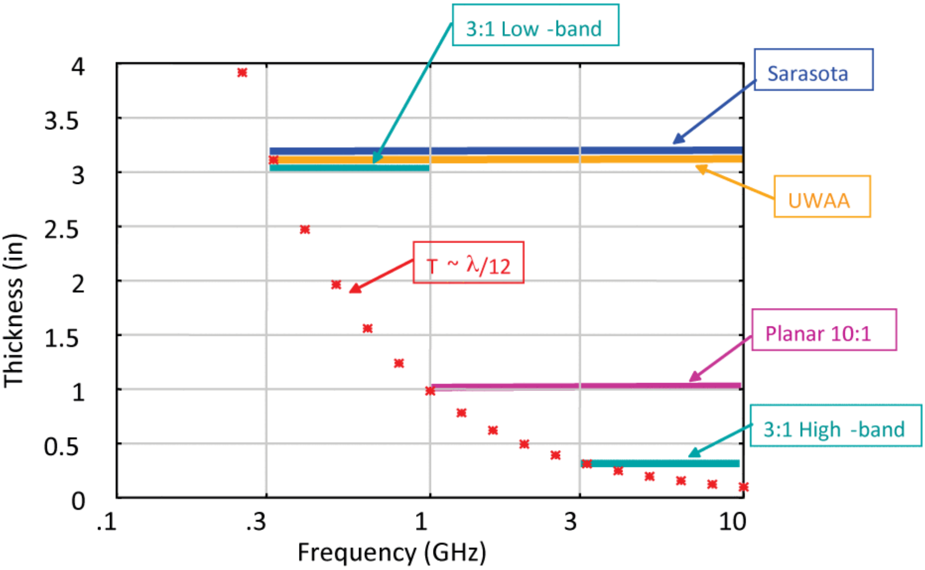

Figure 6.21: Results of several design exercises for fragmented arrays. For air-filled cavities, the antenna thickness is approximately $\lambda/12$ at the lowest operating frequency [7].

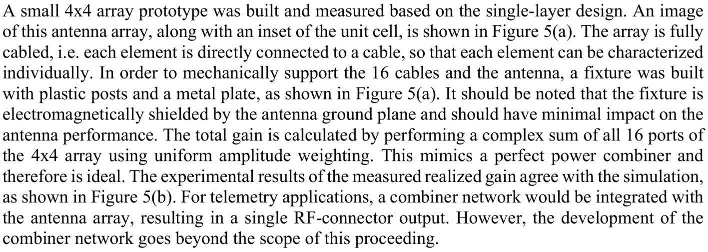

A small 4x4 array prototype was built and measured based on the single-layer design. An image of this antenna array, along with an inset of the unit cell, is shown in Figure 5(a). The array is fully cabled, i.e. each element is directly connected to a cable, so that each element can be characterized individually. In order to mechanically support the 16 cables and the antenna, a fixture was built with plastic posts and a metal plate, as shown in Figure 5(a). It should be noted that the fixture is electromagnetically shielded by the antenna ground plane and should have minimal impact on the antenna performance. The total gain is calculated by performing a complex sum of all 16 ports of the 4x4 array using uniform amplitude weighting. This mimics a perfect power combiner and therefore is ideal. The experimental results of the measured realized gain agree with the simulation, as shown in Figure 5(b). For telemetry applications, a combiner network would be integrated with the antenna array, resulting in a single RF-connector output. However, the development of the combiner network goes beyond the scope of this proceeding.

Figure 6.22: Unbalanced-feed 4×4 prototype array: (a) assembled array with unit cell inset, (b) measured vs. simulated broadside realized gain, and (c) normalized gain for varying array sizes compared to infinite array prediction [4].

feed tower approach described earlier.

A 4×4 prototype array was fabricated and measured to validate the design. Figure 6.22 shows the assembled array with an inset of a single unit cell, the measured broadside realized gain compared with simulation, and the simulated effect of array size on normalized gain. The measured gain of the 4×4 array agrees closely with the FDTD prediction across the L-, S-, and C-bands ($\sim$1.4–6.7 GHz), confirming that the unbalanced feed approach delivers ultra-wideband performance without baluns. The array size study shows that for arrays larger than 8×8 elements, the realized gain is within 1.5 dB of the infinite array prediction.

This prototype array was subsequently scaled to a full 16×16 element array with integrated fragmented power combiners for deployment at the U.S. Army Aberdeen Test Center; the combiner technology is described in Chapter 10.

6.7 Summary and Conclusions

The successful design of ultra-wideband phased arrays has been enabled by several factors. These designs require high-fidelity time-domain electromagnetic solvers. The necessity to optimize over many frequencies simultaneously would be prohibitively time-consuming with frequency-domain codes. All designs described in this chapter were developed using a finite-difference time-domain (FDTD) code (see Appendix A), the results of which are Fourier transformed to produce the requisite range of frequency predictions. In early design stages, it is important to move through iterations rapidly to converge on a good initial design. In the final stages, accurate predictions are required to account for realistic details such as feed structures and material characteristics.

With the appropriate modeling tools and computing infrastructure, the essential features for ultra-wideband planar phased arrays were developed:

1. **Connected arrays** to span several octaves by supporting continuous current paths across element boundaries.

2. **Broadband screen backplanes** consisting of r-card layers to mitigate the half-wave nulls introduced by a conducting ground plane.

3. **Multi-layer radiators** using parasitic face sheets to enhance front-to-back ratio, leveraging the backplane improvements at lower frequencies.
4. **Fragmented aperture element design** to accomplish impedance matching in the presence of feed structures, material substrates, multiple layers, and mutual coupling.

Measured results confirm the success of these design strategies for bandwidths up to 33:1. Preliminary work suggests that phased array operation over bandwidths of 100:1 or more may be achievable.

[Note: The bullet-point outline for this chapter included a section on 100:1 bandwidth designs. This material is not yet available and should be added when ready.]

6.8 Acknowledgement

The author would like to thank Mr. Paul Friederich for his efforts in converting the original "How to make a 33:1 bandwidth array antenna" presentation into the handbook chapter [1] that served as the source material for this chapter.

References

[1] W. Croswell, T. Durham, M. Jones, D. Schaubert, P. G. Friederich, and J. G. Maloney, "Wideband arrays," in *Modern Antenna Handbook*, C. A. Balanis, Ed. John Wiley & Sons, 2011, ch. 12.

[2] J. G. Maloney, M. P. Kesler, P. H. Harms, T. L. Fountain, and G. S. Smith, "The fragmented aperture antenna: FDTD analysis and measurement," in *Millennium Conference on Antennas and Propagation (AP 2000)*, 2000, p. 93.

[3] P. Friederich, L. Pringle, L. Fountain, P. Harms, D. Denison, E. Kuster, S. Blalock, G. Smith, J. Maloney, and M. Kesler, "A new class of broadband planar apertures," in *Antenna Applications Symposium*, Sep. 2001, pp. 561–587.

[4] D. W. Landgren, D. J. P. Dykes, and K. W. Allen, "An unbalanced feed design for wideband phased arrays," *arXiv preprint arXiv:1706.04658*, 2017, international Telemetry Conference. [Online]. Available: https://arxiv.org/abs/1706.04658

[5] D. J. P. Dykes, K. M. Bowland, and K. W. Allen, "Wideband millimeter-wave fragmented aperture antenna," in *2017 IEEE National Aerospace and Electronics Conference (NAECON)*, 2017, pp. 213–216.

[6] D. Landgren, T. Brunasso, K. Allen, D. Dykes, J. Kovitz, J. Perez, J. Dee, J. Marsh, C. Hunter, and G. Smith, "A broadband array with unbalanced feeds : Elements and power combiners based on the fragmented aperture principle," in *2019 IEEE International Symposium on Antennas and Propagation and USNC-URSI Radio Science Meeting*, 2019, pp. 1223–1224.

[7] L. N. Pringle, P. H. Harms, S. P. Blalock, G. N. Kiesel, E. J. Kuster, P. G. Friederich, R. J. Prado, J. M. Morris, and G. S. Smith, "A reconfigurable aperture antenna based on switched links between electrically small metallic patches," *IEEE Transactions on Antennas and Propagation*, vol. 52, no. 6, pp. 1434–1445, Jun. 2004.

Chapter 7

Designing Wide Scan Fragmented Array Antennas

7.1 Introduction

The previous chapters have demonstrated that fragmented aperture arrays can achieve remarkable bandwidths—up to 33:1 and beyond—while maintaining broadside gain that closely tracks the uniform aperture limit. However, one persistent challenge has been maintaining wide scan volume across the full operating bandwidth. This chapter addresses that challenge, describing design techniques that achieve scan volumes exceeding ±60° across the entire design band.

Chapter 6 presented the development of ultra-wideband fragmented arrays, culminating in a 33:1 bandwidth proof-of-concept array. Figure 7.1 shows the measured and predicted embedded element realized gain for that array, confirming excellent agreement between model and measurement across three independent measurement facilities. The broadside gain tracks the uniform aperture area limit well across the 0.3 to 10 GHz design band, and the inset photograph shows the array on the outdoor measurement range.

Despite the excellent broadside performance, this array exhibited a shortcoming in its scan volume. As discussed in Chapter 6 (see Figure 6.20), the principal-plane antenna patterns for the 33:1 array show wide scan volume ($> \pm 60°$) across most of the operating band. However, near the top of the band (approximately 8.5 to 10 GHz), a significant narrowing of the scan volume is evident, reducing the usable scan range to roughly ±40°. In the years since the design of the 33:1 antenna, preventing this upper-band scan volume narrowing has been an active area of research.

A second shortcoming of the 33:1 array is related to aperture efficiency. As visible in Figure 7.1, the array was within 3 dB of the uniform aperture gain limit (better than 50% aperture efficiency), but the majority of the loss was attributable to the resistive backplane required to suppress the ground-plane nulls over such a large bandwidth. This loss limits the array to receive-only or low-power transmit applications.

This chapter describes progress in overcoming these two limitations. First, an im-

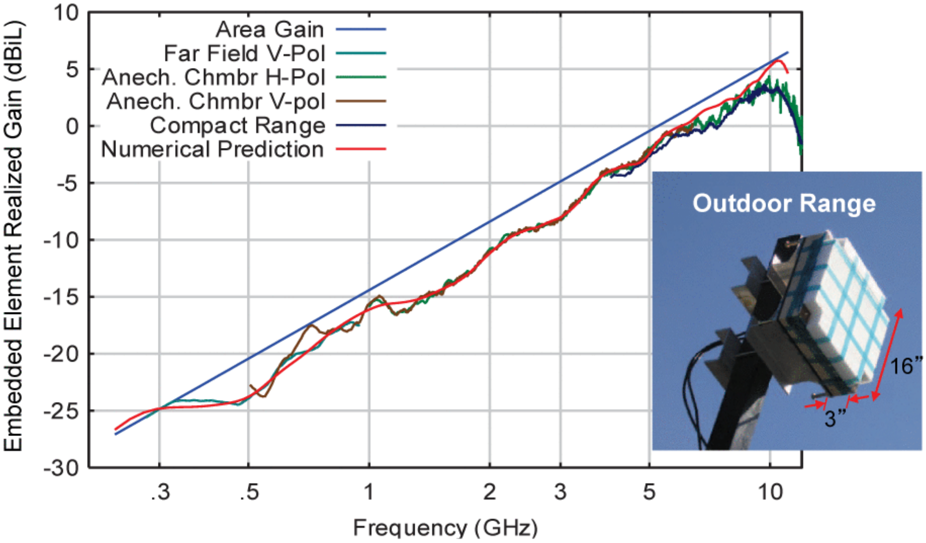

Figure 7.1: Measured and predicted embedded element realized gain (EERG) for the 33:1 bandwidth array. The broadside gain (red line) tracks the uniform aperture area limit (blue line) across the 0.3 to 10 GHz design band. Measurements from three independent facilities (anechoic chamber, compact range, and outdoor range) confirm the model accuracy. Inset: the array on the outdoor measurement range [1].

proved design process using spectral-domain FDTD simulation enables the genetic algorithm to optimize scan performance directly, alleviating the upper-band scan volume narrowing without requiring tighter inter-element spacing. Second, for applications that do not require the extreme bandwidth of the 33:1 design, a simpler antenna structure can be used that avoids the introduction of resistive loss, enabling high-efficiency operation suitable for transmit applications. Third, a laminated printed circuit board (PCB) fabrication approach replaces the traditional machined aluminum construction, yielding a more integrated, mass-producible antenna. These advances are illustrated through the design of a wide-scanning (±60°), whole X-band (8–12 GHz) phased array element.

7.2 Fabrication Approaches

7.2.1 Traditional Construction

Early fragmented aperture array antennas were constructed using the approach depicted in Figure 7.2. This design consists of an array of elements printed on circuit board material, suspended over a conducting ground plane by machined aluminum feed towers. The feed towers enclose differential coaxial lines that provide the dual-polarized excitation to each antenna element. Combining networks and beamforming electronics connect to these coaxial lines in the space behind the ground plane.

This construction method can produce lightweight structures; for example, a 0.6 m × 0.6 m array built in this manner weighed only 4 kg for the entire antenna assembly. This basic construction has been used to build many successful wideband fragmented aperture designs over the past two decades, including the 33:1 bandwidth array and the various designs summarized in the thickness-versus-frequency chart in Chapter 6 (Figure 6.21).

7.2.2 Laminated Printed Circuit Board Construction

While the traditional machined construction produces excellent antenna performance, it is not ideal for mass production, particularly at higher frequencies where the mechanical tolerances become demanding. An alternative approach, shown in Figure 7.3, builds the entire antenna from laminated printed circuit board layers.

In this approach, the fragmented conducting layers, the dielectric spacers between them, and the ground plane are all integrated into a single laminated PCB stack-up. The element feeds, which were previously machined coaxial lines enclosed in aluminum towers, are now implemented as closely spaced plated vias manufactured using standard multi-layer PCB techniques. Feed networks can also be implemented as additional PCB layers, producing a highly integrated antenna panel.

The PCB approach offers several practical advantages. It leverages mature, high-volume PCB manufacturing processes, resulting in antennas that are more repeatable, more easily mass-produced, and potentially less expensive than machined alternatives. These benefits are especially significant at X-band and higher frequencies, where the small feature sizes make machined construction increasingly difficult.

However, the laminated PCB approach also introduces new design challenges:

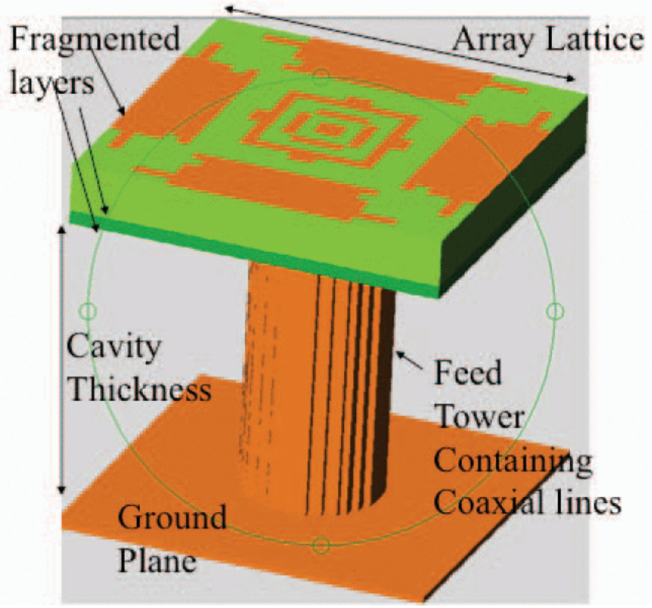

Figure 7.2: Traditional fragmented aperture array construction. Fragmented layers are printed on circuit board material and separated by foam spacers above a machined aluminum ground plane. Feed towers enclose differential coaxial lines that connect to the dual-polarized elements [1].

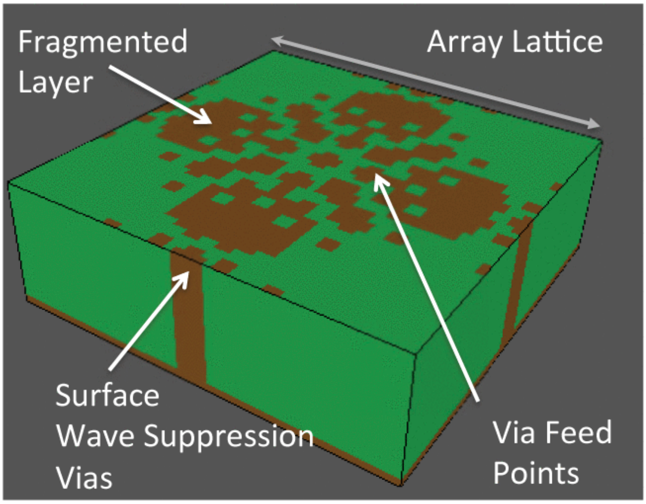

Figure 7.3: Laminated printed circuit board (PCB) fabrication approach. The entire antenna—fragmented layers, dielectric spacers, and ground plane—is built up as a multi-layer PCB stack. Element feeds are plated vias near the center of each unit cell, and surface wave suppression vias are placed near the perimeter [1].

- **Surface wave suppression.** Thick dielectric substrates can support surface waves that cause scan blindness—a condition where the array becomes poorly matched at specific combinations of frequency and scan angle. To prevent this, surface wave suppression vias must be incorporated into the laminated stack-up as an integral part of the design. These vias are visible near the perimeter of the unit cell in Figure 7.3.

- **Dielectric loading.** The presence of dielectric material throughout the cavity between the radiating layers and the ground plane changes the effective wavelength and alters the impedance environment seen by the antenna elements. The design process must account for the specific dielectric properties of the PCB substrate materials.

- **Modified feed structures.** The feeds are no longer simple 50 Ω coaxial lines in air; they are closely spaced vias in a dielectric environment. The characteristic impedance and coupling behavior of these via-based feeds must be accurately modeled during the design process.

All of these effects are captured naturally by the FDTD simulation used in the genetic algorithm design process, so no special analytical treatment is required. The full-wave simulation simply includes the dielectric layers, the vias, and the complete PCB stack-up geometry, and the optimizer works with the true electromagnetic behavior of the structure.

7.3 Spectral-Domain FDTD for Wide Scan Optimization

7.3.1 Limitations of Standard Periodic Boundary Conditions

The design process for fragmented aperture array elements uses a genetic algorithm to optimize a single unit cell of the array, terminated by periodic boundary conditions (PBC) that simulate an infinite array environment. The FDTD method is ideal for this purpose because a single time-domain simulation produces the full frequency-domain response across the entire design bandwidth.

In the standard FDTD implementation of periodic boundary conditions, the PBC is applied as a wrap-around boundary at the edges of the unit cell. This approach naturally models the infinite array at broadside (zero scan angle) and provides the complete broadband response in a single simulation. This is the approach that was used to design the earlier fragmented aperture arrays, including the 33:1 bandwidth design.

However, standard broadside-only PBC does not provide information about the array's scan performance. The scan volume narrowing observed in the 33:1 array (Figure 6.20) was a consequence of optimizing only for broadside performance: the genetic algorithm had no information about off-broadside behavior, so it had no mechanism to prevent scan volume degradation.

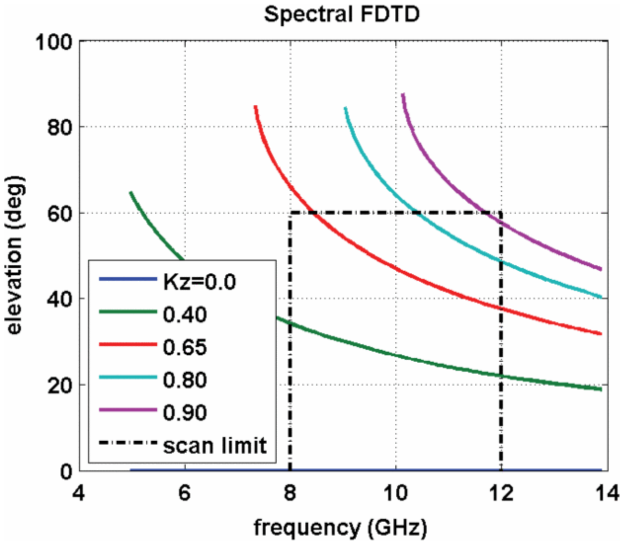

Figure 7.4: Elevation angle versus frequency contours for several normalized transverse wavenumbers K_z used in the spectral-domain FDTD design process. The dashed box indicates the target 8–12 GHz, $\pm 60^\circ$ scan volume. Because the contours are not constant versus frequency, the transverse wavenumber values are chosen to provide denser sampling at higher frequencies and larger scan angles, where scan problems are most likely to occur [1].

7.3.2 The Spectral-Domain FDTD Approach

To incorporate scan performance into the design process, a spectral-domain FDTD approach to periodic boundary conditions [3] was integrated into the design suite. In the spectral-domain formulation, the FDTD simulation is performed at a fixed transverse wavenumber (k_x, k_y) rather than at a fixed scan angle (θ, ϕ). The PBC is still implemented as a wrap-around boundary, but the constant transverse wavenumber assumption means that the effective scan angle is frequency dependent.

Figure 7.4 illustrates this relationship. Each curve shows the elevation angle as a function of frequency for a specific normalized transverse wavenumber K_z. The dashed box indicates the target design space: the 8–12 GHz X-band with a scan volume of $\pm 60^\circ$. Because the contours are not horizontal (i.e., constant angle versus frequency), a single spectral-domain simulation does not map to a single scan angle. Instead, each simulation sweeps through different scan angles as it sweeps through frequency.

7.3.3 Sampling the Scan Volume

The key to successful wide-scan design is to strike the right balance between sampling the scan volume sufficiently and not performing too many simulations (since each simulation adds to the computational cost of every fitness evaluation in the genetic algorithm). The exact number of spectral-domain simulations needed is problem specific, but a useful observation guides the selection of wavenumber samples: poor scan performance, when it occurs, typically manifests at higher frequencies and larger scan angles.

As shown in Figure 7.4, the transverse wavenumber values are chosen to concentrate the sampling in the region of the scan volume where problems are most likely—the upper-right portion of the frequency-angle space. The $K_z = 0$ contour corresponds to broadside at all frequencies, while progressively larger values of K_z sweep through progressively larger scan angles. By including several such simulations in the fitness evaluation, the genetic algorithm receives information about both broadside and off-broadside performance and can optimize accordingly.

This approach adds computational cost to each fitness evaluation, since multiple spectral-domain FDTD simulations must be run for each candidate element design. However, the cost is manageable because the number of required wavenumber samples is typically small (on the order of five to ten), and each individual simulation is no more expensive than the single broadside simulation used in the previous design approach.

7.4 Example: Whole X-Band Array Element

7.4.1 Design Parameters

To illustrate the improved design process and the PCB fabrication approach, a whole X-band (8–12 GHz) phased array element was designed with a target scan volume of $\pm 60^\circ$ in all azimuth planes. The X-band was chosen because it represents a practical frequency range for military radar and communications applications, and because typical printed circuit board elements (e.g., microstrip patches) are not broadband enough to cover the full 8–12 GHz band in a low-profile PCB form factor.

The design begins by selecting the array lattice constant to prevent grating lobes at the maximum scan angle and highest operating frequency:

$$\frac{s}{\lambda_{\text{high}}} = \frac{1}{1+\sin\theta_{\max}} = 0.536 \quad \text{for } \theta_{\max} = 60^\circ \tag{7.1}$$

where s is the element spacing and λ_{high} is the free-space wavelength at the highest operating frequency (12 GHz).

Next, the number of fragmented pixels across the unit cell is selected using the rules of thumb described in Chapter 3: typically 20–30 pixels across the unique quadrant of the element (as illustrated in Figure 7.3). The element is then designed using the genetic algorithm approach with the spectral-domain FDTD providing the fitness evaluation at the normalized K_z and K_y values shown in Figure 7.4.

7.4.2 Broadside Performance

After the genetic algorithm completes the design, the element performance is verified by simulating a large finite array—in this case, 21×21 elements. The embedded element realized gain is obtained by computing the gain of the central element while all surrounding elements are terminated in matched loads.

Figure 7.5 shows the broadside embedded element realized gain as a function of frequency. The gain is within approximately 0.2 dB of the uniform aperture area limit across the entire 8–12 GHz design band. This near-ideal aperture efficiency demonstrates that the PCB fabrication approach, with its dielectric loading and via-based feeds, does not compromise the ability of the fragmented aperture design to efficiently utilize the available aperture area.

7.4.3 Impedance Match

Figure 7.6 compares the VSWR for the embedded element with the VSWR for the infinite array scanned at broadside. Both are well below 2:1 across the design band, but they are not identical. The difference arises because the infinite-array VSWR includes the mutual coupling from all neighboring elements, whereas the embedded element VSWR reflects the impedance seen at the terminals of a single element in the finite array environment.

An important point for phased array design is that it is the *scanned* VSWR (the infinite-array value) that must be kept small, because this is the impedance that the element presents to the beamforming network during scanning. The embedded element VSWR may actually be higher than the scanned VSWR when significant mutual coupling is being exploited to improve the scanned impedance match. This is another example of how the fragmented aperture design approach embraces mutual coupling rather than attempting to minimize it.

7.4.4 Scan Performance

Figures 7.7 through 7.9 show the embedded element realized gain as a function of both azimuth and elevation angle at three frequencies spanning the X-band: 8 GHz (bottom), 10 GHz (middle), and 12 GHz (top). These plots are obtained by simulating the 21×21 finite array with the central element excited and all others terminated, then computing the realized gain pattern of the central element.

At 8 GHz (Figure 7.7), the scan volume is excellent, with strong realized gain extending well beyond 60° in both azimuth and elevation. At 10 GHz (Figure 7.8), the wide scan volume is maintained. At 12 GHz (Figure 7.9), there is some slight degradation in the scan volume in the azimuth direction, but the overall scan performance still substantially exceeds ±60°.

This is a dramatic improvement over the scan performance of the 33:1 array element (Figure 6.20), which showed significant scan volume narrowing to only ±40° in the upper portion of its operating band. The key difference is that the spectral-domain FDTD design process gives the genetic algorithm direct information about the scan performance, allowing it to optimize for wide scan and wide bandwidth simultaneously.

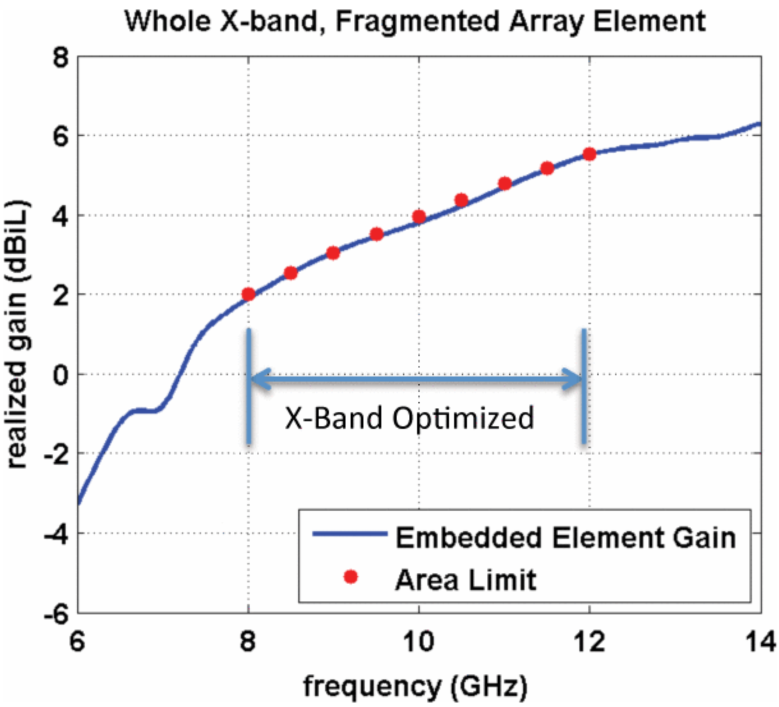

Figure 7.5: Broadside embedded element realized gain for the whole X-band fragmented array element (blue line) compared to the uniform aperture area limit (red dots). The realized gain is within approximately 0.2 dB of the theoretical limit across the 8–12 GHz design band [1].

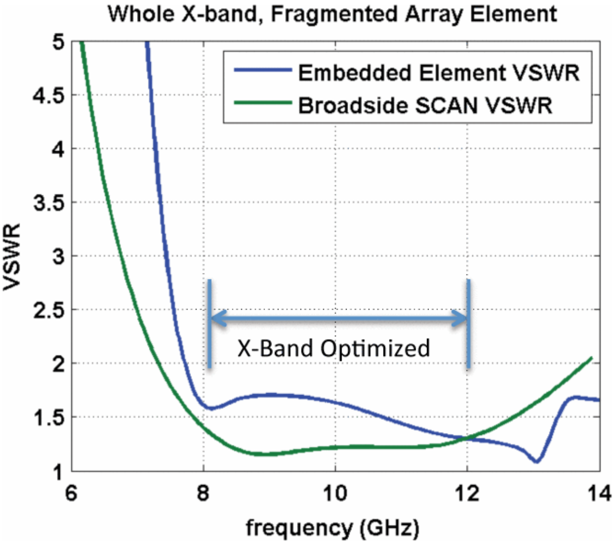

Figure 7.6: VSWR comparison for the X-band fragmented array element. The embedded element VSWR (blue line) and the broadside infinite-array scan VSWR (green line) are both below 2:1 across the design band. The difference between the two reflects the influence of mutual coupling from neighboring elements [1].

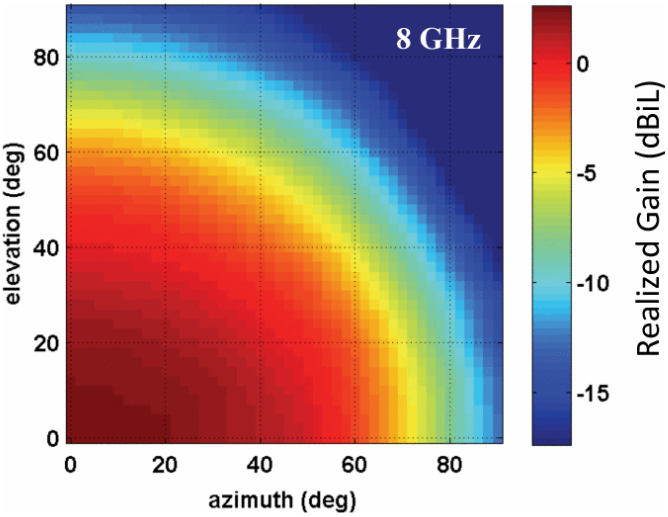

Figure 7.7: Embedded element realized gain at 8 GHz as a function of azimuth and elevation angle for the V-pol feed. The wide scan volume is evident, with usable gain extending well beyond 60° in both planes [1].

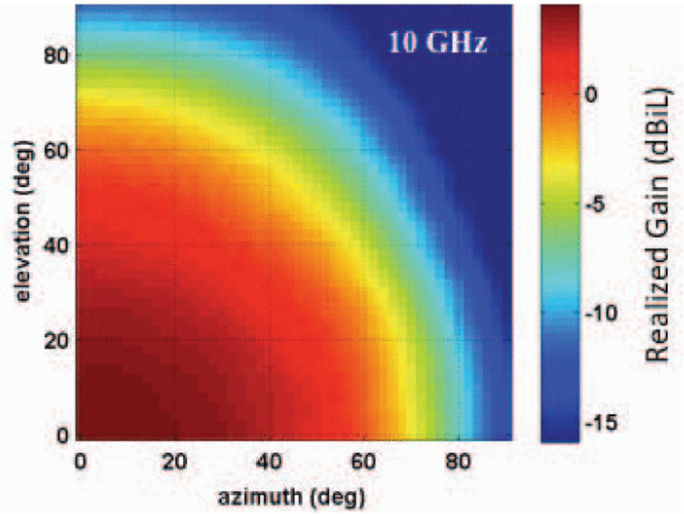

Figure 7.8: Embedded element realized gain at 10 GHz. The wide scan volume (> ±60°) is maintained at the center of the X-band [1].

7.5 Discussion

7.5.1 Bandwidth–Efficiency–Scan Trade Space

The results of this chapter highlight an important trade space in fragmented aperture array design. The 33:1 bandwidth array described in Chapter 6 achieved extraordinary bandwidth but required a lossy broadband screen backplane to suppress ground-plane nulls, limiting the array to receive-only applications. The X-band element described in this chapter achieves a more modest bandwidth (approximately 1.5:1) but does so without the need for a lossy backplane, enabling high-efficiency, transmit-capable operation.

This trade-off is a fundamental consequence of the physics. As discussed in Chapter 6, the broadband screen backplane uses resistive card (r-card) layers to prevent the half-wave nulls that occur when the aperture-to-ground-plane spacing is an integer multiple of $\lambda/2$. For very large bandwidths, these nulls cannot be avoided without some form of loss. For moderate bandwidths (on the order of 2:1 to 3:1), the aperture thickness can be chosen so that no half-wave nulls fall within the operating band, eliminating the need for lossy backplane layers entirely.

7.5.2 PCB Design Rules

The design rules and scaling relationships discussed in Chapter 6 (Section 6.6) apply to the PCB approach as well, with one important modification. The $\lambda/12$ rule of thumb

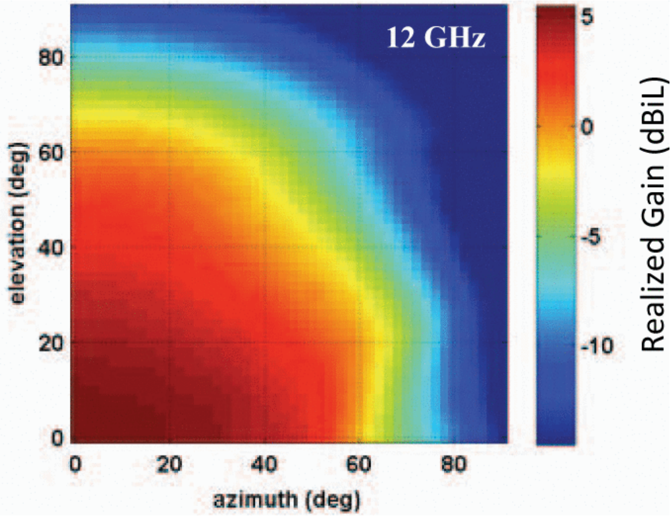

Figure 7.9: Embedded element realized gain at 12 GHz. Some slight reduction in the scan volume is visible in the azimuth direction, but the overall scan volume still substantially exceeds ±60° [1].

for cavity thickness (Figure 6.21) was derived from air-filled cavity designs. For the PCB approach, the cavity is dielectrically loaded, so the relevant wavelength is the wavelength in the substrate material. The modified rule of thumb is:

$$T \approx \frac{\lambda_{\text{substrate}}}{12} = \frac{\lambda_0}{12\sqrt{\epsilon_r}} \tag{7.2}$$

where λ_0 is the free-space wavelength at the lowest operating frequency and ϵ_r is the relative permittivity of the substrate. This dielectric loading results in a physically thinner antenna, which is one of the practical benefits of the PCB approach.

[TODO: Include a thickness vs. frequency chart for PCB designs analogous to the air-filled cavity chart in Chapter 6, once enough PCB designs have been completed to establish the trend.]

7.6 Summary and Conclusions

This chapter described three advances that address key limitations of earlier fragmented aperture array designs:

1. **Spectral-domain FDTD for wide scan optimization.** By incorporating a spectral-domain FDTD approach to periodic boundary conditions into the genetic algorithm design process, the optimizer gains direct information about the array's scan performance at multiple angles. This enables the design of elements with scan volumes exceeding $\pm 60^\circ$ across the full operating bandwidth, a significant improvement over designs optimized only at broadside.

2. **Laminated PCB fabrication.** Replacing the traditional machined aluminum construction with a laminated printed circuit board approach yields a more integrated, more easily mass-produced, and potentially lower-cost antenna, with particular advantages at X-band and higher frequencies where machining tolerances are demanding.

3. **High-efficiency, transmit-capable designs.** For applications with moderate bandwidth requirements (on the order of 1.5:1 to 3:1), the antenna can be designed without a lossy broadband screen backplane, resulting in high aperture efficiency suitable for transmit applications.

These advances were demonstrated through the design of a whole X-band (8–12 GHz) phased array element that achieves broadside gain within 0.2 dB of the uniform aperture area limit and a scan volume exceeding $\pm 60^\circ$ across the design band, all in a laminated PCB form factor.

References

[1] J. G. Maloney, B. N. Baker, R. T. Lee, G. N. Kiesel, and J. J. Acree, "Wide Scan, Integrated Printed Circuit Board, Fragmented Aperture Array Antennas," in Proc. 2011 IEEE International Symposium on Antennas and Propagation, Spokane, WA, July 2011, pp. 1965–1968.

[2] J. G. Maloney, M. P. Kesler, P. H. Harms, and G. S. Smith, Fragmented Aperture Antennas and Broadband Ground Planes, U.S. Patent No. 6,323,809 B1, November 27, 2001.

[3] A. Aminian and Y. Rahmat-Samii, "Spectral FDTD: A novel technique for the analysis of oblique incident plane wave on periodic structures," IEEE Trans. Antennas Propag., vol. 54, no. 6, pp. 1818–1825, June 2006.

[4] C. A. Balanis, Modern Antenna Handbook, Chapter 12, Wiley, 2008.

Chapter 8

Reconfigurable Fragmented Aperture Arrays

8.1 Introduction

The preceding chapters have treated the fragmented aperture antenna as a fixed structure: once the genetic algorithm determines the optimal pixel configuration and the antenna is fabricated, the conducting pattern is permanent. Chapter 5 demonstrated that reconfigurable single-element fragmented apertures can dynamically change their frequency, beam direction, and polarization by switching pixel connections. Chapter 7 showed that fixed fragmented array elements, when designed using spectral-domain FDTD, can achieve scan volumes exceeding $\pm 60^\circ$ across the operating bandwidth.

This chapter describes the convergence of these two ideas: a phased array in which the fragmented aperture element is electronically reconfigured as the beam is steered. The motivation is to overcome a fundamental limitation of any phased array with fixed element geometry—the scan-dependent degradation of the embedded element pattern, which causes the array gain to fall off faster than the physical aperture projection as the beam is steered away from broadside.

8.2 The Scan Loss Problem

8.2.1 Embedded Element Pattern and Scan Rolloff

In a phased array, the gain in any direction is determined by the product of the array factor and the embedded element pattern (EEP). The array factor can be steered to any angle within the visible region by adjusting the element phase weights, and in the absence of grating lobes, the array factor peak tracks the commanded steer direction with negligible loss. The embedded element pattern, however, is a property of the fixed element geometry and its electromagnetic environment—the mutual coupling to neighboring elements, the ground plane, and the feed structure. For a well-designed array element, the EEP typically peaks at or near broadside and rolls off with increasing scan angle.

The physical area of the aperture projected onto the scan direction decreases as $\cos\theta$, where θ is the scan angle measured from broadside. This projected-area loss is a fundamental geometric consequence that no antenna design can overcome: a planar aperture of area A presents an effective collecting area of $A\cos\theta$ when viewed from angle θ. For an ideal element whose EEP exactly followed the projected-area limit, the array gain at scan angle θ would be

$$G(\theta) = G_0 \cos\theta \tag{8.1}$$

where G_0 is the broadside gain. This represents the best possible performance for a planar phased array; no fixed-element design can exceed this limit.

In practice, however, the embedded element pattern of a fixed-geometry array element rolls off faster than $\cos\theta$. The element pattern exhibits frequency-dependent features—ripples, nulls, and asymmetries—that arise from the complex electromagnetic interactions within and between elements. The scan loss is compounded by impedance mismatch: as the beam is steered, the active impedance at each element changes due to the angle-dependent mutual coupling, degrading the impedance match and further reducing the realized gain.

8.2.2 The $\cos^n\theta$ Model

In radar system engineering, the scan loss of a phased array is often modeled as a power of $\cos\theta$:

$$G(\theta) = G_0 \cos^n\theta \tag{8.2}$$

where the exponent n captures the combined effects of projected area ($n = 1$), element pattern rolloff, and scan impedance mismatch. For an ideal element, $n = 1$. In practice, n ranges from 1.3 to 2.5 or higher, depending on the element type, bandwidth, and frequency within the operating band. A value of $n = 1.5$ is a common first approximation for well-designed elements. Radar textbooks often use $n = 2$ as a representative model.

The consequences of $n > 1$ are significant. At $\theta = 60^\circ$, the difference between $\cos^1(60^\circ) = 0.5$ (-3.0 dB) and $\cos^2(60^\circ) = 0.25$ (-6.0 dB) is 3 dB—a factor of two in power. For a radar system, this 3 dB of additional scan loss translates directly into reduced detection range: the fourth-root dependence of radar range on power means that each additional dB of scan loss reduces the detection range by approximately 6%.

Table 8.1 quantifies the impact for $n = 1$ and $n = 2$. At moderate scan angles (30°–45°), the additional loss from $n = 2$ versus $n = 1$ is 1–3 dB. At 60°, the penalty doubles to 6 dB. At very wide scan angles approaching 70°, the $n = 2$ element pattern has rolled off to -18.7 dB—nearly 10 dB worse than the projected-area limit. For systems that require wide-angle coverage, reducing the scan loss exponent from $n \approx 2$ to $n \approx 1$ is a transformative improvement.

8.2.3 Why Fixed Elements Cannot Achieve $n = 1$

The $\cos\theta$ projected-area limit is the best that any fixed-geometry element can achieve, and in practice no fixed element achieves it uniformly across frequency and angle. The

Table 8.1: Scan loss at selected angles for various values of the scan loss exponent n. The additional loss beyond the ideal $\cos\theta$ projection is shown in the rightmost column.

θ	$\cos^1\theta$ (dB)	$\cos^2\theta$ (dB)	Additional loss (dB)
$0°$	0.0	0.0	0.0
$30°$	-1.2	-2.5	1.2
$45°$	-3.0	-6.0	3.0
$60°$	-6.0	-12.0	6.0
$70°$	-9.3	-18.7	9.3

fundamental reason is that a fixed conducting pattern supports a fixed set of current modes. These modes produce a radiation pattern that is optimized (by the GA) for a particular set of conditions—typically broadside or a weighted combination of broadside and a few scan angles (as in Chapter 7). When the beam is steered to an angle that was not explicitly optimized, the fixed current modes radiate with a pattern whose peak does not track the scan direction.

The spectral-domain FDTD approach described in Chapter 7 mitigates this problem by sampling the scan volume during the design process, but it does not eliminate it. The optimizer must balance broadside performance against scanned performance, and the fixed element geometry represents a single compromise. At any given frequency and scan angle, a design specifically optimized for that condition would outperform the compromise design.

8.3 Reconfigurable Array Elements for Scan Management

8.3.1 Concept

The solution suggested by this analysis is straightforward: do not require the element to be a single compromise design. Instead, use a reconfigurable element—a fragmented aperture array element whose pixel configuration can be electronically changed—and re-optimize the configuration for each combination of operating frequency and beam steer direction.

When the array is commanded to steer to angle θ_s, the element is reconfigured to a pixel pattern that has been pre-optimized for that scan angle. The embedded element pattern of the reconfigured element has its peak near θ_s rather than at broadside, so the element pattern does not fight the array factor. The scan loss approaches the $\cos\theta$ projected-area limit because the only remaining loss mechanism is the geometric reduction of the effective aperture area.

This concept can be understood by analogy with the Agile Aperture Antenna of Chapter 5. In that chapter, different switch configurations were designed for different objectives: one for a broadside beam, another for an end-fire beam. The reconfigurable array concept is the same principle applied to every element of a phased array, with the objective for each configuration being maximum embedded element gain in the commanded steer direction.

8.3.2 Design Methodology

The design procedure for a reconfigurable array element follows naturally from the tools developed in earlier chapters. For each desired scan angle θ_s (and, if needed, each frequency sub-band), the genetic algorithm is run in the infinite-array environment with periodic boundary conditions appropriate for that scan angle. The fitness function rewards embedded element realized gain in the direction θ_s, impedance match at the scanned active impedance, and bandwidth coverage.

For a set of M discrete scan angles $\{\theta_1, \theta_2, \ldots, \theta_M\}$, the design process produces M corresponding pixel configurations $\{P_1, P_2, \ldots, P_M\}$. These configurations are stored in a look-up table. When the array controller commands a beam steer to angle θ_s, the appropriate pixel configuration P_s is loaded onto every element simultaneously with the phase weights that steer the array factor.

The spectral-domain FDTD approach of Chapter 7 is used for each design, but with an important distinction. In Chapter 7, the optimizer sampled multiple scan angles simultaneously and sought a single design that performed acceptably across the full scan volume. Here, each optimization focuses on a *single* target scan angle (or a narrow range around it), freeing the optimizer to find the best possible design for that specific condition. The result is a family of designs, each of which is individually superior at its target angle to any single fixed design.

8.3.3 Pre-Computed Design Library

The practical implementation requires a library of pre-computed element configurations spanning the desired scan volume. The library is indexed by scan angle (and possibly frequency), and the array controller selects the appropriate configuration in real time as the beam is steered.

The number of entries in the library depends on the angular resolution required. If the element performance varies slowly with scan angle—as is typical for electrically small pixels—then a coarse angular grid may suffice, with interpolation or nearest-neighbor selection for intermediate angles. Preliminary design studies suggest that scan angle steps of 5° to 10° provide adequate coverage, resulting in a library of approximately 20–50 configurations for hemispherical scan coverage.

[INSERT FIGURE: Conceptual diagram showing a library of pre-computed pixel configurations indexed by scan angle, with the array controller selecting the appropriate configuration for the commanded steer direction.]

For a two-dimensional scan volume, the library must cover both azimuth and elevation, but the symmetry of a square lattice element reduces the required entries. An element with four-fold symmetry requires configurations covering only one octant of the upper hemisphere; the remaining scan directions are obtained by 90° rotations of the element pattern.

8.4 Design Examples

[NOTE: The design examples in this section are based on work performed for the DARPA Arrays at Commercial Timescales (ACT) program. The original design data is being located and, if necessary, will be regenerated using the current design tools. The results described below represent the scope and character of the designs; specific numerical values and figures will be updated when the data is confirmed.]

8.4.1 Frequency Reconfiguration

A first set of design examples demonstrated the ability of a reconfigurable fragmented array element to tune across multiple frequency bands. The element geometry and lattice were held constant, and the pixel configuration was optimized separately for operation in several frequency bands spanning a wide range. In each case, the optimizer was able to find a pixel configuration that produced a well-matched, broadside element with gain near the aperture area limit for the target band.

This result is not surprising given the experience from Chapter 5, where very different switch configurations produced antennas operating in different frequency ranges. What is significant is that the same behavior extends to array elements operating in the infinite-array mutual-coupling environment. The pixel configuration adjusts not only the resonant behavior of the individual element but also the inter-element coupling, effectively re-tuning the array's electromagnetic environment for each frequency band.

[INSERT FIGURE: Several pixel configurations for the same array element, each optimized for a different frequency band. The designs should look visually distinct, illustrating that different frequencies require fundamentally different conducting patterns.]

[INSERT FIGURE: Embedded element realized gain versus frequency for each configuration, showing that each design provides near-aperture-limited gain within its target band.]

8.4.2 Scan Angle Reconfiguration

The more compelling set of design examples demonstrated scan angle reconfiguration. The element was optimized for a fixed frequency band at several discrete scan angles: broadside ($0°$), $30°$, $45°$, $60°$, and beyond.

At each scan angle, the optimizer produced a pixel configuration that placed the embedded element pattern peak near the target angle. Figure 8.1 illustrates the concept: the conducting pattern changes as the target scan angle increases, reflecting the need for different current distributions to radiate efficiently in different directions.

[INSERT FIGURE: Pixel configurations for $\theta = 0°, 30°, 45°, 60°$, showing the evolution of the conducting pattern with scan angle.]

The key result was that the embedded element pattern of each reconfigured design tracked the commanded scan angle, maintaining gain near the $\cos\theta$ projected-area limit out to $60°$ and beyond. This is in contrast to a fixed-element design, which would show progressively degraded gain beyond $45°$.

Figure 8.1: Pixel configurations for the reconfigurable array element at four scan angles. The conducting pattern changes significantly with scan angle, reflecting the different current distributions required to maximize radiation in the target direction.

[INSERT FIGURE: Overlay of embedded element patterns for each reconfigured design, showing the pattern peak tracking the scan angle. A fixed-element pattern should be included for comparison.]

[INSERT FIGURE: Scan loss versus angle, comparing the reconfigurable element ($n \approx 1$) to a fixed element ($n \approx 1.5$–2) and the ideal $\cos\theta$ limit. This is the central result of the chapter.]

It was particularly noteworthy that the reconfigured elements maintained good performance at scan angles beyond 60°. At these extreme angles, fixed elements typically exhibit severe pattern degradation and impedance mismatch. The reconfigurable element avoids these problems because its pixel pattern is specifically tailored for the wide-angle electromagnetic environment, including the dramatically different mutual coupling that occurs at extreme scan angles.

8.5 Scan Loss Reduction: Physical Interpretation

The improvement from reconfigurable scan management can be understood through several complementary perspectives.

8.5.1 Current Distribution Perspective

When a fixed-element array is scanned to a large angle, the current distribution on each element does not change—only the relative phases between elements change. The element still supports the same modes it was designed for at broadside, and these modes do not radiate efficiently in the scanned direction.

In the reconfigurable element, changing the pixel configuration changes the conducting pattern, which changes the allowed current modes. The optimizer finds a pattern that supports current distributions that radiate efficiently toward the target angle. In essence, the element is not merely being phased to a new direction; it is being *redesigned* for that direction.

8.5.2 Impedance Perspective

As a phased array is scanned, the active impedance at each element port changes due to the angle-dependent mutual coupling between elements. For fixed elements, this impedance change is an uncontrollable consequence of the element geometry and the scan angle. At certain combinations of frequency and scan angle, the active impedance can deviate dramatically from the matched condition, causing significant mismatch loss.

Reconfiguring the element pixel pattern changes the mutual coupling between elements, because the electromagnetic fields in the inter-element region depend on the conducting pattern. The optimizer can therefore adjust the pixel pattern to maintain a good impedance match at each scan angle, compensating for the scan-dependent impedance variation that afflicts fixed designs.

8.5.3 Scan Blindness Avoidance

Scan blindness occurs when the active impedance of the array element becomes purely reactive at a specific combination of frequency and scan angle, typically due to the excitation of a surface wave on the array aperture. For fixed-geometry elements, scan blindness can be avoided through careful design (as discussed in Chapter 7), but the available design space is limited by the requirement that the single fixed geometry must also perform well at all other scan angles.

Reconfigurable elements provide additional degrees of freedom to avoid scan blindness. If a particular pixel configuration excites a surface wave at the current operating frequency and scan angle, the configuration can be changed to one that does not. The pixel pattern optimized for each scan angle is inherently free of scan blindness at that angle, because the optimizer would reject any configuration that exhibited it.

8.6 System Considerations

8.6.1 Switching Speed

The practical utility of reconfigurable scan management depends on the switching speed of the pixel reconfiguration mechanism. For electronically steered arrays that change beam direction on a pulse-to-pulse basis (as in modern radar systems), the pixel configuration must be updated within the beam dwell time—typically on the order of microseconds.

The MEMS-based switches discussed in Chapter 5 have switching times of 1–10 μs, which is marginal for pulse-to-pulse beam steering. Solid-state switches (PIN diodes, FETs) are significantly faster, with switching times in the nanosecond range, but they introduce higher insertion loss and nonlinearity. Phase-change materials such as VO2 offer a potential path to fast, low-loss switching, as discussed in Chapter 5.

For applications that do not require pulse-to-pulse agility—for example, communications systems that maintain a fixed beam direction for extended periods—the switching speed requirement is relaxed, and even slower reconfiguration mechanisms may be acceptable.

8.6.2 Calibration

In a conventional phased array, calibration accounts for element-to-element variations in gain and phase. In a reconfigurable array, the calibration must also account for variations between pixel configurations. Each entry in the design library corresponds to a different electromagnetic state of the array, and the calibration coefficients may differ for each state.

A practical calibration approach would characterize the array at each configuration in the design library, storing a separate set of calibration weights for each entry. When the array switches configurations, the corresponding calibration weights are applied.

8.6.3 Design Library Computation

The computational cost of generating the design library is a one-time expense. For a library of M scan angles, M independent genetic algorithm optimizations must be performed. Each optimization has the same computational cost as a single fixed-element design. For the spectral-domain FDTD approach, each design requires on the order of five to ten FDTD simulations per fitness evaluation, and the GA typically converges in 500–2000 generations with a population size of 100–500.

This amounts to a total computational investment of M times the cost of a single fixed design. For $M = 50$ (hemispherical coverage at 5° steps, exploiting symmetry), this is a factor of 50 increase—substantial but well within the capabilities of modern computing clusters, particularly since the optimizations for different scan angles are completely independent and can be run in parallel.

The machine learning methods discussed in Chapter 9 offer a path to dramatically reducing this computational cost. A surrogate model trained on the initial designs could predict the performance of candidate pixel configurations without running full FDTD simulations, accelerating the optimization by orders of magnitude.

8.7 The DARPA ACT Program

8.7.1 Motivation and Program Goals

Today's electromagnetic systems rely on antenna arrays for capabilities that are critical to a wide variety of military applications: multiple beam forming and electronic steering for communications, signal intelligence (SIGINT), radar, and electronic warfare. However, wider adoption of phased arrays has been limited by two persistent problems: lengthy system development times and the inability to upgrade already-fielded capabilities. These problems are exacerbated by the fact that military electronics have evolved at a far slower cadence than commercial electronics, and the performance gap between the RF capabilities of fielded military systems and the continuously improving digital electronics surrounding them continues to widen.

The traditional approach to phased array development—in which each new system is a monolithic, custom design—has resulted in development cycles exceeding a decade and static life cycles of 20 to 30 years, sustained only through costly service-life extension programs. As DARPA program manager Bill Chappell observed, "Current DoD array development programs can take more than a decade and cost tens of billions of dollars" [4].

The DARPA Arrays at Commercial Timescales (ACT) program was announced in February 2013 to push past these traditional barriers. Rather than continuing to pursue monolithic, application-specific array designs, ACT sought to develop shared hardware technologies—a digitally interconnected building block from which larger systems could be formed, scalable and customizable for each application without requiring a full redesign. The program targeted a 30–40% reduction in nonrecurring engineering costs and a fundamental decrease in time-to-deployment for both new systems and upgrades to existing platforms.

The ACT program was organized around three technical areas:

1. **Common building block for RF arrays:** A standardized digital module comprising 80 to 90 percent of an array's core functionality, designed for insertion into a wide range of applications. By leveraging commercial off-the-shelf (COTS) components and commercial CMOS semiconductor technology, this common module would dramatically reduce both development time and per-unit manufacturing cost. Northrop Grumman developed the Integrated Multi-use Phased Array Common Tile (IMPACT) under this thrust.

2. **Reconfigurable electromagnetic interface:** Aperture technology connecting the digital electronics to the radiated signals, capable of spanning S-band to X-band frequencies (and points between) for a wide variety of antenna characteristics. This area aligns directly with the reconfigurable fragmented aperture concept described in this chapter: a pixel-based aperture that can be electronically reconfigured for different frequency bands, scan angles, and operating modes.

3. **Over-the-air coherent array aggregation:** Technology enabling distributed arrays across multiple platforms to function as a single, coherent phased array system. This capability, which extended earlier work from DARPA's Precision Electronic Warfare (PREW) program, would allow, for example, individual radar systems on the ships of a carrier group to coordinate as an integrated distributed array.

A central goal of the ACT program was to enable next-generation, multifunctional active electronically scanned array (AESA) systems capable of simultaneous radar, electronic warfare, and communications functions from a single aperture. The program successfully transitioned to the ACT-IV (Integration and Validation) phase, demonstrating multifunctional array systems capable of simultaneous radar and communications operations.

8.7.2 Georgia Tech's Role in ACT

In January 2013, Georgia Tech researchers were awarded a $2.7 million DARPA grant under the ACT program to develop advanced antenna technologies [4]. The project aimed to accelerate the design and fabrication of phased array antennas by leveraging commercial manufacturing processes, reducing time and costs for defense applications. Georgia Tech researchers supported the program alongside prime contractors including Northrop Grumman and Boeing, contributing to advanced antenna design and integration of common-module architectures.

The Georgia Tech Research Institute (GTRI) developed the Advanced Phased Array Antenna Technology (APAT) system under this effort. The APAT system is an all-digital, modular antenna designed to process signals directly on the antenna elements using radio frequency system-on-chip (RFSoC) technology and high-speed direct RF-sampling digital beamforming. This element-level digital architecture enables the full flexibility of digital beamforming—arbitrary beam patterns, simultaneous multiple beams, and adaptive interference cancellation—at each element.

The APAT represented the largest all-digital antenna system developed for tracking applications, enabling simultaneous, multi-stream data capture for hypersonic flight testing. The all-digital architecture eliminates the analog beamforming network that constrains conventional arrays, allowing the beam patterns and signal processing to be defined entirely in software and updated without hardware modification. The system achieved extremely low latency—on the order of milliseconds—in edge processing for phased-array antenna applications, enabling real-time adaptive beamforming and signal classification.

GTRI's work also contributed to the broader effort in 3D heterogeneous integration (3DHI) of microelectronics, partnering with the Texas Institute for Electronics on a large-scale Department of Defense initiative to advance the packaging and integration technologies that are critical for next-generation common-module array architectures.

8.7.3 Connection to Reconfigurable Fragmented Apertures

The reconfigurable fragmented aperture array concept was proposed as the radiating element technology for the ACT architecture. The combination of a reconfigurable pixel aperture (providing scan-optimized embedded element patterns) with element-level digital processing (providing arbitrary amplitude and phase control) would yield a phased array with performance that cannot be achieved by either technology alone: $\cos\theta$ scan loss across the full scan volume, multi-octave bandwidth, and real-time multifunctional capability.

The ACT program's second technical area—reconfigurable electromagnetic interfaces spanning S-band to X-band—is precisely the application for which the fragmented aperture approach is designed. A single fragmented aperture element, with sufficient pixel resolution and switching capability, can be reconfigured to operate across this entire frequency range. Combined with the common-module digital architecture, this provides the flexible, upgradable RF system that the DoD seeks: one that can be updated as quickly as commercial electronics evolve.

[PLACEHOLDER: Specific design results from the ACT proposal—including element configurations optimized for multiple frequency bands and scan angles, demonstrating scan beyond $60°$—will be included when the original data is located or the designs are regenerated.]

8.8 Summary and Conclusions

This chapter has described a reconfigurable fragmented aperture array concept that addresses the scan loss problem inherent in all phased arrays with fixed element geometry. The key findings are:

1. **Scan loss in fixed-element arrays exceeds the projected-area limit.** The embedded element pattern of a fixed-geometry element rolls off faster than $\cos\theta$, resulting in scan loss that is well modeled by $\cos^n\theta$ with $n = 1.3$–2.5. At $60°$, this represents 2–6 dB of excess loss beyond the unavoidable 3 dB of projected-area loss.

2. **Reconfigurable elements reduce the scan loss exponent to near unity.** By re-optimizing the pixel configuration for each scan angle, the embedded element

pattern peak is made to track the beam steer direction, and the scan loss approaches the $\cos\theta$ projected-area limit ($n \approx 1$).

3. **Reconfigurable elements provide wide-angle scanning beyond $60°$.** Fixed elements typically exhibit severe performance degradation at extreme scan angles. Reconfigurable elements, optimized specifically for each angle, maintain good impedance match and pattern quality to $60°$ and beyond.

4. **Reconfigurable elements naturally avoid scan blindness.** The pixel configuration optimized for each scan angle is inherently free of scan blindness at that angle, providing additional robustness compared to fixed designs that must avoid scan blindness across the entire scan volume simultaneously.

5. **A pre-computed design library makes the concept practical.** The computational cost of optimizing a library of 20–50 scan-angle configurations is a one-time investment that scales linearly with the number of configurations and can be parallelized.

The combination of this reconfigurable scan management with the wide-bandwidth capabilities demonstrated in Chapters 6 and 7 suggests the possibility of a phased array that achieves multi-octave bandwidth with $\cos\theta$ scan loss across the entire scan volume—performance that no fixed-element array can match.

References

[1] W. Croswell, T. Durham, M. Jones, D. Schaubert, P. Friederich, and J. G. Maloney, “Wideband Arrays,” in *Modern Antenna Handbook*, C. A. Balanis, Ed., Hoboken, NJ: Wiley, 2008, ch. 12.

[2] J. G. Maloney, B. N. Baker, R. T. Lee, G. N. Kiesel, and J. J. Acree, “Wide scan, integrated printed circuit board, fragmented aperture array antennas,” in *Proc. 2011 IEEE International Symposium on Antennas and Propagation*, Spokane, WA, Jul. 2011, pp. 1965–1968.

[3] J. G. Maloney, M. P. Kesler, P. H. Harms, and G. S. Smith, “Fragmented aperture antennas and broadband ground planes,” U.S. Patent 6,323,809 B1, Nov. 27, 2001.

[4] Defense Advanced Research Projects Agency, “Starting point for phased array program,” DARPA News, Feb. 2013. [Online]. Available: https://www.darpa.mil/news/2013/starting-point-phase-array-program

Chapter 9

Recent Fragmented Aperture Innovations

9.1 Introduction

The preceding chapters have presented the fragmented aperture antenna concept from its origins through increasingly sophisticated applications: broadband single elements, improved pixel geometries, reconfigurable apertures, ultra-wideband arrays, and wide-scan phased arrays. Throughout this development, spanning more than two decades, the core idea has remained the same: partition a conducting surface into sub-wavelength pixels and use computational optimization to determine which pixels should be conducting and which should not.

In recent years, several research groups have extended the fragmented aperture concept in directions that were not anticipated when the original work began. This chapter surveys three such directions that represent significant advances in the field.

First, researchers at the Georgia Tech Research Institute (GTRI) have developed a fundamentally new way to parameterize the fragmented design space. Instead of optimizing a binary array of pixel states, they define a smooth, continuous *level set function* whose zero-crossings determine the metal boundaries. This *Periodic Level Set Function* (P-LSF) approach converts the combinatorial optimization problem into a continuous one, enabling the use of powerful gradient-free optimizers such as the covariance matrix adaptation evolution strategy (CMA-ES) and dramatically improving convergence.

Second, researchers at the University of Michigan have demonstrated a distributed fragmented antenna in which the individual radiating elements are carried by separate unmanned aerial vehicles (UAVs) in a swarm formation. Near-field electromagnetic coupling between the elements—through their inductive end loads—creates a larger effective aperture with significantly enhanced bandwidth, extending the fragmented aperture concept to mobile, multi-platform scenarios.

Third, emerging work on machine learning and artificial intelligence methods promises to dramatically accelerate the fragmented aperture design process by replacing or augmenting the computationally expensive full-wave simulations that currently dominate the design cycle.

This chapter is intended as a living document that will be updated as these and other innovations mature.

9.2 Level Set Methods for Fragmented Aperture Design

9.2.1 From Binary Pixels to Continuous Parameterization

All of the fragmented aperture designs presented in Chapters 2 through 9 use a binary parameterization: each pixel is assigned a state of 1 (conducting) or 0 (non-conducting), and the collection of pixel states forms the design vector that is optimized by a genetic algorithm. For an aperture with N independent pixels, the design space is the set of vertices of an N-dimensional unit hypercube, $\boldsymbol{\alpha} \in \{0, 1\}^N$. This space is discrete, nonconvex, and completely disjoint—no continuous path connects one design to another.

While genetic algorithms have been remarkably successful in navigating this difficult design space (see Chapters 2, 3, and 7), the binary parameterization imposes fundamental limitations. The mutation and crossover operators of a GA can only flip individual bits, and the resulting design changes are necessarily discontinuous. Moreover, the discrete design space precludes the use of many powerful continuous optimization algorithms that rely on interpolation, gradient information, or covariance estimation.

As the number of pixels grows, these limitations become increasingly severe. The improved mutation algorithm described in Chapter 3 addressed the convergence problem for moderately large pixel counts, but the underlying combinatorial nature of the binary design space remains a fundamental bottleneck.

An alternative approach is to define the material distribution not as a binary array but as a continuous function over the aperture, where the zero-crossings of the function determine the boundaries between conducting and non-conducting regions. This is the essence of the *level set method*, which has a rich history in structural topology optimization [1, 2] and has recently been applied to electromagnetic design problems including antennas and metasurfaces.

9.2.2 The Periodic Level Set Function

Saad-Falcon et al. [3] introduced the *Periodic Level Set Function* (P-LSF), a continuous parameterization specifically designed for periodic electromagnetic structures such as metasurfaces and phased array elements. The P-LSF can serve as a drop-in replacement for the traditional binary fragmented parameterization.

In the P-LSF approach, the material distribution over the unit cell is defined by a level set function $f(\mathbf{x})$ composed of a weighted sum of Gaussian radial basis functions (RBFs):

$$f_{\boldsymbol{\alpha}}(\mathbf{x}) = -T + \sum_{i=1}^{N} \alpha_i \, e^{-\gamma_i^2 \|\mathbf{x}-\mathbf{c}_i\|^2} \tag{9.1}$$

where $\mathbf{c}_i$ are the RBF centers (uniformly spaced across the unit cell), γ_i are scale factors, T is a threshold, and $\boldsymbol{\alpha} = [\alpha_1, \alpha_2, \ldots, \alpha_N]^T$ are the basis coefficients that serve as the design variables. The material distribution is then determined by rounding: metal is placed wherever $f(\mathbf{x}) > 0$, and air wherever $f(\mathbf{x}) \leq 0$. The design variables α_i are real-valued and bounded, $-1 \leq \alpha_i \leq 1$, so the design space is the interior of a continuous, convex hypercube $\boldsymbol{\alpha} \in [-1, 1]^N$.

The key innovation of the P-LSF is the use of *distance wrapping* to enforce periodicity. In a standard level set function, the RBF influence decays to zero at the boundaries of the unit cell, creating material discontinuities when the unit cell is tiled into a periodic array. The P-LSF replaces the Euclidean distance $\|\mathbf{x} - \mathbf{c}\|$ with a *wrapped distance* that accounts for periodicity:

$$\|\mathbf{x} - \mathbf{c}\|_{\text{wrapped}} = \sqrt{\sum_{d=1}^{D} \min_{n \in \mathbb{Z}} (x_d + n \cdot s_d - c_d)^2} \tag{9.2}$$

where s_d is the period in dimension d. This ensures that each RBF's influence wraps continuously around the unit cell boundaries, producing material distributions that are inherently periodic with no discontinuities at the cell edges.

The choice of norm in the distance computation affects the character of the resulting designs. Using the ℓ_2 (Euclidean) norm produces designs with rounded, organic-looking features—curves, circles, and smooth boundaries. Using the ℓ_∞ (Chebyshev) norm produces designs with more rectangular, Manhattan-like features that resemble traditional fragmented designs. The ℓ_1 norm produces intermediate, diamond-shaped features. This flexibility allows the designer to select a parameterization suited to the physics of the problem: broadband objectives tend to favor the smooth features of the ℓ_2 norm, while narrowband resonant structures may benefit from the sharper features of the ℓ_∞ norm.

9.2.3 Optimization and Results

The continuous P-LSF design space enables the use of optimization algorithms beyond genetic algorithms. Saad-Falcon et al. demonstrated significant improvements using the covariance matrix adaptation evolution strategy (CMA-ES) [4], a gradient-free optimizer that models the cost function with a multivariate Gaussian distribution and iteratively updates the covariance matrix to guide the search. CMA-ES has been shown to be highly effective for continuous, nonlinear optimization problems [5], and the P-LSF parameterization makes it directly applicable to fragmented aperture design.

The P-LSF and binary fragmented parameterizations were compared on two design objectives using FDTD electromagnetic simulation. The first was a broadband 2:1 bandpass frequency-selective surface (FSS) operating from 15 to 30 GHz (78% fractional bandwidth). The unit cell was discretized onto a 120×120 grid, with the binary parameterization using 4×4 pixel fragments (915 design variables) and the P-LSF using 32×32 RBFs (1024 continuous design variables). Both the non-dominated sorting genetic algorithm II (NSGA-II) [6] and CMA-ES were applied.

For the broadband bandpass objective, the P-LSF with multi-stage GA optimization converged more quickly and to a higher cost function value than the fragmented parameterization. The P-LSF design achieved better than -10 dB reflection across the 15–30 GHz passband. The optimized metasurface was fabricated on Rogers RO3003

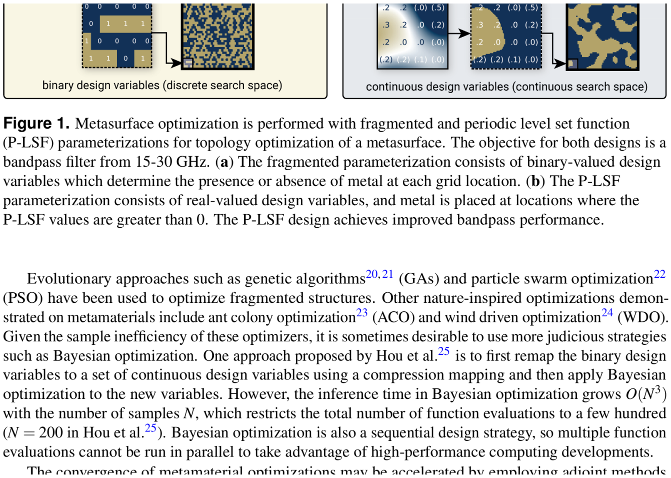

Figure 1. Metasurface optimization is performed with fragmented and periodic level set function (P-LSF) parameterizations for topology optimization of a metasurface. The objective for both designs is a bandpass filter from 15-30 GHz. (**a**) The fragmented parameterization consists of binary-valued design variables which determine the presence or absence of metal at each grid location. (**b**) The P-LSF parameterization consists of real-valued design variables, and metal is placed at locations where the P-LSF values are greater than 0. The P-LSF design achieves improved bandpass performance.

Evolutionary approaches such as genetic algorithms[20,21] (GAs) and particle swarm optimization[22] (PSO) have been used to optimize fragmented structures. Other nature-inspired optimizations demonstrated on metamaterials include ant colony optimization[23] (ACO) and wind driven optimization[24] (WDO). Given the sample inefficiency of these optimizers, it is sometimes desirable to use more judicious strategies such as Bayesian optimization. One approach proposed by Hou et al.[25] is to first remap the binary design variables to a set of continuous design variables using a compression mapping and then apply Bayesian optimization to the new variables. However, the inference time in Bayesian optimization grows $O(N^3)$ with the number of samples N, which restricts the total number of function evaluations to a few hundred ($N = 200$ in Hou et al.[25]). Bayesian optimization is also a sequential design strategy, so multiple function evaluations cannot be run in parallel to take advantage of high-performance computing developments.

The convergence of metamaterial optimizations may be accelerated by employing adjoint methods

Figure 9.1: Comparison of the fragmented (binary) and periodic level set function (P-LSF) parameterizations for topology optimization of a metasurface bandpass filter (15–30 GHz). (a) The fragmented parameterization uses binary-valued design variables on a pixel grid. (b) The P-LSF parameterization uses real-valued design variables in a continuous search space. The P-LSF design achieves improved bandpass performance [3].

substrate and measured in a free-space focused beam system, with close agreement between simulation and measurement.

The second design objective was a dual-band high-Q notch filter, with notch frequencies in the 8–16 GHz and 24–32 GHz bands. For this narrowband problem, the ℓ_∞ norm P-LSF outperformed the ℓ_2 norm, and CMA-ES substantially outperformed the genetic algorithm for both P-LSF variants. The best results were obtained with CMA-ES applied to the ℓ_2 norm P-LSF.

A multi-stage optimization procedure was also demonstrated, in which a coarse P-LSF basis is first optimized and then *upsampled* to a fine basis using a pseudo-inverse technique. This allows the optimizer to quickly converge on a coarse approximation and then refine it, reducing the total number of expensive electromagnetic simulations required.

Howard et al. [7] subsequently applied the P-LSF methodology to the design of a wideband planar phased array element, demonstrating that the technique extends beyond metasurfaces to the phased array antenna designs that are the primary focus of this book. Figure 9.4 illustrates the basic topology optimization routine using a level set function: the smooth topography of the LSF determines the metal/air distribution, which is discretized for electromagnetic simulation, and the optimizer iteratively updates the LSF coefficients to minimize the difference between the simulated and desired system response.

Figure 9.5 compares the convergence rate and realized gain of an LSF-optimized connected array element against a fragmented aperture element designed with the same

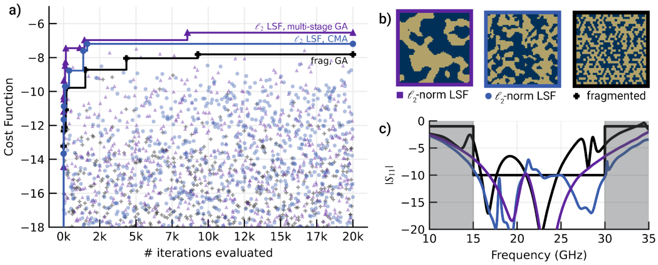

Figure 5. a) For the broadband design objective, the LSF method converged more quickly and to a slightly higher value than the fragmented method. Lines indicate best function evaluations over the course of the optimization, while the scatter plot shows a decimated sampling of the scores for all function evaluations. **b**) The resulting best mask from each optimization is displayed. **c**) Reflection coefficient for each best case

Figure 9.2: Convergence comparison for the broadband bandpass design objective. (a) The P-LSF methods (multi-stage GA and CMA-ES) converge more quickly and to a higher cost function value than the fragmented GA. (b) The resulting best mask from each optimization method. (c) Reflection coefficient comparison showing that the P-LSF designs achieve better passband performance [3].

genetic algorithm and fitness function. The LSF optimization begins improving immediately and converges to higher fitness values, while the fragmented optimization requires many more evaluations before finding competitive designs. The realized gain of the 18×18 element LSF array (with an extra boundary of dummy elements for a total of 155.4 mm × 155.4 mm) ranges from 70% to over 100% aperture efficiency across the 4.35:1 bandwidth.

The non-antenna applications of the P-LSF—including metasurface design and dielectric materials characterization [8]—are discussed in Chapter 10. The open-source Meep FDTD solver [9] has been used to create a publicly available working example of the P-LSF optimization methodology.

9.2.4 Level Set Designs for Fragmented Aperture Antennas

[PLACEHOLDER: This section will present the author's own designs applying the P-LSF approach to the same antenna design problems presented in Chapter 3. Specifically, the skewed-lattice aperture designs operating in the 500 MHz to 2.0 GHz range (see Chapter 3, Section 5.1) will be redesigned using continuous level set parameterization, providing a direct, controlled comparison between the binary GA approach and the P-LSF/CMA-ES approach on identical antenna geometries. Key comparisons will include:

- **Convergence speed (number of function evaluations to reach a given performance level)**

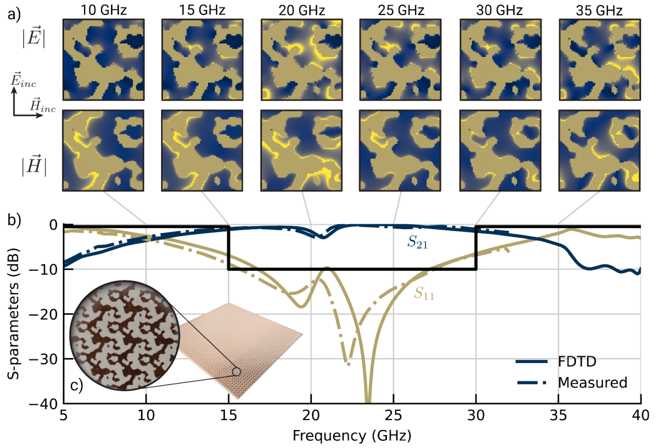

Figure 6. Broadband 2:1 bandpass metasurface. **a**) Field maps generated from FDTD data are shown at discrete frequencies. **b**) S-parameters measured in the focused beam system show good agreement with

Figure 9.3: Fabricated broadband 2:1 bandpass metasurface. (a) FDTD-computed electric and magnetic field maps at six frequencies across the passband. (b) Measured vs. simulated S-parameters showing close agreement; the shaded region indicates the 15–30 GHz design passband. (c) Photograph of the fabricated metasurface on Rogers RO3003 substrate [3].

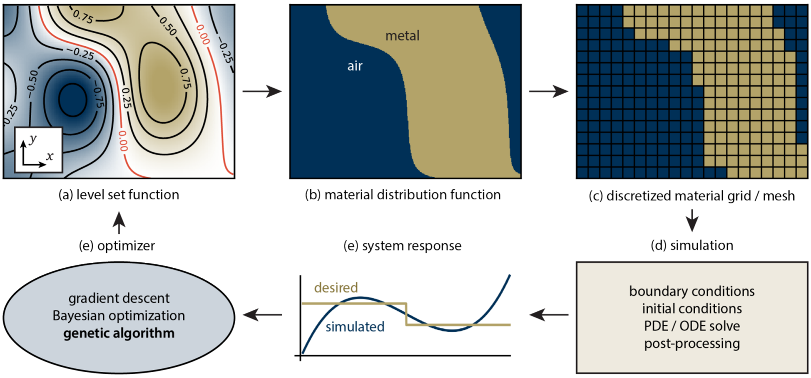

Fig. 1. A flowchart illustrating a basic topology optimization routine. (**a**) The level set function produces a smooth topology of hills and valleys. (**b**) Arrangement of metal on the surface is determined by the points on the LSF above the zero level. (**c**) The material distribution function must be discretized for use in a computational electromagnetic simulation. (**d**) Some example steps used to simulate the material distribution and evaluate its physical properties. (**e**) A comparison between the actual system response for the material distribution function and the desired system response. (**f**) After results are fed into an

Figure 9.4: Topology optimization flowchart using a level set function. (a) The LSF produces a smooth topography of hills and valleys. (b) Metal is placed where the LSF exceeds the threshold. (c) The material distribution is discretized onto a simulation grid. (d) Full-wave electromagnetic simulation. (e) The simulated response is compared to the desired response. (f) The optimizer updates the LSF coefficients [7].

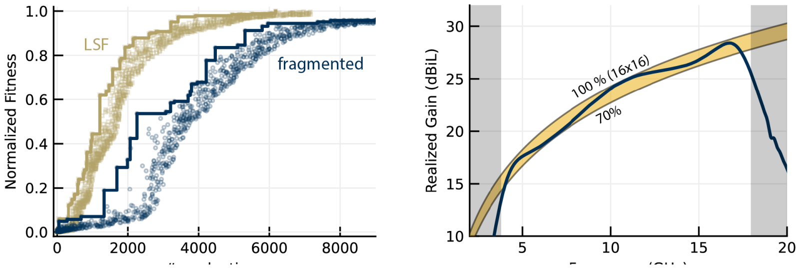

Figure 9.5: Comparison of LSF and fragmented aperture optimization for a connected array element. Left: convergence of normalized fitness—the LSF parameterization converges faster and to higher values. Right: broadside realized gain of the 18×18 LSF-designed array, showing 70–100% aperture efficiency across a 4.35:1 bandwidth [7].

- **Final design quality (realized gain, impedance match)**
- **Character of the optimized designs (smooth P-LSF features vs. rectilinear fragmented features)**
- **Effect of norm choice (ℓ_2 vs. ℓ_∞) on antenna performance**

This work is in progress.]

9.3 Distributed Fragmented Antennas on Mobile Platforms

9.3.1 Concept

At VHF and lower frequencies, the physical size of antennas becomes a significant challenge for mobile platforms. A conventional half-wave dipole at 240 MHz is approximately 62 cm long—too large for small robotic platforms such as unmanned aerial vehicles (UAVs) with maximum dimensions of 15–20 cm. Electrically small antennas that fit on such platforms suffer from narrow bandwidth and poor radiation efficiency, severely limiting data rate and communication range.

Barani, Harvey, and Sarabandi [10] proposed an elegant solution that applies the fragmented aperture philosophy to this problem: instead of placing a single large antenna on a single platform, distribute the antenna across a *formation* of platforms and exploit near-field electromagnetic coupling between the individual elements to synthesize a larger effective aperture. The concept is illustrated schematically in Figure 9.6.

The key insight is that a cluster of coupled antennas occupying a given volume has a lower radiation quality factor Q than any single antenna confined to a smaller subvolume, and can therefore radiate efficiently over a wider bandwidth. The fragmented antenna is "assembled" by flying the platforms into formation, and "disassembled" when they disperse.

9.3.2 Single Element Design

Each UAV carries a single miniaturized antenna: an inductively end-loaded folded dipole printed on Rogers RO4003C substrate ($\varepsilon_r = 3.55$, $\tan\delta = 0.0027$). The inductive end loads—wire loops at each end of the dipole arms—serve two purposes. First, they reduce the physical length of the antenna by increasing the electrical length per unit of physical length; the end-loaded antenna is confined to a volume of $12 \times 10 \times 10$ cm ($0.096\lambda_0 \times 0.08\lambda_0 \times 0.08\lambda_0$ at 240 MHz) with a total mass of 18 g including the matching network. Second, the end loads produce strong near-field magnetic and electric fields that extend over distances of 100–150 mm from the antenna, enabling coupling to adjacent elements in the formation.

When operating in isolation, the single miniaturized antenna provides a -10 dB return loss bandwidth of only 2.4 MHz ($\sim 1\%$) with a 25 Ω input impedance—typical of the severe bandwidth limitations of electrically small antennas.

Barani et al. also considered folded and threefold versions of the dipole element. An n-fold dipole has an input impedance approximately n^2 times that of a single dipole,

1726 IEEE TRANSACTIONS ON ANTENNAS AND PROPAGATION, VOL. 66, NO. 4, APRIL 2018

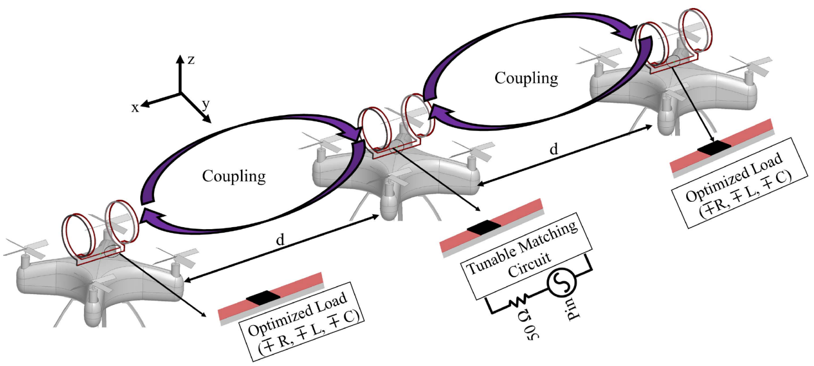

Fig. 1. Proposed fragmented antenna concept for bandwidth enhancement of miniaturized antenna elements mounted on robotic flyers.

Figure 9.6: Proposed distributed fragmented antenna concept for bandwidth enhancement of miniaturized antenna elements mounted on robotic flyers. Three UAVs in formation carry inductively end-loaded folded dipole antennas; near-field coupling between adjacent elements creates a larger effective radiating aperture. Only the center antenna (driver) is actively excited; the two assistive antennas are terminated with optimized loads [10].

BARANI *et al.*: FRAGMENTED ANTENNA REALIZATION

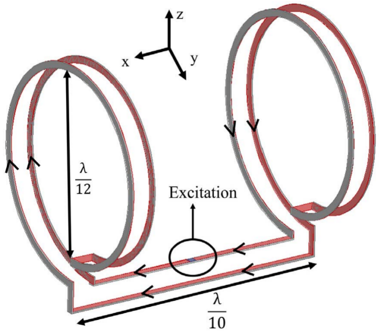

Figure 9.7: Configuration of a single inductively end-loaded folded dipole antenna element. The element is confined to a volume of $\lambda/12 \times \lambda/10$ at the operating frequency of 240 MHz. The inductive end loads (wire loops) increase the electrical length and produce strong near-field coupling to adjacent elements [10].

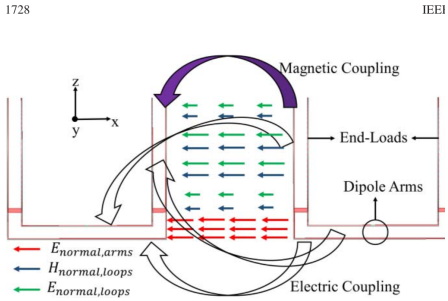

Figure 9.8: Three coupling mechanisms between adjacent antennas in the distributed fragmented configuration: magnetic (inductive) coupling between end loads via their normal magnetic fields (dominant mechanism), electric (capacitive) coupling between dipole arms, and capacitive coupling between end loops and dipole arms [10].

which can be exploited to achieve better impedance matching in the coupled configuration. The threefold version also exhibits stronger near-field coupling over longer distances due to the larger end-loop diameters.

9.3.3 Coupling Mechanisms and Optimization

In the proposed three-element configuration, only the center antenna (the "driver") is excited; the two adjacent antennas (the "assistive" elements) are passively terminated with optimized lumped-element loads. Three coupling mechanisms operate between adjacent elements:

1. **Magnetic (inductive) coupling** between the end loops of adjacent antennas, via their normal magnetic fields. This is the dominant coupling mechanism.
2. **Electric (capacitive) coupling** between the dipole arms of adjacent antennas.
3. **Capacitive coupling between end loops and dipole arms** of adjacent antennas, arising from the strong normal electric field produced by the non-uniform current distribution on the loops.

The coupled signal from the driver is received by the assistive antennas, re-radiated, and also reflected back to the driver through the terminating loads. The assistive antennas thus augment the radiation of the driver, increasing both bandwidth and gain.

The terminating loads on the assistive antennas are optimized using a cost function that balances fractional bandwidth and average radiation efficiency:

$$C(\text{load}) = \alpha \frac{\Delta f}{f_0} + \beta\,\bar{\eta} \tag{9.3}$$

where $\Delta f / f_0$ is the fractional bandwidth, $\bar{\eta}$ is the average radiation efficiency over the -10 dB bandwidth, and α and β are weighting constants. The optimization showed that purely reactive loads (capacitive or inductive) provide the best tradeoff: they enhance bandwidth without dissipating power and maintain high radiation efficiency. The optimal load for a separation distance of $d = 12$ cm was found to be a series capacitor of $C = 4.4$ pF.

The capacitive load introduces a second resonance at a frequency shifted above the driver's natural resonance. The enhanced bandwidth of the coupled configuration results from the merging of the driver and assistive antenna resonances—the same principle of coupled resonators that underlies the bandwidth enhancement in many filter and antenna designs.

9.3.4 Sensitivity and Platform Effects

A practical concern for a formation-based antenna is the sensitivity of performance to variations in inter-element spacing and alignment. Barani et al. investigated these effects through full-wave simulation.

Separation distance: As the inter-element distance d increases from 12 to 16 cm (one to 1.33 element lengths), the bandwidth decreases from 18.4 to 13.5 MHz due to weaker coupling, while the input impedance decreases from 126 Ω to 100 Ω. Radiation efficiency remained above 97% (simulated) for all distances.

Lateral misalignment: Shifting the assistive antennas by up to 4 cm in the lateral direction produced modest bandwidth degradation. The relatively wide near-field profiles of the end loads maintain coupling over a broad spatial region, making the configuration tolerant of typical UAV flight formation errors.

Platform effects: Placing the antenna on a small dielectric UAV body ($\varepsilon_r = 4$, 20 cm × 20 cm) caused only a small shift in center frequency, because the platform is much smaller than the operating wavelength ($\sim \lambda/6$) and occupies a small fractional volume around the radiating element. For metallic platforms, however, the platform and antenna would need to be co-designed to account for electromagnetic interactions.

Tunable matching circuit: To accommodate the impedance variations caused by changing formation geometry, a tunable matching network was designed using a varactor diode. The L-section matching circuit consists of a fixed inductor ($L = 68$ nH), a fixed capacitor ($C_1 = 1.5$ nF), a varactor (C_2, controlled by a DC bias voltage V_B), and a 1:1 Balun transformer. This circuit can dynamically match the antenna impedance as the formation distance varies, enabling the driver antenna to also operate independently when the assistive elements are absent.

9.3.5 Fabrication and Measurement Results

The three-element coupled antenna array was fabricated and measured in the anechoic chamber at the University of Michigan. Key measured results include:

- **Bandwidth:** For $d = 12$ cm, the measured -10 dB bandwidth was 18.4 MHz (7.7% fractional bandwidth), compared to 2.4 MHz (1%) for the isolated single element—a 7.7-fold improvement.

- **Radiation efficiency:** Measured radiation efficiencies of 86.4%, 88.2%, and

80.4% for $d = 12$, 14, and 16 cm, respectively. The reduction from the simulated 97% was attributed to Balun transformer insertion loss (~ 0.7 dB).

- **Peak gain:** Approximately 1 dB higher than the isolated single element across the bandwidth.
- **Radiation pattern:** Patterns characteristic of a dipole antenna with somewhat higher directivity due to the larger effective aperture.

The close agreement between simulation and measurement validates the design approach and confirms that the fragmented antenna concept can be successfully extended to multi-platform, formation-based configurations.

9.4 Machine Learning and AI-Accelerated Design

9.4.1 The Computational Bottleneck

The computational bottleneck in fragmented aperture design has always been the full-wave electromagnetic simulation required to evaluate each candidate design. As described in Chapters 2 and 3, the genetic algorithm must evaluate thousands to tens of thousands of candidate pixel configurations over the course of an optimization, and each evaluation requires a complete FDTD simulation (or set of simulations, when scan performance must be sampled as in Chapter 7). For the designs presented in earlier chapters, a single design optimization can consume days to weeks of computation time on modern parallel hardware.

This cost is tolerable for a one-time design, but it becomes prohibitive when the design space must be explored more broadly—for example, when generating the library of scan-angle configurations described in Chapter 8, when performing parameter sweeps over element geometry, or when optimizing multi-layer structures with many design variables. Machine learning and artificial intelligence methods offer the prospect of dramatically accelerating this design cycle by replacing or augmenting the computationally expensive full-wave simulations.

Several distinct approaches have emerged in recent years, and they are largely complementary: surrogate-based optimization replaces the simulator with a fast approximation, inverse design methods bypass the optimization loop entirely, and hybrid methods combine ML acceleration with physics-based simulation. The broader field of AI-assisted antenna design is surveyed comprehensively in [11] and [12].

9.4.2 Surrogate-Based Optimization

The most straightforward application of machine learning to antenna design is the construction of a *surrogate model*—a fast, data-driven approximation to the electromagnetic simulation that can be evaluated in milliseconds rather than minutes. The surrogate is trained on a dataset of (pixel configuration, performance metric) pairs generated by running full-wave simulations on a representative sample of designs. Once trained, the surrogate replaces the simulator in the optimization loop, enabling the genetic algo-

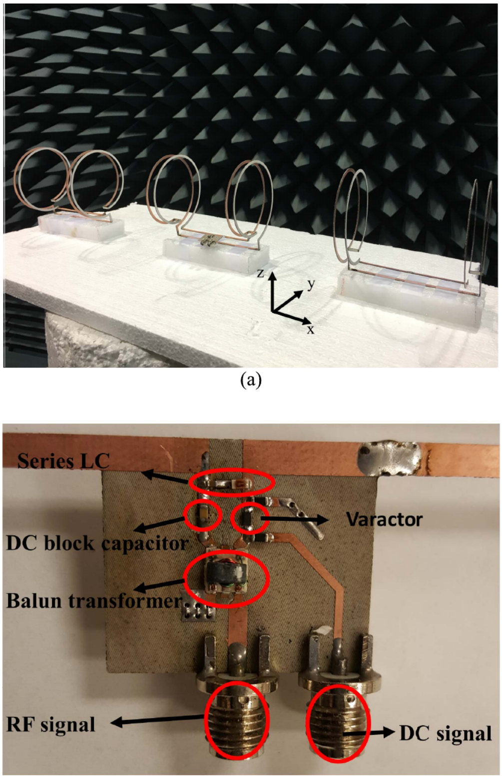

(a)

(b)

Fig. 16. (a) Fabricated antennas inside anechoic chamber. (b) Fabric
tunable matching circuit integrated with the driver antenna.

Figure 9.9: Fabricated distributed fragmented antenna. (a) Three coupled inductively end-loaded folded dipole antennas inside the anechoic chamber at the University of Michigan. (b) Close-up of the fabricated tunable matching circuit integrated with the driver antenna, showing the varactor diode, balun transformer, series LC, and DC block capacitor [10].

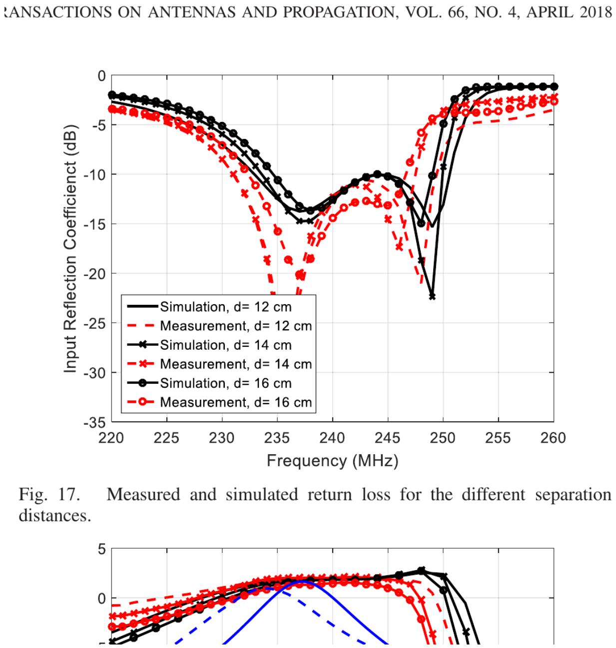

ANSACTIONS ON ANTENNAS AND PROPAGATION, VOL. 66, NO. 4, APRIL 2018

Fig. 17. Measured and simulated return loss for the different separation distances.

Figure 9.10: Measured and simulated return loss for the distributed fragmented antenna at three separation distances (d = 12, 14, and 16 cm) compared to the isolated single antenna. The coupled configuration achieves a measured -10 dB bandwidth of 18.4 MHz at $d = 12$ cm, compared to only 2.4 MHz for the single element—a 7.7-fold improvement [10].

rithm (or any other optimizer) to evaluate orders of magnitude more candidates in the same wall-clock time.

Wu et al. [13] demonstrated a machine-learning-assisted optimization framework for antenna geometry design in which a convolutional neural network (CNN) was trained to predict antenna performance metrics (return loss, gain, bandwidth) directly from a pixelated representation of the antenna geometry. The CNN treats the binary pixel grid as an image, making it a natural fit for the fragmented aperture parameterization. The trained surrogate was then used within a Gaussian process-based Bayesian optimization loop to efficiently search the design space. The authors reported convergence to high-quality designs using an order of magnitude fewer full-wave simulations than a conventional GA approach.

Jacobs [14] applied CNN regression to predict the resonant frequencies of dual-band pixelated microstrip antennas directly from the pixel pattern. The network was trained on 10,000 FDTD simulations and achieved prediction accuracy of better than 2% on unseen designs, with evaluation times of microseconds per design. In earlier work, Jacobs [15] extended deep neural networks to model the full gain pattern of multi-band pixelated antennas, demonstrating that the directional radiation characteristics—not just scalar performance metrics—can be accurately captured by neural network surrogates.

Wang et al. [16] proposed a quasi-bisection method assisted by a machine learning model for bandwidth optimization of pixelated patch antennas, combining the efficiency of ML prediction with a systematic search strategy that provably converges.

9.4.3 Inverse Design with Neural Networks

Surrogate-based optimization still requires an explicit optimization loop, even though each iteration is fast. A more ambitious approach is *inverse design*: training a neural network to directly map from a desired performance specification to a pixel configuration that achieves it. If successful, this approach would replace the entire optimization process with a single forward pass through a trained network.

Gupta et al. [17] demonstrated a tandem neural network architecture for inverse design of multiband pixelated antennas. The tandem network consists of two sub-networks trained sequentially: a *forward model* that predicts antenna performance from the pixel pattern, and an *inverse model* that generates a pixel pattern from a desired performance specification. The inverse model is trained to minimize the discrepancy between the desired specification and the forward model's prediction of the generated design, avoiding the well-known one-to-many problem in which multiple different pixel configurations can produce similar performance. The tandem architecture ensures that the generated designs are physically realizable and electromagnetically consistent.

Li et al. [18] applied residual neural networks (ResNets) to the inverse design of pixelated antennas, exploiting the skip connections in the ResNet architecture to maintain gradient flow through deep networks with many layers. The deeper network captures more complex relationships between the pixel pattern and the antenna response, enabling accurate inverse design for multi-objective specifications.

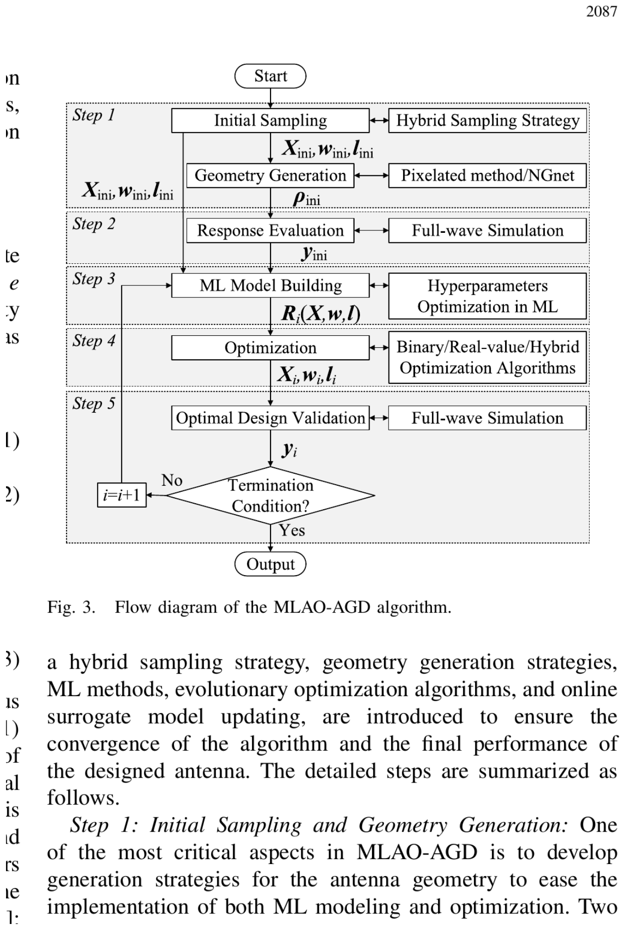

2087

Fig. 3. Flow diagram of the MLAO-AGD algorithm.

a hybrid sampling strategy, geometry generation strategies, ML methods, evolutionary optimization algorithms, and online surrogate model updating, are introduced to ensure the convergence of the algorithm and the final performance of the designed antenna. The detailed steps are summarized as follows.

Step 1: Initial Sampling and Geometry Generation: One of the most critical aspects in MLAO-AGD is to develop generation strategies for the antenna geometry to ease the implementation of both ML modeling and optimization. Two

Figure 9.11: Flowchart of the machine-learning-assisted optimization for antenna geometry design (MLAO-AGD) algorithm. The process iterates between geometry generation, full-wave simulation, ML model building, and optimization, with the ML surrogate model accelerating the search by reducing the number of expensive electromagnetic simulations required [13].

2418 IEEE ANTENNAS AND WIRELESS PROPAGATION LETTERS, VOL. 20, NO. 12, DECEMBER 2021

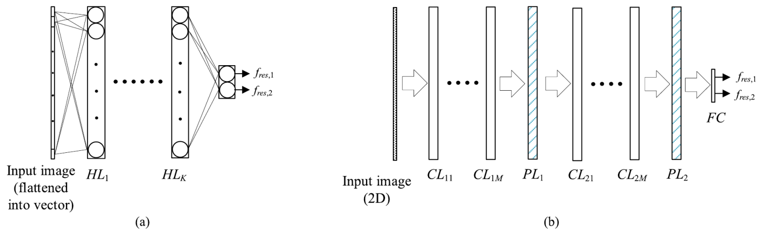

Fig. 1. Schematic representations of the neural networks implemented in the present study. Each network outputs the two resonant frequencies $f_{\rm res,1}$ and $f_{\rm res,2}$. (a) Standard feedforward neural-network architecture (HL$_i$ is the ith hidden layer). (b) Convolutional neural network architecture. CL$_{1j}$, $j = 1, \ldots, M$ and CL$_{2k}$, $k = 1, \ldots, M$ are two blocks of convolutional layers that are each followed by a pooling layer, namely PL$_1$ and PL$_2$. FC is a fully connected layer. The input image is a matrix of ones and zeros representing the pixelated region (footprint $P_x \times P_y$) of the pixelated dual-band antenna (cf. Fig. 2). All convolutional layer feature maps and pooling layers are 2-D layers.

Figure 9.12: Comparison of neural network architectures for pixelated antenna modeling. (a) A standard feedforward network takes the pixel pattern as a flattened vector, losing spatial information. (b) A convolutional neural network (CNN) takes the 2D pixel grid directly as an image input, preserving the spatial relationships between pixels that determine the antenna's electromagnetic behavior [14].

GUPTA et al.: TANDEM NEURAL NETWORK BASED DESIGN OF MULTIBAND ANTENNAS 6309

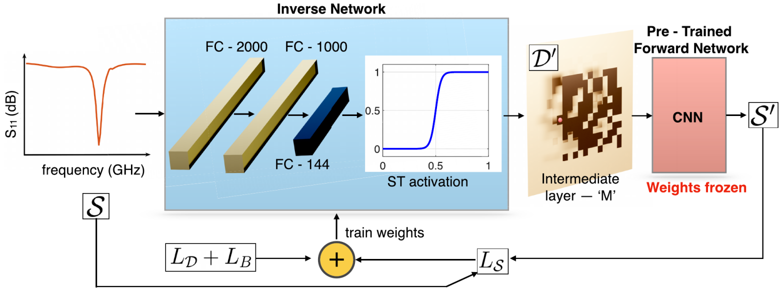

Figure 9.13: Tandem neural network architecture for inverse design of multiband pixelated antennas. The inverse network takes a desired S_{11} spectrum as input and produces a binary antenna design at an intermediate layer. This design is then evaluated by a pre-trained (frozen) forward CNN to predict the resulting spectrum. The tandem architecture avoids the one-to-many problem of direct inverse design [17].

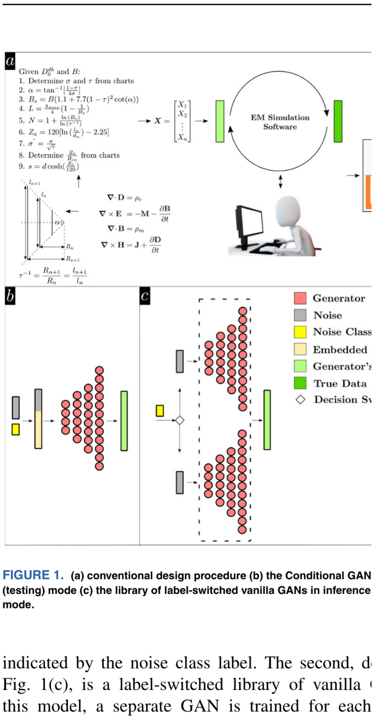

FIGURE 1. **(a) conventional design procedure (b) the Conditional GAN (testing) mode (c) the library of label-switched vanilla GANs in inference mode.**

indicated by the noise class label. The second, d
Fig. 1(c), is a label-switched library of vanilla
this model, a separate GAN is trained for each

Figure 9.14: Comparison of antenna design approaches: (a) conventional design using analytical equations and parametric optimization, (b) conditional GAN (CGAN) approach where a trained generator produces structural parameters from noise and class labels, and (c) library of label-switched vanilla GANs for different design classes [19].

9.4.4 Generative Models

Generative models—neural networks that learn to produce new samples from a training distribution—offer a particularly promising direction for antenna design. Rather than predicting the performance of a given design (forward modeling) or generating a single design for a given specification (inverse design), generative models can produce a *diverse set* of candidate designs that satisfy the specifications, giving the designer multiple options to choose from.

Noakoasteen et al. [19] demonstrated the use of generative adversarial networks (GANs) for antenna design. The GAN was trained on a dataset of antenna geometries and their corresponding performance metrics, and was then able to generate synthetic antenna designs that achieved specified performance targets. The GAN approach also addresses a persistent practical challenge in ML-assisted antenna design: the cost of generating training data. By using the GAN to generate synthetic training examples, the authors reduced the number of expensive full-wave simulations required to build the training dataset.

9.4.5 GA Acceleration and Hybrid Methods

Between the extremes of pure simulation and pure ML prediction, hybrid methods combine machine learning with evolutionary optimization to accelerate convergence without fully replacing the physics-based simulator.

Jayasinghe and Uduwawala [20] demonstrated early work on genetic algorithm optimization of broadband pixelated patch antennas, establishing baseline convergence rates for conventional GA approaches. Jayasinghe, Anguera, and Uduwawala [21] extended this to multiband designs, showing that GA optimization of pixelated antennas could produce designs robust to fabrication tolerances—an important practical consideration that ML-generated designs must also address.

Sun, Jiang, and Wang [22] applied an elite-preserving genetic algorithm to the design of pixelated near-zero refractive index metamaterials, demonstrating that GA-based pixelated optimization extends naturally to metamaterial structures beyond antennas. The application of fragmented aperture methods to metamaterials and other non-antenna electromagnetic structures is discussed further in Chapter 10.

Ehrenborg and Gustafsson [23] took a different approach, using genetic algorithm optimization of pixelated antennas in conjunction with physical bounds analysis. By comparing the GA-optimized designs against theoretical Q-factor limits, they provided rigorous evidence that the GA was finding designs close to the physical optimum—an important validation that becomes even more relevant as ML methods are used to accelerate or replace the GA.

9.4.6 Outlook

The application of machine learning to fragmented aperture antenna design is still in its early stages, and several open challenges remain. Training data generation remains expensive, since each training example requires a full-wave simulation. The generalization of trained models to antenna geometries, materials, or frequency ranges outside the training distribution is not guaranteed. And the "black box" nature of neural network predictions makes it difficult to extract physical insight from the optimized designs.

Despite these challenges, the trajectory is clear. As the design problems become more computationally demanding—larger pixel counts, multi-layer structures, multi-objective specifications, and the design library generation described in Chapter 8—the need for ML acceleration will become increasingly acute. The combination of surrogate-based optimization (for fast fitness evaluation), inverse design (for rapid initial design generation), and physics-based simulation (for final design verification) is likely to become the standard workflow for fragmented aperture design.

[PLACEHOLDER: This section will be expanded with the author's own results applying ML methods to fragmented aperture antenna design as they become available.]

9.5 Summary

The fragmented aperture antenna concept, first introduced more than 25 years ago, continues to inspire innovation in the antenna community. This chapter has surveyed three active areas of development.

The Periodic Level Set Function (P-LSF) introduced by Saad-Falcon et al. [3] provides a mathematically elegant reformulation of the fragmented design space. By replacing the binary pixel states with a continuous, smooth function whose zero-crossings define the metal boundaries, the P-LSF converts the combinatorial optimization problem into a continuous one. This enables the use of powerful optimizers such as CMA-ES and accelerates convergence, while also producing designs with richer geometric features—smooth curves and arbitrary boundary shapes—that are not achievable with rectangular pixels.

The distributed fragmented antenna of Barani et al. [10] extends the fragmented aperture concept to mobile, multi-platform scenarios. By distributing miniaturized radiating elements across a formation of UAVs and exploiting near-field electromagnetic coupling, this approach achieves bandwidth and gain improvements that would be impossible with single antenna small enough to fit on a UAV platform. The measured 7.7-fold bandwidth improvement demonstrates the practical potential of this approach for VHF communications in swarm robotics applications.

Machine learning and AI methods are rapidly maturing as tools for antenna design. Surrogate models based on convolutional neural networks can predict antenna performance from pixel patterns in microseconds, enabling orders-of-magnitude acceleration of the genetic algorithm optimization loop. Inverse design networks and generative adversarial networks go further, producing candidate designs directly from performance specifications without an explicit optimization loop. These methods promise to address the computational bottleneck that has been the primary limitation of the fragmented aperture design methodology since its inception, and will be particularly transformative for the design library generation required by the reconfigurable array concept of Chapter 8.

These three innovations are largely complementary. One can envision, for example, using ML-accelerated optimization with a P-LSF parameterization to design the individual elements of a distributed coupled antenna system. As these and other advances mature, the fragmented aperture concept will continue to expand in capability and find new applications.

References

[1] D. Guirguis and M. F. Aly, “A derivative-free level-set method for topology optimization,” *Finite Elements in Analysis and Design*, vol. 120, pp. 41–56, 2016.

[2] D. Guirguis, D. Melek, W. W. Aly, and M. F. Aly, “High-resolution non-gradient topology optimization,” *Journal of Computational Physics*, vol. 372, pp. 107–125, 2018.

[3] A. Saad-Falcon, C. Howard, J. Romberg, and K. Allen, “Level set methods for gradient-free optimization of metasurface arrays,” *Scientific Reports*, vol. 14, p. 16674, Jul. 2024, arXiv preprint: 2307.07606.

[4] N. Hansen, S. D. Müller, and P. Koumoutsakos, “Reducing the time complexity of the derandomized evolution strategy with covariance matrix adaptation (CMA-ES),” *Evolutionary Computation*, vol. 11, no. 1, pp. 1–18, 2003.

[5] M. D. Gregory, Z. Bayraktar, and D. H. Werner, “Fast optimization of electromagnetic design problems using the covariance matrix adaptation evolutionary strategy,” *IEEE Transactions on Antennas and Propagation*, vol. 59, no. 4, pp. 1275–1285, 2011.

[6] K. Deb, A. Pratap, S. Agarwal, and T. Meyarivan, “A fast and elitist multiobjective genetic algorithm: NSGA-II,” *IEEE Transactions on Evolutionary Computation*, vol. 6, no. 2, pp. 182–197, 2002.

[7] C. T. Howard, A. Saad-Falcon, D. W. Landgren, and K. W. Allen, “Topology optimization of a wideband planar phased array element using periodic level set functions,” in *2024 IEEE International Symposium on Phased Array Systems and Technology (ARRAY)*, 2024, pp. 1–7.

[8] C. Howard *et al.*, “A loss tangent measurement surface for free space focused beam characterization of low-loss dielectrics,” in *2022 IEEE International Symposium on Phased Array Systems and Technology (PAST)*, 2022, pp. 1–6.

[9] A. F. Oskooi, D. Roundy, M. Ibanescu, P. Bermel, J. D. Joannopoulos, and S. G. Johnson, “MEEP: A flexible free-software package for electromagnetic simulations by the FDTD method,” *Computer Physics Communications*, vol. 181, no. 3, pp. 687–702, 2010.

[10] N. Barani, J. F. Harvey, and K. Sarabandi, “Fragmented antenna realization using coupled small radiating elements,” *IEEE Transactions on Antennas and Propagation*, vol. 66, no. 4, pp. 1725–1735, 2018.

[11] N. Sarker, P. Podder *et al.*, “Applications of machine learning and deep learning in antenna design, optimization and selection: A review,” *IEEE Access*, vol. 11, pp. 103 890–103 915, 2023.

[12] M. K. Shereen, X. Liu, X. Wu, S. U. Din, A. Naseem, S. Niazi, and M. I. Khattak, “Innovations in metamaterial and metasurface antenna design: The role of deep learning,” *Materials Today Electronics*, vol. 13, p. 100162, 2025.

[13] Q. Wu, W. Chen, C. Yu, H. Wang, and W. Hong, “Machine-learning-assisted optimization for antenna geometry design,” *IEEE Transactions on Antennas and Propagation*, vol. 72, no. 3, pp. 2083–2097, 2024.

[14] J. P. Jacobs, “Accurate modeling by convolutional neural-network regression of resonant frequencies of dual-band pixelated microstrip antenna,” *IEEE Antennas and Wireless Propagation Letters*, vol. 20, no. 12, pp. 2417–2421, 2021.

[15] ——, “Accurate and efficient modeling of gain patterns of multiband pixelated antenna by deep neural networks,” in *2022 International Conference on Electromagnetics in Advanced Applications (ICEAA)*, 2022, pp. 306–306.

[16] Q. Wang, Z. Pang, D. Gao, P. Liu, X. Pang, and X. Yin, “Machine learning-assisted quasi-bisection method for pixelated patch antenna bandwidth optimization,” *IEEE Antennas and Wireless Propagation Letters*, vol. 23, no. 12, pp. 4807–4811, 2024.

[17] A. Gupta, E. A. Karahan, C. Bhat, K. Sengupta, and U. K. Khankhoje, “Tandem neural network based design of multiband antennas,” *IEEE Transactions on Antennas and Propagation*, vol. 71, no. 8, pp. 6308–6318, 2023.

[18] M. Li, Y. Wang, and M. Zhu, “Inverse design of pixelated antenna based on residual neural network,” in *2025 International Applied Computational Electromagnetics Society Symposium (ACES-China)*, 2025, pp. 1–3.

[19] O. Noakoasteen, J. Vijayamohanan, A. Gupta, and C. Christodoulou, “Antenna design using a GAN-based synthetic data generation approach,” *IEEE Open Journal of Antennas and Propagation*, vol. 3, pp. 488–495, 2022.

[20] J. M. J. W. Jayasinghe and D. N. Uduwawala, “Design of broadband patch antennas using genetic algorithm optimization,” in *2010 5th International Conference on Industrial and Information Systems (ICIIS)*, 2010, pp. 60–61.

[21] J. W. Jayasinghe, J. Anguera, and D. N. Uduwawala, “A simple design of multi band microstrip patch antennas robust to fabrication tolerances for GSM, UMTS, LTE, and bluetooth applications by using genetic algorithm optimization,” *Progress In Electromagnetics Research M*, vol. 27, pp. 255–269, 2012.

[22] S. Sun, Y. Jiang, and J. Wang, “Automatic design of pixelated near-zero refractive index metamaterials based on elite-preserving genetic algorithm optimization,” *Results in Physics*, vol. 48, p. 106461, 2023.

[23] C. Ehrenborg and M. Gustafsson, “Physical bounds and automatic design of antennas above ground planes,” in *2016 URSI International Symposium on Electromagnetic Theory (EMTS)*, 2016, pp. 353–356.

Chapter 10

Fragmented Apertures Applied to Other Electromagnetic Structures

10.1 Introduction

The preceding chapters have focused exclusively on the application of the fragmented aperture design methodology to antennas—radiating structures that convert guided electromagnetic energy into free-space radiation (or the reverse). However, the core idea behind the fragmented aperture approach—partitioning a conducting surface into subwavelength pixels and using computational optimization to determine the optimal pattern—is not limited to antenna design. The same methodology can be applied to any electromagnetic structure whose performance depends on the spatial distribution of conducting material.

This chapter surveys several non-antenna applications of the fragmented aperture concept. These include broadband phase surfaces, RF power combining networks, pixelated absorbers, pixelated waveguide components, and metamaterials. In each case, the same design machinery described in the earlier chapters—a pixelated conducting surface, a genetic algorithm (or other optimizer), and a full-wave electromagnetic simulation—is applied to a structure whose function is fundamentally different from that of an antenna.

10.2 Fragmented Broadband Phase Surfaces

An early and important application of the fragmented aperture concept was the design of surfaces with broadband transmission phase properties. Just as the pixel pattern on a radiating aperture can be optimized to achieve desired antenna characteristics, the pixel pattern on a standalone surface can be optimized to achieve a specific phase response as electromagnetic waves pass through it.

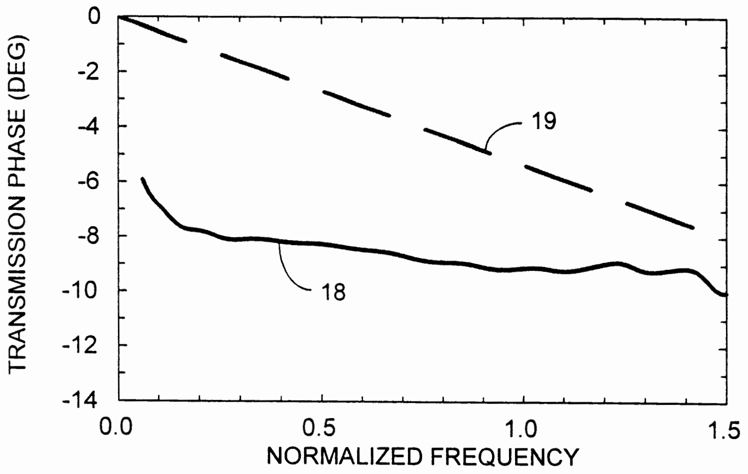

Figure 10.1: Transmission phase comparison demonstrating the broadband properties of a fragmented surface. The fragmented surface (curve 18) maintains a flatter phase response than the reference solid conductor (curve 19) over a wide normalized frequency range [1].

A conventional solid conducting surface reflects all incident energy and imparts a frequency-dependent phase shift upon reflection. Similarly, transmission through a partially transparent surface depends on the size, shape, and arrangement of the conducting regions. For a solid conductor, the transmission phase varies rapidly with frequency. By fragmenting the conducting surface into an optimized pattern of conducting and non-conducting pixels, it is possible to design a surface that provides a more uniform phase response over a wider bandwidth.

Figure 10.1 shows the transmission phase through a fragmented surface (curve 18) compared with a reference solid conducting surface (curve 19), from the original patent [1]. The fragmented surface maintains a substantially flatter phase response across the normalized frequency range, demonstrating that the fragmented pixel pattern can be used to engineer broadband phase behavior.

This result was significant because it demonstrated that the fragmented aperture concept extends beyond antenna design to the engineering of electromagnetic surfaces with tailored transmission and reflection properties. The broadband phase behavior of fragmented surfaces subsequently informed the development of the broadband screen backplanes described in Chapter 6, which use fragmented conducting layers in combination with resistive card (r-card) layers to achieve ultra-wideband ground plane performance for phased array antennas.

The concept of designing surfaces with optimized phase properties is closely related to the broader field of frequency-selective surfaces (FSS) and metasurfaces. As described in Chapter 9, Saad-Falcon et al. [2] applied the Periodic Level Set Function parameterization to design broadband bandpass and narrowband notch filter metasurfaces, achieving excellent agreement between simulation and measurement. Howard et al. [3] applied similar techniques to design resonant periodic surfaces for dielectric materials characterization, where the resonance magnitude depends linearly on the loss tangent of an adjacent dielectric sample. These recent developments demonstrate that the fragmented aperture approach to surface design has matured from the original broadband phase concept into a versatile tool for engineering a wide range of electromagnetic surface behaviors.

10.3 Fragmented RF Power Combiners

An important practical challenge in phased array antenna systems is the design of the power combining network that combines the signals from multiple array elements into a single output port (for receive) or distributes a single input signal to multiple elements (for transmit). Conventional power combiners use commercial off-the-shelf (COTS) components—Wilkinson dividers, hybrid couplers, or resistive dividers—connected by microstrip or stripline transmission lines. These COTS networks can be bulky, expensive, and lossy, particularly when they must operate over wide bandwidths.

Landgren et al. at GTRI recognized that the fragmented aperture optimization process could be applied to the design of power combiner networks, not just radiating surfaces. The key insight is that a power combiner is simply another electromagnetic structure whose performance—insertion loss, reflection, isolation, and bandwidth—depends on the spatial distribution of conducting material on a dielectric substrate. By treating the combiner as a pixelated conducting pattern and optimizing it with a genetic algorithm and FDTD simulation, the same design machinery used for fragmented aperture antennas can produce optimized combiner networks.

10.3.1 Fragmented Combiner Concept

Landgren et al. [4] demonstrated this concept by designing a fragmented combiner network for a 4×4 phased array antenna intended for fire-control radar telemetry applications, covering the L-, S-, and C-bands (1.4–6.7 GHz, a 4.8:1 bandwidth). The combiner network replaces the conventional Wilkinson divider tree with a single printed circuit board layer containing an optimized fragmented conducting pattern.

The fragmented combiner design required two separate optimized components: an interfacial combiner that interfaces the unbalanced antenna feed structure with a microstrip transmission line, and an internal combiner that provides the actual power division. A collection of these two logical units was arranged to form a 16:1 combiner for the 4×4 array. The design process used a genetic algorithm coupled with FDTD simulation, with the fitness function targeting minimum insertion loss, low reflection, and high isolation across the 1.4–6.7 GHz band.

rray Antenna Design with
ombiner Technology

runasso, James B. Dee, Jonathan Perez,

Figure 10.2: Comparison of a conventional COTS Wilkinson combiner network (left) and a fragmented combiner network (right), both designed for a 4×4 array with a 16:1 combining ratio. The fragmented combiner replaces discrete components with a single optimized conducting pattern [4].

Figure 10.2 shows the key innovation: the conventional COTS Wilkinson combiner network (left) uses discrete components and transmission line segments, while the fragmented combiner network (right) replaces all of these with a single optimized conducting pattern on a PCB substrate. Both are designed for a 4×4 array with a 16:1 combining ratio and the same physical footprint.

10.3.2 Measured Results

The fragmented combiner was fabricated on Rogers 4350B substrate and experimentally characterized. The measured insertion loss of the fragmented combiner was lower than that of a conventional COTS Wilkinson combiner across the entire operating band. The ideal insertion loss for a 16:1 combiner is -12 dB (-3 dB per 2:1 stage); the fragmented combiner was within 2.5 dB of this ideal, compared to larger losses for the COTS version.

Figure 10.3 shows photographs of the fabricated combiner boards and the measured insertion loss comparison. The COTS combiner (a) has Wilkinson divider chips soldered onto the substrate, while the fragmented combiner (b) is a single etched copper pattern with no discrete components. The measured insertion loss (c) confirms that the fragmented combiner achieves lower loss than the COTS version across the entire L- to C-band operating range.

The fragmented combiner was then integrated with a 4×4 fragmented aperture antenna array. Landgren et al. [5] reported that the complete antenna system—fragmented aperture elements with fragmented combiners and unbalanced feeds—achieved the program performance goals across the 1.4–6.7 GHz bandwidth. The measured realized gain of the 4×4 array with the fragmented combiner exceeded that of the same array with COTS combiners across the full band.

Figure 10.4 shows the broadside realized gain of the 4×4 array with the fragmented combiner (blue) compared to the COTS combiner (red). The fragmented combiner array achieves higher realized gain across the entire L- to C-band, with the improvement

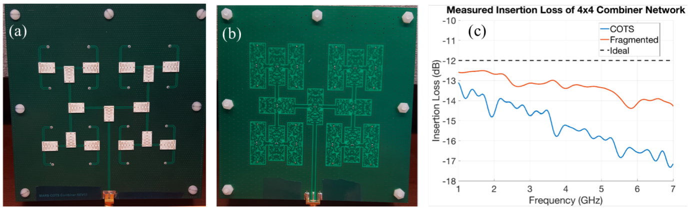

Figure 10.3: Fabricated combiner boards and measured performance: (a) COTS Wilkinson combiner with discrete chips, (b) fragmented combiner with a single etched pattern, and (c) measured insertion loss comparison showing lower loss for the fragmented design across the operating band [4].

attributable to the lower insertion loss of the fragmented combiner network. The inset shows the driven layer of the 4×4 antenna array.

10.3.3 Full-Scale Array Validation

Based on the success of the 4×4 prototype, GTRI fabricated and tested the full 16×16 element array with fragmented combiners. Landgren et al. [5] reported the measured realized gain of the full array, which met the program specifications from L-band through C-band.

Figure 10.5 shows the measured realized gain of the full 16×16 array at broadside. The measured gain (blue) meets or exceeds the program goal (solid black line) across the 1.4–6.7 GHz design bandwidth. The modeled gain without power combiners (red) represents the theoretical performance of the antenna elements alone; the difference between the red and blue curves is the insertion loss of the combiner network. The uniform aperture directivity limit (dashed black) provides an upper bound.

The fragmented combiner technology demonstrates that the pixelated optimization approach extends naturally from antennas to passive microwave networks. The same genetic algorithm and FDTD simulation framework that designs the radiating aperture can also design the feed network behind it, producing an integrated system in which every conducting layer—radiator, ground plane, and combiner—is computationally optimized.

10.4 Fragmented Metamaterials

The fragmented aperture design methodology has also been applied to the design of metamaterials—artificial electromagnetic structures that exhibit properties not found in natural materials. The pixelated representation used for fragmented aperture antennas is a natural fit for metamaterial design, since metamaterials are typically periodic structures composed of sub-wavelength conducting elements whose geometry determines

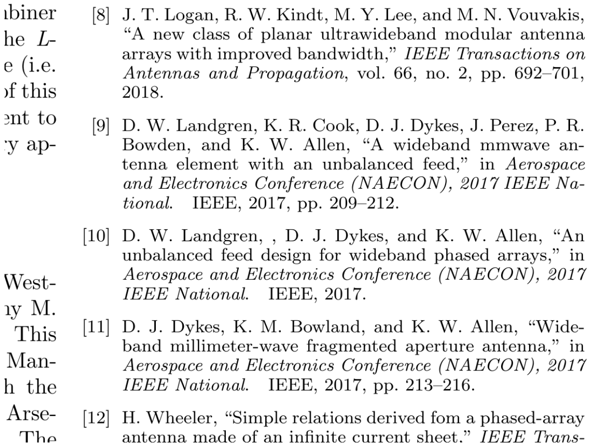

ıbiner
he *L*-
e (i.e.
ɔf this
ɜnt to
ꞏy ap-

West-
ɿy M.
This
Man-
h the
Arse-

[8] J. T. Logan, R. W. Kindt, M. Y. Lee, and M. N. Vouvakis, "A new class of planar ultrawideband modular antenna arrays with improved bandwidth," *IEEE Transactions on Antennas and Propagation*, vol. 66, no. 2, pp. 692–701, 2018.

[9] D. W. Landgren, K. R. Cook, D. J. Dykes, J. Perez, P. R. Bowden, and K. W. Allen, "A wideband mmwave antenna element with an unbalanced feed," in *Aerospace and Electronics Conference (NAECON), 2017 IEEE National*. IEEE, 2017, pp. 209–212.

[10] D. W. Landgren, , D. J. Dykes, and K. W. Allen, "An unbalanced feed design for wideband phased arrays," in *Aerospace and Electronics Conference (NAECON), 2017 IEEE National*. IEEE, 2017.

[11] D. J. Dykes, K. M. Bowland, and K. W. Allen, "Wideband millimeter-wave fragmented aperture antenna," in *Aerospace and Electronics Conference (NAECON), 2017 IEEE National*. IEEE, 2017, pp. 213–216.

[12] H. Wheeler, "Simple relations derived fom a phased-array antenna made of an infinite current sheet," *IEEE Trans-*

Figure 10.4: Broadside realized gain comparison: fragmented combiner (blue) vs. COTS Wilkinson combiner (red) integrated with the same 4×4 fragmented aperture array. The fragmented combiner achieves higher gain across the operating band due to lower insertion loss. Inset: driven layer of the antenna array [4].

across the whole design bandwidth.

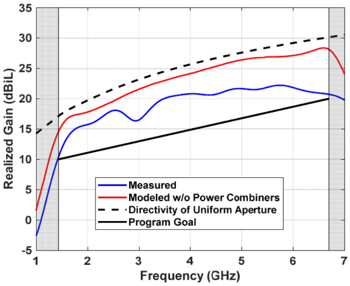

Figure 10.5: Measured realized gain of the 16×16 fragmented aperture array with integrated fragmented combiners (blue), compared to the model without combiners (red), the program performance goal (solid black), and the uniform aperture directivity limit (dashed black). The system meets the program goal across the full 1.4–6.7 GHz bandwidth [5].

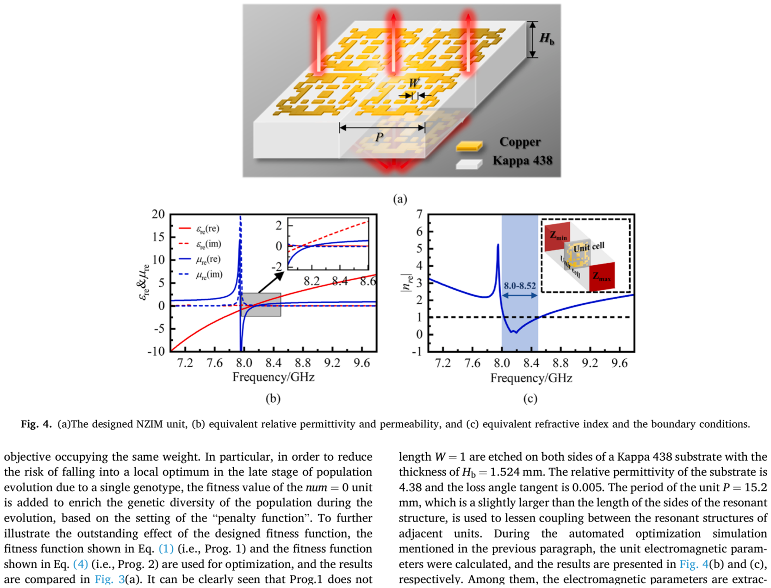

Fig. 4. (a)The designed NZIM unit, (b) equivalent relative permittivity and permeability, and (c) equivalent refractive index and the boundary conditions.

objective occupying the same weight. In particular, in order to reduce the risk of falling into a local optimum in the late stage of population evolution due to a single genotype, the fitness value of the *num* $= 0$ unit is added to enrich the genetic diversity of the population during the evolution, based on the setting of the "penalty function". To further illustrate the outstanding effect of the designed fitness function, the fitness function shown in Eq. (1) (i.e., Prog. 1) and the fitness function shown in Eq. (4) (i.e., Prog. 2) are used for optimization, and the results are compared in Fig. 3(a). It can be clearly seen that Prog.1 does not

length $W = 1$ are etched on both sides of a Kappa 438 substrate with the thickness of $H_b = 1.524$ mm. The relative permittivity of the substrate is 4.38 and the loss angle tangent is 0.005. The period of the unit $P = 15.2$ mm, which is a slightly larger than the length of the sides of the resonant structure, is used to lessen coupling between the resonant structures of adjacent units. During the automated optimization simulation mentioned in the previous paragraph, the unit electromagnetic parameters were calculated, and the results are presented in Fig. 4(b) and (c), respectively. Among them, the electromagnetic parameters are extrac-

Figure 10.6: Pixelated NZIM design by Sun et al.: (a) optimized 14×14 unit cell on Kappa 438 substrate, (b) extracted relative permittivity and permeability showing near-zero values around 8.2 GHz, and (c) equivalent refractive index demonstrating $|n_{\text{re}}| < 1$ across the 8.0–8.52 GHz band [6].

the effective material properties.

Sun, Jiang, and Wang [6] applied an elite-preserving genetic algorithm to the design of pixelated near-zero refractive index metamaterials (NZIM). Near-zero index metamaterials have been proposed for applications including directive emission, cloaking, and tunneling. The pixelated approach allows the optimizer to discover complex unit cell geometries that achieve the desired near-zero index behavior across a specified frequency band, without requiring the designer to select a specific metamaterial topology (such as split-ring resonators or complementary structures) in advance. This is the same philosophy as fragmented aperture antenna design: the optimizer discovers the structure, rather than having it imposed by the designer.

Sun et al. designed an NZIM unit operating between 8.0 and 8.52 GHz using a 14×14 pixel lattice with quarter-symmetry, reducing the binary chromosome to 28 independent bits. The unit cell was etched on both sides of a Kappa 438 substrate and optimized using CST Microwave Studio driven by a Python-controlled elite-preserving genetic algorithm (EGA). Figure 10.6 shows the optimized NZIM unit cell and its extracted electromagnetic properties: the relative permittivity and permeability both approach zero near 8.2 GHz, yielding a refractive index $|n_{\text{re}}| < 1$ across the 8.0–8.52 GHz band.

To validate the NZIM performance, Sun et al. fabricated a 5×5 array of NZIM unit cells and loaded it as a cladding layer above a rectangular microstrip patch antenna

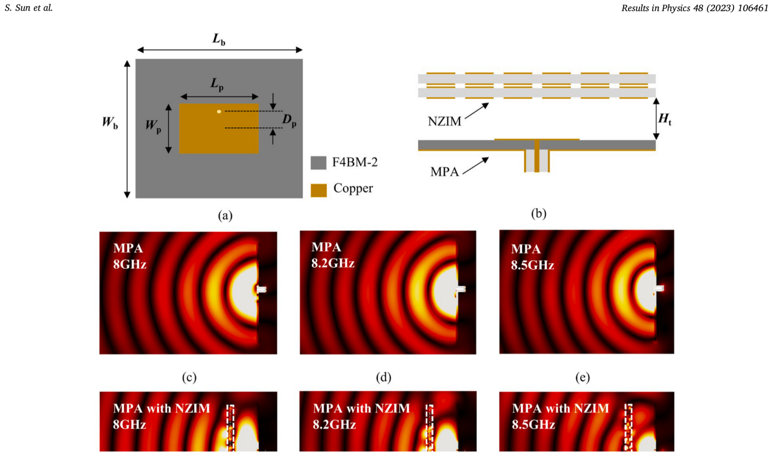

Figure 10.7: Fabricated MPA and NZIM prototypes with near-field distributions: (a) MPA geometry, (b) side view showing NZIM cladding placement, (c–e) electric field of MPA alone at 8.0, 8.2, and 8.5 GHz showing spherical wavefronts, and (f–h) electric field with NZIM cladding showing quasi-planar wavefronts [6].

(MPA) resonating at 8.2 GHz. The near-field simulation results show that the spherical waves radiated by the MPA are transformed into quasi-plane waves after passing through the NZIM cladding, confirming the beam-shaping effect. Figure 10.7 shows the fabricated prototypes and the near-field distributions with and without the NZIM superstrate. The field distributions clearly demonstrate the transition from spherical to quasi-planar wavefronts when the NZIM is present.

The measured results confirmed that the NZIM significantly improves the MPA directivity, with an average gain enhancement of 5.3 dB and a maximum gain improvement of 6.05 dB. Figure 10.8 shows the experimental setup and measured performance: the near-field test system, reflection coefficient comparison, radiation patterns at 5.8 GHz, and realized gain with and without the NZIM cladding. Compared to previous manually designed NZIMs that achieved 1–5 dB gain enhancement, the automated pixelated design achieves 6.05 dB—a result enabled by the optimizer's ability to explore the full design space of the 14×14 pixel grid.

As described in Chapter 9, the Periodic Level Set Function (P-LSF) methodology developed by Saad-Falcon et al. [2] has been applied to the design of broadband frequency-selective surfaces and narrowband metasurface filters. The P-LSF approach is particularly well suited for periodic electromagnetic structures because the distance wrapping technique (Equation 9.2 in Chapter 9) ensures that the material distribution is inherently periodic, with no discontinuities at the unit cell boundaries. The broadband 2:1 bandpass FSS (15–30 GHz) and dual-band high-Q notch filter demonstrated by Saad-Falcon et al. represent state-of-the-art examples of computationally optimized metasurface design.

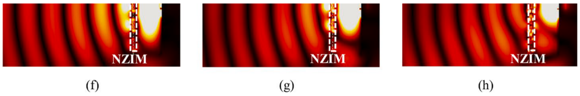

Fig. 5. The fabricated prototypes of MPA and NZIM cladding. (a) Top view of MPA and its geometrical parameters (mm) with $L_b = 76$, $W_b = 76$, $W_p = 9.9$, $L_p = 13.5$, $D_p = 2.8$, and $H_t = 19.2$, (b) side view of MPA, (c, d&e) the electric field of MPA at 8 GHz, 8.2 GHz, and 8.5 GHz, (f, g&h) the electric field of MPA with NZIM at 8 GHz, 8.2 GHz, and 8.5 GHz.

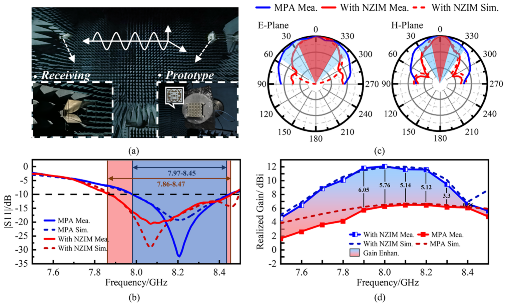

Fig. 6. Experimental environment and data. (a) Near-field test system, (b) S11, (c) radiation patterns at 5.8 GHz, and (d) gains.

Figure 10.8: Experimental validation of the pixelated NZIM: (a) near-field test system with fabricated prototypes, (b) measured and simulated reflection coefficients, (c) radiation patterns at 5.8 GHz, and (d) realized gain comparison showing up to 6.05 dB gain enhancement with the NZIM cladding [6].

Howard et al. [3] applied the P-LSF methodology to a different class of electromagnetic structure: resonant periodic surfaces for dielectric materials characterization. The optimized surface exhibits a resonance whose magnitude depends linearly on the loss tangent of an adjacent dielectric sample, enabling accurate, non-destructive measurement of dielectric loss. This is a compelling example of the versatility of the fragmented approach—the same design machinery that produces antennas can also produce precision measurement instruments.

10.5 Pixelated Absorbers

Electromagnetic absorbers are structures designed to capture incident electromagnetic energy and convert it to heat, minimizing both reflection and transmission. Absorbers have important applications in radar cross-section (RCS) reduction, electromagnetic compatibility, and antenna measurement chambers. The pixelated design approach is well suited to absorber design because the absorption properties depend directly on the geometry and distribution of conducting (and resistive) elements on a surface.

Zhao et al. [7] demonstrated a novel absorber design based on a pixelated frequency-selective surface (FSS) with integrated lumped resistors, optimized using an estimation of distribution algorithm (EDA). The absorber consists of four layers: a pixelated FSS layer, a substrate, a dielectric (honeycomb) spacer, and a metallic ground plane. The FSS unit cell is pixelated into a 10×10 grid of sub-wavelength conducting patches, with lumped resistors placed at selected locations between adjacent pixels. Figure 10.9

shows the absorber layer structure and the simulated unit cell geometry.

The key innovation of Zhao et al.'s approach is the use of EDA rather than a conventional genetic algorithm. EDA builds a probabilistic model of the design space and samples new candidates from the learned distribution, which is particularly effective for problems where the positions of metallic pixels and resistors are correlated. Three parameters are jointly optimized: the metallic pixel positions ($\mathbf{F}_{\mathrm{position}}$), the resistor positions ($\mathbf{R}_{\mathrm{position}}$), and the resistor values ($\mathbf{R}_{\mathrm{value}}$). The fitness function balances the absorption bandwidth (below -6 dB reflectivity) with the mean reflectivity across the 2–6 GHz target band.

Figure 10.10 shows the optimized unit cell geometries and reflectivity performance. The pixelated FSS with resistors (a) achieves two strong absorption peaks at 3.64 GHz (-8.67 dB) and 5.86 GHz (-9.77 dB), while the version without resistors (b) exhibits only weak absorption. The loaded resistors fundamentally change the absorbing mechanism by providing the necessary energy dissipation.

The optimized absorber was fabricated and measured in a microwave anechoic chamber. Figure 10.11 shows the fabricated samples and measured reflectivity curves. The measured absorption band (-6 dB reflectivity) extends from 3.13 to 6.42 GHz, with reflectivity values of -14.39 dB at 3.80 GHz and -10.14 dB at 5.68 GHz. The total thickness of the absorber is only 4 mm, corresponding to approximately 0.04λ at the lowest operating frequency and 0.08λ at the highest—making this an ultra-thin wideband absorber. The measured results fit well with simulations, validating the EDA-based pixelated design approach.

Lee et al. [8] extended the pixelated absorber concept to ultra-wideband operation by using two stacked GA-optimized metasurface layers separated by PMI foam dielectric spacers, backed by a carbon fiber reinforced polymer (CFRP) reflector. Each metasurface layer uses a 20×20 pixel grid with x/y-axis symmetry (55 independent pixels per layer), printed with carbon paste via silk-screen printing on polyimide film. The dual-layer approach creates multiple destructive interference paths that broaden the absorption bandwidth dramatically.

Figure 10.12 shows the optimized metasurface patterns and simulated reflectance performance. The GA-optimized design achieves greater than 90% absorption (reflectance below -10 dB) from 2.2 to 18 GHz—a 156% fractional bandwidth covering the entire S- through Ku-band range.

The absorber was fabricated as a composite structure with a glass fiber reinforced polymer (GFRP) protective outer layer, making it suitable for aerospace applications. Figure 10.13 shows the fabricated metasurface layers and the assembled composite absorber. The prototype passed MIL-STD-810H environmental durability testing (temperature cycling and humidity exposure), demonstrating the practical viability of pixelated absorber technology for real-world deployment. The total thickness is 13 mm ($0.06\lambda_0$ at 2 GHz), and absorption remains above 90% for incidence angles up to 30° in both TE and TM polarizations.

10.6 Pixelated Waveguide Components

The pixelated design concept has also been applied to waveguide-based structures, particularly substrate integrated waveguide (SIW) horn antennas. SIW technology im-

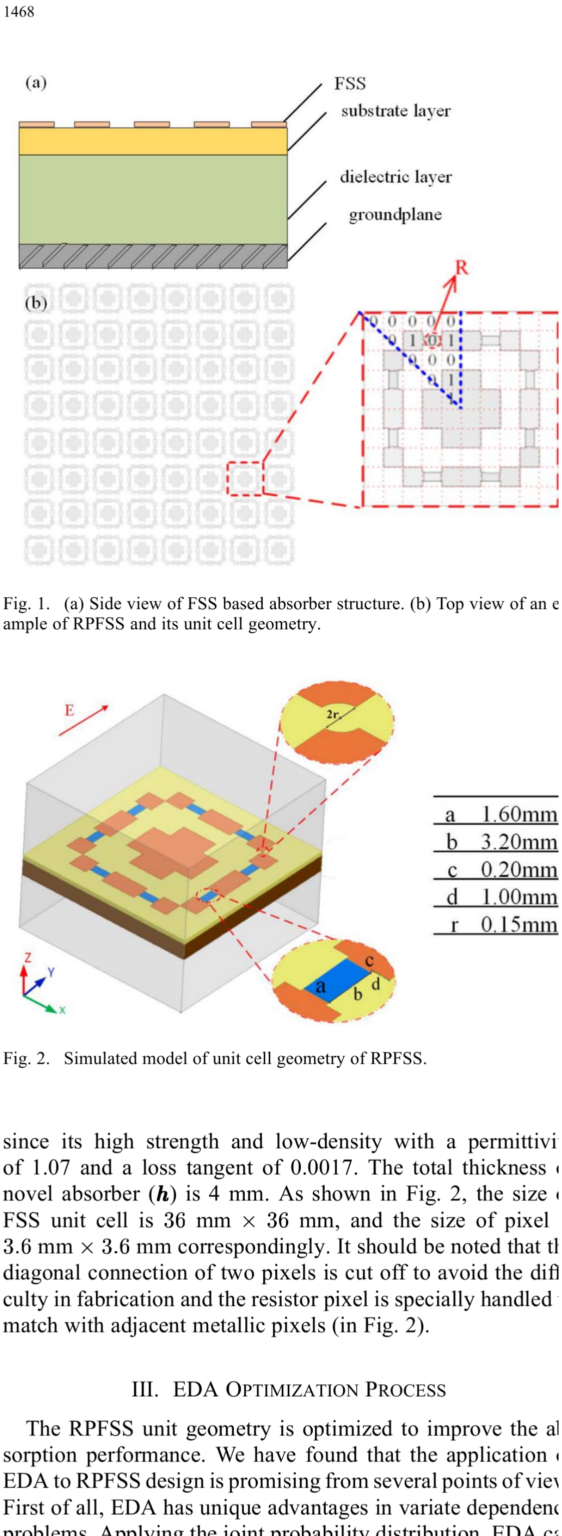

Fig. 1. (a) Side view of FSS based absorber structure. (b) Top view of an e
ample of RPFSS and its unit cell geometry.

a	1.60mm
b	3.20mm
c	0.20mm
d	1.00mm
r	0.15mm

Fig. 2. Simulated model of unit cell geometry of RPFSS.

since its high strength and low-density with a permittivi
of 1.07 and a loss tangent of 0.0017. The total thickness
novel absorber ($\boldsymbol{h}$) is 4 mm. As shown in Fig. 2, the size
FSS unit cell is 36 mm × 36 mm, and the size of pixel
3.6 mm × 3.6 mm correspondingly. It should be noted that t
diagonal connection of two pixels is cut off to avoid the diffi
culty in fabrication and the resistor pixel is specially handled
match with adjacent metallic pixels (in Fig. 2).

III. EDA OPTIMIZATION PROCESS

The RPFSS unit geometry is optimized to improve the a
sorption performance. We have found that the application
EDA to RPFSS design is promising from several points of vie
First of all, EDA has unique advantages in variate dependen
problems. Applying the joint probability distribution, EDA c

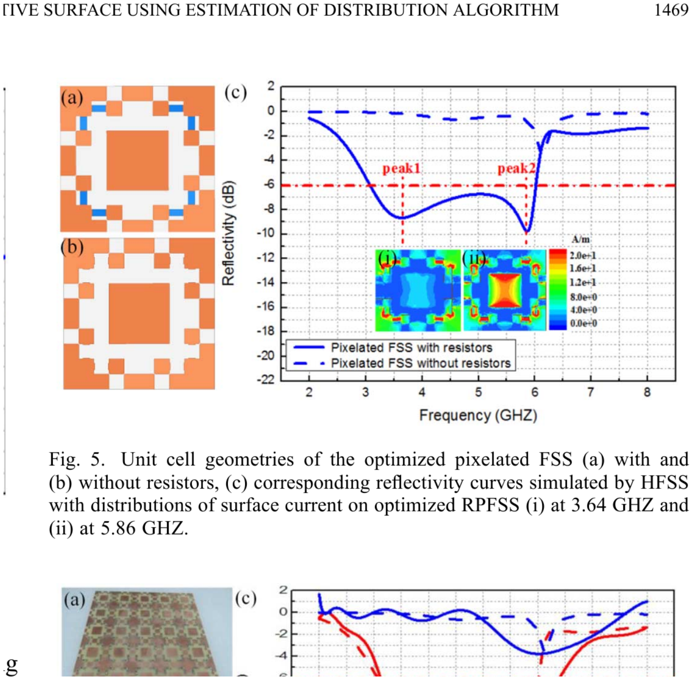

IVE SURFACE USING ESTIMATION OF DISTRIBUTION ALGORITHM 1469

Fig. 5. Unit cell geometries of the optimized pixelated FSS (a) with and (b) without resistors, (c) corresponding reflectivity curves simulated by HFSS with distributions of surface current on optimized RPFSS (i) at 3.64 GHZ and (ii) at 5.86 GHZ.

Figure 10.10: Optimized pixelated FSS unit cells and performance: (a) with resistors, (b) without resistors, and (c) corresponding simulated reflectivity curves showing two strong absorption peaks for the resistor-loaded design. Insets show surface current distributions at the two absorption peaks [7].

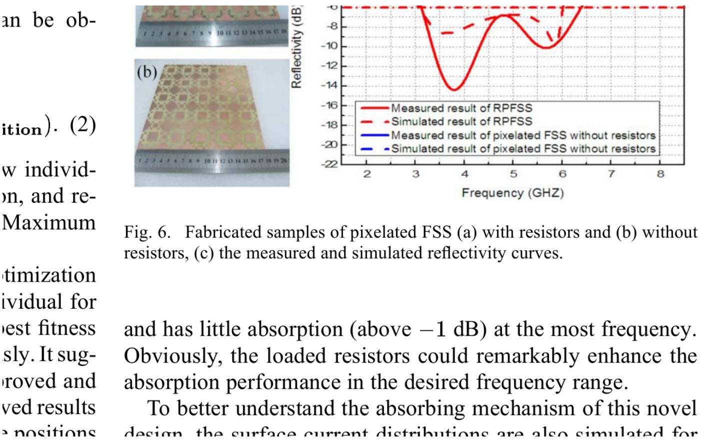

an be ob-

ition). (2)

w individ-
ɔn, and re-
Maximum

timization
ividual for
est fitness
sly. It sug-
roved and
ved results
positions

Fig. 6. Fabricated samples of pixelated FSS (a) with resistors and (b) without resistors, (c) the measured and simulated reflectivity curves.

and has little absorption (above −1 dB) at the most frequency. Obviously, the loaded resistors could remarkably enhance the absorption performance in the desired frequency range.

To better understand the absorbing mechanism of this novel design, the surface current distributions are also simulated for

Figure 10.11: Fabricated pixelated FSS absorber samples: (a) with resistors, (b) without resistors, and (c) measured and simulated reflectivity curves confirming wideband absorption from 3.13 to 6.42 GHz [7].

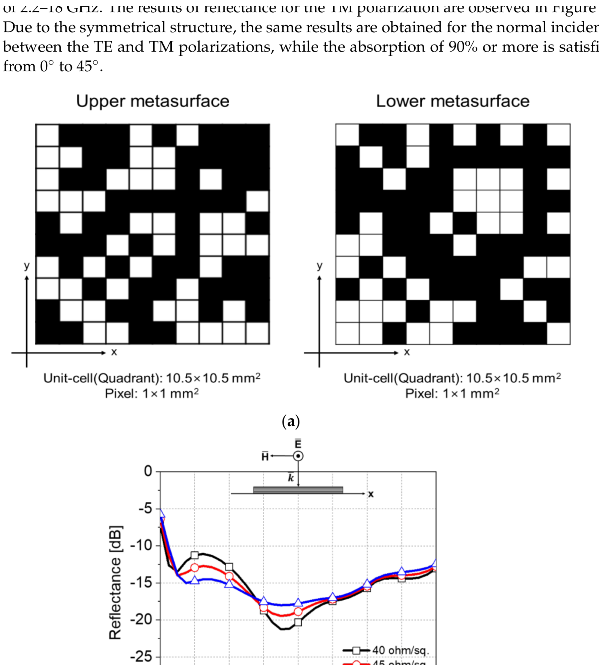

of 2.2–18 GHz. The results of reflectance for the TM polarization are observed in Figure
Due to the symmetrical structure, the same results are obtained for the normal incider
between the TE and TM polarizations, while the absorption of 90% or more is satisfi
from 0° to 45°.

Figure 10.12: GA-optimized dual-layer pixelated absorber by Lee et al.: (a) upper and lower metasurface pixel patterns (20×20 grids with x/y symmetry), and (b) simulated reflectance vs. sheet resistance, showing >90% absorption from 2.2 to 18 GHz at the optimal 40 Ω/sq [8].

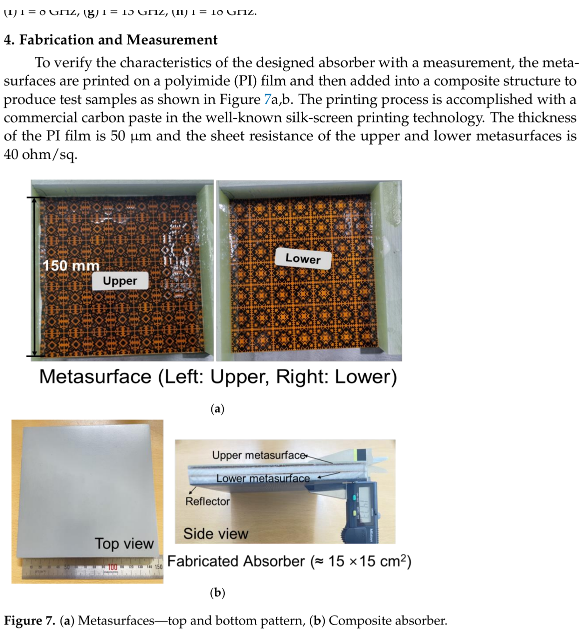

(f) f = 8 GHz, (g) f = 15 GHz, (h) f = 18 GHz.

4. Fabrication and Measurement

To verify the characteristics of the designed absorber with a measurement, the metasurfaces are printed on a polyimide (PI) film and then added into a composite structure to produce test samples as shown in Figure 7a,b. The printing process is accomplished with a commercial carbon paste in the well-known silk-screen printing technology. The thickness of the PI film is 50 µm and the sheet resistance of the upper and lower metasurfaces is 40 ohm/sq.

Figure 7. (**a**) Metasurfaces—top and bottom pattern, (**b**) Composite absorber.

Figure 10.13: Fabricated pixelated composite absorber: (a) silk-screen printed upper and lower metasurface patterns on polyimide film, and (b) assembled composite absorber showing top view and side view with layer stack (GFRP, metasurfaces, PMI foam, CFRP reflector) [8].

plements conventional rectangular waveguide structures in planar printed circuit board form using rows of metallized vias as the waveguide sidewalls, enabling low-cost fabrication and easy integration with planar circuits. However, SIW horn antennas typically suffer from narrow bandwidth, high sidelobe levels, and unequal beamwidths in the E- and H-planes.

Zechmeister, Lacik, and Kadlec [9] applied pixelated optimization to the design of SIW horn antennas operating in the 24 GHz ISM band. The antenna aperture is extended beyond the conventional flared horn and overlaid with a pixelated grid of dielectric and air-filled cells. By optimizing the binary pattern of filled and empty cells, the radiation properties—beamwidth, sidelobe level, gain, and impedance match—can be controlled simultaneously.

The optimization used a novel heuristic algorithm called Binary Ink Stamp Optimization (BISO), which is inspired by stamps with different ink saturation levels. BISO reflects the significance of individual bits during the optimization process, giving it an advantage over standard genetic algorithms for binary pattern problems. The fitness function combines terms for reflection coefficient, beamwidth equality in the E- and H-planes, sidelobe level, and gain. Figure 10.14 shows the simplified model of the pixelated SIW horn antenna and the optimized design with the SIW feeding structure.

Two antenna designs were demonstrated: a linearly polarized (LP) version and a circularly polarized (CP) version using an antipodal configuration. Both use a single-layer structure—a key advantage over multi-layered approaches—and are fabricated using low-cost 3D printing for the dielectric substrate with copper foil for the metallization.

The LP antenna achieves a measured gain of 14.2 dBi at the 24 GHz ISM band center frequency, with reflection coefficient below -18 dB across the full band. The E- and H-plane half-power beamwidths are 26.5° and 25°, respectively—nearly equal, which is the primary design objective. Figure 10.15 shows the manufactured prototype, and Figure 10.16 shows the measured radiation patterns confirming good agreement with simulation and nearly equal beamwidths.

The CP version uses an antipodal structure with top and bottom metal layers to generate circular polarization. The pixelated grid uses 6×28 cells with 13 parameterized column lengths to control the pixel pattern shape. The measured CP antenna achieves 8.9 dBi RHCP gain, an axial ratio below 3 dB across the 24 GHz ISM band, sidelobe levels below -7.4 dB, and half-power beamwidths of 30.6° and 33.4° in the two principal planes. Figure 10.17 shows the manufactured CP prototype.

In a follow-up study, Zechmeister and Lacik [10] improved the CP design by replacing the binary pixelization with a four-state scheme (air, 0.6 mm, 1.0 mm, and 1.6 mm diameter holes), providing finer control over the dielectric distribution. The improved design is 29% shorter than the original, with a wider -10 dB reflection coefficient bandwidth of 21.4%, a 3 dB axial ratio bandwidth of 4.6%, and improved beamwidth equality (less than 1° difference between principal planes).

The pixelated SIW horn work demonstrates that the fragmented aperture philosophy extends naturally to volumetric waveguide structures. Rather than optimizing a planar conducting pattern, the optimizer controls the three-dimensional distribution of dielectric material within the horn, achieving performance that would be difficult to obtain through conventional parametric design.

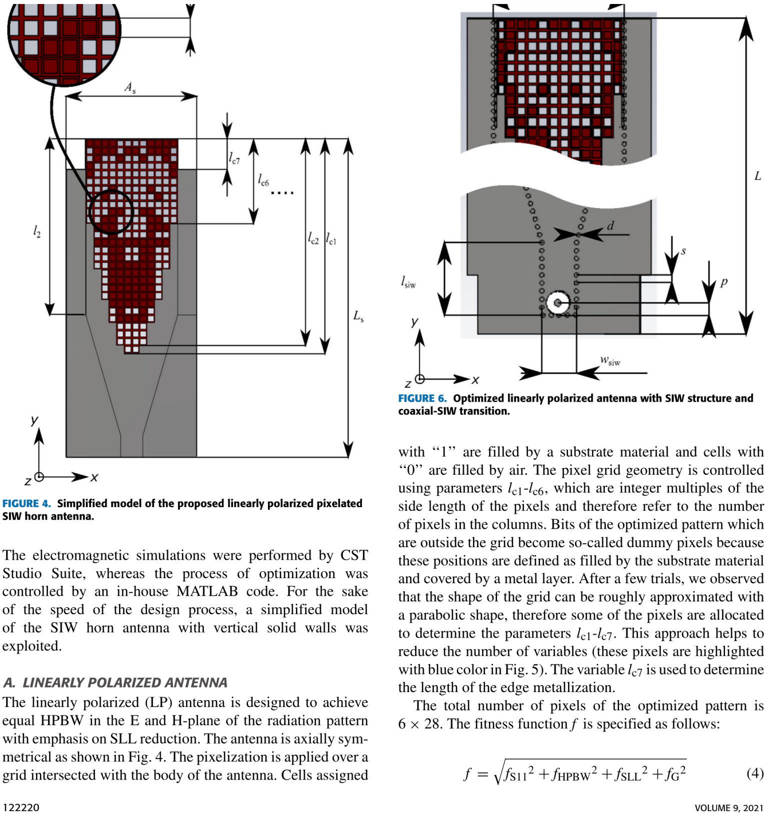

FIGURE 4. **Simplified model of the proposed linearly polarized pixelated SIW horn antenna.**

The electromagnetic simulations were performed by CST Studio Suite, whereas the process of optimization was controlled by an in-house MATLAB code. For the sake of the speed of the design process, a simplified model of the SIW horn antenna with vertical solid walls was exploited.

A. LINEARLY POLARIZED ANTENNA

The linearly polarized (LP) antenna is designed to achieve equal HPBW in the E and H-plane of the radiation pattern with emphasis on SLL reduction. The antenna is axially symmetrical as shown in Fig. 4. The pixelization is applied over a grid intersected with the body of the antenna. Cells assigned with "1" are filled by a substrate material and cells with "0" are filled by air. The pixel grid geometry is controlled using parameters l_{c1}-l_{c6}, which are integer multiples of the side length of the pixels and therefore refer to the number of pixels in the columns. Bits of the optimized pattern which are outside the grid become so-called dummy pixels because these positions are defined as filled by the substrate material and covered by a metal layer. After a few trials, we observed that the shape of the grid can be roughly approximated with a parabolic shape, therefore some of the pixels are allocated to determine the parameters l_{c1}-l_{c7}. This approach helps to reduce the number of variables (these pixels are highlighted with blue color in Fig. 5). The variable l_{c7} is used to determine the length of the edge metallization.

FIGURE 6. **Optimized linearly polarized antenna with SIW structure and coaxial-SIW transition.**

The total number of pixels of the optimized pattern is 6 × 28. The fitness function f is specified as follows:

$$f = \sqrt{f_{S11}{}^2 + f_{HPBW}{}^2 + f_{SLL}{}^2 + f_G{}^2} \qquad (4)$$

Figure 10.14: Pixelated SIW horn antenna design by Zechmeister et al.: (left) simplified model showing the pixelated region applied over the horn aperture, and (right) optimized linearly polarized antenna with SIW structure and coaxial-SIW transition. The dielectric part is 3D-printed and the metal layer is cut copper foil [9].

ıwidths Using BISO

IEEE Access

Figure 10.15: Manufactured prototype of the linearly polarized pixelated SIW horn antenna. The dielectric is 3D-printed XT co-polyester and the metal is cut copper foil with soldered vias [9].

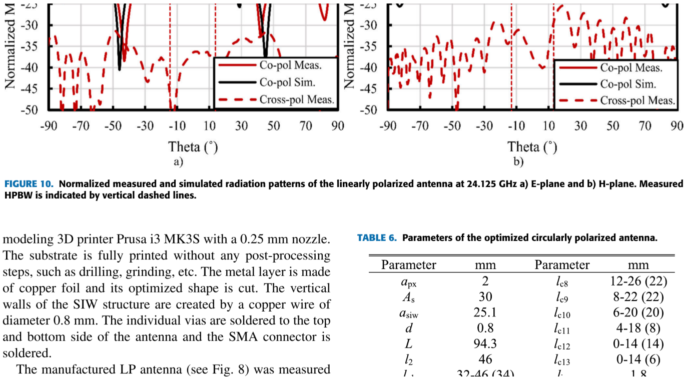

FIGURE 10. **Normalized measured and simulated radiation patterns of the linearly polarized antenna at 24.125 GHz a) E-plane and b) H-plane. Measured HPBW is indicated by vertical dashed lines.**

modeling 3D printer Prusa i3 MK3S with a 0.25 mm nozzle. The substrate is fully printed without any post-processing steps, such as drilling, grinding, etc. The metal layer is made of copper foil and its optimized shape is cut. The vertical walls of the SIW structure are created by a copper wire of diameter 0.8 mm. The individual vias are soldered to the top and bottom side of the antenna and the SMA connector is soldered.

The manufactured LP antenna (see Fig. 8) was measured

TABLE 6. **Parameters of the optimized circularly polarized antenna.**

Parameter	mm	Parameter	mm
a_{px}	2	$l_{\mathrm{c}8}$	12-26 (22)
A_{s}	30	$l_{\mathrm{c}9}$	8-22 (22)
a_{siw}	25.1	$l_{\mathrm{c}10}$	6-20 (20)
d	0.8	$l_{\mathrm{c}11}$	4-18 (8)
L	94.3	$l_{\mathrm{c}12}$	0-14 (14)
l_2	46	$l_{\mathrm{c}13}$	0-14 (6)

Figure 10.16: Measured and simulated radiation patterns of the linearly polarized pixelated SIW horn antenna at 24.125 GHz: (a) E-plane and (b) H-plane. The nearly equal half-power beamwidths (26.5° and 25°) confirm the effectiveness of the pixelated optimization [9].

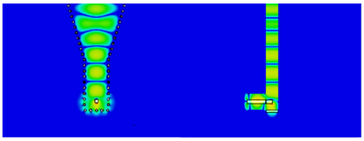

a) b)

FIGURE 14. **Normalized E-field distribution of the circularly polarized antenna at 24.125 GHz in a) xy plane and b) yz plane.**

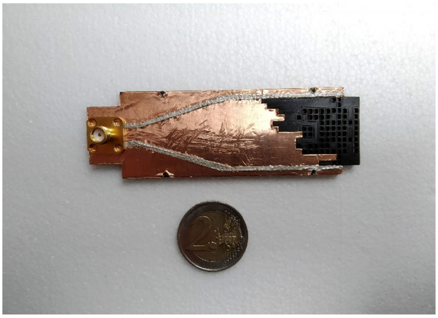

Figure 10.17: Manufactured prototype of the circularly polarized pixelated SIW horn antenna, shown alongside a coin for scale. The antipodal structure achieves RHCP with 8.9 dBi gain and axial ratio below 3 dB across the 24 GHz ISM band [9].

10.7 Pixelated Radomes and RCS Reduction

A particularly compelling application of pixelated and optimized metasurface design is in the development of low-observable radomes—protective enclosures for antennas that must transmit in-band signals efficiently while minimizing out-of-band radar cross section (RCS). Conventional frequency-selective surface (FSS) radomes reflect out-of-band energy back toward the source, creating a significant RCS signature. By combining pixelated phase gradient metasurfaces with bandpass FSS structures, and optimizing the composite design with algorithms such as particle swarm optimization (PSO), it is possible to redirect out-of-band energy away from the monostatic direction while maintaining high in-band transmission.

Haji-Ahmadi et al. [11] demonstrated a pixelated checkerboard metasurface for ultra-wideband RCS reduction. The design uses a chessboard arrangement of two types of pixelated artificial magnetic conductor (AMC) unit cells, each optimized via binary particle swarm optimization (BPSO) to produce a specific reflection phase. Each cell uses a 16×16 pixel grid with 8-fold symmetry, reducing the optimization to 36 independent bits per cell type (72 total). The two cell types are arranged in a checkerboard pattern such that their reflected fields maintain a $180° \pm 37°$ phase difference, causing destructive interference in the broadside direction and scattering the energy into other angles.

Figure 10.18 shows the optimized pixelated unit cell layouts and the resulting out-of-phase reflection bandwidth. The BPSO optimizer discovers irregular, non-intuitive conducting patterns that would be impossible to design analytically.

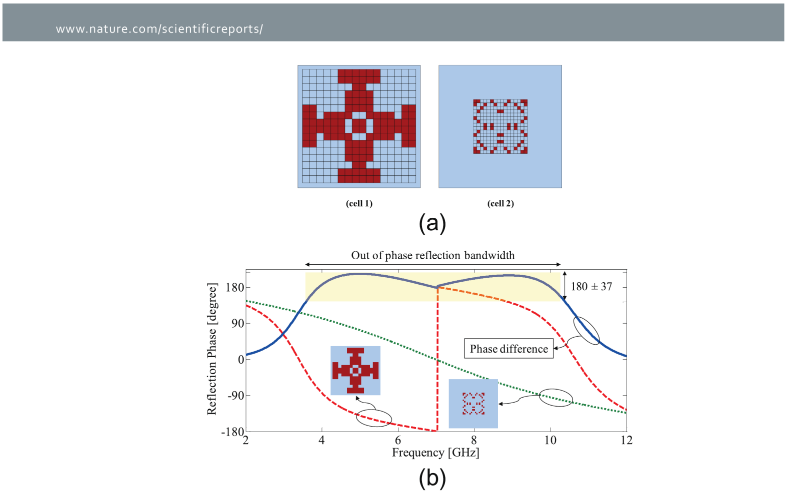

Figure 10.18: Pixelated checkerboard RCS reducer by Haji-Ahmadi et al.: (a) optimized pixelated unit cell layouts for cell type 1 and cell type 2, and (b) reflection phase from each cell and phase difference, showing the required 180° ± 37° out-of-phase condition maintained from 3.6 to 10.4 GHz [11].

The pixelated checkerboard metasurface was fabricated on Rogers RO4003c substrate with a PTFE spacer and measured in an anechoic chamber. Figure 10.19 shows the fabricated prototype and the measured monostatic RCS comparison. The measured 10 dB RCS reduction bandwidth extends from 3.8 to 10.7 GHz (95% fractional bandwidth), with a maximum reduction of 36.5 dB at 7.3 GHz. This significantly outperforms prior checkerboard designs based on conventional (non-pixelated) AMC unit cells, which achieved fractional bandwidths of only 41–63%.

Pang et al. [12] proposed a broadband low-scattering radome that combines phase gradient metasurfaces with an FSS, achieving over 10 dB RCS reduction from 7.95 to 18.12 GHz (a 78% relative bandwidth) while maintaining less than 1 dB insertion loss in the 15.95–17.7 GHz passband. The PSO-optimized structure is ultra-thin at only 0.08λ at the lowest operating frequency. *[Figures and detailed discussion to be added when the full paper is obtained.]*

These radome and RCS reduction designs illustrate how the pixelated optimization approach addresses a fundamentally different electromagnetic challenge: rather than maximizing radiation or absorption, the goal is to simultaneously control transmission (in-band) and scattering (out-of-band) properties of a surface.

10.8 Pixelated Energy Harvesting

The pixelated metasurface concept has also been applied to electromagnetic energy harvesting—the capture of ambient or intentionally transmitted RF energy and its conversion to usable DC power. Energy harvesting metasurfaces must efficiently absorb in-

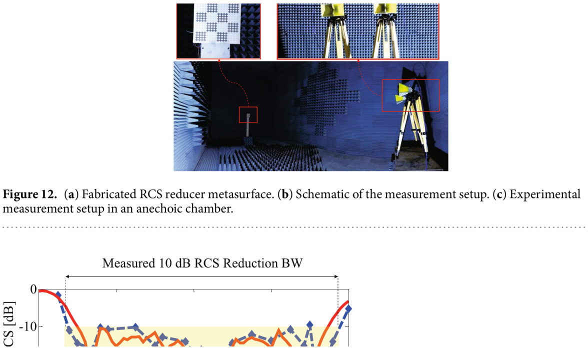

Figure 12. (**a**) Fabricated RCS reducer metasurface. (**b**) Schematic of the measurement setup. (**c**) Experimental measurement setup in an anechoic chamber.

Figure 10.19: Measured and simulated monostatic RCS of the pixelated checkerboard metasurface, normalized to an equal-size metal plate. The measured 10 dB RCS reduction bandwidth extends from 3.8 to 10.7 GHz (95% fractional bandwidth), with a maximum reduction of 36.5 dB at 7.3 GHz [11].

cident electromagnetic energy across multiple frequency bands and polarizations, then couple it to resistive loads (or rectifying circuits) through vias.

Ghaderi et al. [13] demonstrated a pixelated metasurface for dual-band, multi-polarization electromagnetic energy harvesting. The unit cell combines a ring resonator (for the 2.45 GHz WiFi band) and a symmetric electric-LC (ELC) resonator (for the 6 GHz band), with resistive loads connected through vias to the ground plane. The cell surface is pixelated into a 27×27 grid (0.41 mm pixel resolution) with 4-fold symmetry, yielding approximately 105 independent optimization variables. The BPSO algorithm simultaneously optimizes the pixel pattern, load resistance ($R = 240\ \Omega$), and gap size ($g = 0.25$ mm).

Figure 10.20 shows the BPSO-optimized pixelated unit cell. The irregular, fractal-like conducting pattern discovered by the optimizer combines the dual-band resonant behavior with efficient coupling to the via-connected loads. The design achieves polarization-independent operation—a critical requirement for harvesting ambient RF energy arriving from arbitrary directions and polarizations.

A 9×9 array of the optimized unit cells was fabricated on Rogers RT/duroid 6006 substrate and measured in an anechoic chamber. Figure 10.21 shows the measurement setup. The measured harvesting efficiency exceeds 90% at both 2.45 and 6 GHz for all polarization angles, confirming the polarization-independent design. The delivered power is also insensitive to incidence angle from 0° to 45° for both TE and TM polarizations. This work demonstrates that the pixelated optimization approach can produce electromagnetic structures optimized for energy capture rather than radiation or scattering—yet another application of the same fundamental design philosophy.

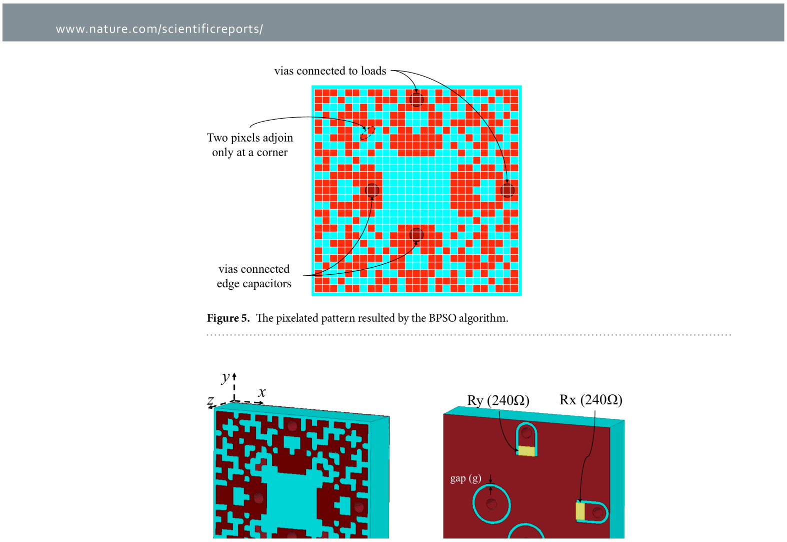

www.nature.com/scientificreports/

Figure 5. The pixelated pattern resulted by the BPSO algorithm.

Figure 10.20: BPSO-optimized pixelated energy harvesting unit cell by Ghaderi et al.: (top) 3D view of the optimized 27×27 pixel pattern showing the irregular conducting geometry with vias to loads and edge capacitors, and (bottom) top and bottom views of the fabrication-ready design with 240 Ω resistive loads [13].

10.9 Pixelated Microwave Filters

Microwave filters are fundamental components in communication systems, and their design has traditionally relied on analytical synthesis methods based on coupled resonator theory. Gomez et al. [14] demonstrated that the pixelated inverse design approach can produce compact bandpass and notch filters in coplanar waveguide (CPW) technology, achieving performance comparable to conventional designs in a significantly smaller footprint.

The filter design region is a pixelated area within a CPW transmission line, where each pixel is either conducting (copper) or absent (etched away). The optimization uses a genetic algorithm combined with direct binary search and randomization mutation, driven by CST Microwave Studio simulations. The design begins with a coarse 24×16 grid (400 μm pixels) and refines to a 48×32 grid (200 μm pixels). A key innovation is the integration of short-circuited stubs at the top and bottom of the pixelated region, which dramatically improves stopband rejection.

Figure 10.22 shows the proposed pixelated notch filter schematic and the fabricated prototype. The filter is fabricated on Rogers Kappa 438 substrate via UV laser ablation, which precisely removes copper to define the pixelated pattern at 200 μm resolution. The irregular conducting pattern discovered by the optimizer bears no resemblance to conventional coupled-line or interdigitated filter topologies.

Figure 10.23 shows the measured and simulated S-parameters. The filter without short-circuited stubs achieves a notch depth of -26 dB at 5 GHz, while the version

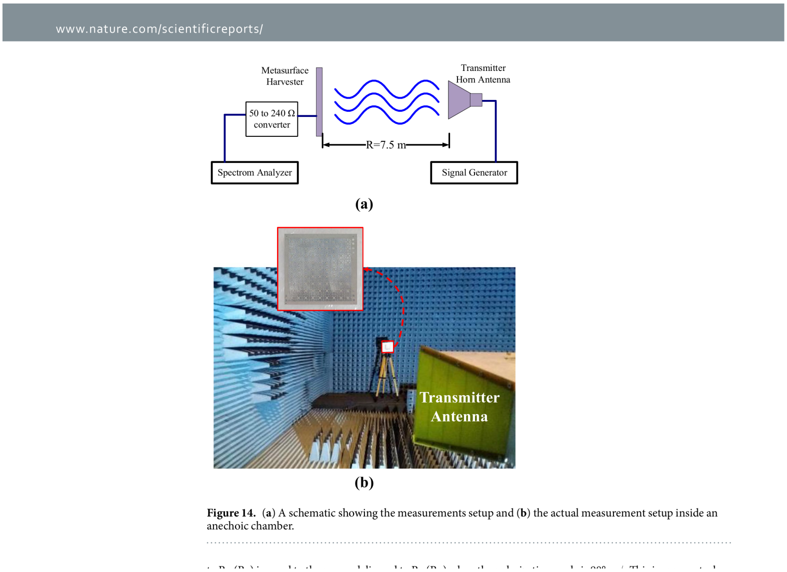

Figure 14. (**a**) A schematic showing the measurements setup and (**b**) the actual measurement setup inside an anechoic chamber.

Figure 10.21: Measurement of the pixelated energy harvesting metasurface: (a) schematic of the test setup with 50-to-240 Ω converter and spectrum analyzer, and (b) anechoic chamber photograph showing the 9×9 array under test with a transmitter horn antenna [13].

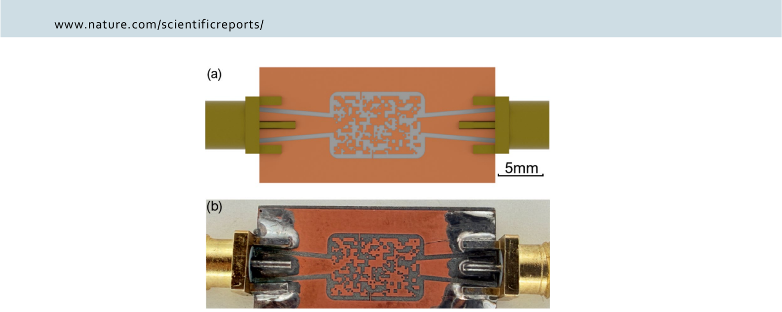

Figure 10.22: Pixelated microwave notch filter by Gomez et al.: (a) schematic showing the irregular optimized conducting pattern in a CPW structure, and (b) photograph of the fabricated filter on Rogers Kappa 438 substrate with SMA connectors [14].

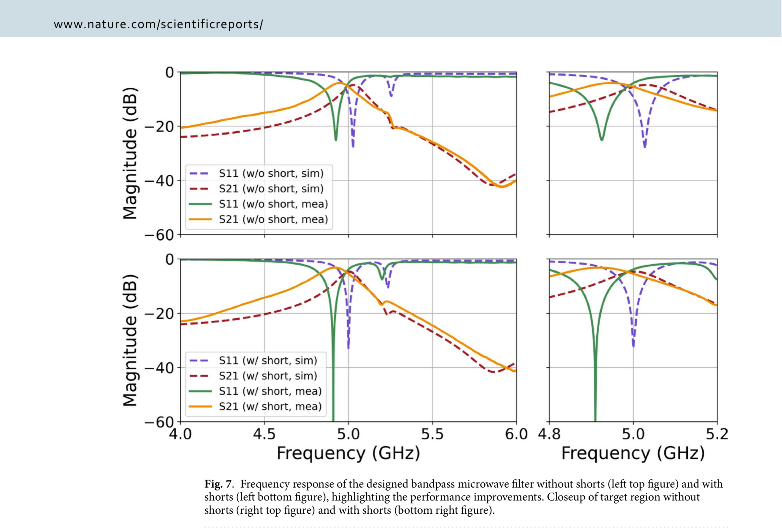

www.nature.com/scientificreports/

Fig. 7. Frequency response of the designed bandpass microwave filter without shorts (left top figure) and with shorts (left bottom figure), highlighting the performance improvements. Closeup of target region without shorts (right top figure) and with shorts (bottom right figure).

Figure 10.23: Measured and simulated S-parameters of the pixelated filter: (top) without short-circuited stubs showing -26 dB notch depth, and (bottom) with shorted stubs achieving -61 dB notch depth—a 35 dB improvement. The pixelated design area is less than half the size of an equivalent conventional filter [14].

with shorted stubs reaches -61 dB—a 35 dB improvement. The pixelated filter occupies only 61.5 mm^2, less than half the area of an equivalent third-order Chebyshev interdigitated filter. This compact size, combined with the single-layer, via-free construction, makes pixelated filters attractive for integrated microwave circuits.

10.10 Summary

The examples in this chapter demonstrate that the fragmented aperture concept is not limited to antenna design. The core methodology—pixelated conducting surfaces optimized by evolutionary algorithms with full-wave electromagnetic evaluation—applies to any electromagnetic structure whose performance depends on the spatial distribution of conducting material:

- **Broadband phase surfaces** with engineered transmission phase properties, as demonstrated in the original patent.
- **RF power combiners** that outperform conventional COTS components in insertion loss and bandwidth, enabling integrated all-fragmented antenna systems.
- **Pixelated absorbers** that achieve ultra-thin, wideband absorption through jointly optimized conducting pixels and lumped resistors.

- **Pixelated waveguide components**, specifically SIW horn antennas with optimized dielectric distributions that achieve equal beamwidths and circular polarization in single-layer structures.
- **Radomes and RCS reduction** surfaces that combine optimized metasurfaces with frequency-selective structures for simultaneous in-band transmission and out-of-band scattering control.
- **Energy harvesting** metasurfaces that efficiently capture dual-band, multi-polarization RF energy for wireless power transfer applications.
- **Microwave filters** with pixelated conducting patterns that achieve compact notch and bandpass responses in single-layer CPW structures.
- **Metamaterials and metasurfaces** including near-zero index materials with measured 6 dB gain enhancement, broadband frequency-selective surfaces, and resonant structures for materials characterization.

As the fragmented aperture design process continues to be refined—through improved optimization algorithms (Chapter 3), continuous parameterizations (Chapter 9), and machine learning acceleration (Chapter 9)—its application to non-antenna electromagnetic structures will expand further. Any electromagnetic problem that can be cast as "what pattern of conducting material on a surface optimizes a given performance metric?" is a candidate for the fragmented aperture approach.

References

[1] J. G. Maloney, M. P. Kesler, P. H. Harms, and G. S. Smith, "Fragmented aperture antennas and broadband ground planes," U.S. Patent No. 6,323,809 B1, Nov. 2001.

[2] A. Saad-Falcon, C. Howard, J. Romberg, and K. Allen, "Level set methods for gradient-free optimization of metasurface arrays," *Scientific Reports*, vol. 14, p. 16674, Jul. 2024, arXiv preprint: 2307.07606.

[3] C. Howard *et al.*, "A loss tangent measurement surface for free space focused beam characterization of low-loss dielectrics," in *2022 IEEE International Symposium on Phased Array Systems and Technology (PAST)*, 2022, pp. 1–6.

[4] D. W. Landgren, T. Brunasso, J. B. Dee, J. Perez, D. J. P. Dykes, J. M. Marsh, C. P. Hunter, and K. W. Allen, "Wideband phased array antenna design with fragmented combiner technology," in *IEEE National Aerospace and Electronics Conference (NAECON)*, Jun. 2018, pp. 602–606.

[5] D. Landgren, T. Brunasso, K. Allen, D. Dykes, J. Kovitz, J. Perez, J. Dee, J. Marsh, C. Hunter, and G. Smith, "A broadband array with unbalanced feeds : Elements and power combiners based on the fragmented aperture principle," in *2019 IEEE International Symposium on Antennas and Propagation and USNC-URSI Radio Science Meeting*, 2019, pp. 1223–1224.

[6] S. Sun, Y. Jiang, and J. Wang, “Automatic design of pixelated near-zero refractive index metamaterials based on elite-preserving genetic algorithm optimization,” *Results in Physics*, vol. 48, p. 106461, 2023.

[7] M. Zhao, X. Yu, Q. Wang, P. Kong, Y. He, L. Miao, and J. Jiang, “Novel absorber based on pixelated frequency selective surface using estimation of distribution algorithm,” *IEEE Antennas and Wireless Propagation Letters*, vol. 14, pp. 1467–1470, 2015.

[8] C. Lee, K. Kim, P. Park, Y. Jang, J. Jo, T. Choi, and H. Lee, “Ultra-wideband electromagnetic composite absorber based on pixelated metasurface with optimization algorithm,” *Materials*, vol. 16, p. 5916, 2023.

[9] J. Zechmeister, J. Lacik, and P. Kadlec, “The design of pixelated siw horn antennas with nearly equal beamwidths using binary ink stamp optimization,” *IEEE Access*, vol. 9, pp. 122 216–122 227, 2021.

[10] J. Zechmeister and J. Lacik, “Pixelated circularly polarized siw horn antenna with nearly equal beamwidths in principal planes,” in *2022 24th International Microwave and Radar Conference (MIKON)*, 2022, pp. 1–4.

[11] M.-J. Haji-Ahmadi, V. Nayyeri, M. Soleimani, and O. M. Ramahi, “Pixelated checkerboard metasurface for ultra-wideband radar cross section reduction,” *Scientific Reports*, vol. 7, p. 11437, 2017.

[12] X. Pang, T. Zhang, M. Hu, H. Zhang, and Q. Zheng, “Broadband low-scattering and high-efficiency transmission radome by combining phase gradient metasurface and FSS,” *Optics Communications*, vol. 563, p. 130598, 2024.

[13] B. Ghaderi, V. Nayyeri, M. Soleimani, and O. M. Ramahi, “Pixelated metasurface for dual-band and multi-polarization electromagnetic energy harvesting,” *Scientific Reports*, vol. 8, p. 13227, 2018.

[14] M. A. Gomez, W. Jia, S. Blair, and B. Sensale-Rodriguez, “Compact bandpass pixelated microwave filters with short-circuited stubs via inverse design,” *Scientific Reports*, vol. 15, p. 25606, 2025.

Appendix A

Computational Modeling of Antennas

A.1 Acknowledgement

The author would like to personally thank Professor Glenn Smith, Georgia Tech Regents Professor Emeritus, for his tremendous help in compiling this appendix on the computational modeling of antennas. Much of this material was published in the Balanis Antenna Engineering Handbook [41] and earlier in the Taflove book on computational electrodynamics [7].

A.2 Introduction

The finite-difference time-domain (FDTD) method is a computational procedure for solving Maxwell's equations that is based on a clever algorithm first proposed by Kane S. Yee in 1966 [1]. When Yee proposed his algorithm, the method was computationally intensive in terms of both storage and run time, and only problems of very modest size could be solved using the best computational facilities (mainframe computers). Since then the power of computers has steadily increased, as has the popularity of the FDTD method. The first comprehensive analyses of practical antennas using the method were performed during the early 1990s, and today such computations are routinely performed on personal computers [2]–[6].

The purpose of this appendix is to introduce the reader to the fundamentals of the FDTD method as applied to practical antennas. After studying this material, the reader should understand both the power and the limitations of the method and be in a position to decide whether the FDTD method is suitable for analyzing a particular antenna problem. Because of the limited space, we cannot provide the details for implementing the method in a computer program. Readers interested in writing their own program are referred to [7] for the details; others may wish to use one of the commercially available FDTD computer codes.

A.3 The Basic FDTD Algorithm

In the Yee algorithm, both space and time are discretized, with the increments in space for rectangular coordinates being Δx, Δy, Δz and the increment in time being Δt [8], [9]. Figure A.1 is a schematic drawing showing a typical volume in which Maxwell's equations are to be solved. The volume is divided into unit cells, and the electromagnetic constitutive parameters ($\epsilon = \epsilon_r \epsilon_o$, $\mu = \mu_r \mu_o$, σ) can vary from cell to cell to define different objects within the volume.[1] The six components of the electromagnetic field $(E_x, E_y, E_z; H_x, H_y, H_z)$ are distributed over a unit cell (Yee cell) as shown in the inset of Figure A.1. Notice that all of the components are located at different points within the cell, and the components of H are displaced from those of E by one half of a spatial increment, e.g., $\Delta x/2$. Although not shown in the figure, the components of H are also evaluated at points displaced by one half of a time increment, $\Delta t/2$, from those of E.

The partial derivatives in Maxwell's equations are approximated by ratios of differences, for example,

$$\frac{\partial E_x}{\partial z} \approx \frac{\Delta E_x}{\Delta z}, \quad \frac{\partial H_y}{\partial t} \approx \frac{\Delta H_y}{\Delta t} \tag{A.1}$$

For the spatial derivatives, the increment in the numerator is formed by differencing corresponding field components from adjacent unit cells, and for the temporal derivatives, it is formed by differencing field components from two adjacent time steps, e.g., t and $t + \Delta t$. The discretized Maxwell's equations are arranged to form two sets of difference equations known collectively as "update equations." The first set, which we will call A, determines the change in the magnetic field, $H(t + \Delta t/2) - H(t - \Delta t/2)$, from the electric field at an intermediate time step, $E(t)$. The second set, which we will call B, determines the change in the electric field, $E(t + \Delta t) - E(t)$, from the magnetic field at an intermediate time step, $H(t + \Delta t/2)$.

At the start of the computation, we have the initial conditions: throughout the computational volume, the electric field is known at time $t = 0$, and the magnetic field is known at the earlier time $t = -\Delta t/2$. The update equations A are then used with the initial conditions to obtain the magnetic field at time $t = \Delta t/2$. Next, the update equations B are used with the magnetic field just obtained and the electric field at time $t = 0$ to obtain the electric field at time $t = \Delta t$. This procedure of alternately applying update equations A and B to advance the solution in time is known as "marching-in-time" or "stepping-in-time." It is repeated until the electromagnetic field is known throughout the computational volume at the desired time $t = t_{\text{max}} = N_t \Delta t$.

The choice for the increments of space and time (Δx, Δy, Δz, and Δt) is critical to the success of the algorithm, because their size determines how well the solution to the difference equations approximates the solution to Maxwell's equations. The spatial and temporal increments cannot be chosen independently; for convergence (as $\Delta x \to 0$, $\Delta t \to 0$, etc.) and stability of the algorithm, the increments must satisfy the Courant-Friedrichs-Lewy condition, which for free space is

---

[1] Here we mention only simple materials with constant permittivity, permeability, and electrical conductivity. In the FDTD method there are techniques to handle more complicated materials, such as those with dispersive and anisotropic properties [9].

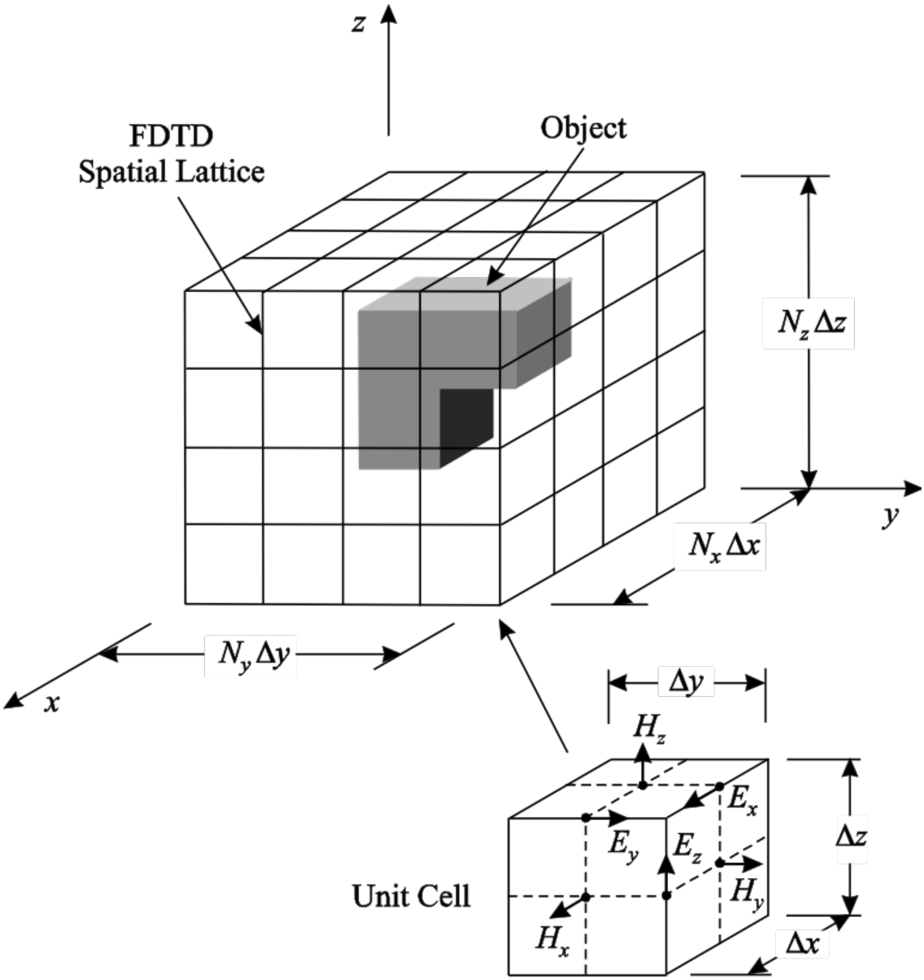

Figure A.1: Schematic drawing showing the computational volume, FDTD spatial lattice, and unit cell.

$$c\Delta t\sqrt{\frac{1}{\Delta x^2}+\frac{1}{\Delta y^2}+\frac{1}{\Delta z^2}} \leq 1. \tag{A.2}$$

For cubical cells, $\Delta x = \Delta y = \Delta z$, Equation (A.2) becomes $S = c\Delta t/\Delta x \leq \sqrt{1/3}$, where S is referred to as the "Courant number," and a reasonable choice is $S = 1/2$.

Additional restrictions on the spatial and temporal increments can only be obtained from knowledge of the variation of the field (the solution) in space and time. We must make Δz and Δt in Equation (A.1) small enough that the errors incurred by replacing the derivatives by the ratios of differences are acceptable. One obvious requirement is that the size of the spatial cells must be small enough to resolve all of the important structural features and the local field surrounding these features. Another requirement is that the error introduced by a phenomenon known as "numerical dispersion" must be negligible.

When there is numerical dispersion, a pulse that starts out with one shape ends up with a different shape after propagating through the FDTD lattice. Numerical dispersion is caused by the different frequency components of the pulse propagating through the lattice with different phase velocities. It can be quantified by considering a time-harmonic plane wave of angular frequency ω propagating in free space along one of the axes of the FDTD lattice, say the x axis. Assuming cubical cells, the numerical phase velocity, $\bar{v}_p$, for the wave, normalized to the speed of light in free space c, is

$$\frac{\bar{v}_p}{c} = \pi\left\{N_\lambda \sin^{-1}\left[\frac{1}{S}\sin\left(\frac{\pi S}{N_\lambda}\right)\right]\right\}^{-1}, \tag{A.3}$$

in which $N_\lambda = \lambda/\Delta x$ is the number of cells per wavelength [10]. Figure A.2 is a graph of this equation showing the relative error in the phase velocity in percent (solid line) and a related quantity, the error in the phase per cell in degrees (dashed line). Notice that the phase velocity is less than the speed of light, and that the error decreases monotonically with an increase in N_λ. For large N_λ (say $N_\lambda > 10$), the error in the phase velocity is approximately $(\pi^2/6)(1-S^2)/N_\lambda^2$, so halving the cell size reduces the error by a factor of four. In theory, any desired accuracy can be obtained by increasing N_λ.

Ideally, given an electromagnetics problem, we would like to estimate accurately the computational resources (computer memory and execution time) required to solve the problem using the FDTD method. This estimate is highly dependent on the problem and the computer being used. In practice, the estimate is usually made by comparing the requirements for the problem under consideration with those of a "benchmark problem" that has been run using a particular FDTD code on a particular computer. Even though the specific requirements are computer dependent, general rules for the scaling of the required memory and execution time with cell size are easily obtained.

Consider a computational volume that is a cube composed of cubical FDTD cells; then the total number of cells is $N = N_x^3$. Because only the most recent values of the electric and magnetic fields are needed at each step of the algorithm, the total storage required scales as N or N_x^3, i.e., as the third power of the number of cells along the edge of the cubical volume. The simulation must be run for a time roughly proportional to that required for light to cross the volume, $t_{\text{max}} \propto N_x \Delta x/c$. Thus, the number of time

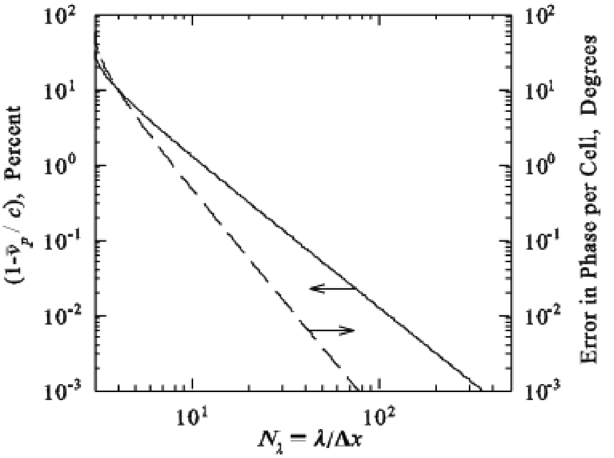

Figure A.2: Numerical dispersion as a function of the number of cells per wavelength, N_λ, for a time-harmonic plane wave propagating along one of the axes of an FDTD lattice of cubical cells. Solid line: the relative error in the phase velocity in percent. Dashed line: the error in the phase per cell in degrees. $S = 0.5$.

steps required is $N_t = t_{\text{max}}/\Delta t \propto N_x/S \propto N_x$. The execution time is proportional to the product of the number of cells with the number of times the cells must be updated: $N \times N_t \propto N_x^4$. The execution time therefore scales as the fourth power of the number of cells along the edge of the cubical volume. If we halve the dimensions of the cells, the storage will increase by a factor of 8, and the execution time will increase by a factor of 16.

A.4 Formulation of the Antenna Problem in the FDTD Method

Antennas are customarily used in two states: transmission and reception. While the two states are related through the reciprocity inherent in Maxwell's equations, not all quantities for one state can be obtained from the other. Thus, we must have two separate FDTD formulations for the antenna problem: one for the transmitting antenna and the other for the receiving antenna.

A.4.1 Transmitting Antenna

Figure A.3(a) is a schematic drawing showing the basic elements involved in the FDTD analysis of a transmitting antenna. The figure is for a cross section through the computational volume, and the antenna is located near the center of the volume. The arrangement used to excite the antenna is shown in Figure A.4(a). The antenna is connected to the source by a transmission line (waveguide) of characteristic impedance R_o, and the source is matched to the characteristic impedance (there is no reflection for a wave entering the source).[2] The specified excitation is the outward-propagating (incident) voltage wave $V_t^+(t)$ for a single mode at the reference plane in the line. At this reference plane there is also a voltage $V_t^-(t)$ associated with an inward-propagating (reflected) wave.

The finite computational volume in Figure A.3(a) is surrounded by an absorbing boundary. The objective for this boundary is to reproduce at its interior surface the same conditions for the electromagnetic field that would exist if the volume were infinite. Stated differently, if we consider the electromagnetic field within the volume to be composed of a spectrum of plane waves, both outward propagating and evanescent, all of these waves should be absorbed without reflection by the boundary. The most effective absorbing boundaries in use today are the perfectly matched layers (PMLs). Their implementation is discussed in the literature [11], [12].

The FDTD method provides the electromagnetic field for all lattice points within the finite computational volume. However, for many antenna applications, we need the radiated or far-zone field, which is the field in the limit as the radial distance from the antenna becomes infinite ($r \to \infty$). This field can be obtained by applying a near-field to far-field (NFFF) transformation. For this transformation, a closed surface S is placed around the antenna and inside the absorbing boundary, as shown by the dashed line in Figure A.3. The field (E^t and H^t) on this surface is obtained for the time period of interest and used to calculate the following electric and magnetic surface current densities:

$$J_s(r', t) = \hat{n} \times H^t(r', t), \tag{A.4}$$

$$M_s(r', t) = -\hat{n} \times E^t(r', t). \tag{A.5}$$

Here, as shown in Figure A.3(b), r' locates a point on the surface, and $\hat{n}$ is the outward-pointing unit vector normal to the surface at that point. Outside the surface S, these currents produce the same electromagnetic field as the transmitting antenna (E^t, H^t), and inside the surface they produce a null field ($E = 0$, $H = 0$).

At the position r, the radiated or far-zone field (indicated by the additional superscript r) is obtained using these currents with a version of Huygens' principle for electromagnetic fields [8]:

$$E^{tr}(r, t) = \frac{\mu_o}{4\pi r} \iint\limits_S \left\{ \hat{r} \times \hat{r} \times \frac{\partial}{\partial t'} \left[J_s(r', t') \right] + \frac{1}{\eta_o} \hat{r} \times \frac{\partial}{\partial t'} \left[M_s(r', t') \right] \right\}_{t' = t_r} dS', \tag{A.6}$$

$$H^{tr}(r, t) = \frac{1}{\eta_o} \hat{r} \times E^{tr}(r, t), \tag{A.7}$$

in which the retarded time is

---

[2] Throughout this appendix we will assume that the characteristic impedance of a transmission line is real, a resistance.

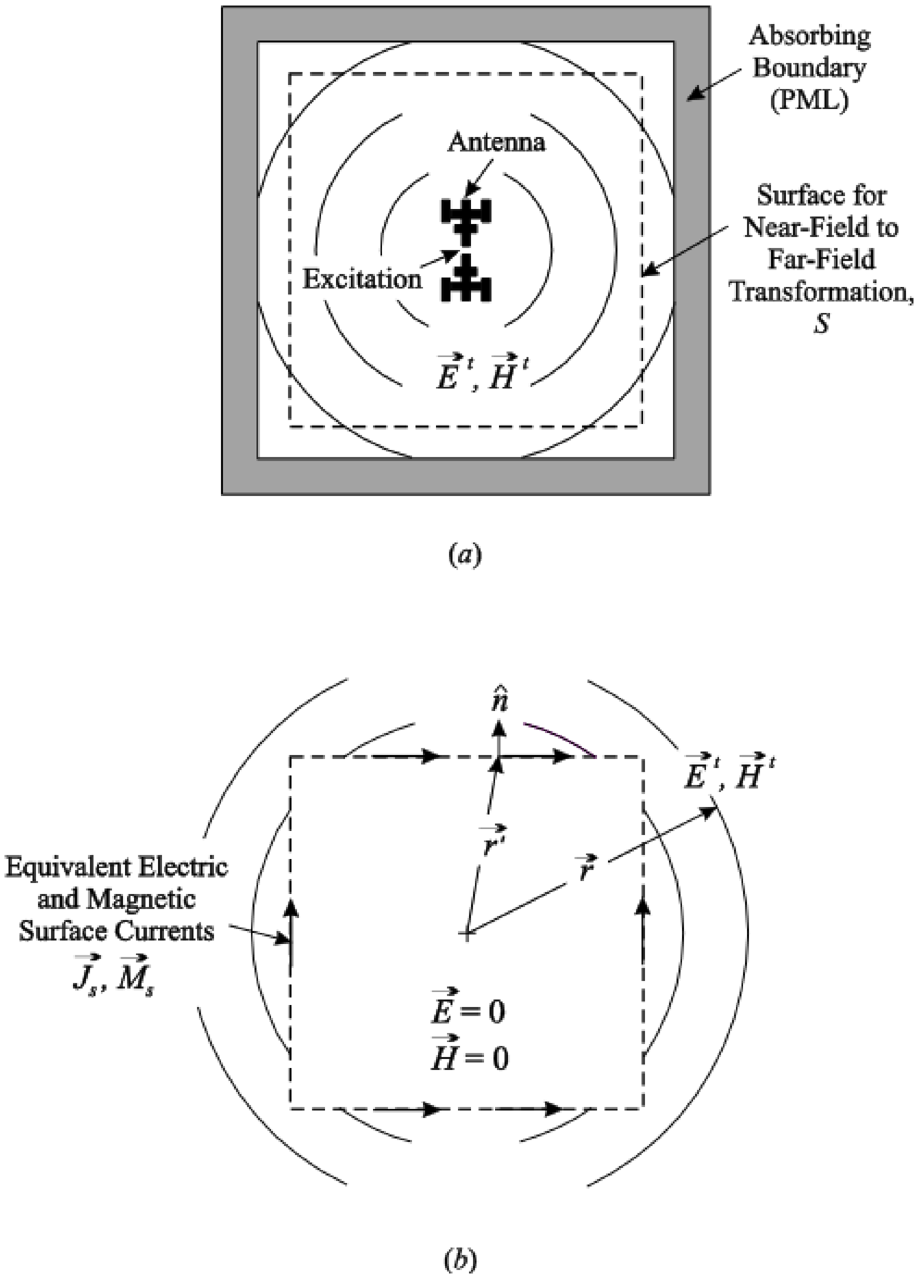

Figure A.3: (a) Schematic drawing showing the basic elements involved in the FDTD analysis of a transmitting antenna. (b) Details for the near-field to far-field transformation.

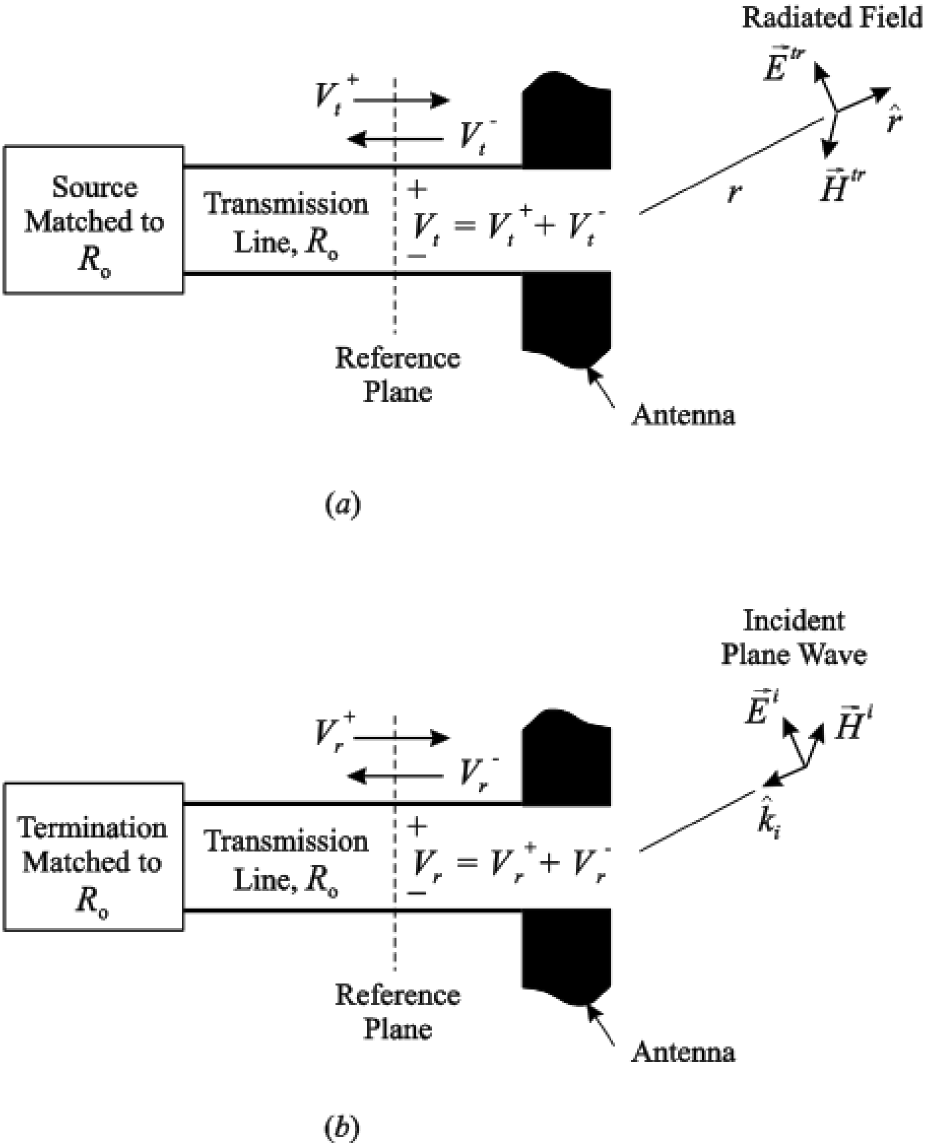

Figure A.4: The details for the feed region of (a) the transmitting antenna and (b) the receiving antenna. The characteristic impedance of the transmission line is R_o, and the source and termination are matched to this impedance.

$$t_r = t - (r - \hat{r} \cdot \vec{r}\,')/c \tag{A.8}$$

and $\eta_o = \sqrt{\mu_o/\epsilon_o}$ is the wave impedance of free space.

In some situations, we may require the near field at points that are so far from the antenna that it is impractical to extend the computational volume to include them. In such cases, a near-field to near-field (NFNF) transformation can be used: the FDTD analysis is performed for a volume such as that shown in Figure A.3(a), and the field on the surface of the volume is transformed to obtain the near field outside the volume. Details for the NFNF transformation can be found in [13], [14].

A.4.2 Receiving Antenna

Figure A.5(a) is a schematic drawing showing the basic elements involved in the FDTD analysis of a receiving antenna. As for the transmitting antenna, the figure is for a cross section through the computational volume, and the finite computational volume is surrounded by an absorbing boundary. The excitation for the antenna is an incident, transverse electromagnetic (TEM) plane wave propagating in the direction $\hat{k}_i$ with the field

$$E^i(r,t), \quad H^i(r,t) = \frac{1}{\eta_o}\hat{k}_i \times E^i(r,t). \tag{A.9}$$

Here, the vector E^i is transverse to $\hat{k}_i$, viz, $\hat{k}_i \cdot E^i = 0$.

The closed surface S with outward-pointing unit normal vector $\hat{n}$ is placed around the antenna and inside the absorbing boundary. As shown in Figure A.5(b), the following electric and magnetic surface current densities are placed on this surface to produce the incident field (E^i, H^i) inside the surface and a null field ($E = 0$, $H = 0$) outside the surface:

$$J_s(r,t) = -\hat{n} \times H^i(r,t), \quad M_s(r,t) = \hat{n} \times E^i(r,t). \tag{A.10}$$

For the receiving antenna, we generally want to know the voltage produced in the antenna by the incident wave. The arrangement used to accomplish this is shown in Figure A.4(b). The antenna is connected to the termination by a transmission line (waveguide) of characteristic impedance R_o, and the termination is matched to the characteristic impedance (there is no reflection for a wave entering the termination). The desired response is the inward-propagating voltage wave $V_r^-(t)$ for a single mode at the reference plane in this line.

The scattered field is the field produced by the currents induced in the antenna by the incident field. Notice from Figure A.5(a) that the field inside the surface S is the total field, i.e., the sum of the incident and scattered fields ($E^r = E^i + E^s$, $H^r = H^i + H^s$). However, the field outside the surface, in the region between the surface and the absorbing boundary, is only the scattered field (E^s, H^s). If we are interested in the scattering properties of the antenna, we can obtain them from knowledge of the field in this region. For example, the far-zone scattered field can be determined using a near-field to far-field transformation, as in the case for the transmitting antenna. The surface for the transformation must be placed between the surface for the plane-wave source and the absorbing boundary.

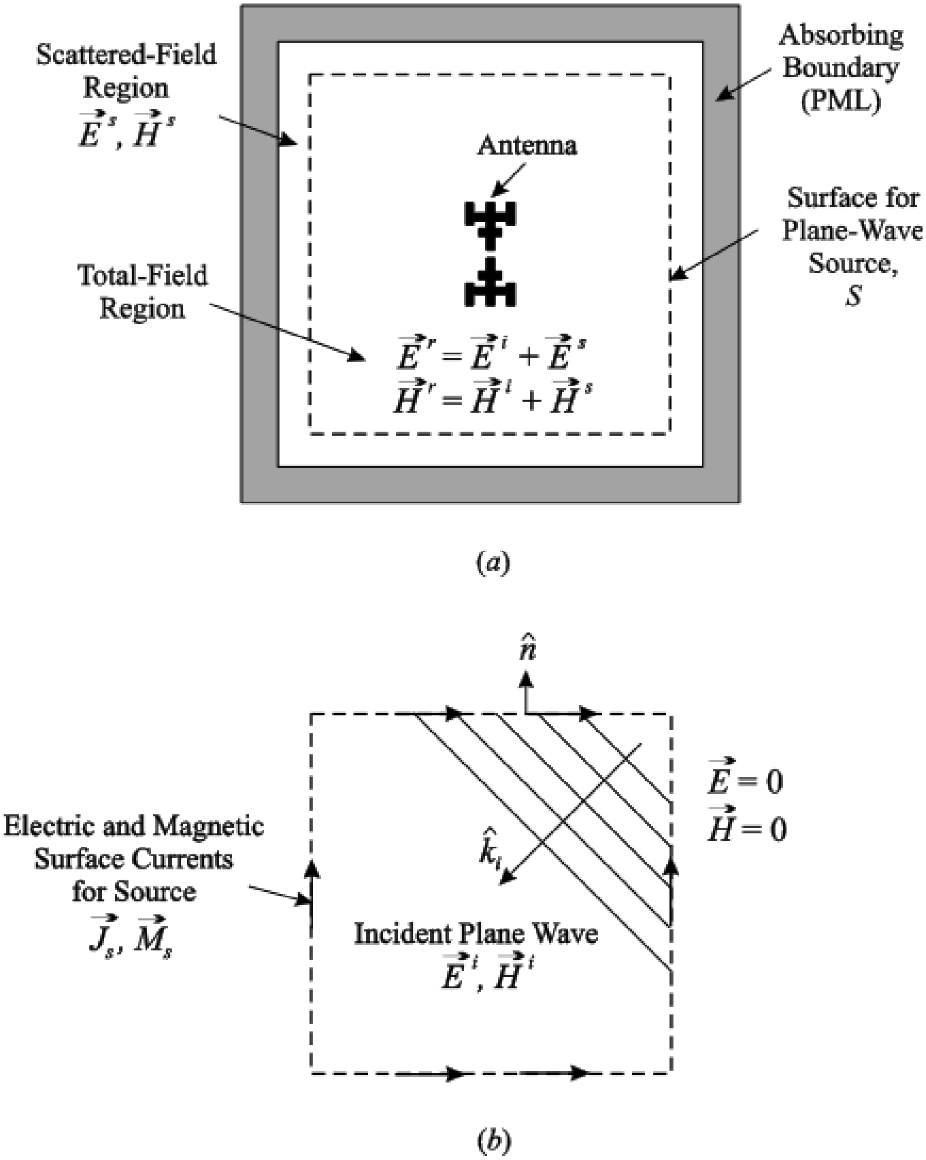

Figure A.5: (a) Schematic drawing showing the basic elements involved in the FDTD analysis of a receiving antenna. (b) Details for the plane-wave source.

A.4.3 Reciprocity

As mentioned earlier, some quantities for the states of transmission and reception are related through reciprocity. For example, when the arrangements shown in Figure A.4 are used for the source and termination, the following relationship applies [15]:

$$V_t^+(t) * V_r^-(t) = \frac{2\pi R_o}{\eta_o} \left[c \int_{t'=-\infty}^{t} E^i(0,t')dt' \right] \cdot * \left[rE^{tr}(-r\hat{k}_i, t + r/c) \right], \quad (A.11)$$

in which $*$ indicates time convolution, and $\cdot *$ indicates the scalar product with time convolution. Here, the origin for the spherical coordinate system is centered on the antenna, as in Figure A.4(a), and the incident electric field E^i is evaluated at the origin ($r = 0$) of this system. The radiated electric field E^{tr} is evaluated at the radial distance r in the direction $(-\hat{k}_i)$ from which the incident field arrives and at the time $t + r/c$. This relationship can sometimes be used to eliminate the need for analyzing one of the two states (transmission or reception) when the other is known, or it can be used for verifying results from one state with results from the other.

A.4.4 Frequency Domain

The FDTD method is inherently a time-domain technique. When quantities are needed in the frequency domain (angular frequency ω), they are obtained using the discrete Fourier transformation, which is indicated by $V(t) \leftrightarrow V(\omega)$. The quantities customarily used for evaluating the performance of an antenna in the frequency domain are determined from the transformed variables. For the transmitting antenna, the voltage reflection coefficient Γ_A and input impedance Z_A are

$$\Gamma_A(\omega) = \frac{V_t^-(\omega)}{V_t^+(\omega)}, \quad (A.12)$$

$$Z_A(\omega) = R_o \left[\frac{1 + \Gamma_A(\omega)}{1 - \Gamma_A(\omega)} \right], \quad (A.13)$$

and the realized gain G_{Rel} (gain including mismatch) and gain G in the direction $\hat{r}$ are

$$G_{\text{Rel}}(\hat{r},\omega) = \frac{4\pi r^2 \hat{r} \cdot \text{Re}[S_c^{tr}(r,\omega)]}{\text{Power available from source}} = \frac{4\pi R_o r^2 |E^{tr}(r,\omega)|^2}{\eta_o |V_t^+(\omega)|^2}, \quad (A.14)$$

$$G(\hat{r},\omega) = \frac{4\pi r^2 \hat{r} \cdot \text{Re}[S_c^{tr}(r,\omega)]}{\text{Power accepted by antenna}} = \frac{1}{1 - |\Gamma_A(\omega)|^2} G_{\text{Rel}}(\hat{r},\omega), \quad (A.15)$$

in which S_c is the complex Poynting vector.

For the receiving antenna, the realized effective area $A_{\text{Rel}}(\hat{k}_i,\omega)$ and the effective area $A_e(\hat{k}_i,\omega)$ for an incident plane wave propagating in the direction $\hat{k}_i$ are

$$A_{\mathrm{Rel}}(\hat{k}_i,\omega) = \frac{\text{Power accepted by termination}}{\hat{k}_i \cdot \mathrm{Re}[S_c^i(r,\omega)]} = \frac{\eta_o}{R_o}\frac{|V_r^-(\omega)|^2}{|E^i(\omega)|^2}, \tag{A.16}$$

and

$$A_e(\hat{k}_i,\omega) = \frac{\text{Power available from antenna}}{\hat{k}_i \cdot \mathrm{Re}[S_c^i(r,\omega)]} = \frac{1}{1-|\Gamma_A(\omega)|^2}A_{\mathrm{Rel}}(\hat{k}_i,\omega). \tag{A.17}$$

The gain and the effective area are related through reciprocity (Equation A.11); for a polarization match we have[3]

$$G(\hat{r},\omega) = \frac{4\pi}{\lambda^2}A_e(-\hat{r},\omega). \tag{A.18}$$

A.4.5 Input Signals

When we are interested in the performance of an antenna over a band of frequencies, a pulsed input signal is useful, followed by the Fourier transform to obtain the desired frequency-domain response. A natural choice for the pulse shape is the Gaussian pulse shown as a solid line in Figure A.6(a),

$$\begin{aligned} f(t) &= \exp\left[-(t/\tau_p)^2/2\right], \\ F(\omega) &= \sqrt{2\pi}\,\tau_p \exp\left[-(\omega\tau_p)^2/2\right], \end{aligned} \tag{A.19}$$

in which τ_p is the characteristic time. However, the spectrum for the Gaussian pulse contains significant low-frequency content (including dc), and this usually is not radiated by the antenna (the dc component never is). Thus, the field near the antenna may take an unacceptably long time to settle when a Gaussian pulse is used.

A better choice is the differentiated Gaussian pulse shown as a dashed line in Figure A.6(a),

$$\begin{aligned} f(t) &= -\left(\frac{t}{\tau_p}\right)\exp\left\{-\left[(t/\tau_p)^2-1\right]/2\right\}, \\ F(\omega) &= j\sqrt{2\pi}\,\omega\tau_p^2 \exp\left\{-\left[(\omega\tau_p)^2-1\right]/2\right\}, \end{aligned} \tag{A.20}$$

or the sinusoid of frequency ω_o amplitude modulated by a Gaussian pulse shown in Figure A.6(b),

$$\begin{aligned} f(t) &= \exp\left[-(t/\tau_p)^2/2\right]\sin(\omega_o t), \\ F(\omega) &= j\sqrt{\pi/2}\,\tau_p\left\{\exp\left[-(\omega+\omega_o)^2\tau_p^2/2\right] - \exp\left[-(\omega-\omega_o)^2\tau_p^2/2\right]\right\}. \end{aligned} \tag{A.21}$$

---

[3] For a polarization match, the state of polarization for the incident plane wave in a particular direction (reception) is matched to the state of polarization for the radiated field in the same direction (transmission). For example, if the radiated electric field is linearly polarized, the electric field of the incident plane wave is linearly polarized and points in the same direction. If the radiated electric field is right-handed circularly polarized, the electric field of the incident plane wave is right-handed circularly polarized.

Table A.1: Characteristics for Various Input Signals.

[Missing content: Table data for characteristics of various input signals was not provided in the source material.]

[Note: Verify the coefficient in Equation A.21; the Fourier transform expression was incomplete in the source material.]

The differentiated Gaussian pulse has a rather large fractional bandwidth that is fixed; for example, the bandwidth associated with the points at which the spectrum is 10% (-20 dB) of the maximum is **[missing value]**, where $\omega_{\text{pk}} = 1/\tau_p$ is the frequency at the peak. The modulated sinusoid has a variable fractional bandwidth that is controlled by the relative width of the modulating pulse, $\omega_o \tau_p$; for example, the bandwidth associated with the points at which the spectrum is 10% of the maximum is $\Delta\omega/\omega_o \approx 4.29/\omega_o\tau_p$ (when $\omega_o\tau_p \gg 1$). For the case shown in Figure A.6(b), $\omega_o\tau_p = 15$, so the fractional bandwidth is $\Delta\omega/\omega_o \approx 0.29$, which is much narrower than the fractional bandwidth for the differentiated Gaussian pulse shown in Figure A.6(a).

A.5 Examples of the Use of the Method for Antenna Analysis

In the previous sections, we presented the fundamentals of the FDTD method and described in general how the method is used to analyze an antenna for both transmission and reception. In this section, we show results obtained by applying the method to analyze particular antennas. These examples were chosen to illustrate specific issues that arise and must be dealt with when applying the method.

A.5.1 Cylindrical Monopole: Theoretical Model Versus Experimental Model

The ultimate test for any physical theory is how well its predictions agree with experimental measurements, and this is certainly the case for electromagnetic theory when applied to antennas. One of the most important factors that affect the agreement is how closely the theoretical model for the antenna matches the experimental model. To examine this issue we consider the FDTD analysis of the cylindrical monopole, the image equivalent of the cylindrical dipole, which is arguably the most fundamental antenna.

The monopole antenna, shown in Figure A.7(a), is formed by extending the metallic center conductor of a coaxial line the distance h above an infinite metallic image plane [2], [8]. The dimensions of the transmission line, inner conductor radius a and outer conductor radius b, are chosen so that only the TEM mode propagates in the line for the signals of interest. The FDTD model for the transmitting monopole is shown in Figure A.7(b). All of the conductors in the model are perfect (perfect electric conductors, PECs), and the structure is surrounded by a PML [16]. Because of the rotational symmetry of the structure and the excitation, a two-dimensional cylindrical lattice (ρ, z) with the spatial increments $\Delta\rho$ and Δz is used in the FDTD analysis. A "one-way source" excites the coaxial line, consisting of the electric and magnetic

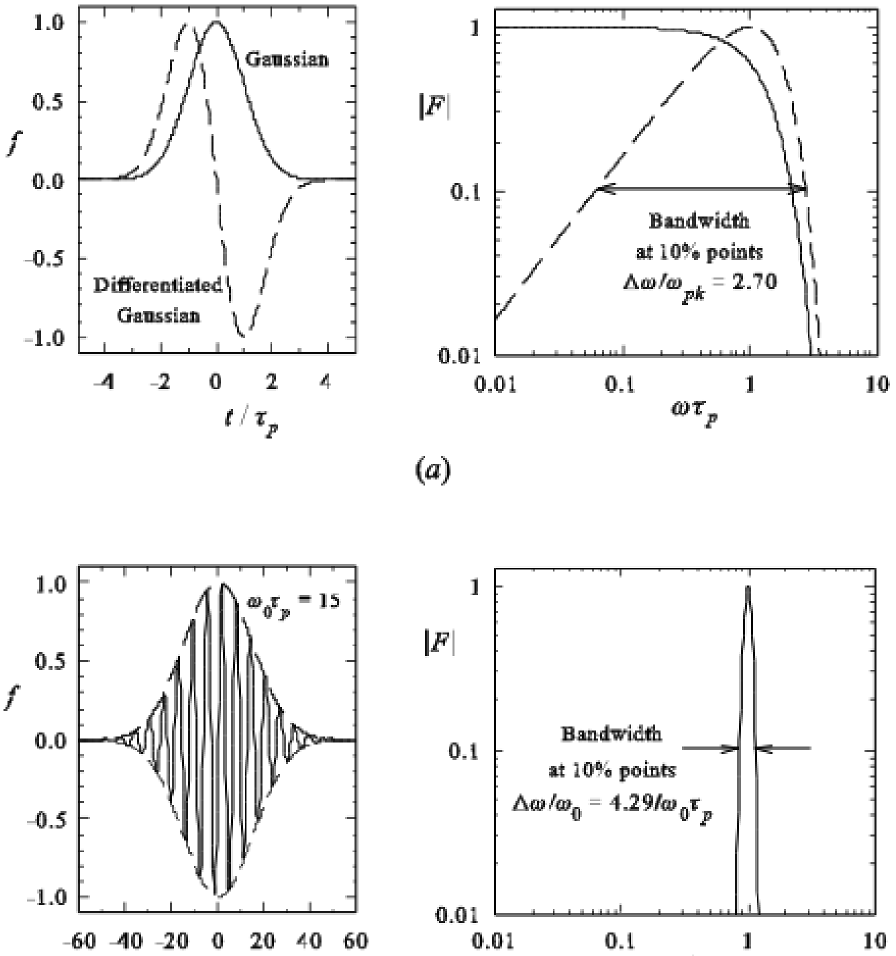

Figure A.6: (a) The Gaussian pulse (solid line) and the differentiated Gaussian pulse (dashed line) and the magnitude of their Fourier transforms. (b) The sinusoid of frequency ω_o amplitude modulated by a Gaussian pulse and the magnitude of its Fourier transform. All waveforms are normalized to have a maximum value of 1.0.

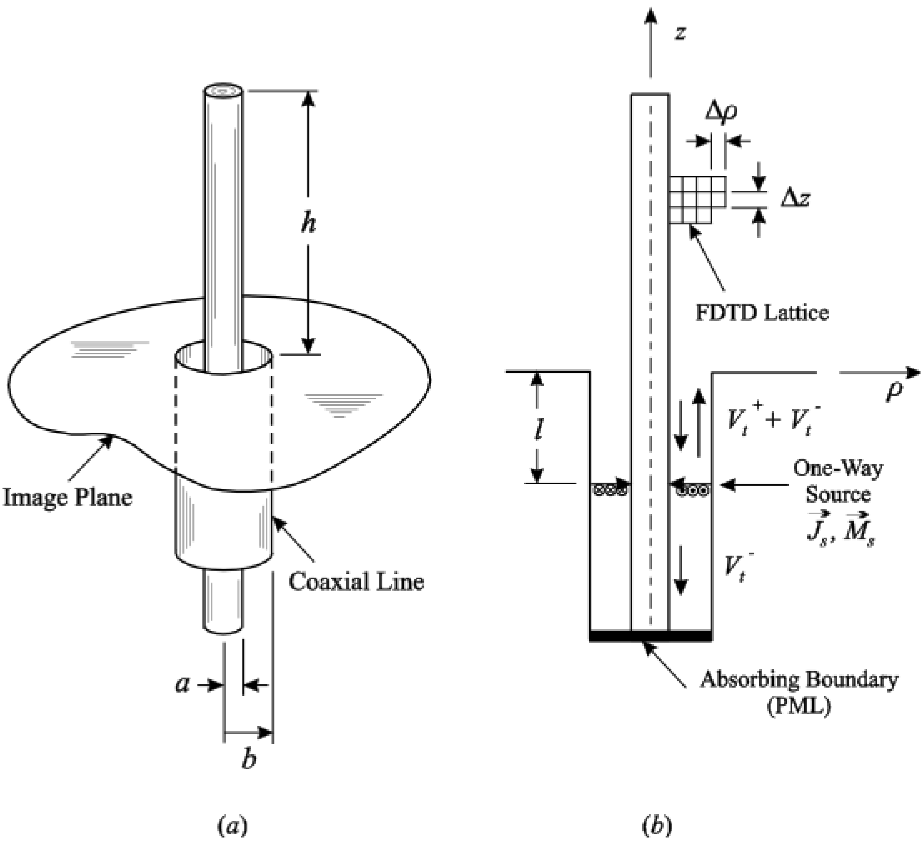

Figure A.7: (a) Cylindrical monopole antenna fed through an image plane from a coaxial transmission line. (b) FDTD model for the cylindrical monopole antenna. The PML that surrounds the computational space is not shown.

surface currents

$$J_s(\rho, t) = -\frac{V_t^+(t)}{2\pi R_o \rho}\hat{\rho}, \quad M_s(\rho, t) = -\frac{\eta_o V_t^+(t)}{2\pi R_o \rho}\hat{\phi} \tag{A.22}$$

on the plane $z = -l$ that produce the incident TEM voltage wave, V_t^+, above the source and a null field below the source. An absorbing boundary is placed at the bottom of the line. With this configuration, only the reflected TEM voltage wave, V_t^-, appears below the source, so it is easily determined. Notice the similarity of this arrangement to the plane-wave source used with the receiving/scattering antenna in Figure A.5.

Figure A.8 is a comparison of results from the FDTD simulation (solid line) with measurements (dots) made on an experimental model corresponding to the geometry in Figure A.7(a). The height of the monopole is $h = 5.0$ cm, and the dimensions of the coaxial line (precision line with APC-7 connector) are $a = 1.52$ mm, $b = 3.5$ mm, which gives a characteristic impedance of $R_o = (\eta_o/2\pi)\ln(b/a) = 50\ \Omega$. The excitation V_t^+ is a unit-amplitude Gaussian pulse in time (Equation A.19), with the characteristic time $\tau_p = 0.161\tau_a$, where $\tau_a = h/c$ is the time for light to travel the length of the monopole.

Figure A.8(a) is for the reflected voltage, V_t^-, in the transmission line, and Figure A.8(b) is for the electric field on the image plane at the radial distance $\rho/h = 12.7$; both are shown as a function of the normalized time t/τ_a. In Figure A.8(a), we see the initial reflection of the incident pulse from the drive point (A), followed by its initial reflection from the open end of the monopole (B). As expected, these events are separated by roughly the time for light to make a round trip on the monopole, $(t_B - t_A)/\tau_a \approx 2$. Additional reflections of decreased amplitude occur each time the pulse encounters the drive point and the open end. In Figure A.8(b), we see that radiation occurs each time the pulse encounters the drive point or the open end of the monopole. As expected, the initial radiation from the drive point (A) is separated from the initial radiation from the open end of the monopole (B) by roughly the time for light to travel the length of the monopole, $(t_B - t_A)/\tau_a \approx 1$. The agreement between the theoretical and measured results is very good.

The FDTD method inherently provides information about the electromagnetic field within the computational volume over the entire period of the simulation. Only a small fraction of this information is used when investigating conventional antenna parameters, such as the results shown in Figure A.8. Sometimes this additional information can be used to perform "numerical experiments" that improve our understanding of the radiation process for the antenna. This is illustrated in Figure A.9, which shows the instantaneous Poynting vector in the region surrounding the monopole [17]. On the right-hand side of these figures, the logarithm of the magnitude of the Poynting vector, $|S|$, is plotted on a color scale. The intensity of the field increases as the hue goes from blue to red, and the range for the values of $|S|$ displayed is $10^4 : 1$. On the left-hand side, the arrows indicate the direction of the Poynting vector, and the length of an arrow is proportional to the logarithm of $|S|$. The excitation is a Gaussian voltage pulse with $\tau_p = 0.0537\tau_a$. For this value of τ_p, about three non-overlapping pulses fit along the length of the monopole, so the reflections associated with different points are separated and easily identified.

In Figure A.9(a), the pulse has just left the drive point and is traveling up the monopole. A spherical wavefront W_1 centered on the drive point has formed, and it is attached to the outward-propagating pulses of charge/current on the monopole and image plane. In Figure A.9(b), the pulse has encountered the open end of the monopole, and it is traveling back down the monopole. A second spherical wavefront W_2 centered on the open end has formed, and it connects the inward-propagating pulse of charge/current on the monopole with the wavefront W_1. Additional wavefronts, W_2', W_3, etc., shown in Figure A.9(c), are produced each time the pulse encounters the drive point and the open end. All of these spherical wavefronts travel outward at the speed of light. The Poynting vectors are seen to be predominantly normal to the wavefronts, which indicates that energy is being transported away from both the drive point and the open end.

The input impedance or admittance $Y_A(\omega) = 1/Z_A(\omega) = G_A(\omega) + jB_A(\omega)$ of the monopole antenna is a useful parameter for practical applications, and it is also a sensitive measure of the accuracy of any theoretical model. It is easily calculated from

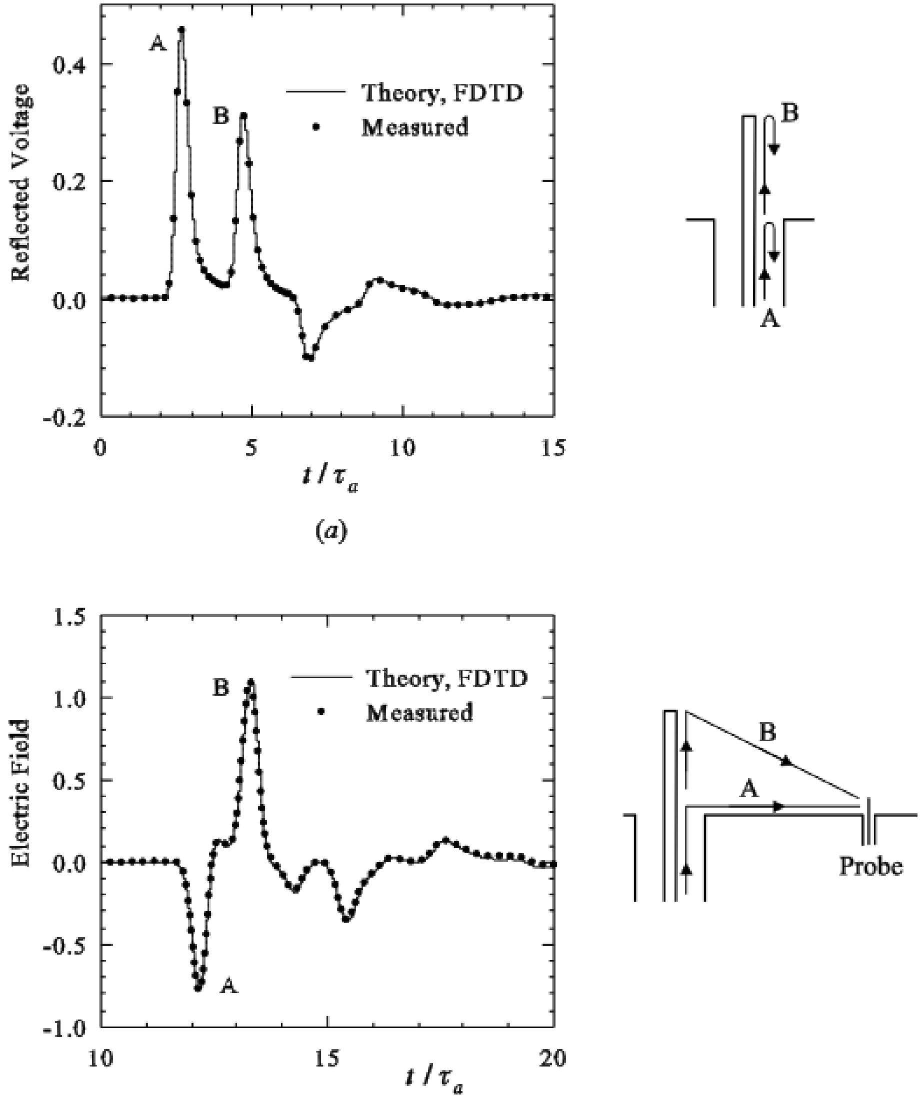

(*a*)

(*b*)

Figure A.8: Comparison of theoretical and measured results for the cylindrical monopole antenna. (a) Reflected voltage in the coaxial line. (b) Electric field on the image plane at $\rho/h = 12.7$.

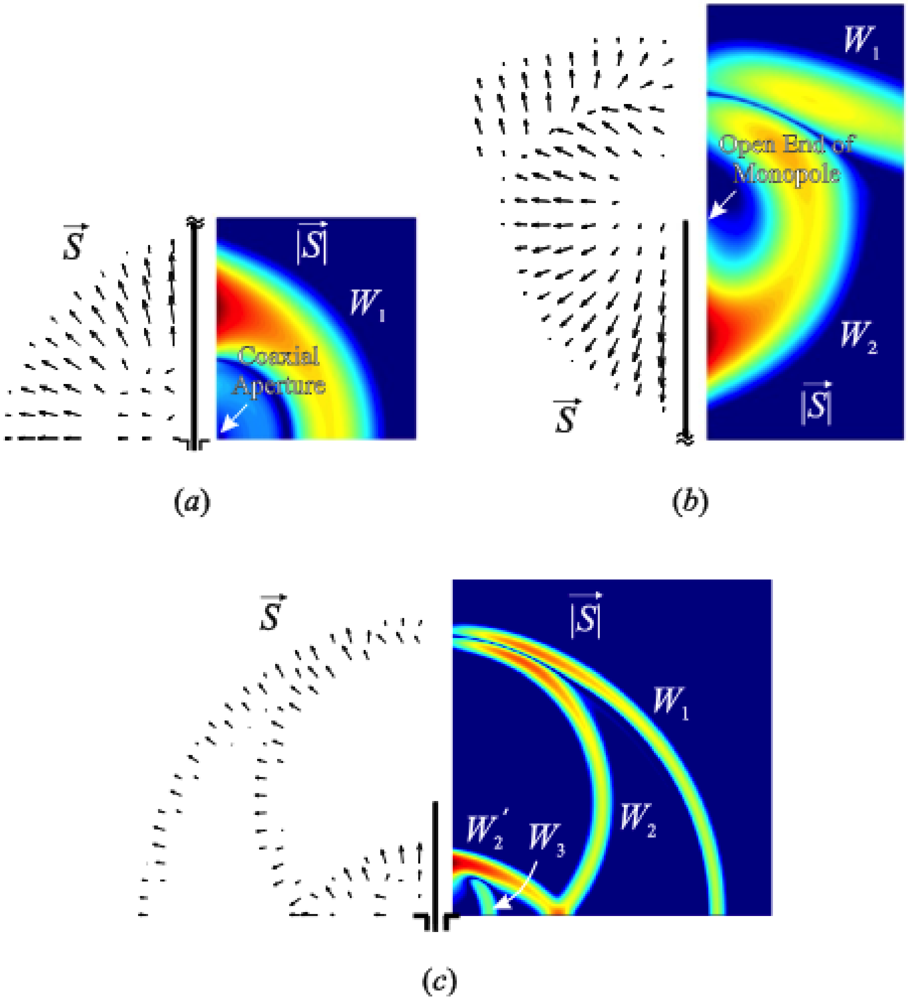

Figure A.9: Three snapshots in time showing the magnitude (right) and direction (left) of the Poynting vector surrounding the cylindrical monopole antenna. Logarithmic scaling is used for both plots. Notice that (a) and (b) only show a portion of the monopole. (After Smith and Hertel [17], © 2001 IEEE.)

Table A.2: FDTD Discretization Parameters for the Cylindrical Monopole Antenna.

[Missing content: Table data for discretization parameters (A, B, C) was not provided in the source material. Should include cell size, number of cells across the gap, number of cells along monopole, and cells per wavelength at the highest frequency.]

the FDTD time-domain results using Equations (A.12) and (A.13). In Figure A.10 the input admittance is graphed as a function of frequency for a monopole with the same dimensions as used for Figure A.8 [18]. FDTD results (lines) for three different levels of discretization (A, B, C) are compared with measurements (dots). The parameters for the three levels of discretization are given in Table A.2.

In this graph we observe the convergence of the FDTD method. Consider the input susceptance, B_A; the result for discretization A is slightly displaced from the measured values, while the results for discretizations B and C are essentially the same as the measured values. Hence, we can conclude that, for practical purposes, the FDTD results for the input admittance have converged to the measured values at discretization B, which corresponds to four FDTD cells across the gap in the coaxial line or 101 cells along the length of the monopole. Note that the dimensions of the FDTD cell for this example had to be chosen so that an integral number of cells fit along the dimensions of the antenna, so the cells are not perfectly square. Discretization B corresponds to 135 cells per wavelength at the highest frequency ($f = 4.5$ GHz) and a relative error in the phase velocity (Equation A.3 and Figure A.2 for $S = 0.5$) of only $6.77 \times 10^{-3}\%$. For this example, it is not the error in the phase velocity that determines the accuracy of the solution. The fine details of the structure must be accurately modeled, and this requires cells that are much smaller than needed for a small error in the phase velocity.

The very good agreement between the theoretical results and the measurements evident in Figures A.8 and A.10 is a consequence of the close match of the theoretical model for the monopole, Figure A.7(b), to the experimental model, Figure A.7(a). In some cases, additional constraints on the analysis require a reduction in the fidelity of the FDTD model, and such good agreement cannot be expected. To illustrate the effect a reduction in the fidelity of the model can have on the accuracy of the results, we examine some common simplifications used for the FDTD model of the monopole.

For the models shown in Figure A.11, the cylindrical conductor of the monopole has been replaced by an equivalent square conductor [19]. Thus, the monopole can now be analyzed using the conventional three-dimensional rectangular FDTD lattice rather than the two-dimensional cylindrical lattice of Figure A.7(b).

The excitation for the monopole has also been changed from that in Figure A.7(b). For the model in Figure A.11(a), the so-called "hard source" is used. This specifies the total voltage $V_t = V_t^+ + V_t^-$ across the gap of length l_g at the base of the monopole. For the model in Figure A.11(b), a virtual one-dimensional transmission line is connected across the gap at the base of the monopole [20]. This transmission line contains the same elements as the transmission line in Figure A.7(b), in particular, a one-way source that specifies the incident voltage V_t^+. We refer to this line as virtual because it does not appear in the FDTD lattice surrounding the monopole. It is in a different location and coupled to the monopole through the voltage and current at its terminals. The hard

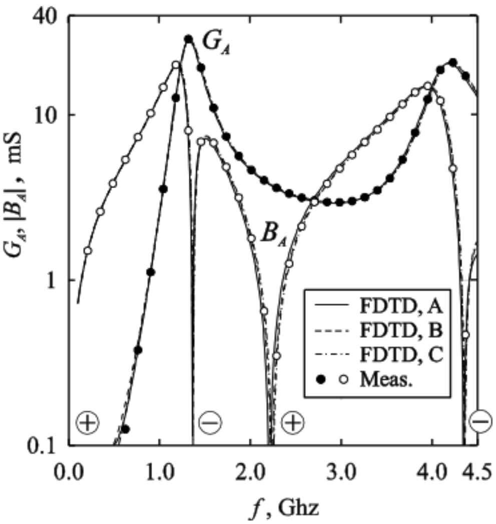

Figure A.10: Comparison of theoretical and measured results for the input admittance of the cylindrical monopole antenna. Results are shown for three levels of discretization (A, B, C) in the FDTD method. (After Hertel and Smith [18], © 2003 IEEE.)

source, while simple to implement, suffers from two drawbacks not present with the transmission line feed. There is no damping in the hard source, unless resistance is added, so the currents on the antenna can ring for a long period of time. Also, the total voltage is specified, so the reflected voltage, a quantity often of interest in time-domain simulations, is not readily available.

In Figure A.12, FDTD results for the input admittance for both models in Figure A.11 are compared with measurements made with the configuration shown in Figure A.7(b) [18]. The level of discretization used is such that the simulations have converged for practical purposes. The theoretical results for the input conductance, G_A, for both models are in very good agreement with the measurements; however, those for the input susceptance, B_A, differ from the measurements, particularly for the hard source (dashed line). The difference in susceptance is a consequence of the geometry for the simplified models not accurately representing the experimental model, Figure A.7(a), in the vicinity of the drive point (the aperture of the coaxial line). The susceptance for the simplified models can be brought into better agreement with the measured results by adding a small capacitance in parallel with the terminals of the monopole [18].

A.5.2 Metallic Horns and Spirals: Stair-Stepped Surfaces

For the monopole antennas discussed in the previous section, the boundaries of the FDTD cells as well as the boundaries of all material regions (PECs) coincided with surfaces of constant coordinate. Thus, the boundaries of material regions never passed obliquely through an FDTD cell. This is a special case that is not encountered for most antennas.

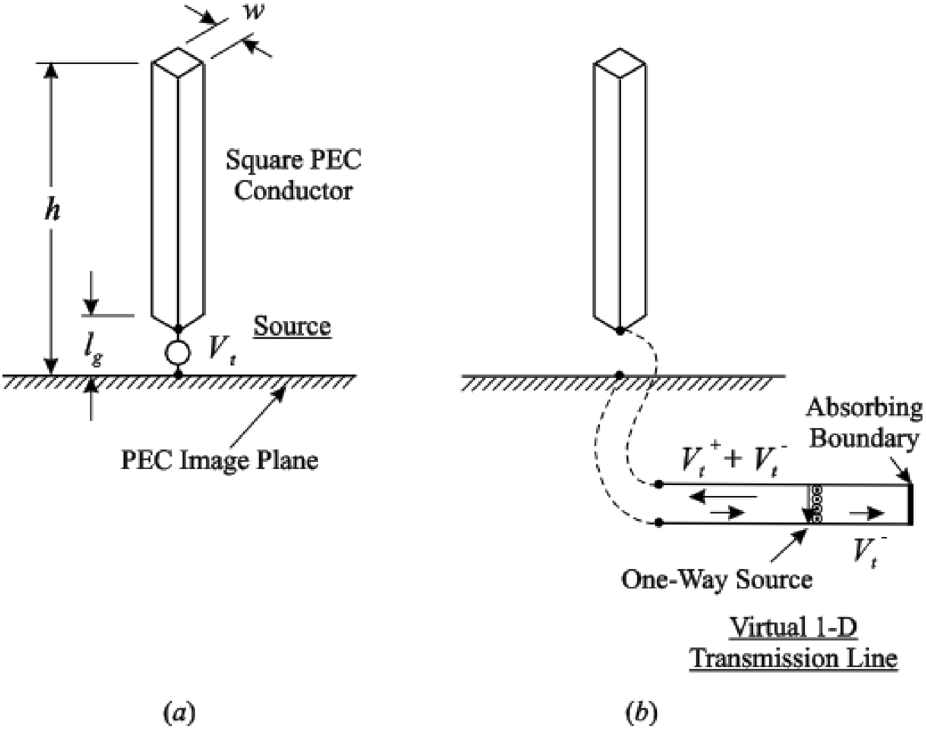

Figure A.11: Simplified models for the cylindrical monopole antenna. (a) Model incorporating a "hard source." (b) Model incorporating a virtual one-dimensional transmission line. The monopole conductor has a square cross section in both models.

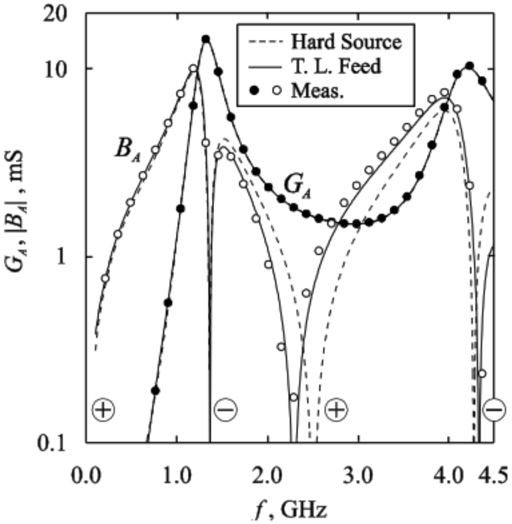

Figure A.12: Comparison of theoretical and measured results for the input admittance of the cylindrical monopole antenna. Results are shown for the two simplified FDTD models. (After Hertel and Smith [18], © 2003 IEEE.)

Figure A.13(a) illustrates the more general case. It shows the cross section of a PEC object with the rectangular FDTD lattice superimposed. The curved surface of the object does not coincide with any of the lattice lines. For the computation we only need to know the field in the FDTD cells that are exterior to the PEC, because both E and H are zero inside the PEC. There are different approaches that can be used for this case. One approach is to introduce non-rectangular FDTD cells that conform to the surface of the object; these cells could be used throughout the computational volume or just adjacent to the object [21]–[23]. Another much simpler approach, shown in Figure A.13(b), is to deform the curved surface of the object so that it conforms to the rectangular FDTD lattice. The surface of the object is said to be replaced by a "stair-stepped" or "staircase" approximation. The stair-stepped approximation will introduce an error, but often the error can be made negligible by choosing the size of the staircase to be small compared to the physical dimensions of the object [24], [25]. The stair-stepped approximation is commonly used, and it is the only approach we will consider in this introductory treatment.

We now consider two practical antennas for which the stair-stepped approximation was used in modeling the structure in the FDTD analysis. As these examples will show, when properly used, the approximation can yield results that are in good agreement with experimental measurements. The first example is the metallic, pyramidal horn shown in Figure A.14 (Flann Microwave Instruments Ltd. Model 1624-20). Antennas like this are used in many microwave applications, and sometimes they serve as gain standards (standard gain horns). The small drawings at the bottom of the figure show the lengths and angles that describe this particular horn antenna: $a = 10.95$ cm, $b = 7.85$ cm,

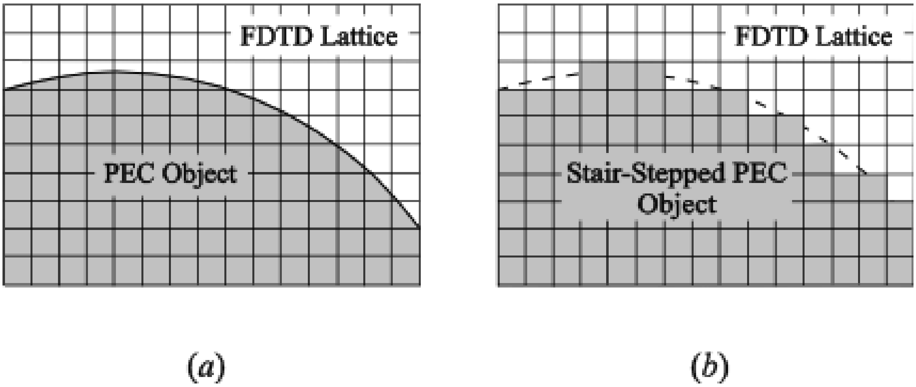

Figure A.13: (a) Rectangular FDTD lattice superimposed on the cross section of an object that is a perfect electric conductor (PEC). (b) The surface of the object has been deformed to conform to the rectangular lattice; the surface of the object has been replaced by a stair-stepped approximation.

$D = 2.284$ cm, $l_w = 5.08$ cm, $\alpha = 10.74°$, and $\beta = 8.508°$. The waveguide feeding the horn is type WR-90 (X-Band, with the operational bandwidth 8.2–12.4 GHz).

In the FDTD model, the cubical cells have the side length $\Delta x = 0.635$ mm, and the perfectly-conducting walls are plates two cells thick. The inset shows the faces of the individual cells that model the bottom wall of the horn; the cells are shown seven times actual size. The slanted sides of the horn are stair stepped, as indicated in the figure, with a "tread length-to-rise" of approximately six cells to one. The horn is fed by a probe inserted into the section of rectangular waveguide, and the incident and reflected voltages in a one-dimensional transmission line ($R_o = 50\ \Omega$) connected to the probe are used in the analysis.

The structure is symmetrical about the x-z plane, and this symmetry was used in the analysis to reduce the size of the computational volume, which was $519 \times 116 \times 183$ cells. The sides of the antenna were 20 cells from the PML absorbing boundary (10 cells thick), except the front side (radiating aperture), which was 40 cells from the absorbing boundary.

The pyramidal horn was first analyzed as a transmitting antenna. The excitation in the transmission line, $V_t^+(t)$, was a differentiated Gaussian pulse (Equation A.20) with the characteristic time $\tau_p = 1.59 \times 10^{-11}$ s. This pulse has significant energy over the operational bandwidth of the horn: 8.2–12.4 GHz. The peak of the spectrum for the pulse is at 10.0 GHz, and the spectrum drops to 10% of the peak at 600 MHz and 27.6 GHz.

At the highest frequency (shortest wavelength) within the operational bandwidth of the horn we have $\Delta x = 0.0226\lambda$, which corresponds roughly to 38 cells per wavelength. From this result, we can estimate the numerical dispersion using Figure A.2 or Equation (A.3). The relative error in the phase velocity is about 0.1%, which is equivalent to 8.1×10^{-3} degrees of phase error per cell, or a total error of 4.2 degrees of phase error for propagation across the longest side of the computational volume.

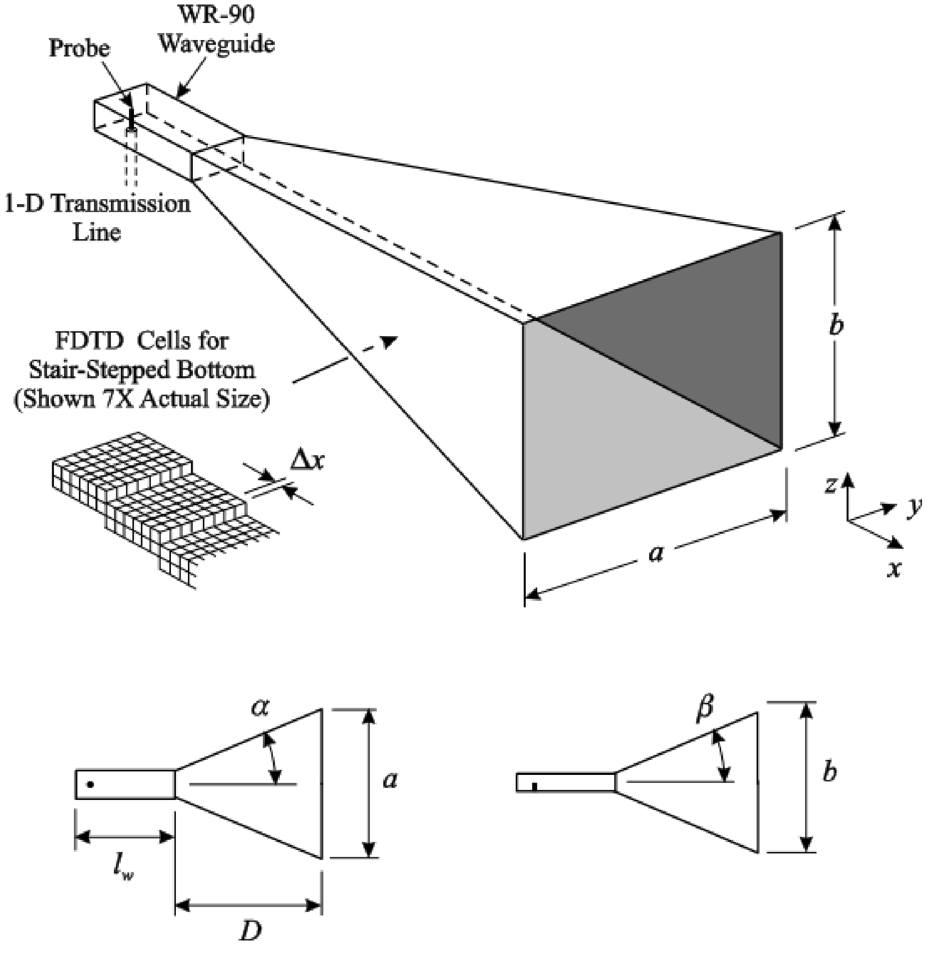

Figure A.14: Schematic drawing for the pyramidal horn antenna. The inset shows the FDTD cells used to model the bottom of the horn.

Figure A.15 is a comparison of the FDTD results (solid line) for this antenna with measurements (dots). The measured data were kindly supplied by Dr. David G. Gentle of the National Physical Laboratory, Teddington, Middlesex, U.K. Figures A.15(a) and A.15(b) show the E- and H-plane field patterns at the frequency 10 GHz, and Figure A.15(c) shows the gain on boresight as a function of frequency. The results from the FDTD calculations are in very good agreement with the measurements. The small differences that do exist in the H-plane field pattern are for angles at which the field is very weak, 50 dB below the peak. We note that the precise details of the probe feeding the waveguide in the FDTD model do not affect the calculation of the gain (Equation A.15) of the horn. This would not be the case if the realized gain (Equation A.14) were determined.

The pyramidal horn was also analyzed as a receiving antenna. For this case, a plane wave was incident from the boresight direction ($\hat{k}_i = -\hat{x}$) with the electric field pointing in the z direction. The incident electric field was a differentiated Gaussian pulse in time (Equation A.20) with the same characteristic time as used for the transmitting case, $\tau_p = 1.59 \times 10^{-11}$ s. The effective area obtained from the receiving analysis was converted to a gain using Equation (A.18), and the result is shown as a dashed line in Figure A.15(c). As expected from reciprocity, the results from the two FDTD calculations (transmitting and receiving) are nearly identical.

The FDTD method provides the field throughout the computational volume, and it can be used to construct graphical results that illustrate the process of radiation for the transmitting horn antenna. For such illustrations, we want an excitation whose spectrum lies within the operational bandwidth of the antenna. Frequencies outside of this band will either be cutoff in the waveguide or overmode the waveguide. A good choice for the voltage $V_t^+(t)$ is the sinusoid of frequency ω_o amplitude modulated by a Gaussian pulse, i.e., Equation (A.21) shown in Figure A.6(b). With $f_o = \omega_o/2\pi = 10.0$ GHz and $\tau_p = 7.96 \times 10^{-11}$ s, the spectrum for this signal is 10% of its peak at $f = 5.7$ GHz and $f = 14.3$ GHz.

Figure A.16 shows three gray-scale plots for the magnitude of the electric field on the x-z plane of the transmitting antenna. In Figure A.16(a) the pulse has entered the horn from the waveguide, but it has not reached the aperture. The spacing between the white lines (nulls) roughly corresponds to one half of a guide wavelength. Notice that this spacing decreases on going from the throat of the horn towards the aperture. In the rectangular waveguide, the guide wavelength is about 1.3 times the free-space wavelength, whereas at the aperture of the horn it is closer to the free-space wavelength. Figure A.16(b) is for a time when the pulse has reached the aperture. Notice that the white lines in the horn near the aperture are distorted; there is a small segment that is concave to the right. This is caused by the reflection from the aperture that is traveling back toward the throat of the horn. Directly in front of the aperture, the radiated wave is roughly planar. In Figure A.16(c), the field has propagated away from the horn, and a spherical wavefront has formed that is approximately centered on the aperture. The change in the shade of gray in going around the antenna (dark in front to light in back) clearly shows a large "front-to-back ratio" for the horn. In the forward direction, minima appear along the wavefront, and these minima will define the main beam in the far zone. Back in the horn, the field has several minima and maxima across its width, indicating the presence of higher-order modes that were excited when the initial pulse

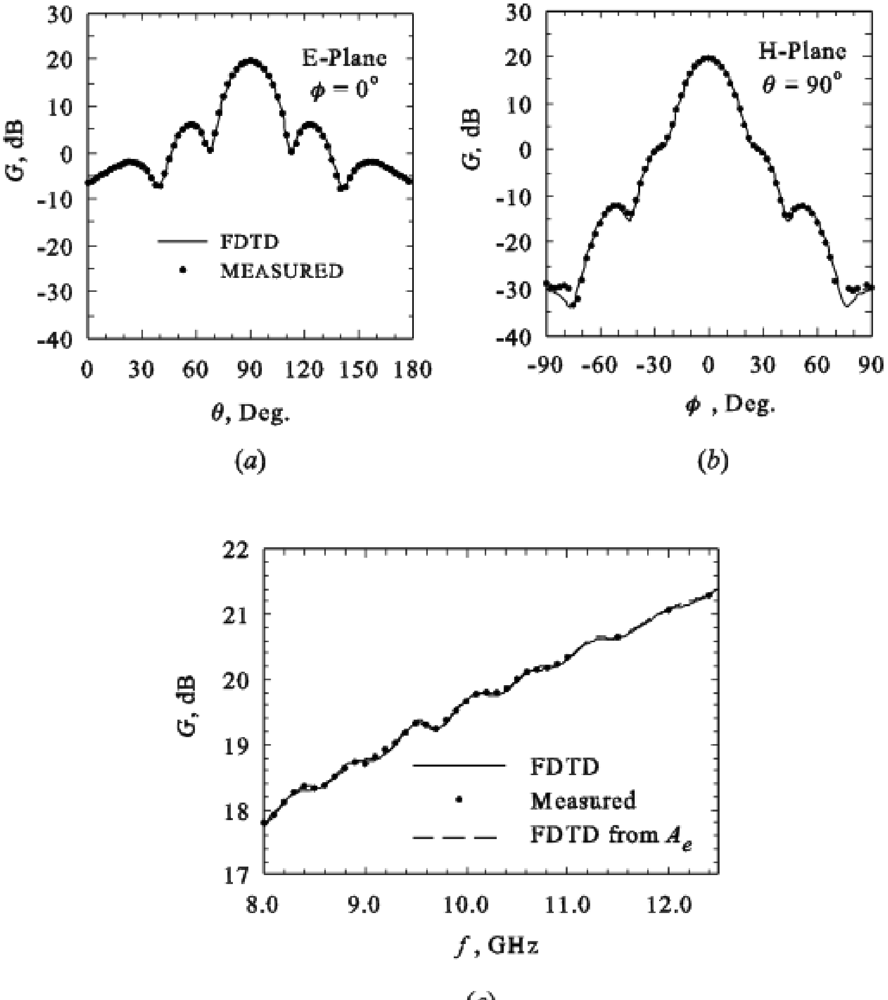

Figure A.15: Comparison of theoretical and measured results for the pyramidal horn antenna. (a) E-plane pattern and (b) H-plane pattern at 10 GHz. (c) Boresight gain versus frequency.

encountered the aperture.

The second example is the two-arm, conical spiral antenna shown in Figure A.17 [26]. It is used in applications that require an antenna to radiate circular polarization over a broad bandwidth. This antenna is formed by winding two metallic strips around the surface of a truncated cone. The angles and dimensions for the particular antenna we consider are $d = 1.9$ cm, $D = 15.2$ cm, $\theta_o = 7.5^\circ$, $\alpha = 75^\circ$, and $\delta = 90^\circ$. It is designed to have constant gain and input impedance ($Z_A \approx 100\ \Omega$) over an operational bandwidth extending from $f_{\text{min}} = 0.5$ GHz to $f_{\text{max}} = 3.3$ GHz.

In the FDTD model, the arms of the spiral are formed by making selected faces of the cubical cells ($\Delta x = 0.8$ mm) PEC. The result is the stair-stepped approximation in Figure A.18. For clarity, only the lower 10% of the antenna is shown in the figure. The spiral is fed by a one-dimensional transmission line ($R_o = 100\ \Omega$) connected at the bottom of the antenna, the same arrangement as used with the monopole antenna in Figure A.11(b). The excitation in the transmission line, $V_t^+(t)$, is a differentiated Gaussian pulse (Equation A.20), whose spectrum is centered on the operational bandwidth of the antenna.

The computational volume was $691 \times 240 \times 240$ cells, with the sides of the antenna 15 cells from the PML absorbing boundary (10 cells thick), except the bottom side (main direction for radiation), which was 30 cells from the absorbing boundary. At the highest frequency (shortest wavelength) within the operational bandwidth of the antenna we have $\Delta x = 0.0093\lambda$, which corresponds roughly to 107 cells per wavelength. From this result, we can estimate the numerical dispersion using Figure A.2 or Equation (A.3). The relative error in the phase velocity is about 0.01%, which is equivalent to 3.6×10^{-4} degrees of phase error per cell, or a total error of 0.25 degrees of phase error for propagation across the longest side of the computational volume. As with the earlier case of the monopole antenna, it is not the error in the phase velocity that determines the accuracy of the solution but the degree to which the fine details of the structure are modeled.

Figure A.19 is a comparison of the FDTD results (solid line) for this antenna with measurements (dashed line). Figure A.19(a) shows the magnitude of the reflection coefficient at the terminals of the antenna, and Figure A.19(b) shows the realized gain (Equation A.14) at boresight ($-\hat{z}$ direction) as a function of frequency. The results from the FDTD calculations are in fairly good agreement with the measurements. The differences that do exist are most likely caused by elements in the experimental model that were not included in the theoretical model. In the experimental model, the metallic arms were on a very thin dielectric substrate (Kapton, thickness 0.051 mm), which was not included in the theoretical model. In addition, the terminal measurements were made through a balun, and the imperfections in the balun were not taken into account.

The FDTD method provides detailed information about the electromagnetic field surrounding the spiral, and it can be used to graphically illustrate how energy is radiated from this structure [27]. Figure A.20 shows three gray-scale plots of the magnitude of the x component of the electric field on the x-z plane. Each plot is for a different normalized time t/τ_L, where τ_L is the time for light to travel the length of the spiral arm. We can see that the radiation is roughly periodic with the spacing between the nulls (white lines) being $\lambda/2$. The frequency corresponding to this wavelength is indicated on each plot. These plots clearly show that the region from which radiation leaves

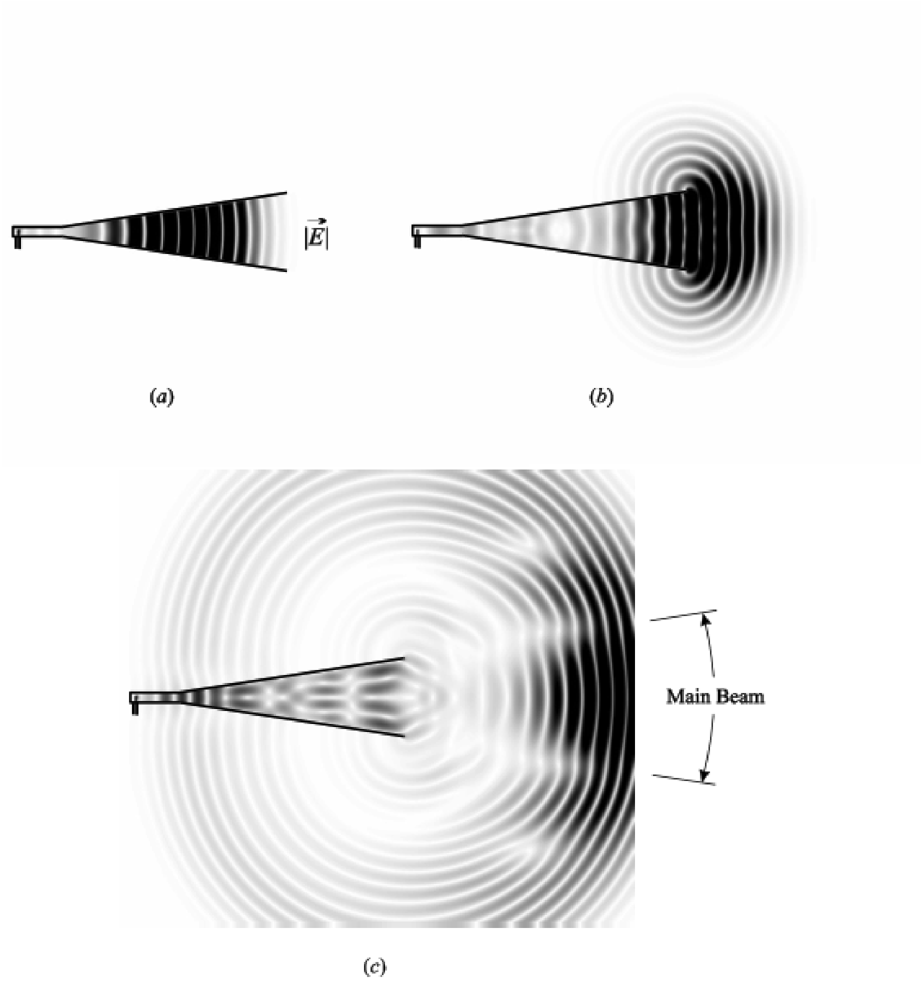

Figure A.16: Gray-scale plots for the magnitude of the electric field on the vertical symmetry plane of the transmitting horn antenna. The excitation is a sinusoid amplitude modulated by a Gaussian pulse.

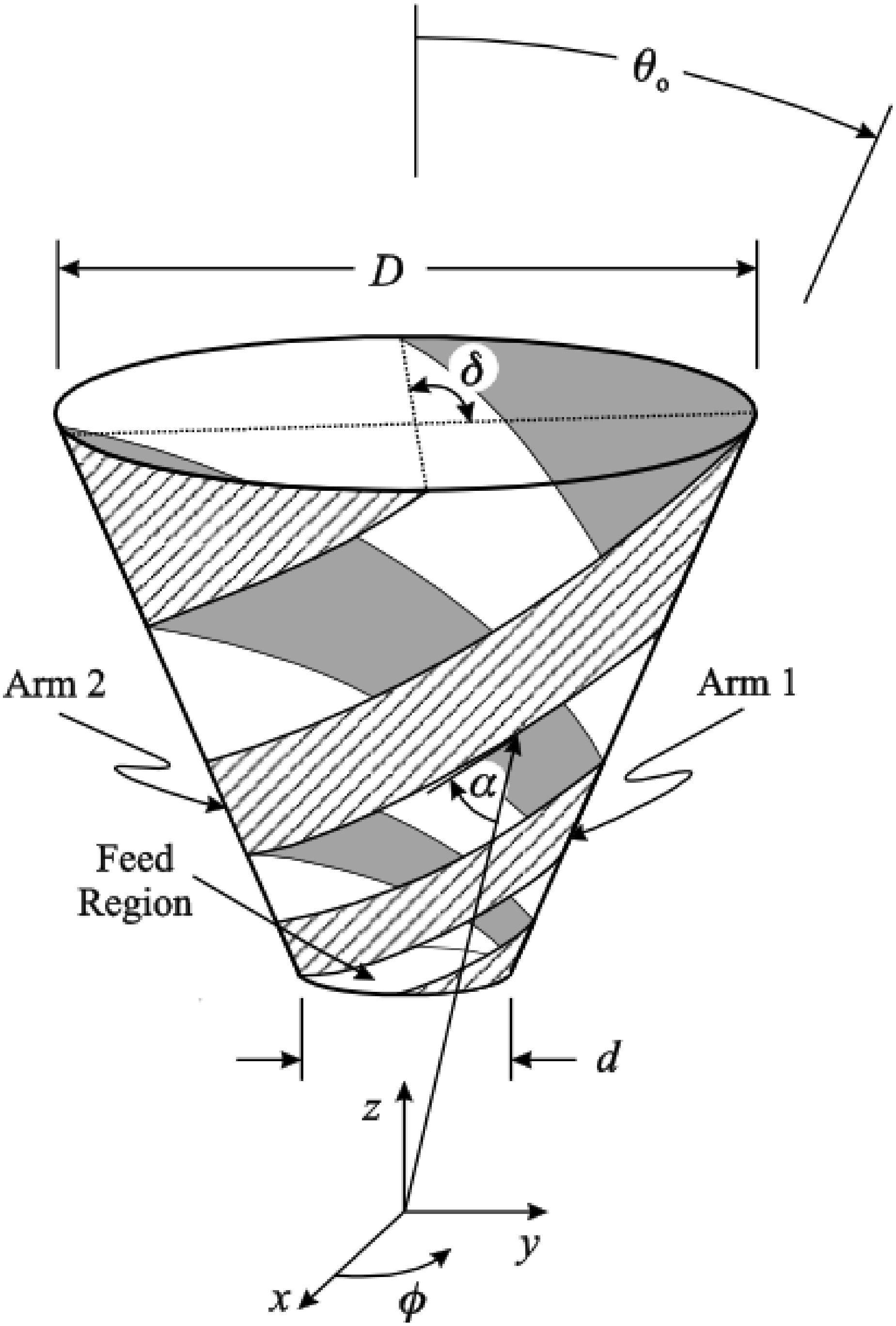

Figure A.17: Geometry for the two-arm conical spiral antenna. (After Hertel and Smith [26], © 2002 IEEE.)

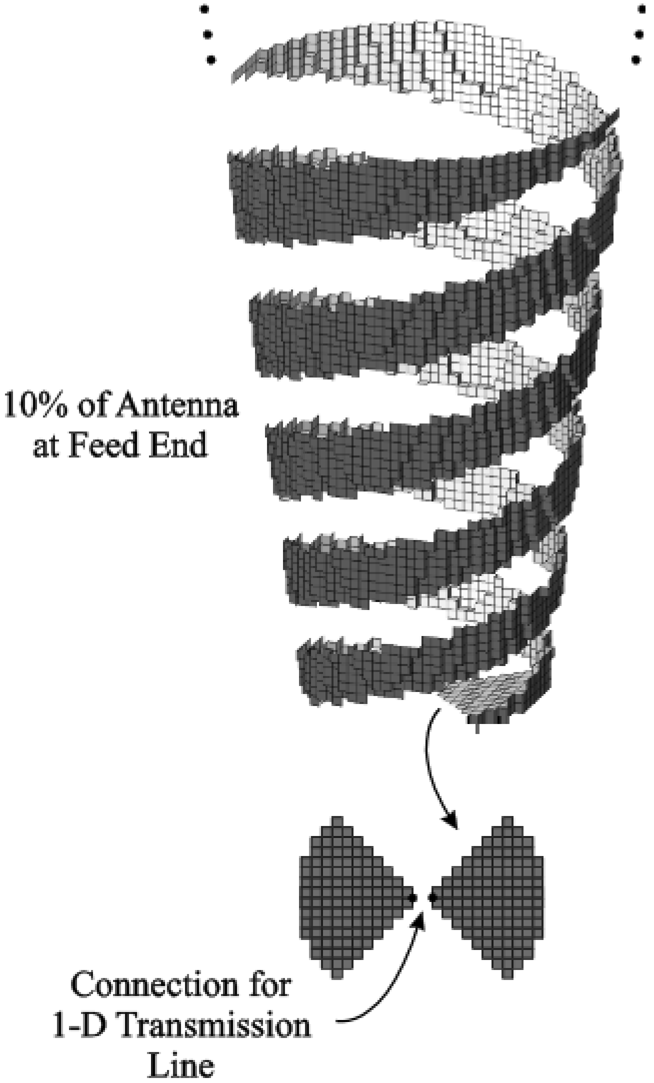

Figure A.18: Schematic drawing showing the arrangement of FDTD cells used to model the conical spiral antenna. For clarity, only the lower 10% of the antenna is shown. (After Hertel and Smith [26], © 2002 IEEE.)

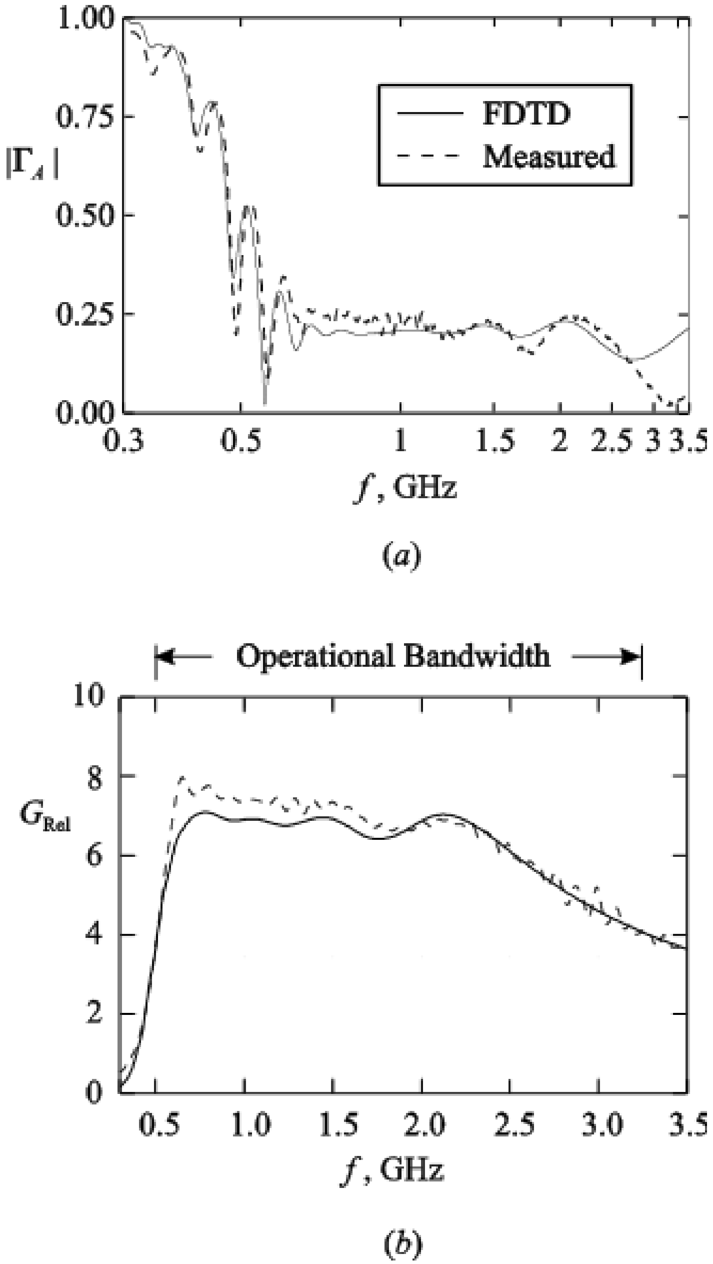

Figure A.19: Comparison of theoretical and measured results for the conical spiral antenna. (a) Magnitude of reflection coefficient versus frequency. (b) Realized gain in the boresight direction versus frequency. (After Hertel and Smith [26], © 2002 IEEE.)

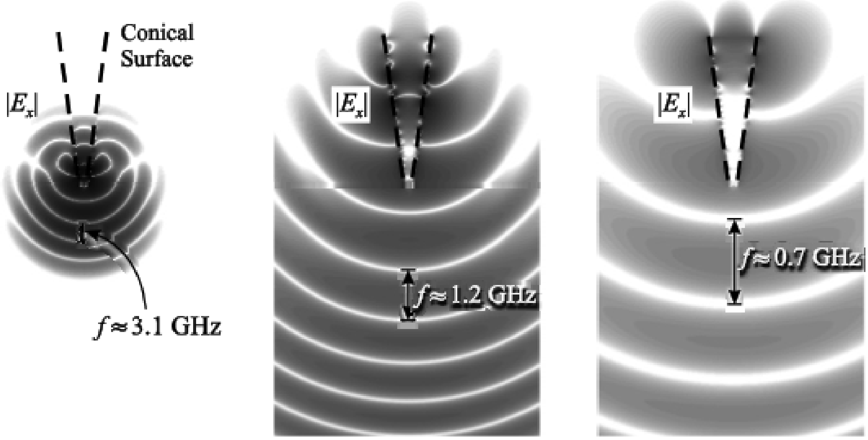

(a) (b) (c)

Figure A.20: Gray-scale plots for the magnitude of the electric field near the conical spiral antenna for three instants in time: (a) $t/\tau_L = 0.1$, (b) $t/\tau_L = 0.6$, and (c) $t/\tau_L = 1.1$, where τ_L is the time for light to travel the length of the spiral arm. (After Hertel and Smith [27], © 2003 IEEE.)

the antenna changes with the wavelength, moving from the small end (diameter d) for the shortest wavelengths (highest frequencies) to the large end (diameter D) for the longest wavelengths (lowest frequencies). This is in keeping with the "active-region concept," which states that the radiation originates at the cross section of the spiral that is approximately one wavelength in circumference [28].

In the previous two examples, the stair-stepped approximations used for the geometry of the antennas in the FDTD models were adequate for obtaining theoretical results in good agreement with the measurements. This is a consequence of choosing the size of the steps to be small compared to the dimensions defining the geometry of the antennas. For example, for the pyramidal horn, the height of the stair step is only about 10% of the smallest dimension of the antenna (the height of the rectangular waveguide). We will now consider a case in which the stair-stepped approximation leads to significant errors in the calculated results.

The transverse electromagnetic (TEM) horn is a simple antenna used for applications that require broad bandwidth. The FDTD model for the monopole version of this antenna is shown in Figure A.21(a). It is formed from a PEC plate that is an isosceles triangle of side length s and angle at the apex α. The plate is inclined at the angle $\beta/2$ to the PEC image plane, and the antenna is fed by a transmission line connected between the apex of the plate and the image plane. The plate/image plane forms a TEM transmission line, and for the example to be discussed ($\alpha = 25.4°$, $\beta = 11.2°$), the characteristic impedance of this line is $R_o \approx 50\ \Omega$ [29]–[31]. The transmission line feeding the antenna has the same characteristic impedance.

The plate for this antenna is stair stepped in the FDTD model in the manner shown in Figure A.21(b). Two different sizes for the staircase will be examined: Case A for which the rise is $\Delta z = 1$ mm and the tread length is $\Delta s = 1$ cm, and Case B for which $\Delta z = 2$ mm and $\Delta s = 2$ cm. Notice that the level of discretization for Case B is twice as coarse as that for Case A. The smallest dimensions for the horn are at the drive point, where the initial tread for both cases is 4 mm above the image plane. So for Case A, the rise of the staircase, Δz, is about 25% of the smallest dimension of the horn; whereas, for Case B it is about 50% of the smallest dimension.

Figure A.22(a) shows the reflected voltage, $V_t^-(t)$, in the feeding transmission line of the horn when the incident voltage, $V_t^+(t)$, is a unit-amplitude, differentiated Gaussian pulse (Equation A.20) with the characteristic time $\tau_p = 5.31 \times 10^{-11}$ s. The peak of the spectrum for the pulse is at 3.0 GHz. The solid line is for Case A and the dashed line is for Case B. The initial reflection from the drive point is evident and is similar for both cases, and the reflection from the open end of the horn has been windowed out. There is a pronounced ripple in the result for the coarser staircase, Case B. The ripple is clearly due to the staircase, because its period roughly corresponds to the round-trip time on a tread, which is $\Delta t = 2\Delta s_B/c \approx 2.5\tau_p$. Notice that the amplitude of the ripple decreases with time. This is because the reflections that occur later in time are from stair steps further out along the antenna, where the rise of the staircase, Δz, is a smaller fraction of the separation between the plate and the image plane.

Figure A.22(b) shows the magnitude of the Fourier transform (spectrum) of the reflection coefficient for the antenna. Notice that the results for the two cases, A and B, are quite different. Specifically, for Case B there is a distinct dip in the reflection coefficient near $2f\Delta s_B/c = 1$ ($f = 7.5$ GHz). At this frequency, $\Delta s_B/\lambda = 1/2$, so the small reflections from all of the steps in the staircase add in phase.

To avoid the problem described above, we must use a finer staircase, such as in Case A. For TEM horns with low characteristic impedance (generally small β), this can require a very fine level of discretization. A similar problem is encountered with bow-tie antennas with low characteristic impedance [32].

A.5.3 Microstrip Patches: Excessive Ringing for Narrow-Band Antennas

The antennas we examined in the previous section, a conical spiral and horns, are fairly wideband antennas. Now we consider the other extreme, namely, narrowband antennas. For our example, we use the basic, rectangular microstrip patch antenna shown in Figure A.23.

In the mid-1980s, Chang et al. made extensive measurements of this antenna, and first we compare our FDTD results with their measurements [33]. The dimensions for a patch designed for frequencies around $f = 7.0$ GHz are $s = 1.1$ cm, $w = 1.7$ cm, and $h = 3.175$ mm. As shown in the figure, the probe of the feeding coaxial line ($R_o = 50\ \Omega$) is displaced from the broad side of the patch by $l_p = 1.5$ mm. In the model, the dielectric substrate is 10 cm × 10 cm with the electrical properties $\epsilon_r = 2.33$ and $\sigma = 2.1 \times 10^{-3}$ S/m, and the ground plane is infinite. The inci-

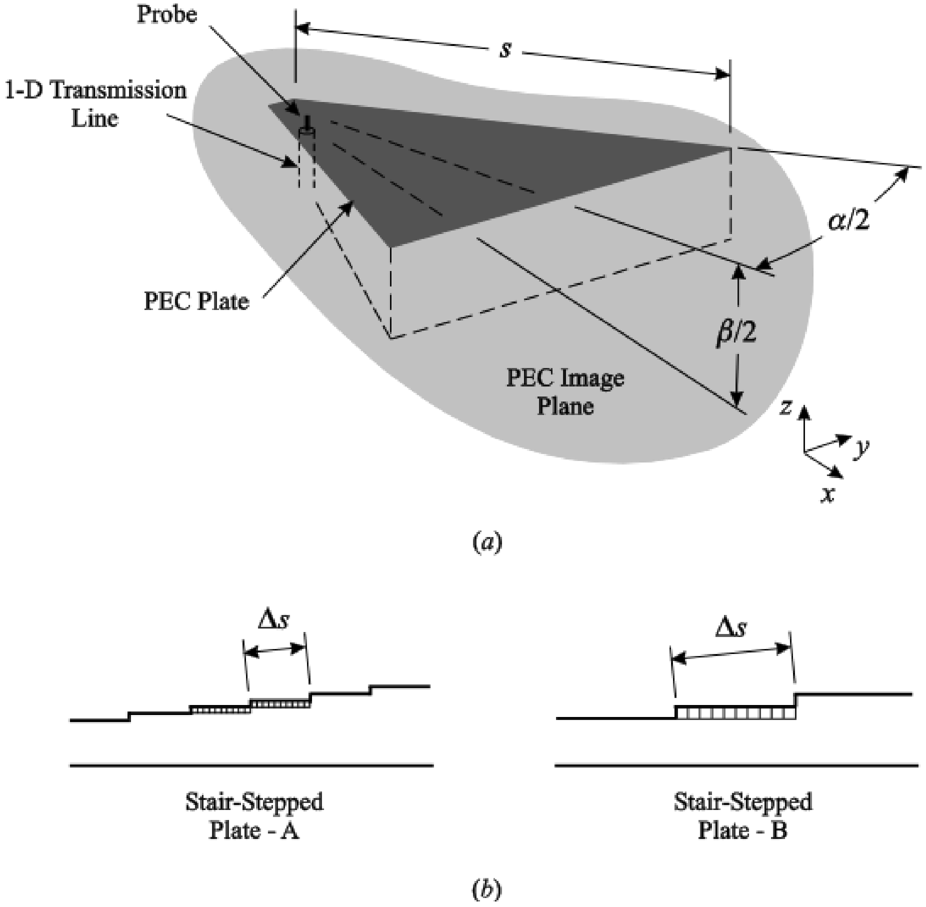

Figure A.21: (a) Schematic drawing for the TEM horn antenna (monopole configuration). (b) Cross sections showing the stair-stepped approximation to the plate for two different cases, A and B.

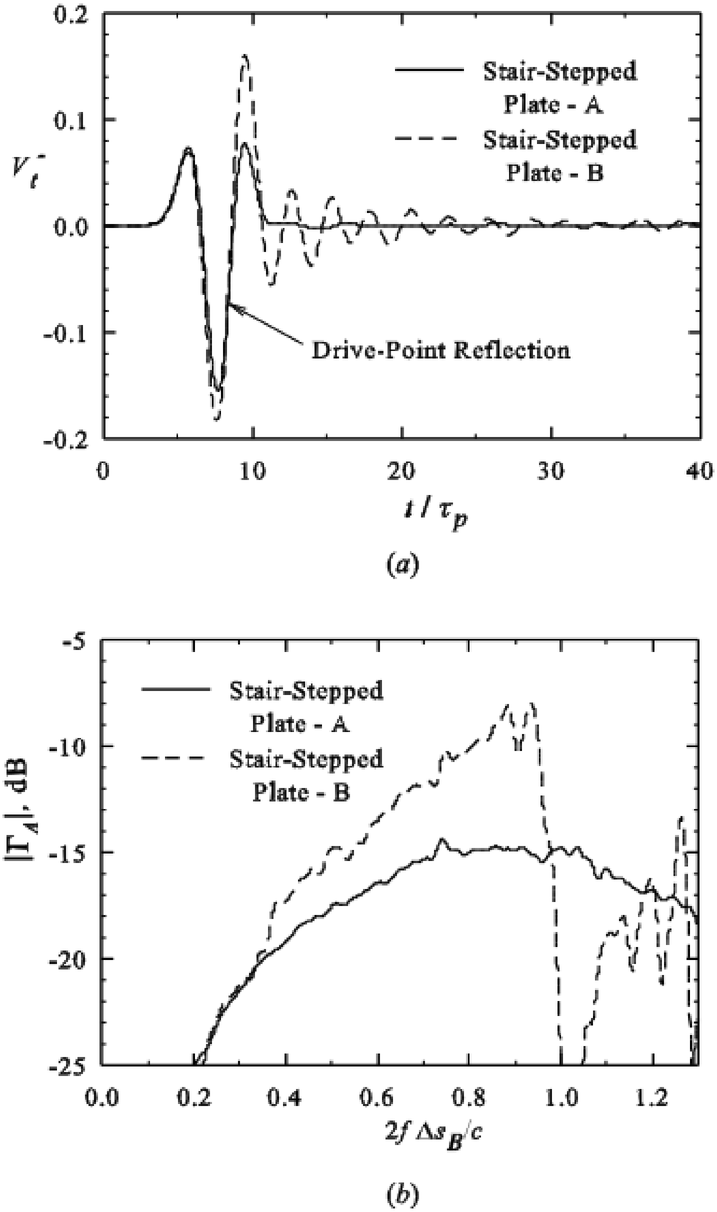

Figure A.22: Results for two different stair-stepped approximations (A and B) applied to the TEM horn antenna. (a) The reflected voltage in the feeding transmission line; the reflection from the open end of the horn has been windowed out. (b) The magnitude of the Fourier transform of the reflection coefficient for the antenna.

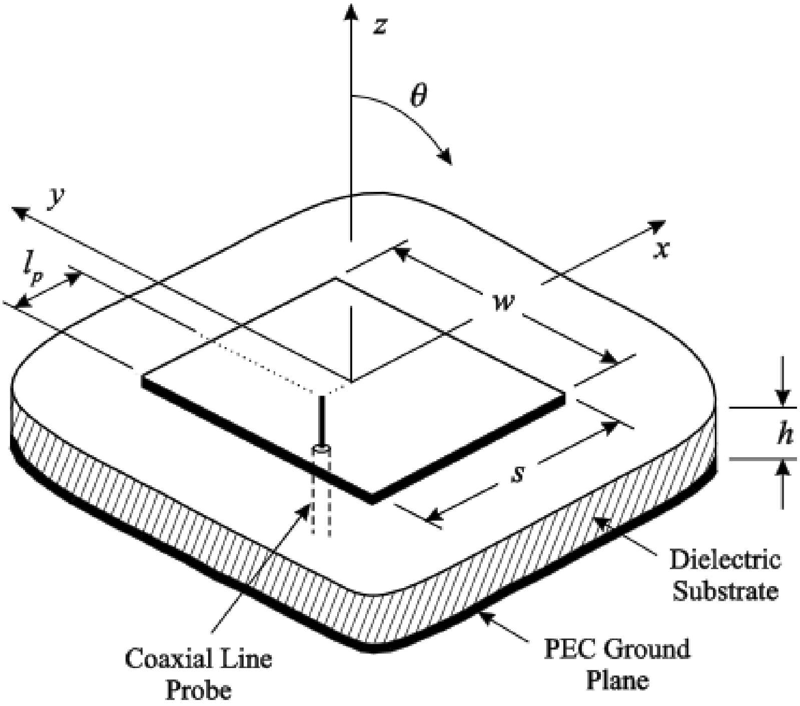

Figure A.23: Rectangular microstrip patch antenna fed by a coaxial line probe.

dent voltage, $V_t^+(t)$, in the feeding transmission line is a unit-amplitude, differentiated Gaussian pulse (Equation A.20) with the characteristic time $\tau_p = 2.65 \times 10^{-11}$ s. The peak of the spectrum for this pulse is at 6.0 GHz.

The dimensions of the FDTD rectangular cells ($\Delta x = 0.529$ mm, $\Delta y = 0.500$ mm, $\Delta z = 0.500$ mm) were chosen so that all of the details of the coaxial feed line could be included in the model, and the time step was $\Delta t = 9.44 \times 10^{-13}$ s. The number of time steps, N_t, required for the simulation was determined by observing the magnitude of the reflected voltage $|V_t^-|$ in the feeding transmission line versus the normalized time $t/\Delta t$; this is shown in Figure A.24(a). Notice that the vertical scale is logarithmic. When $t/\Delta t = 3000$, the reflected voltage has dropped by six orders of magnitude from its peak, and it is at the noise level for the computation. So any number of time steps greater than three thousand was deemed adequate for the simulation ($N_t = 4000$ was actually used).

Figure A.25 is a comparison of the FDTD theoretical results with the measurements. The graph in Figure A.25(a) shows the magnitude of the reflection coefficient versus frequency: theory (solid line) and measurement (dots). The agreement is reasonably good, particularly when we consider that some of the geometrical detail for the measurement, such as the precise geometry at the feed, were not known for use in the FDTD model.

The field patterns were measured with the 10 cm × 10 cm substrate mounted at the center of a circular aluminum image plane of diameter 1 m. We chose not to model this configuration with the same fine resolution used for the FDTD calculation of the reflection coefficient, because of the large amount of memory that would be required. Instead, larger cells were used with the dimensions $\Delta x = 1.59$ mm, $\Delta y = 1.42$ mm, $\Delta z = 1.57$ mm. The use of the larger cells causes little error in the far-zone field patterns. The FDTD and measured field patterns for the frequency $f = 6.8$ GHz are compared in Figure A.25(b). These plots show the gain (Equation A.15) versus angle, normalized to 0 dB at the peak. Results are given for both the E plane (x-z plane, solid line and dots) and the H plane (y-z plane, dashed line and triangles). Again the agreement is reasonably good.

For our second example, we chose a rectangular microstrip patch antenna designed to operate around $f = 1.9$ GHz that is similar to one reported in the literature [34]. The dimensions for the patch are $s = 5.12$ cm, $w = 6.0$ cm, and $h = 1.575$ mm, and the probe of the feeding coaxial line ($R_o = 50\ \Omega$) is displaced from the broad side of the patch by $l_p = 1.64$ cm. The dielectric substrate ($\epsilon_r = 2.2$ and $\sigma = 1.1 \times 10^{-3}$ S/m) and the ground plane are the same size: 11.5 cm × 11.5 cm. The incident voltage, $V_t^+(t)$, in the feeding transmission line is a unit-amplitude, differentiated Gaussian pulse (Equation A.20) with the characteristic time $\tau_p = 1.061 \times 10^{-10}$ s, and the peak of the spectrum for this pulse is at 1.5 GHz. Again, the parameters for the FDTD simulation allow complete modeling of the details of the coaxial feed line ($\Delta x = 0.529$ mm, $\Delta y = 0.500$ mm, $\Delta z = 0.500$ mm, $\Delta t = 9.91 \times 10^{-14}$ s). The electrical thickness of the substrate for this example is about one eighth of that for the previous example, $h/\lambda = 0.010$ (for $f = 1.9$ GHz) versus $h/\lambda = 0.077$ (for $f = 7.3$ GHz), so we expect this antenna to have a significantly narrower bandwidth [35].

Figure A.24(b) shows the magnitude of the reflected voltage $|V_t^-|$ in the feeding transmission line (logarithmic scale) versus the normalized time $t/\Delta t$. As a conse-

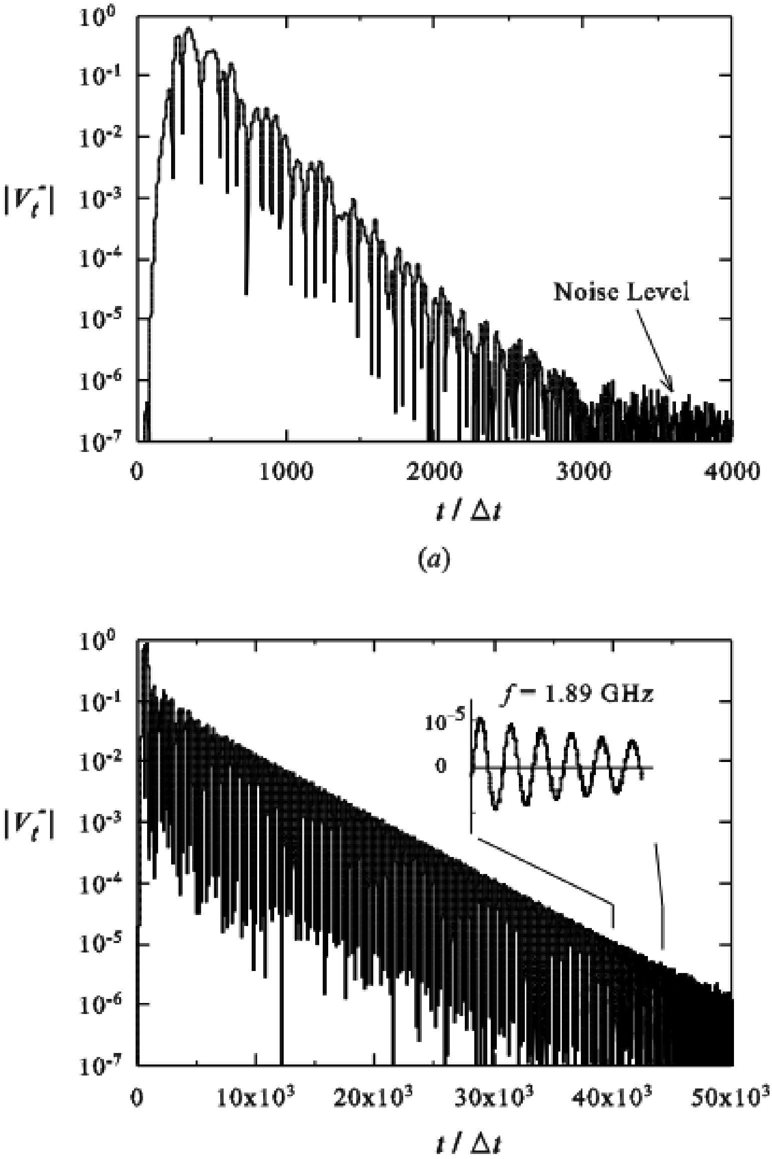

(a)

(b)

Figure A.24: The magnitude of the reflected voltage in the feeding coaxial line versus the normalized time. (a) Rectangular microstrip patch. (b) Narrow-band, rectangular microstrip patch.

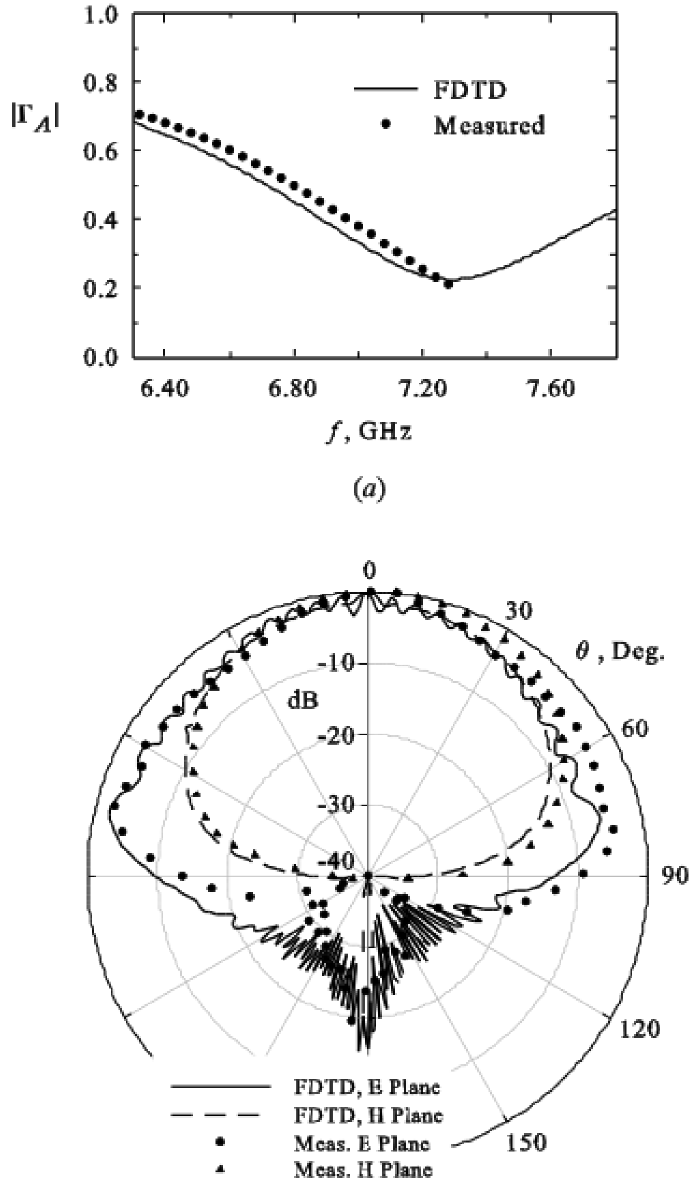

(a)

(b)

Figure A.25: Comparison of theoretical and measured results for the rectangular microstrip patch antenna. (a) Magnitude of reflection coefficient versus frequency. (b) Field patterns for E and H planes at the frequency $f = 6.8$ GHz. Measured results from [33].

quence of the narrower bandwidth, the reflected voltage decreases much more slowly with increasing $t/\Delta t$ than in the previous example, Figure A.24(a). The reflected voltage has dropped by six orders of magnitude from its peak and is approaching the noise level for the computation when $t/\Delta t = 50{,}000$. So about fifty thousand time steps ($N_t = 50{,}000$) are required for the simulation, as compared to three thousand for the previous example! The inset in Figure A.24(b) shows the magnitude of the reflected voltage, plotted on a linear scale, for times around $t/\Delta t = 40{,}000$. The voltage is seen to be a slowly decaying sinusoid at the frequency $f \approx 1.89$ GHz.

In Figure A.26 we show the magnitude of the reflection coefficient versus frequency for simulations with different numbers of time steps: $N_t = 8{,}000$, $N_t = 24{,}000$, and $N_t = 50{,}000$. For each case, a Hanning window is applied in time to eliminate truncation artifacts. The antenna is seen to be matched at the frequency $f = 1.89$ GHz, and the "apparent" bandwidth for the match is seen to depend on the number of time steps used for the simulation. Thus, if one were to underestimate the number of time steps required for the simulation to converge, one would think that the antenna had a much wider bandwidth for the reflection coefficient than it actually has. With the detailed analysis presented above, this point may appear to be obvious. However, sometimes, particularly when a computation is automated, this degree of analysis may not be performed every time a parameter for the antenna, such as the thickness of the substrate, is changed.

In some cases, special techniques can be applied to shorten the computation for a narrow-bandwidth antenna. For example, because of the well-defined, decaying sinusoidal waveform in the reflection coefficient for this antenna, a shorter computation time, say $N_t = 20{,}000$, could be used with an extrapolation for the remainder of the waveform. Such techniques are discussed in the literature [36].

A.6 Summary and Conclusions

In this appendix, we have presented an introduction to the finite-difference time-domain method, aimed at readers who have little or no experience with the method. We have limited the presentation to the basics of the method, avoiding mention of many refinements that are generally restricted to particular applications. To give the reader a sense of the breadth of application allowed by these refinements, we present a partial list below.

- Techniques for handling materials with dispersive properties (properties that are a function of the frequency), anisotropic properties (properties that depend on the direction of the field components), and nonlinear properties.
- Methods for incorporating impedance boundary conditions.
- Subcell methods for treating material sheets that are thinner than an FDTD cell.
- Methods for incorporating periodic boundary conditions, which are useful in treating antenna arrays.
- Higher-order FDTD schemes that have lower error (numerical dispersion) than the conventional Yee algorithm.

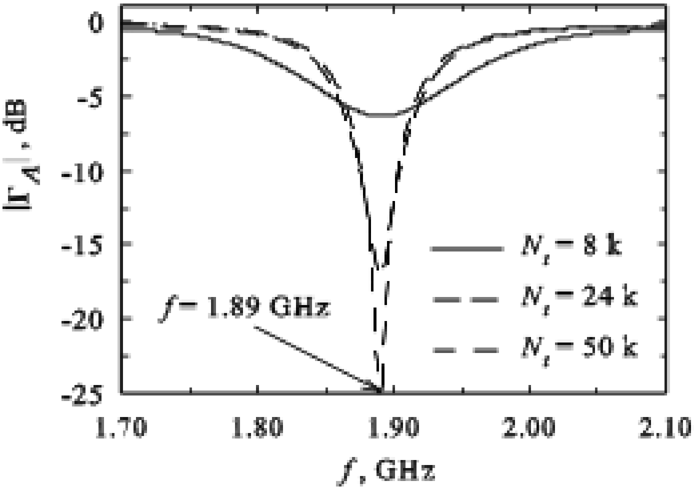

Figure A.26: Narrow-band, rectangular microstrip patch antenna. Magnitude of reflection coefficient versus frequency for three different numbers of time steps.

- Techniques for incorporating nonuniform and nonorthogonal grids.
- Special procedures for handling objects that are bodies of revolution.

The brevity of this appendix precluded the derivation of the mathematical formulas associated with the method, e.g., FDTD update equations, equations for the perfectly matched layer, etc. These formulas can be found in the comprehensive treatment of the method contained in the book edited by Taflove and Hagness [9]. A comprehensive web site on the method is maintained by J. B. Schneider at Washington State University: `www.fdtd.org`. This site contains searchable lists of books, journal papers, conference papers, and dissertations.

To assess the popularity of the FDTD method, a search was done with INSPEC for documents that included either "finite-difference time-domain" or "FDTD" in the title.[4] The results of the search, presented in Figure A.27, clearly show the rapid growth in the popularity of the method over the last twenty-five years.

The emphasis throughout this appendix has been on the application of the FDTD method to the analysis of antennas. After brief discussions of the special formulations associated with transmitting and receiving antennas, the details for the analysis of a few different types of antennas were presented. Because of the brevity of this appendix, no attempt was made to mention all of the different antennas that have been analyzed with the method. Many individuals have used the method to treat antennas; as an indication

---

[4] A few of these documents apply the finite-difference time-domain method to problems other than electromagnetic, such as acoustic problems.

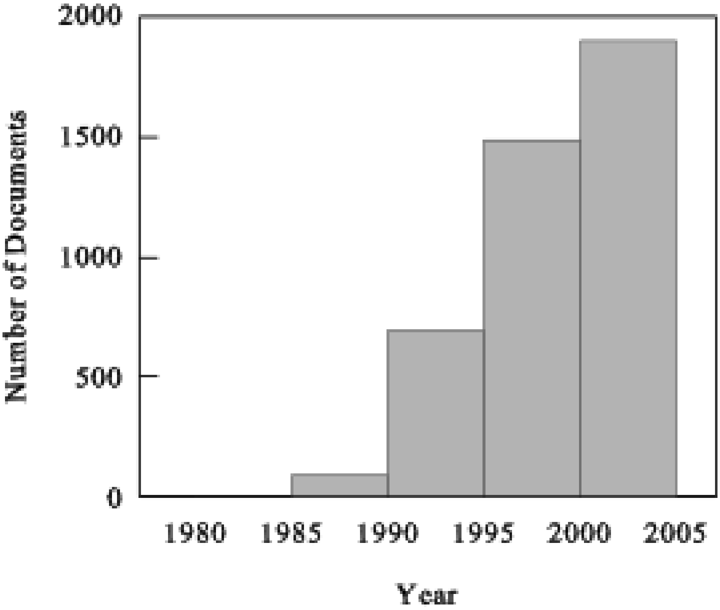

Figure A.27: Number of documents published over a twenty-year span that include the words “finite-difference time-domain” or “FDTD” in the title. Each bar shows the total number of documents published during a five-year period.

of the number, the INSPEC search mentioned above listed over 500 documents with FDTD and antenna(s) in the title.

All of the numerical results presented in the examples were obtained by the authors or their students. Thus, we have very detailed knowledge for each example and can make fairly accurate statements about the results. These examples were chosen not only to show the power of the FDTD method, particularly the good agreement with experimental measurements, but also to show that the method has some limitations—albeit, the limitations are sometimes due to the crudeness of the theoretical model for the antenna or the choice of the parameters for the simulation. The refinement of the FDTD method and its application to practical problems is an ongoing story, and undoubtedly there will be some exciting accomplishments made in the future.

One area with great promise is the use of the method for antenna synthesis. Here we do not mean the conventional approach in which the method is coupled with an optimization routine and used to choose the parameters for a standard antenna (dipole, horn, etc.) so that certain criteria for the performance are met. What we have in mind for antenna synthesis is quite different—a more modern approach. In this approach, the structure of the antenna is not completely predetermined with only a few parameters to be chosen, but the structure of the antenna is actually developed as part of the synthesis. The FDTD method is well suited for use in such schemes; because of the flexibility of the method, a new structure can easily be introduced. The antenna structure is changed by simply changing the electromagnetic constitutive parameters associated with individual cells. *The earlier chapters in this book describe the "fragmented aperture" concept, which relied heavily on the FDTD method as described in this appendix* [37]–[40].

References

[1] K. S. Yee, "Numerical Solution of Initial Boundary Value Problems Involving Maxwell's Equations in Isotropic Media," IEEE Trans. Antennas Propagat., Vol. AP-14, pp. 302–307, May 1966.

[2] J. G. Maloney, G. S. Smith, and W. R. Scott, Jr., "Accurate Computation of the Radiation from Simple Antennas Using the Finite-Difference Time-Domain Method," IEEE Trans. Antennas Propagat., Vol. AP-38, pp. 1059–1068, July 1990.

[3] J. J. Boonzaaier and C. W. Pistorius, "Thin Wire Dipoles: A Finite-Difference Time-Domain Approach," Electronics Lett., Vol. 26, pp. 1891–1892, October 1990.

[4] D. S. Katz, M. J. Picket-May, A. Taflove, and K. R. Umashankar, "FDTD Analysis of Electromagnetic Wave Radiation from Systems Containing Horn Antennas," IEEE Trans. Antennas Propagat., Vol. AP-39, pp. 1203–1212, August 1991.

[5] P. A. Tirkus and C. A. Balanis, "Finite-Difference Time-Domain Method for Antenna Radiation," IEEE Trans. Antennas Propagat., Vol. AP-40, pp. 334–340, March 1992.

[6] R. J. Luebbers and J. Beggs, "FDTD Calculation of Wide-Band Antenna Gain and Efficiency," IEEE Trans. Antennas Propagat., Vol. AP-40, pp. 1403–1407, November 1992.

[7] J. G. Maloney and G. S. Smith, "Modeling of Antennas," Chapter 7 in A. Taflove, Editor, Advances in Computational Electrodynamics, The Finite-Difference Time-Domain Method, pp. 409–460, Artech House, Boston, 1998. Also, J. G. Maloney, G. S. Smith, E. Thiele, O. Gandhi, N. Chavannes, and S. Hagness, Chapter 14 in A. Taflove and S. Hagness, Editors, Computational Electrodynamics: The Finite-Difference Time-Domain Method, 3rd Edition, pp. 607–676, Artech House, Boston, 2005.

[8] G. S. Smith, An Introduction to Classical Electromagnetic Radiation, Cambridge University Press, Cambridge, UK, 1997.

[9] A. Taflove and S. C. Hagness, Editors, Computational Electrodynamics: The Finite-Difference Time-Domain Method, 3rd Edition, Artech House, Boston, 2005.

[10] J. B. Schneider and C. L. Wagner, "FDTD Dispersion Revisited: Faster-Than-Light Propagation," IEEE Microwave and Guided Wave Lett., Vol. 9, pp. 54–56, February 1999.

[11] S. Gedney, "An Anisotropic Perfectly Matched Layer-Absorbing Medium for the Truncation of FDTD Lattices," IEEE Trans. Antennas Propagat., Vol. AP-44, pp. 1630–1639, December 1996.

[12] S. Gedney, "Perfectly Matched Layer Absorbing Boundary Conditions," Chapter 7 in A. Taflove and S. C. Hagness, Editors, Computational Electrodynamics: The Finite-Difference Time-Domain Method, 3rd Edition, pp. 273–328, Artech House, Boston, 2005.

[13] K. L. Shlager and G. S. Smith, "Near-Field to Near-Field Transformation for Use With FDTD Method and Its Application to Pulsed Antenna Problems," Electronics Lett., Vol. 30, pp. 1262–1264, August 1994.

[14] K. L. Shlager and G. S. Smith, "Comparison of Two Near-Field to Near-Field Transformations Applied to Pulsed Antenna Problems," Electronics Lett., Vol. 31, pp. 936–938, June 1995.

[15] G. S. Smith, "A Direct Derivation of a Single-Antenna Reciprocity Relation for the Time Domain," IEEE Trans. Antennas Propagat., Vol. AP-52, pp. 1568–1577, June 2004.

[16] J. G. Maloney, M. P. Kesler, and G. S. Smith, "Generalization of PML to Cylindrical Geometries," 13th Annual Review of Progress in Applied Computational Electromagnetics, Monterey, CA, pp. 900–908, March 1997.

[17] G. S. Smith and T. W. Hertel, "On the Transient Radiation of Energy from Simple Current Distributions and Linear Antennas," IEEE Antennas Propagat. Magazine, Vol. 43, pp. 49–62, June 2001.

[18] T. W. Hertel and G. S. Smith, "On the Convergence of Common FDTD Feed Models for Antennas," IEEE Trans. Antennas Propagat., Vol. AP-51, pp. 1771–1779, August 2003.

[19] R. W. P. King, The Theory of Linear Antennas, p. 20, Harvard Univ. Press, Cambridge, MA, 1956.

[20] J. G. Maloney, K. L. Shlager, and G. S. Smith, "A Simple FDTD Model for Transient Excitation of Antennas by Transmission Lines," IEEE Trans. Antennas Propagat., Vol. AP-42, pp. 289–292, February 1994.

[21] S. Dey and R. Mittra, "A Locally Conformal Finite-Difference Time-Domain (FDTD) Algorithm for Modeling Three-Dimensional Perfectly Conducting Objects," IEEE Microwave and Guided Wave Lett., Vol. 7, pp. 273–275, September 1997.

[22] A. Taflove, M. Celuch-Marcysiak, and S. Hagness, "Local Subcell Models of Fine Geometrical Features," Chapter 10 in A. Taflove and S. C. Hagness, Editors, Computational Electrodynamics: The Finite-Difference Time-Domain Method, 3rd Edition, pp. 407–462, Artech House, Boston, 2005.

[23] S. Gedney, F. Lansing, and N. Chavannes, "Nonuniform Grids, Nonorthogonal Grids, Unstructured Grids, and Subgrids," Chapter 11 in A. Taflove and S. C. Hagness, Editors, Computational Electrodynamics: The Finite-Difference Time-Domain Method, 3rd Edition, pp. 463–516, Artech House, Boston, 2005.

[24] A. C. Cangellaris and D. B. Wright, "Analysis of the Numerical Error Caused by the Stair-Stepped Approximation of a Conducting Boundary in FDTD Simulations of Electromagnetic Phenomena," IEEE Trans. Antennas Propagat., Vol. AP-39, pp. 1518–1525, October 1991.

[25] R. Holland, "Pitfalls of Staircase Meshing," IEEE Trans. Electromagnetic Compatibility, Vol. 35, pp. 434–439, November 1993.

[26] T. W. Hertel and G. S. Smith, "Analysis and Design of Two-Arm Conical Spiral Antennas," IEEE Trans. Electromagnetic Compatibility, Vol. 44, pp. 25–37, February 2002.

[27] T. W. Hertel and G. S. Smith, "On the Dispersive Properties of the Conical Spiral Antenna and Its Use for Pulsed Radiation," IEEE Trans. Antennas Propagat., Vol. AP-51, pp. 1426–1433, July 2003.

[28] J. D. Dyson, "The Characteristics and Design of the Conical Log-Spiral Antenna," IEEE Trans. Antennas Propagat., Vol. AP-13, pp. 488–499, July 1965.

[29] K. L. Shlager, G. S. Smith, and J. G. Maloney, "Accurate Analysis of TEM Horn Antennas for Pulse Radiation," IEEE Trans. Electromagnetic Compatibility, Vol. 38, pp. 414–423, August 1996.

[30] R. T. Lee and G. S. Smith, “On the Characteristic Impedance of the TEM Horn Antenna,” IEEE Trans. Antennas Propagat., Vol. AP-52, pp. 315–318, January 2004.

[31] R. T. Lee and G. S. Smith, “A Design Study for the Basic TEM Horn Antenna,” IEEE Antennas Propagat. Magazine, Vol. 46, pp. 86–92, February 2004.

[32] K. L. Shlager, G. S. Smith, and J. G. Maloney, “Optimization of Bow-Tie Antennas for Pulse Radiation,” IEEE Trans. Antennas Propagat., Vol. AP-42, pp. 975–982, July 1994.

[33] E. Chang, S. A. Long, and W. F. Richards, “An Experimental Investigation of Electrically Thick Rectangular Microstrip Antennas,” IEEE Trans. Antennas Propagat., Vol. AP-34, pp. 767–772, June 1986.

[34] H. Abdallah, W. Wasylkiwskyj, K. Parikh, and A. Zaghloul, “Comparison of Return Loss Calculations with Measurements of Narrow-Band Microstrip Patch Antennas,” ACES Journal, Vol. 19, pp. 184–186, November 2004.

[35] D. R. Jackson and N. G. Alexopoulos, “Simple Approximate Formulas for the Input Resistance, Bandwidth, and Efficiency of a Resonant Rectangular Patch,” IEEE Trans. Antennas Propagat., Vol. AP-39, pp. 407–410, March 1991.

[36] S. Chebolu, R. Mittra, and W. D. Becker, “The Analysis of Microwave Antennas Using the FDTD Method,” Microwave Journal, Vol. 39, pp. 134–150, January 1996.

[37] J. G. Maloney, P. H. Harms, M. P. Kesler, T. L. Fountain, and G. S. Smith, “Novel, Planar Antennas Designed Using the Genetic Algorithm,” 1999 USNC/URSI Radio Science Meeting, Orlando, FL, p. 237, July 1999.

[38] J. G. Maloney, M. P. Kesler, P. H. Harms, T. L. Fountain, and G. S. Smith, “The Fragmented Aperture Antenna: FDTD Analysis and Measurement,” Millennium Conference on Antennas and Propagation (AP 2000), Davos, Switzerland, 4 pages, April 2000.

[39] J. G. Maloney, M. P. Kesler, P. H. Harms, and G. S. Smith, Fragmented Aperture Antennas and Broadband Ground Planes, U.S. Patent No. 6,323,809 B1, November 27, 2001.

[40] L. N. Pringle, P. H. Harms, S. P. Blalock, G. N. Kiesel, E. J. Kuster, P. G. Friederich, R. J. Prado, J. M. Morris, and G. S. Smith, “A Reconfigurable Aperture Antenna Based on Switched Links Between Electrically Small Metallic Patches,” IEEE Trans. Antennas Propagat., Vol. AP-52, pp. 1434–1445, June 2004.

[41] **[Incomplete reference: Balanis Antenna Engineering Handbook chapter — need full citation with chapter number, page range, edition, and year.]**